Generation of Few-Photon States with Excitons and Biexcitons in Semiconductor Quantum Dots

Dissertation

submitted in partial fulfillment of the requirements for the degree of

Dr. rer. nat.

to the Department of Physics at Paderborn University, Germany

by

David Bauch

Paderborn, December 29, 2024

Examination Committee

Prof. Dr. Stefan Schumacher

Prof. Dr. Jens Förstner

Prof. Dr. Klaus D. Jöns

Dr. Hendrik Rose

Kurzfassung

In der Quanteninformationstheorie ist eine präzise Kontrolle über Quantenzustände von entscheidender Bedeutung. Phänomene wie Verschränkung, Superposition und Interferenz von Quantenteilchen ermöglichen die Darstellung und Manipulation von Quantenbits (Qubits), die fundamental für Quantencomputing, Quantenkryptographie und fortschrittliche Quantenkommunikationstechnologien sind. Wenig-Photonen-Emitter spielen dabei eine entscheidende Rolle, da sie die Erzeugung solcher Zustände mit hoher Güte ermöglichen, was für die Entwicklung skalierbarer und robuster Quanteninformationssysteme unerlässlich ist.

Diese Arbeit untersucht die theoretische Erzeugung von Wenig-Photonen-Zuständen mithilfe von Halbleiterquantenpunkten und optischen Resonatoren für Anwendungen in der Quanteninformationsverarbeitung. Quantenpunkte sind nanoskopische Halbleiterstrukturen und hervorragende Photonenquellen, da sie durch die dreidimensionale Einschränkung der Ladungsträger diskrete Energiestrukturen ausbilden, insbesondere Exzitonen, Biexzitonen und Trionen. Diese Energiekonfigurationen ermöglichen die Emission von Photonen, die sowohl optisch als auch elektronisch präzise kontrolliert werden können, was sie zu idealen Kandidaten für Quantentechnologien macht. Es werden drei Hauptthemen untersucht: Zunächst wird das Anregungsproblem bei der resonanten Anregung von Quantenpunkten in Resonatoren umgangen, indem ein nicht-resonantes System angeregt und mittels ultraschneller elektrischer Steuerung der Energien durch den Quantum-Confined-Stark-Effekt in Resonanz gebracht wird, was die Qualität der emittierten Photonen maximiert. Anschließend ermöglicht ein spektral breiter zirkularer Bragg-Resonator die Erzeugung von Photonen, die sowohl ununterscheidbar als auch verschränkt sind. Abschließend wird die Erzeugung eindimensionaler linearer Clusterzustände durch Emission von Photonenketten aus gestapelten Quantenpunkten mittels Spin-Hole-Trionen untersucht, was numerisch mit hoher Güte realisierbar und essenziell für zahlreiche Protokolle im Quantencomputing ist. Die numerische Auswertung der Systemdynamiken erfolgt mithilfe der von Neumann Gleichung, der Polaron-Master Gleichung und der Pfadintegralmethode. Durch Berücksichtigung idealer und realistischer Parameter, einschließlich Verluste und Dephasierung, wird die Robustheit der Methoden demonstriert. Die Ergebnisse dieser Arbeit bieten wertvolle Einblicke in die Optimierung von Quantenpunkt-Emittern und in die Entwicklung von Wenig-Photonen-Quantenzuständen für zukünftige Quantentechnologien.

Abstract

In quantum information theory, precise control over quantum states is essential. Phenomena such as entanglement, superposition, and interference of quantum particles enable the representation and manipulation of quantum bits in quantum computing, cryptography, and advanced communication technologies. Few-photon emitters play a critical role in achieving this control by allowing for the high-fidelity generation, manipulation, and detection of photonic quantum states. These states are fundamental for the development of scalable and robust quantum information systems.

This study investigates the theoretical generation of few-photon states utilizing semiconductor quantum dots, with selective integration of optical cavities, for quantum information processing applications. Quantum dots are nanoscale structures and excellent candidates due to the discrete energy configurations arising from the three-dimensional confinement of charge carriers, specifically excitons, biexcitons, and trions. These energy configurations allow for the emission of photons that can be precisely manipulated both optically and electronically, making them highly relevant for quantum technologies. This research addresses three key challenges in generating few-photon quantum states. First, the excitation of quantum dots states, where conventional resonant excitation is hindered by spectral overlap with cavity modes, is augmented by employing ultrafast electric control of energy levels via the quantum confined Stark effect. This decouples the excitation process from the emission, restoring optimal photon emission characteristics. Second, a spectrally broad circular Bragg cavity is introduced to mediate the production of photons from biexcitons that are both indistinguishable and entangled, overcoming the typical trade-off between these two properties while ensuring the practicability of the resonator. Third, the creation of one-dimensional linear cluster states is investigated by emitting trains of photons from stacked quantum dots using spin-hole trions. These cluster states, essential for quantum computing protocols, are numerically generated with high fidelity, even in the presence of losses. The numerical evaluation and theoretical validation of the dynamics of the systems are performed by solving the von Neumann equation using the Polaron Master Equation and Path Integral methods. By considering both ideal and realistic conditions - including radiative losses, pure dephasing, and electron-phonon coupling - the robustness of the results in practical scenarios and their implementability is demonstrated. The findings provide valuable insights into optimizing quantum dot emitter devices and show how cavity resonators enhance the production of high-fidelity photonic quantum states. This work lays a solid foundation for future advancements in quantum information technologies.

Scientific Contributions

Publications

[P1] **David Bauch**, Dirk Heinze, Jens Förstner, Klaus D. Jöns, and Stefan Schumacher. *Ultrafast electric control of cavity mediated single-photon and photon-pair generation with semiconductor quantum dots.* Physical Review B **104**, 085308 (2021).

[P2] **David Bauch**, Dustin Siebert, Klaus D. Jöns, Jens Förstner, and Stefan Schumacher. *On-demand indistinguishable and entangled photons using tailored cavity designs.* Advanced Quantum Technologies **7**, 2300142 (2024).

[P3] **David Bauch**, Nikolas Köcher, Nils Heinisch, and Stefan Schumacher. *Time-bin entanglement in the deterministic generation of linear photonic cluster states.* APL Quantum **1**, 036110 (2024).

[P4] Nils Heinisch, Nikolas Köcher, **David Bauch**, and Stefan Schumacher. *Swing-up dynamics in quantum emitter cavity systems: Near ideal single photons and entangled photon pairs.* Physical Review Research **6**, L012017 (2024).

[P5] Lukas Hanschke, Thomas K. Bracht, Eva Schöll, **David Bauch**, Eva Berger, Patricia Kallert, Melina Peter, Ailton J. Garcia Jr., Saimon F. Covre da Silva, Santanu Manna, Armando Rastelli, Stefan Schumacher, Doris E. Reiter, and Klaus D. Jöns, *Experimental measurement of the reappearance of Rabi rotations in semiconductor quantum dots.* 10.48550/arXiv.2409.19167 (2024).

This work builds upon the foundations established in [P1-P3] and incorporates insights from [P4,P5], synthesizing and extending the topics explored in these publications.

Conferences

[C1] **David Bauch**, Dirk Heinze, Jens Förstner, Klaus D. Jöns, and Stefan Schumacher. *Ultrafast electric control of cavity mediated photons from a semiconductor quantum-dot* (Talk). DPG Conference Regensburg, Regensburg, Germany (8. September 2022).

[C2] **David Bauch**, Dustin Siebert, Jens Förstner, Klaus D. Jöns, and Stefan Schumacher. *Generation of indistinguishable and entangled photons at telecom frequencies using tailored cavity designs* (Talk). DPG conference in Dresden, Dresden, Germany (29. März 2023).

[C3] **David Bauch**, Nikolas Köcher, Nils Heinisch, and Stefan Schumacher. *Dynamics of Robust Photonic Cluster-State Generation from Quantum-Dot Molecules* (Talk). DPG conference in Berlin, Berlin, Germany (19. März 2024).

Other

All simulations presented in this work and in the foundational publications were performed using custom-developed software specifically created for this purpose. The source code is available at

[S1] **David Bauch**. ***QDaCC: Quantum Dot and Cavity Computing***. github.com/david-bauch/QDaCC (2023).

Although not directly related to this thesis, this work is still noteworthy and deserves mention

[S2] Jan Wingenbach, **David Bauch**, Xuekai Ma, Robert Schade, Christian Plessl, and Stefan Schumacher. ***PHOENIX - Paderborn Highly Optimized and Energy efficient solver for two-dimensional Nonlinear Schroedinger equations with Integrated eXtensions.*** github.com/davidbauch/PHOENIX (2024).

Contents

Introduction 1

Classical information processing is integral to modern life, driving devices such as computers, smartphones, and various electronic appliances. These devices often connect to the internet, forming the *Internet of Things* (IoT). In classical information processing, binary units known as bits - represented as 0s and 1s - are used to encode information. Although bits can be managed electronically or mechanically, the information content of a single bit is inherently limited by its binary nature.

Typically, electrons are used in the form of electric currents to control electronic transistors, which serve as the fundamental units of classical information processing. These transistors can be switched on or off, corresponding to logical 1s or 0s, respectively. Extensive research has focused on making these transistors faster, smaller, and more energy-efficient [1]. However, as transistors shrink in size, they approach physical limits imposed by quantum mechanics.

In recent decades, various theoretical limits have been proposed for the minimum size of transistor-based electronics [2, 3]. Estimates suggest that this limit could be as large as 10 nm. Despite these predictions, technological advancements have pushed the size of transistors into the single-digit nanometer range [4, 5]. However, when transistors become extremely small, quantum effects such as electron tunneling dominate, rendering these components impractical for conventional use [3].

In response to these limitations, *quantum information processing* (QIP) has gained significant interest and relevance in the scientific community over the past few decades [6–10]. Unlike classical communication systems that rely on binary bits to represent information, quantum information processing utilizes quantum particles as information carriers. These quantum carriers are not restricted to binary states but can encode and exchange information in a far more complex manner, as visualized in Fig. 1.1, panel (a).

The primary objective of quantum information processing is to achieve rapid and reliable data transfer over long distances, facilitating communication between disparate data sources and processing units. Beyond communication, quantum information processing extends to various other critical fields, including quantum computing [11–17], quantum key distribution [18, 19], and quantum cryptography [20–22]. These fields impose stringent

requirements on the quantum information carriers, necessitating highly precise and reliable emitters to ensure the integrity and security of data transmission and processing.

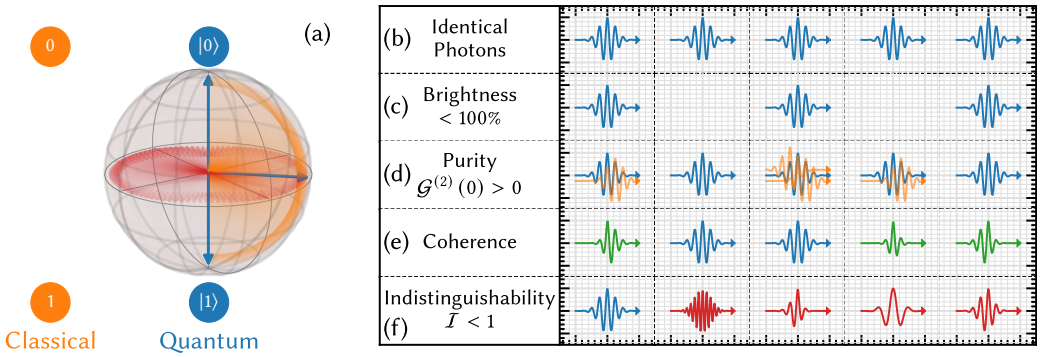

Figure 1.1: Classical bit vs photonic quantum bit (a) A classical bit, represented by a system being either in the zero ("0") or one ("1") state (orange dots), is compared to a quantum bit, where the superposition of two states $|0\rangle$ and $|1\rangle$ is used to encode information. This enables the quantum bit to carry significantly more information than its classical counterpart, indicated by the blurred arrows. **(b-f)** Various quality aspects of the photon emitter source are depicted. In an ideal scenario, the photons are identical, coherent, and thus indistinguishable, achieving 100% brightness and unity purity. Inspired by Michler, *Quantum dots for quantum information technologies*, [23].

Numerous approaches exist for creating emitters in quantum information processing, each exploiting different quantum phenomena such as superposition of quantum states and quantum entanglement. These methods involve various physical systems [24, 25], including atoms [26], trapped ions [27], superconducting circuits for single-photon detection [28–30], nanowires [31, 32], color centers and vacancies [33], and quantum dots [23, 34–41]. Each system offers a unique set of advantages and challenges, making the selection of an appropriate emitter a critical aspect of quantum information processing. Quantum dots, in particular, are promising due to the discrete energy levels arising from the three-dimensional confinement of charge carriers, scalability, and compatibility with existing semiconductor technology, allowing for deterministic photon emission and precise control over quantum states.

Advancements in this field involve exploring materials, timescales, interaction strengths, and scalability to optimize the performance of quantum information carriers [23, 42]. These efforts aim to enable and enhance the capabilities of quantum technologies, ensuring practical and efficient methods for real-world applications. This study focuses on a specific aspect of this research landscape by investigating quantum dots as sources for photon

generation, which then serve as quantum information carriers. In the following sections, the properties of photons relevant to quantum information processing will be discussed, followed by an exploration of semiconductor systems used for their generation.

1.1 Photons as Quantum Information Carriers

Classically, light is perceived as a vector field characterized by its intensity, phase, and other macroscopic properties, such as the vectorial polarization. A deeper investigation into the nature of light reveals that it is composed of individual particles called *photons*. For classical light, the number of photons is Poisson-distributed around a given intensity maximum. Initially, the framework of intensity remains applicable, but as the investigation progresses into the quantum realm with fewer photons, it enters the domain of few-photon physics, where only a small number of countable photons exist [43].

In the few-photon regime, photon states exhibit distinct quantum properties such as purity, indistinguishability, and entanglement, which are critical for quantum applications. Purity, for instance, measures how effectively photons behave as individual single photons. When photons cluster together, known as *bunching*, they resemble classical light and exhibit lower purity [18, 39, 44–46]. Conversely, when photons are completely separated, known as *antibunching*, their purity reaches unity, indicating the presence of true single photons. Achieving high photon purity is essential for quantum information processing applications [47–49], ensuring that the emitter produces well-defined, single-photon states.

Indistinguishability is another crucial property that measures the similarity of photons emitted by a source [13, 50, 51]. High indistinguishability indicates that photons are nearly identical in terms of emission frequency and coherence [52–54], enabling interference between multiple photons [55]. This property is vital for implementing quantum gates, which are the building blocks of quantum circuits, as well as for applications in quantum computing, cryptography, and communication technologies [11, 12, 14, 20–22, 42, 56–58]. Experimentally, sources capable of producing highly indistinguishable and pure photons have been successfully implemented [46].

In certain scenarios, generating more than one photon is desirable, particularly when two photons can be quantum mechanically entangled [59, 60]. Quantum entanglement is a phenomenon in which two or more particles become correlated such that the quantum state of each particle cannot be described independently of the state of the others, even when

the particles themselves are separated, for example by distance. This intrinsic correlation means that measurements performed on one particle are directly related to measurements on the other(s), reflecting the inseparable nature of their shared quantum state. Entangled photons are essential for numerous quantum technologies, including quantum teleportation [61], entanglement swapping for quantum repeaters [62, 63], quantum key distribution [56, 64, 65], quantum error correction [66, 67], and superdense coding [68].

Quantum teleportation, for example, enables the transfer of quantum information between different locations without physically moving the particle. This process involves entangling two particles, with one particle sent to the receiving location. A joint measurement is performed on the particle to be teleported and one member of the entangled pair, effectively transferring the state of the particle to the second entangled particle at the receiving location. This protocol is foundational for quantum communication and the development of a quantum internet.

In quantum key distribution, entanglement is employed to ensure secure communication. Entangled photon pairs can be used to generate shared, random cryptographic keys between distant parties. Any attempt to intercept the communication disturbs the entanglement, making the eavesdropping detectable and providing a level of security unattainable with classical cryptography [56, 65, 69].

Entanglement is also critical in quantum error correction, which safeguards quantum information from decoherence and other quantum noise [10, 67]. Quantum error correction codes rely on the creation of highly entangled states among multiple photonic qubits, allowing errors to be detected and corrected without directly measuring the qubits. This preserves the quantum information and enables reliable quantum computation. Entangled states are also essential for quantum algorithms such as Shor's algorithm for integer factorization [70, 71] and Grover's search algorithm [72], offering exponential speedup for specific problems.

The significance of entangled photons is further underscored by their ideal properties as quantum information carriers. Photons are robust against decoherence and can travel long distances with minimal loss, even at non-zero temperatures [73]. The generation, manipulation, and detection of entangled photons are thus central to the advancement of quantum information technologies. Techniques to create entangled photon pairs, such as spontaneous parametric down-conversion, four-wave mixing, or deterministic two-photon emission, are fundamental to these applications [73].

Achieving high degrees of entanglement often compromises photon indistinguishability and purity, since the intrinsic multi-photon requirements for entanglement introduce complexities that degrade these properties [51, 74]. Addressing these challenges remains a significant focus of research [75–80], with the generation of indistinguishable and entangled photons being crucial for realizing quantum gates, making high-quality photons indispensable [81]. Achieving unity values in photon properties, as visualized in Fig. 1.1, panel (b), is essential for classifying photon sources in terms of reliability and efficiency.

Quantum dots have emerged as a leading candidate for the generation of high quality photons due to their ability to deterministically produce single or few-photon states [34, 82, 83] on demand [84–86], with precise control over the emission properties [84, 87–91]. Their versatility, combined with compatibility for integration into telecommunications systems [92–97], makes them a critical component in the advancement of quantum information processing technologies.

The next section introduces quantum dots as photon emitters, focusing on the electronic states within these structures. Understanding the emerging energy configurations and how they facilitate controlled photon emission provides a foundation for leveraging quantum dots in advanced quantum information protocols.

1.2 Electronic States in Semiconductor Quantum Dots

The energy landscape emerging from a given arrangement of semiconductor material can be determined by analyzing the system's n-dimensional density of states (DOS), generally given by $\mathrm{DOS}(E)_n = \frac{1}{V}\sum_{i=1}^{N}\delta(E-E_i)$, with energy E, volume V and particle number N [98, 99]. The density of states is a function that describes the number of available quantum states at each energy in a material and is strongly dependent on the energy dispersion of the system. The transition from macroscopic structures to the microscopic regime is elucidated using this metric and is visualized in Fig. 1.2, assuming parabolic free-particle energy dispersion.

In three dimensions, commonly associated with a macroscopic, bulk material, the electronic energy of the system is proportional to the square of the density of states, with $E_{3\mathrm{D}} \propto \mathrm{DOS}^2$ [101]. With rising expansion of the material, the energy landscape becomes more complex, resulting in a characteristic band structure for the energy distribution. When the system is reduced to a two dimensional surface, the total electronic energy is proportional to

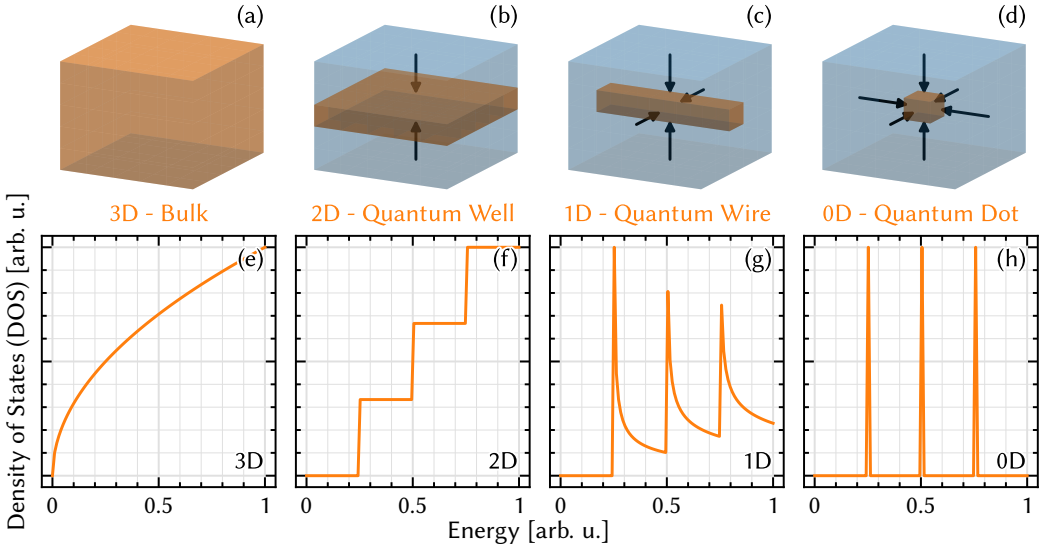

Figure 1.2: Schematic representation of the reduction process from 3D to 0D materials using the Density of States. **(a-d)** depict the spatial confinement of the material, resulting from the lower band gap energy in the orange material vs the blue material. The black arrows indicate the dimensions of confinement. **(e-h)** depict a schematic representation of the DOS for the confinements depicted above. Inspired by [100].

a constant value after a threshold DOS is exceeded, with $E_{2D} \propto$ DOS. Further reducing the dimensionality to one, such as in the case of a linear atomic or molecular chain, the electronic energy scales with the reciprocal square of the DOS, such that $E_{1D} \propto \text{DOS}^{-2}$. Finally, in the limit of zero dimensions, only a small set of states is available, leading to discrete energy levels. As true zero-dimensional objects are not practical for real-world implementations, a quasi-zero-dimensional object only a few nanometers in size is considered, retaining characteristics from higher-dimensional systems with confinement strong enough to predominantly localize the energies [102, 103]. These structures are referred to as quantum dots (QDs) in the following discussion.

Quantum dots are microscopic, nanometer sized structures composed of semiconductor materials, such as Gallium Arsenide (GaAs) [104, 105], Indium Arsenide (InAs) [75, 106–108] or similar materials [109–111], and are commonly embedded into a semiconductor environment. These materials exhibit band gaps that span from just under one to several electronvolts, encompassing the near-infrared [18, 112], visible, and ultraviolet regions of the spectrum of light [113, 114]. Quantum dots operating in the near-infrared are particularly interesting for telecommunication applications [18], where wavelengths around the telecom

bands of 1550 nm are optimal to minimize losses within the optical fibers used for data transmission [92–96]. Common fabrication methods include using advanced etching [115–117] or epitaxial growth [117, 118] techniques, where layers of material are precisely deposited to form the desired nanostructures. Common methods include the Stranski-Krastanov growth, where the formation of quantum dots is driven by strain-induced islanding on a lattice-mismatched substrate [107, 111]. Other methods include colloidal synthesis [119–121] and droplet epitaxy [118, 122], each offering unique advantages for specific applications such as control over size, shape and density of the dots.

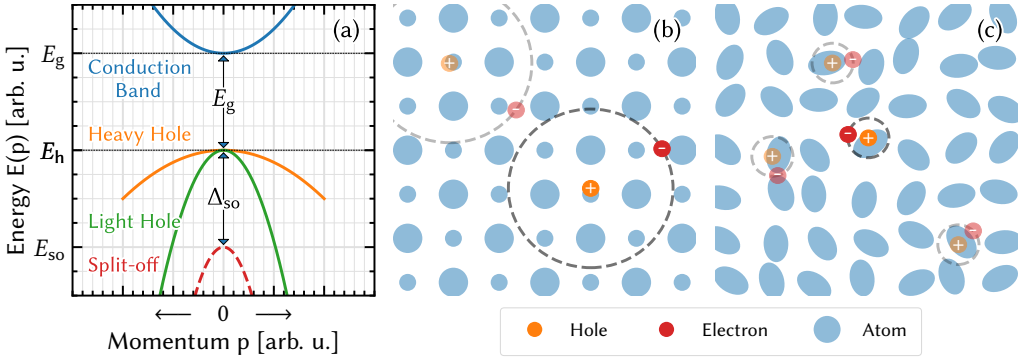

Figure 1.3: Schematic parabolic electronic dispersion for a bulk semiconductor such as GaAs or InAs in panel **(a)** with no light-heavy-hole splitting. The split-off band, offset by Δ_{so}, emerges intrinsically due to disturbances in the material, including internal stress, spin-orbit interactions, other exchange mechanisms of particles, or external influences such as electric or magnetic fields. The energy differences between the bands depends strongly on the semiconductor material. In a true zero-dimensional structure, this dispersion vanishes, leaving only discrete energy levels E_g and E_h. Panel (b) shows a schematic representation of Wannier-Mott excitons within a semiconductor lattice and panel (c) a Frenkel exciton within an organic lattice.

Within the zero-dimensional quantum dot, negatively charged electrons can be separated from their host atoms by optical or vibrational means, leaving behind positively charged holes. In higher-dimensional structures, such as bulk semiconductors, these charge carriers are free to move and exhibit continuous energy bands following a parabolic dispersion relation, as visualized in Fig. 1.3, panel (a). However, in quantum dots, strong three-dimensional confinement leads to quantization of energy levels, resulting in discrete energies. Due to Coulomb interactions between the electrons and holes, an electron can remain bound to a hole in s- or p-type orbits, forming an electron-hole pair known as an *exciton* quasi-particle. Excitons are composite bosons with energies determined by the band gap of the material and the exciton binding energy [34]. In the inorganic semiconductor materials referenced

in this work, the distance between the electron and the hole is usually much larger than a single unit cell inside the semiconductor lattice, forming a Wannier-Mott exciton. In contrast, for organic materials, both the electron and hole typically remain localized at a single lattice site, forming a Frenkel exciton. Both exciton types are visualized in Fig. 1.3, panels (b,c). Optical transitions in excitons necessitate a change in angular momentum of $\Delta M = 1$. Excitons with $|M| \neq 1$ are optically inactive and are termed *dark* excitons. In contrast, excitons with $|M| = 1$, referred to as *bright* excitons, can couple directly to photonic fields via their electronic transition dipole [123–125], rendering them optically active. These bright excitons, capable of absorbing and emitting light, are central to applications in quantum information processing and related technologies and will be discussed and explored in the following.

Two Level Configuration of the Exciton

An effective approach to model an exciton is through a two-level system with distinct energy states, as depicted in Fig. 1.4, panel (a). In a true zero-dimensional quantum dot, exciton dispersion is absent, allowing for a simplified model using discrete energy levels. This basic description omits more complex effects, such as higher-order excited states, delocalization, and direct environmental interactions. However, these effects can be reintroduced into the numerical description.

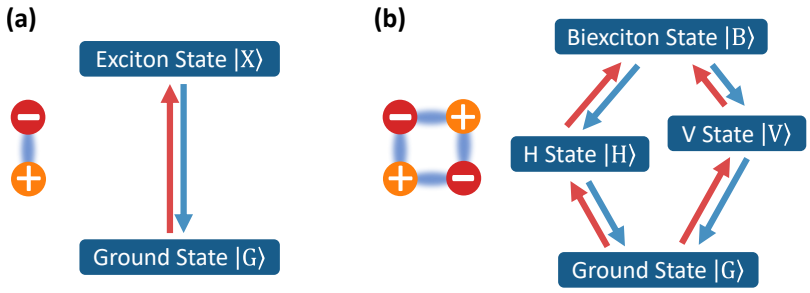

Figure 1.4: Two level system of the exciton and four level system of the biexciton with optical transitions indicated by the red and blue arrows. **(a)** The exciton is composed of a single electron (red), bound to a hole (orange), leading to a two-level energy configuration. **(b)** The biexciton is composed of two excitons, where attractive Coulomb interactions between the excitons result in a bound state. The attractive Coulomb interactions overcome the repulsion of like-charged particles and result in an energy configuration resembling a diamond. Each of the transitions, marked by the arrows, can be driven by either absorbing (red) or emitting (blue) a photon.

The system is characterized by the ground state $|G\rangle$ and the excited state $|X\rangle$, where the excited state represents the presence of an exciton. Typically, the ground state energy is set to zero, with $E_G = 0$ while the excited state energy E_X depends on the semiconductor material. In this model, the quantum dot is treated as a true zero-dimensional structure, allowing the system to be described solely by the configuration of the lowest energy levels. Transitions between the ground and excited states are governed by the operators $|G\rangle\langle X|$ and $|X\rangle\langle G|$, which function as electronic annihilation and creation operators, respectively. These transitions can be driven optically, where the absorption of a photon results in the creation of an exciton. Conversely, the exciton can re-emit a photon upon annihilation of the excited state, making it an ideal source for single-photon emission. Further details on the theoretical treatment of excitons are provided in Chapter 2.

Despite its simplicity, this two-level model effectively describes and predicts numerous quantum experiments. This model is particularly useful for high-fidelity measurements and the generation of very pure and indistinguishable single photons [126–129]. The ability to generate single photons with such precision is crucial for many applications in quantum information processing, including quantum computing, cryptography, and communication technologies. The high purity and indistinguishability of the photons ensure that quantum protocols operate reliably [130], which is fundamental to the development of advanced quantum systems. Different methods for the generation and manipulation of these photons are addressed in Chapters 5 to 7.

Four Level Configuration of the Biexciton

Two excitons can bind into a coupled state through Coulomb interaction, leading to the formation of a biexciton. Despite the repulsive Coulomb forces between like-charged particles (two electrons or two holes), the mixing of one electron with two holes and vice versa can result in an attractive interaction between the excitons. This interaction forms a stable biexciton, as illustrated by the diamond-shaped energy configuration in Fig. 1.4, panel (b). The energy of the biexciton is reduced by the binding energy [109]. Typically, this binding energy is positive. Although anti-bonding biexcitons with negative binding energies also exist, they are not considered in this study. To form a stable biexciton, the two excitons typically occupy states with orthogonal polarizations, conventionally labeled as $|X_H\rangle$ and $|X_V\rangle$, representing horizontal (H) and vertical (V) polarization, respectively.

New selection rules for optical transitions emerge from the biexciton system, as shown in Fig. 1.4, panel (b). Both excitons can be individually excited from the ground state $|G\rangle$

by photon absorption, and further excited into the biexciton state $|B\rangle$ by absorbing an additional photon. A total of two photons must be absorbed or emitted to create or annihilate a biexciton, respectively [108, 131, 132], enabling the generation of entangled photon pairs [75, 88, 133–135], which are crucial for advanced quantum communication protocols [136, 137] and quantum computing. Due to asymmetries in the underlying quantum dot, the individual excitons display slight energy mismatches, commonly referred to as the fine structure splitting energy [133, 138–140], modifying the exciton energies such that $E_{H/V} = E_X \pm E_{fsp}/2$. This splitting is known to reduce the entanglement of emitted photons by adding which-path information to the emission [141]. Despite its potential for generating entangled twin photons, the biexciton emission process often results in photons with low indistinguishability, primarily due to the sequential decay of the excitons, as discussed in Chapter 6. However, the interaction between exciton and biexciton states provides important insights into light-matter interactions, offering significant opportunities for applications in quantum information theory.

Three Level Configuration of the Trion

Further structures in quantum dot systems include V-type and Λ-type energy configurations, illustrated in Fig. 1.5, which are comparable to the upper and lower parts of the biexciton energy structure. These configurations arise when considering systems with three charged particles, either two holes and one electron, or two electrons and one hole. Again, the individual particles are bound through the Coulomb interactions and single transitions can be driven by or emit a single photon.

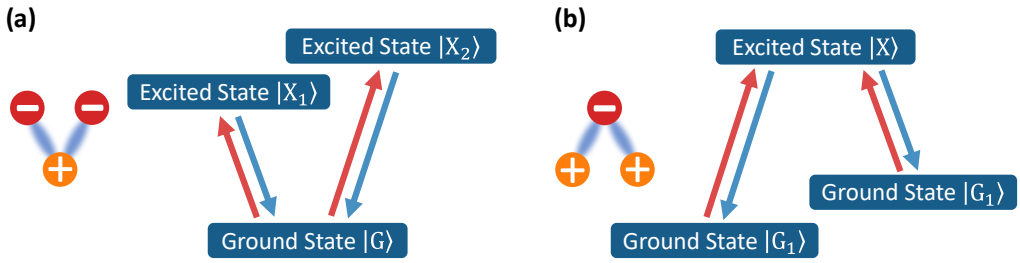

Figure 1.5: Trion states in a V-type configuration indicating a negatively charged trion in panel **(a)** as well as a Λ-type configuration indicating a positively charged trion in panel **(b)**. The naming convention here is *excited state*, because these excited fermionic states are not necessarily limited to excitons.

In these scenarios, the resulting quasi-particles are known as trions, characterized by their

total electric charge. A positive trion consists of two holes and one electron, while a negative trion consists of two electrons and one hole. These trions can be viewed as extensions of the exciton and biexciton systems, where the additional charge alters the energy landscape and interaction dynamics.

A positively charged spin-hole trion, for example, is prominently featured in Chapter 7. This system is characterized by the interaction between a single electron and two holes. Similar to the biexciton, trions exhibit distinct selection rules for optical transitions and can generate photons with specific polarization characteristics. In V-type and Λ-type systems, the transitions between states are governed by similar principles as those seen in biexcitons. The energy levels can be manipulated to achieve the desired quantum states, facilitating the emission of high-quality photons with specific properties. These configurations expand the toolkit available for quantum information processing, allowing for more sophisticated manipulation of quantum states, and further facilitating the generation of advanced photonic states.

1.3 The Quantum Resonator

In the quantum realm, an optical resonator functions similarly to the resonating chamber in a classical sound resonator. When a steel string is plucked, it oscillates and produces a sound that is relatively quiet on its own. However, when this string is positioned near a resonating chamber, the sound is significantly amplified and potentially altered. This analogy is illustrated in Fig. 1.6, panel (a). This principle of resonance and amplification finds analogous application at the quantum mechanical scale, where it involves the interaction of photon and electronic wave functions within a resonating chamber recognized as an optical *cavity* [38, 50, 89, 142, 143].

Optical cavities typically consist of two or more mirrors that confine photons, allowing them to bounce back and forth to form a standing wave inside the cavity. This confinement amplifies the interaction between photons and the wave functions of the quantum dot states positioned inside the cavity [87, 143, 144]. By modifying the properties of the light field, the quantum resonator selectively amplifies certain wavelengths while suppressing others, thereby controlling the emission characteristics of the quantum dot [84]. These cavities are typically fabricated using semiconductor materials similar to those used for quantum dots [95]. This resonant enhancement and selective amplification are crucial for optimizing

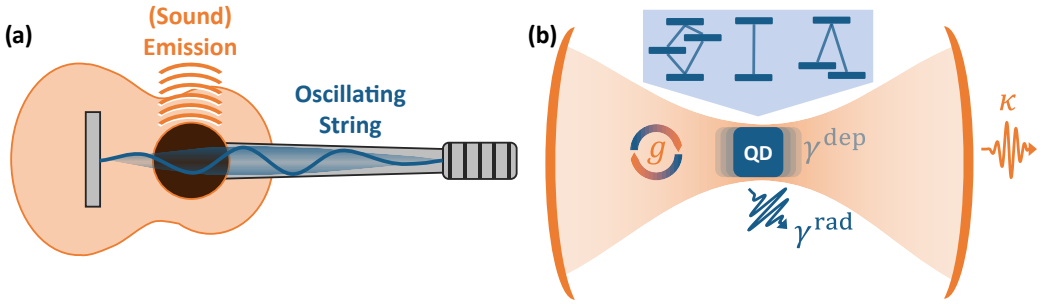

Figure 1.6: Classical and quantum oscillator (a) Schematic representation of a guitar using a single steel string, forming a classical oscillator (blue) coupled to a resonance chamber (orange), which amplifies the sound emission. **(b)** Quantum resonator, depicted schematically using mirrors (orange), the lightfield of which is coupled to the electronic states of a quantum dot (blue). The quantum dot hosts the electronic systems, specifically illustrated here for a biexciton, exciton, and a generic trion (from left to right). When the quantum dot states decay, they emit photons either into the cavity, which are then emitted at rate κ, or into a non-cavity mode with rate γ_{rad}. The strength of the coupling is mediated by the coupling constant g. The quantum dot may further couple to its semiconductor environment, resulting in dephasing of the quantum states at rate γ_{dep}.

the performance of quantum dot emitters in applications such as quantum information processing and communication technologies [89].

The cavity enhances the spontaneous emission of photons from the quantum dot through the Purcell effect [93]. The photon number inside the cavity $\hat{n}$ interacts with the electronic transitions, boosting the emission rate. By carefully designing the cavity to match the emission wavelength of the quantum dot, the interaction between the electronic states of the quantum dot and the photonic field inside the cavity is intensified. This interaction is described by the Hamiltonian formalism, a theoretical framework in both classical and quantum mechanics that captures the total energy of a system, including kinetic and potential components, and governs its evolution over time [98, 99, 145]. In the context of this work, the Hamiltonian captures the energy exchange between the electronic dipole transitions and the photonic field within the cavity. This interaction underlies phenomena such as Rabi oscillations and the Purcell effect, which modifies the spontaneous emission rate of the quantum dot. The temporal dynamics governed by the central Hamiltonian will be explored in later sections.

Cavities can take various forms, such as Fabry-Pérot resonators with two parallel mirrors, or photonic crystal cavities where periodic dielectric structures create a photonic band gap that traps light [129]. Other designs include circular periodic cavities [89, 93, 146], such

as the one featured in Chapter 6. In all cases, the objective is to confine light in a small volume and increase the interaction strength between the light and the matter inside the cavity, as shown in Fig. 1.6, panel (b). Here, the coupling between the quantum dot states and the cavity light field is characterized by the light-matter coupling constant g. This enhanced interaction is highly beneficial for quantum information processing applications, as it allows for efficient single-photon sources [13], quantum gates, and other components critical to developing scalable quantum technologies.

By understanding and controlling these light-matter interactions, quantum devices that exploit the coupling between electronic and photonic states can be designed and optimized. This is a central theme explored in Chapters 5 and 6, where high-quality single and twin photons with optimal properties are numerically generated.

1.4 Outline and Current Points of Interest

After establishing the foundational concepts of excitons, biexcitons, and other charged particles and their interplay within quantum dots and optical cavities, it is crucial to explore current developments and ongoing research in this dynamic field, as the intricate behaviors and properties of these quantum systems open numerous avenues for technological advancements and scientific inquiry. Accordingly, the following chapter provides a comprehensive theoretical framework for the dynamics of electronic quantum dot states inside photonic quantum cavities, introducing the general Hamiltonian for an N-level system with arbitrary coupling between the electronic levels, followed by a theoretical description of the photonic oscillator, or cavity. The fundamental system dynamics are discussed, elaborating on the theoretical framework employed, and the temporal dynamics of the system are evaluated using the von Neumann equation, providing insights into the evolution of quantum states over time. The concept of coupling to the semiconductor environment is also explored, highlighting various loss effects that can occur due to coupling between the system and the semiconductor environment, including vibrational fluctuations known as phonons [147–149]. A detailed explanation of the numerical methods used to describe phonons is provided to ensure a thorough understanding of their impact on the system. Moreover, the dynamics of the predominantly utilized biexciton emission are established to provide a baseline for reference before proceeding to the results derived from the foundational work, which focuses on three main topics:

Enhancing the Quantum Dot Excitation Using Ultrafast Electric Control

One crucial aspect of working with quantum dot excitons, biexcitons, or any further fermionic excited state is the excitation process, typically achieved using optical pulses [150–154] or continuous wave pumping from a laser [155]. The elementary setup involves using a laser whose frequency matches the frequency of the electronic transition desired for the excitation. For an isolated exciton, this method works quite effectively. In experiments, filtering out the laser light can be accomplished by employing different polarizations for the excitation and emission processes [142]. However, practical implementation is often more complex, especially when a cavity mediates a rapid decay of the electronic states. Consequently, various excitation schemes have been developed [54, 80]. One approach is off-resonant excitation [94], optionally leveraging electron-phonon coupling [148, 149, 156, 157], while others include dichromatic excitation using two pulses [126, 150, 158], chirped laser pulses through the adiabatic rapid passage [127, 152, 159, 160] or the recently developed SUPER excitation scheme [161–166].

In Chapter 5, the excitation problem for quantum dot excitons and biexcitons within an optical cavity is addressed using a novel approach. The electronic states of interest are excited resonantly, but they are initially off-resonant with the cavity. Subsequently, the electronic state is moved into resonance with the cavity to trigger the emission of the photon(s). This strategy allows for tunable, high fidelity excitation of the electronic states and subsequent photon emission. A detailed examination of these interactions offers a new perspective on excitation dynamics in quantum dot systems. Notably, tunability is crucial for achieving broad applicability of devices in quantum information processing[80, 118, 167–169], and this approach aligns directly with that requirement. The preliminary work that forms the foundation of the results shown in Chapter 5 has been thoroughly established in Bauch et al., *Ultrafast electric control of cavity mediated single-photon and photon-pair generation with semiconductor quantum dots*, [145].

Achieving Simultaneous Indistinguishability and Entanglement in Two Photon Emission

Single photon indistinguishability is crucial for certain aspects of quantum information processing, such as reliability and reproducibility. Moreover, entanglement is mandatory for implementing many quantum protocols. Generating entangled photon pairs, where each photon is indistinguishable, presents a significant challenge since only a few emitters

are suitable for producing such photons. One of the most promising sources for these types of photons is the biexciton two-photon emission from a quantum dot [170].

In Chapter 6, a cavity is used around the biexciton-to-exciton transition to significantly enhance the decay rate of the biexciton state. This results in the production of highly indistinguishable photons while preserving a high degree of entanglement. By leveraging the enhanced emission properties provided by the cavity, the photons meet the stringent requirements necessary for advanced quantum information processing applications. Additionally, the emitter generates photons at telecom frequencies [89, 171, 172], offering optimal conditions for quantum information processing applications [94, 173]. The underlying studies that support the findings illustrated in Chapter 6 are explored in Bauch et al., *On-demand indistinguishable and entangled photons using tailored cavity designs*, [174], which was featured on the cover of the *Advanced Quantum Technologies* journal.

Generating One-Dimensional Linear Cluster States Through the Emission of Photon Trains

The final challenge addressed in Chapter 7 is the generation and classification of large photonic states with many entangled photonic information carriers. These states are crucial for many applications in quantum computing [175, 176]. In this scenario, photons are emitted from a spin-hole trion without the presence of a cavity [177]. The photons are emitted at discrete time intervals, with each photon being entangled in time with its preceding and succeeding photon [178–183]. This sequential entanglement forms what is known as a linear cluster state [175, 184].

The focus is on investigating the generation of these linear cluster states and elaborating on the classification of their entanglement properties. Understanding and accurately classifying the entanglement aspect is essential for leveraging these states in practical quantum computing applications, ensuring that they meet the necessary criteria for complex quantum operations. Here, the expectation values of stabilizer generator expressions are used to assess the entanglement [185, 186]. The groundwork for Chapter 7 has been published in Bauch et al., *Time-bin entanglement in the deterministic generation of linear photonic cluster states*, [187].

Finally, a comprehensive conclusion and outlook are presented to complete this work.

Part I

Theoretical Framework

Hamiltonian and Time Evolution

2

The temporal evolution of quantum systems interacting with electromagnetic fields is fundamentally governed by the Hamiltonian. This operator describes the energy eigenstates of both the electronic states within a quantum dot and the photonic modes within an optical cavity. The interaction between the electronic and photonic states is captured by the coupling terms in the Hamiltonian.

Transitions between electronic states in a quantum dot are modeled as oscillating electric dipoles [103, 188], which behave similarly to harmonic oscillators. These oscillators couple to other oscillators, such as the photonic modes within a cavity. In this framework, second quantization is employed to represent the photonic field via the photon number operator $\hat{n} = \hat{b}^\dagger \hat{b}$, where $\langle \hat{n} \rangle$ denotes the average photon number in the cavity. The creation and annihilation of photons are governed by the operators $\hat{b}^\dagger$ and $\hat{b}$, satisfying the commutation relations $[\hat{b}, \hat{b}^\dagger] = 1$ and $[\hat{b}, \hat{b}] = [\hat{b}^\dagger, \hat{b}^\dagger] = 0$. For the electronic states within the quantum dot, the limited number of discrete energy levels justify the direct use of bra-ket notation, where transitions between the ground and excited states for a given configuration of electronic states are represented by operators such as $|\mathrm{G}\rangle\langle\mathrm{X}|$ and $|\mathrm{X}\rangle\langle\mathrm{G}|$. These transitions correspond to the creation and annihilation of the excited state, respectively.

Electronic state operators, represented in *bra-ket* notation as $|i\rangle\langle i|$. Due to the limited Hilbert space of the quantum dot states, these operators are expressed in matrix form, with a single unit entry on the main diagonal, corresponding to the occupation of state i. Operators describing transitions between these states, such as $|i\rangle\langle j|$ for $i \neq j$, are characterized by their off-diagonal non-zero entries. Similarly, the cavity occupation number operator, $\hat{n}_c$, is diagonal with integer values representing the photon count in the cavity mode. This formalism supports efficient numerical evaluation using matrix-vector or matrix-matrix multiplication techniques, which is detailed in Appendix A.4.

The resulting Hamiltonian governing the electronic and photonic state energies reads

Equation 2.1

$$\mathcal{H}_0 = \underbrace{\sum_{i \in \mathrm{S}} E_i \, |i\rangle\langle i|}_{\text{exciton states}} + \underbrace{\sum_{\mathrm{c} \in \mathrm{M}} E_\mathrm{c} \hat{\mathrm{n}}_\mathrm{c}}_{\text{cavity modes}} \quad .$$

Here, E_i denotes the energy associated with the electronic state i, and S is the set of all electronic states. The ground state energy is typically re-normalized to zero, such that $E_\mathrm{G} = 0$. Similarly, E_c represents the energy corresponding to the cavity mode c, where M is the set of all cavity modes. These energies can be converted into frequencies ω_i via $E_i = \hbar\omega_i$, or into wavelengths λ_i using $E_i = \frac{\hbar v_c}{2\pi\lambda_i}$, where v_c is the speed of light. The partial Hamiltonian $\mathcal{H}_0$ describes the energy of the uncoupled system, limited to the independent oscillators without interactions. Section 2.3 elaborates on the analytical treatment of this contribution.

Inter-State Transitions and Cavity Coupling

The interaction between the quantum dot electronic dipole and the photonic field in the cavity is described by the *coupling Hamiltonian*. The dipole moment is defined as $\vec{d} = -q\vec{r}$, where q is the electric charge and $\vec{r}$ is the displacement of the charged particle, interacting with the cavity electric field $\vec{E}(\vec{R})$ at position $\vec{R}$. The interaction Hamiltonian is thus given by $\mathcal{H}_1 \equiv -\vec{d} \cdot \vec{E}(\vec{R})$ [188]. The interaction strength is linearly proportional to the magnitude of this interaction. The resulting interaction Hamiltonian for the quantum dot-cavity system, incorporating exciton-photon interactions and external driving interactions, is given by

Equation 2.2

$$\mathcal{H}_1 = \sum_{\substack{i \neq j \in \mathrm{S} \\ \mathrm{c} \in \mathrm{M}}} \underbrace{|i\rangle\langle j| \, \hbar g_{i,j,\mathrm{c}} \hat{\mathrm{b}}_\mathrm{c}}_{\text{exciton-photon}} + \underbrace{|i\rangle\langle j| \, \Omega_{i,j}(t)}_{\text{exciton-pulse}} + \underbrace{\Omega_\mathrm{c}(t) \hat{\mathrm{b}}_\mathrm{c}}_{\text{pulse-photon}} + \underbrace{\Delta(t) \, |i\rangle\langle i|}_{\text{shift}} + \text{H.c.}$$

The first term in Eq. (2.2) describes the interaction between the electronic states in the quantum dot and the cavity mode, where $|i\rangle\langle j|$ represents the electronic transition operators, and $\hat{\mathrm{b}}_\mathrm{c}$ denotes the annihilation operator for the cavity mode c. The coupling strength between the electronic states and the cavity mode is denoted by $g_{i,j,\mathrm{c}}$. This coupling constant is typically assumed to be real, and thus symmetric, such that $g_{i,j,\mathrm{c}} = g^*_{i,j,\mathrm{c}}$. This part of the

interaction Hamiltonian captures the interplay between the electronic oscillators and the cavity oscillators, including the creation and annihilation of cavity photons through the modulation of electronic state populations. Notably, since no restrictions are placed on the indices i and j, even non-energy conserving processes are included in this term, which will be addressed later in Section 2.3.1. The second term in Eq. (2.2) models the direct driving of the electronic transitions using an external oscillator, typically describing optical driving using laser pulses. This aspect will be further elaborated in Section 2.4.

It is possible to incorporate many more physically allowed processes in this framework, such as the direct coupling of the external oscillator with the cavity light field operators, as well as time-dependent shifts of the electronic states, highlighted in gray in Eq. (2.2), respectively. While the former is not utilized in this work and serves only as an illustrative example, the latter will be actively studied in Chapter 5. Further additional processes not described in this work may include intra-cavity coupling, where photons from different cavities interact.

The total Hamiltonian describing the system is then constructed by the sum of all the sub-Hamiltonians, with

$$\mathcal{H} = \sum_i \mathcal{H}_i = \mathcal{H}_0 + \mathcal{H}_1 + \sum_{i>1} \mathcal{H}_i \,, \tag{2.3}$$

where components with $i > 1$ represent extensions of the quantum-dot-cavity system, including electron-phonon coupling, which is described in Chapter 3. The following section presents a detailed exploration and derivation of the von Neumann equation used to evaluate the temporal dynamics of the system defined by the Hamiltonian Eq. (2.3).

2.1 Von Neumann Equation of Motion

The state of the system at any given time is represented by the density matrix ρ. In quantum mechanics, the time evolution of a pure state is governed by the Schrödinger equation

$$\mathrm{i}\hbar \frac{\partial \Psi}{\partial t} = \mathrm{i}\hbar \dot{\Psi} = \mathcal{H}\Psi \,. \tag{2.4}$$

However, for mixed states and open quantum systems, which are influenced by interactions with the surrounding environment, the density matrix formalism more generally describes

their time evolution. For the given electronic system and cavity modes, the density matrix can be written as

$$\rho = \sum_{i\in S,\mathrm{c}\in M} |i\rangle \otimes |\mathrm{c}\rangle \langle i| \otimes \langle \mathrm{c}| = \sum_{m,n} |m\rangle\langle n| \ . \tag{2.5}$$

Here, m and n denote each possible state in the total Hilbert space, including both the electronic and photonic states.

To describe the time evolution of the density matrix, the time evolution operator, or *propagator*, $\hat{\mathcal{U}}(t_0, t_1)$, is introduced. This operator transforms the initial density matrix $\rho(t_0)$ into the density matrix at a later time t_1 via $\rho(t_1) = \hat{\mathcal{U}}(t_0, t_1)\rho(t_0)\hat{\mathcal{U}}^\dagger(t_0, t_1)$. The propagator is expressed as $\hat{\mathcal{U}}(t_0, t_1) = \mathcal{T}\exp\left[-\frac{\mathrm{i}}{\hbar}\int_{t_0}^{t_1}\mathcal{H}(t)\mathrm{d}t\right]$, where $\mathcal{T}$ denotes the time-ordering operator. Expanding this propagator yields the Dyson series [98, 189]

$$\hat{\mathcal{U}}(t_0, t_1) = 1 + \sum_{n=1}^{\infty}\left(\frac{1}{\mathrm{i}\hbar}\right)^n \int_{t_0}^{t_1}\mathrm{d}t_2 \int_{t_0}^{t_2}\mathrm{d}t_3 \ldots \int_{t_0}^{t_{n-1}}\mathrm{d}t_n \mathcal{T}\prod_{i=1}^{n}\mathcal{H}(t_i) \ . \tag{2.6}$$

The Dyson series provides a systematic method to compute the time evolution operator for time-dependent Hamiltonians. In cases where $[\mathcal{H}(t_1), \mathcal{H}(t_2)] = 0$ for $t_1 \neq t_2$, the propagator simplifies, and the time-ordering operator $\mathcal{T}$ becomes trivial. By considering the derivative of the time-dependent density operator in this formalism, the von Neumann equation is derived, governing the time evolution of the density matrix, with

$$\frac{\partial}{\partial t}\rho(t) = \dot{\rho}(t) = \underbrace{\dot{\hat{\mathcal{U}}}(t)\rho(0)\hat{\mathcal{U}}^\dagger(t)}_{=-\frac{\mathrm{i}}{\hbar}H(t)\rho(t)} + \underbrace{\hat{\mathcal{U}}(t)\dot{\rho}(0)\hat{\mathcal{U}}^\dagger(t)}_{=0 \text{ since } \dot{\rho}(0)=0} + \underbrace{\hat{\mathcal{U}}(t)\rho(0)\dot{\hat{\mathcal{U}}}^\dagger(t)}_{=\frac{\mathrm{i}}{\hbar}\rho(t)H(t)} , \tag{2.7}$$

which simplifies into the von Neumann equation [98, 99, 190]

Equation 2.8

$$\frac{\partial\rho}{\partial t} = \mathcal{L}[t] = -\frac{\mathrm{i}}{\hbar}\left[\mathcal{H}(t), \rho(t)\right] + \sum_{\hat{\mathrm{O}}}\mathcal{L}_{\hat{\mathrm{O}}}^{\mathrm{env}}\left[\rho(t)\right] \ .$$

The von Neumann equation offers a practical framework for numerically evaluating the time evolution of the density matrix, particularly when using adaptive time-stepping methods such as the DP-45 method to explicitly integrate the von Neumann equation. This is further discussed in Appendix A.4.1. In this equation, the Liouvillian operator $\mathcal{L}[t]$ describes the time evolution of the density matrix, while the additional terms $\mathcal{L}_{\hat{\mathrm{O}}}^{\mathrm{env}}$

represent environmental interactions modeled via Lindblad operators [190, 191]. These terms phenomenologically account for losses and dephasing, further elaborated upon in Section 2.2.

The von Neumann equation is particularly advantageous due to the straightforward method in calculating expectation values, which can be expressed as [191]

$$\left\langle \hat{O} \right\rangle = \mathrm{Tr}\left\{ \rho(t)\hat{O} \right\} = \sum_i \langle i| \rho(t)\hat{O} |i\rangle \ . \tag{2.9}$$

This allows for efficient calculation of expectation values from the density matrix, ensuring that all relevant observables are derived using the matrix trace $\mathrm{Tr}\{\circ\}$ without significantly increasing computational complexity.

All simulations are conducted until $\frac{\partial}{\partial t} \sum_n \langle n| \rho(t) |n\rangle = 0$ for all $t > t_{\max}$. This property ensures that simulations continue until the occupation of each state stabilizes, signaling that all relevant temporal dynamics have concluded. The value of $t_{\max}$ is adjusted based on the system and simulation parameters, ensuring proper evaluation in each scenario.

2.2 Open Quantum System - Environmental Coupling

Here, the various possible $\mathcal{L}^{\mathrm{env}}_{\hat{O}}$ terms from Eq. (2.8) are elaborated upon. The quantum dot and the cavity can both couple to the environment in several ways, defined solely by their respective creation and annihilation operators. To incorporate the phenomenological dissipative behavior of any of these system operators, Lindbladian rate contributions are used. The Lindbladian for a given system operator $\hat{O}$ is expressed as

$$\mathcal{L}_{\hat{O}}[\rho] = \frac{1}{2}\left(2\hat{O}\rho\hat{O}^\dagger - \hat{O}^\dagger\hat{O}\rho - \rho\hat{O}^\dagger\hat{O} \right) , \tag{2.10}$$

commonly referred to as the *Lindblad super operator*. This formalism allows for the inclusion of various phenomenological processes, such as the decay and dephasing of states, while preserving the trace of the density matrix. Consequently, the time evolution of the density matrix is no longer fully unitary, indicating the system is an *open quantum system*. This framework provides a comprehensive description of how the system interacts with its environment, modeling the non-unitary evolution due to dissipative processes that cannot be captured by the von Neumann equation alone [191].

2.2.1 Electronic State Decay and Dephasing

Focusing first on the electronic operators, consider $\hat{O} = \sqrt{\gamma_{\mathrm{rad},ij}}\,|i\rangle\langle j|$ with $E_j > E_i$, which represents an electronic annihilation operator, and thus an electronic transition, scaled with the loss rate $\gamma_{\mathrm{rad},ij}$. Applying Eq. (2.10), the resulting Lindbladian for radiative decay of the electronic states is given by

$$\begin{aligned}\mathcal{L}^{\mathrm{rad}}[\rho] &= \sum_{\substack{i,j\in S\\ i\neq j, E_i<E_j}} \gamma_{\mathrm{rad},ij}\mathcal{L}_{|i\rangle\langle j|}[\rho] \\ &= \sum_{\substack{i,j\in S\\ i\neq j, E_i<E_j}} \frac{\gamma_{\mathrm{rad},ij}}{2}\left(2\,|i\rangle\langle j|\,\rho\,|j\rangle\langle i| - |j\rangle\langle j|\,\rho - \rho\,|j\rangle\langle j|\right) . \end{aligned} \tag{2.11}$$

Expression Eq. (2.11) describes the radiative decay of the electronic states into free, non-cavity optical modes with a rate $\gamma_{\mathrm{rad},ij}$. If not otherwise stated, $\gamma_{\mathrm{rad},ij} =: \gamma_{\mathrm{rad}}$ is independent on the state indices i, j. Emissions through this mechanism are only traceable using the emission probability of the respective transition and are usually considered as losses to the cavity modes. Typically, the radiative lifetime $\tau_{\mathrm{rad}} = 1/\gamma_{\mathrm{rad}}$ of quantum dot states ranges from a few hundred picoseconds to a few nanoseconds [106, 118].

For $\hat{O} = \sqrt{\gamma_{\mathrm{dep},ij}}\,(|j\rangle\langle j| - |i\rangle\langle i|)$ with $E_j > E_i$, which represents an electronic inversion operator and is directly connected to the state population, applying Eq. (2.10) yields

$$\begin{aligned}\mathcal{L}^{\mathrm{dep}}[\rho] &= \sum_{\substack{i,j\in S\\ i\neq j, E_i<E_j}} \gamma_{\mathrm{dep},ij}\mathcal{L}_{|j\rangle\langle j|-|i\rangle\langle i|}[\rho] \\ &= \sum_{\substack{i,j\in S\\ i\neq j, E_i<E_j}} \frac{\gamma_{\mathrm{dep},ij}}{2}\,|j\rangle\langle j|\,\rho\,|i\rangle\langle i| . \end{aligned} \tag{2.12}$$

Expression Eq. (2.12) describes the dephasing of the state population, resulting in the decay of state coherences with rate $\gamma_{\mathrm{dep},ij}$. Again, if not otherwise stated, $\gamma_{\mathrm{dep},ij} =: \gamma_{\mathrm{dep}}$. A small dephasing rate can be used to simulate electron-phonon induced dephasing, resulting in what is known as the zero-phonon line [192], or *pure dephasing*. Typically, $\gamma_{\mathrm{dep}} \approx 1\,\mu\mathrm{eV}\cdot\mathrm{T}$, scales linearly with low temperatures [110, 193]. However, this method is often shown to be unfavorable since electron-phonon coupling can be included directly, and the Lindbladian rate can greatly exaggerate the influence of the zero phonon line. Therefore, while useful for initial approximations, more accurate models are necessary for detailed simulations of electron-phonon interactions [194]. Nevertheless, this Lindblad contribution also describes

other sources of dephasing, and is used to include spin dephasing in Chapter 7.

The general temporal behavior for both loss mechanisms is illustrated in Fig. 2.1. Radiative decay leads to the excited state populations approaching zero, whereas dephasing results in a maximally mixed state with equal occupations for all states involved.

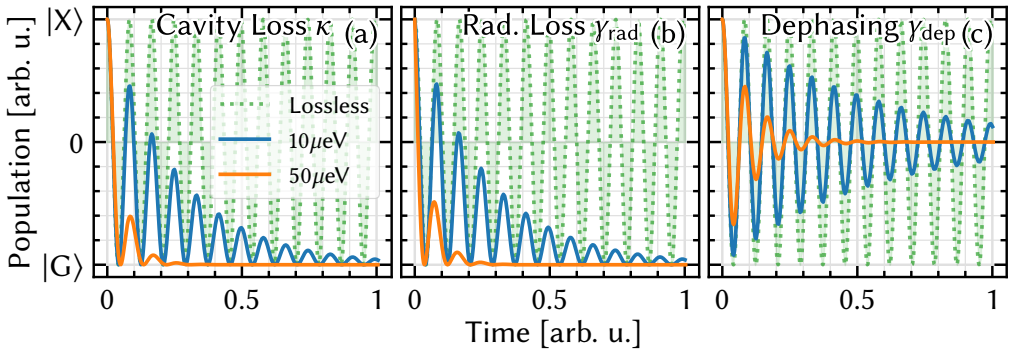

Figure 2.1: Impact of the decay and dephasing mechanisms for the toy model from Eq. (2.16) representing a two-level system coupled to a single mode cavity with $E_C = E_X = 1\,\text{eV}$ and $\hbar g = 50\,\mu\text{eV}$. The inversion $|X\rangle\langle X| - |G\rangle\langle G|$ is displayed on the y-axis. All panels depict the dynamics of an initially fully populated excited state $|X\rangle$. Panel **(a)** depicts the influences of cavity losses κ. Panel **(b)** shows the same results for radiative loss γ_{rad} instead. Notably, when the rate of decay for the electronic states or cavity photons is equal, the resulting dynamics are almost identical. Panel **(c)** presents the electronic states experiencing dephasing using γ_{dep}, resulting in a maximally mixed state.

2.2.2 Resonator Losses and Purcell Enhancement

For the photonic operators, a similar approach is applied as with the electronic operators. Using $\hat{O} = \sqrt{\kappa_c}\hat{b}_c$, the Lindbladian for the cavity mode c is given by

$$\begin{aligned}\mathcal{L}^{\text{Cav}}[\rho] &= \sum_{c\in M} \kappa_c \mathcal{L}_{\hat{b}_c}[\rho] \\ &= \sum_{c\in M} \frac{\kappa_c}{2}\left(2\hat{b}_c\rho\hat{b}_c^\dagger - \hat{n}_c^\dagger\rho - \rho\hat{n}_c\right)\end{aligned} \tag{2.13}$$

Expression 2.13 indicates that the cavity population $\hat{n}_c = \hat{b}_c^\dagger\hat{b}_c$ decays with a rate κ_c. If not stated otherwise, loss rates for different cavity modes are assumed to be equal with $\kappa_c =: \kappa$. The cavity photons suffer from losses due to imperfect mirrors in the resonator structure, a feature often desired for efficient photon extraction. The loss of photon population

effectively lowers the lifetime $\tau = 1/\kappa$ of the cavity photon field. Typical values for the cavity losses range from $\kappa \approx g$ (strong coupling) to many times the cavity coupling with $\kappa \ll g$ (weak coupling).

From the cavity loss rate κ, additional figures of merit can be calculated to characterize the cavity. One such metric is the cavity Q-factor, defined as

$$Q = \frac{\omega_c}{\kappa}\,, \tag{2.14}$$

where $\omega_c = E_c/\hbar$ is the cavity frequency and κ is the respective cavity loss rate. High Q-factors translate into low loss rates κ and thus, long lifetimes of the cavity photons. High absolute coupling values g may be overshadowed by even larger loss rates κ, yielding low Q-factors even though the raw light-matter coupling is strong. This is exploited in Chapter 6 for advanced photon generation.

Additionally, the cavity-induced enhancement, referred to as the Purcell enhancement [93, 195, 196], can be calculated using

$$\frac{\gamma_{\text{cavity}}}{\gamma_{\text{rad}}} = \underbrace{\frac{2g^2}{\gamma_{\text{rad}}\kappa}}_{\substack{\mathcal{F}_P \\ \text{Purcell} \\ \text{Enhancement}}} \cdot \underbrace{\frac{\kappa^2}{(\Delta E/\hbar)^2 - \kappa^2}}_{\substack{\leq 1 \\ \text{Spectral} \\ \text{Detuning}}} \cdot \underbrace{\frac{\left|\vec{E}(\vec{r})\right|}{\left|\vec{E}_{\text{max}}\right|}}_{\substack{\leq 1 \\ \text{Spatial} \\ \text{Mismatch}}} \cdot \underbrace{\left(\frac{\vec{d}\cdot\vec{E}(\vec{r})}{dE}\right)^2}_{\substack{\leq 1 \\ \text{Polarization} \\ \text{Selective}}}. \tag{2.15}$$

The ratio of the cavity decay rate γ_{cavity} and the radiative decay γ_{rad} represents the radiation emitted from an electric point dipole inside the cavity compared to the radiation emitted in an infinite, homogeneous bulk material. For simplicity, it is assumed that there is no spatial detuning and no polarization selection, meaning these components are grayed-out in Eq. (2.15), indicating they are not used in the formula. Purcell enhancement is used as a figure of merit in Chapter 6, providing a crucial measure of the efficiency and effectiveness of the cavity in enhancing the emission properties of the quantum dot system.

In an anticipatory manner, consider a simple two-level system coupled to a single mode cavity

$$\mathcal{H} = \underbrace{E_X\,|X\rangle\langle X| + E_c\hat{n}}_{\mathcal{H}_0} + \underbrace{\left(\hbar g\,|X\rangle\langle G|\,\hat{b} + \text{H.c.}\right)}_{\mathcal{H}_1}\,, \tag{2.16}$$

which is commonly referred to as the *Jaynes-Cummings Model* (JCM) [197–199]. Here, the

states are limited to a two level system, modeling a single exciton, and a single optical cavity, optionally with large numbers of photons. The ground state energy is set to zero with $E_G = 0$.

For this system, when $g \gtrapprox \kappa$, *Rabi oscillations* occur [104, 108, 200], which is displayed in Fig. 2.1 (green dotted lines). The amplitude and frequency of the Rabi oscillations is determined by the coupling strength and detuning between the quantum dot and the cavity mode. This coupling results in periodic energy exchange between the two systems with a frequency given by $\Omega_R = \sqrt{g^2 + \Delta^2}$, where g is the coupling constant and $\Delta = (E_X - E_c)/\hbar$ is the detuning between the quantum dot state and the cavity. The Rabi oscillations exhibit a sinusoidal behavior in the excited state population [200]. With rising detuning, the frequency of oscillation rises while the amplitude diminishes. When cavity losses are non-zero, *damping* of these oscillations is observed at various rates, as visualized in Fig. 2.1. Here, the numerical effects of pure dephasing of the quantum dot states as well as radiative decay of the states is also visualized using the same toy model from Eq. (2.16). When $\kappa \gg g$, the system experiences over-damping, leading to the disappearance of oscillations.

2.3 Interaction Picture Transformation

The analytical treatment of the previously described Hamiltonian requires further preparation. First, consider the complete time evolution operator of Eq. (2.22) obtained using the Schrödinger equation [98, 201] from Eq. (2.4) with

$$\hat{\mathcal{U}}(t) = \mathcal{T} e^{-\mathrm{i}/\hbar \int_0^t \mathcal{H}(t)\mathrm{d}t} \,. \tag{2.17}$$

The transformation is split into time-independent operators $\mathcal{H}_0$ and time-dependent operators $\mathcal{H}_i$. Typically, $\mathcal{H}_0$ includes high-frequency components, which can be analytically addressed by applying a unitary transformation based on $\mathcal{H}_0$. This approach bypasses the need for the high numerical precision that would otherwise be required to capture the rapid dynamics induced by $\mathcal{H}_0$. The self-adjoined transformation into the interaction frame is then given by

$$\hat{\mathcal{U}}_I(t) = e^{-\mathrm{i}/\hbar \mathcal{H}_0 t} \,. \tag{2.18}$$

Because the Hamiltonian describing the energy landscape of the system is time independent with $\mathcal{H}_0(t_1) = \mathcal{H}_0(t_2)$, and therefore $[\mathcal{H}_0(t_1), \mathcal{H}_0(t_2)] = 0$, Eq. (2.18) can be calculated

analytically. An operator in the interaction frame is then defined by its corresponding transformed operator in the Schrödinger frame, with

$$\hat{\mathrm{O}}_{\mathrm{I}}(t) = \hat{\mathcal{U}}^{\dagger}(t)\hat{\mathrm{O}}_{\mathrm{S}}\hat{\mathcal{U}}(t)\ . \tag{2.19}$$

Evaluating Eq. (2.19) for electronic and photonic operators yields

$$|i\rangle\langle j|_{\mathrm{I}}(t) = |i\rangle\langle j|\, e^{\mathrm{i}(\omega_i-\omega_j)t} \text{ and} \tag{2.20}$$

$$\hat{\mathrm{b}}_{\mathrm{I}}(t) = \hat{\mathrm{b}}e^{\mathrm{i}\omega t}\ , \tag{2.21}$$

which are then used to build the transformed Hamiltonian. Furthermore, applying this transformation to the Lindbladians Eqs. (2.11) to (2.13) reveals that they remain unchanged in the interaction frame. From this point onward, the subscript is dropped, as all operators are assumed to be in the interaction frame in respect to $\mathcal{H}_0$ unless noted otherwise. The time evolution through $\mathcal{H}_1$ is then calculated by iteratively integrating the von Neumann equation Eq. (2.8). Due to the unitarity of the transformation, the expectation values remain the same in both the interaction and Schrödinger picture.

2.3.1 Rotating Wave Approximation

As previously introduced, the Hamiltonian typically contains high-frequency components, which are treated analytically using the interaction picture transformation. This same transformation can be applied again to remove additional high-frequency components that are not relevant to the current analysis because they occur on different time scales or violate conservation laws.

Consider the simple interaction Hamiltonian for a two-level system

$$\mathcal{H} = \underbrace{E_{\mathrm{X}}\,|\mathrm{X}\rangle\langle\mathrm{X}|}_{\mathcal{H}_0} + \Big(\underbrace{\Omega_0\cos(\omega_0 t)\,|\mathrm{X}\rangle\langle\mathrm{G}| + \mathrm{H.c.}}_{\mathcal{H}_1}\Big)\ , \tag{2.22}$$

where Ω_0 is a constant describing the coupling between the ground state $|\mathrm{G}\rangle$ and the excited state $|\mathrm{X}\rangle$ via a generic oscillator with frequency ω_0. At this point, the source of the oscillating term is arbitrary. Possible sources of the oscillation include light fields induced by a laser or a cavity. The energy difference of the ground and excited state is given by $E_{\mathrm{X}} = \hbar\omega_{\mathrm{X}}$.

Performing the interaction picture transformation for $\mathcal{H}_1$ using the time independent Hamiltonian emerging from the electronic states $\mathcal{H}_0$ yields

$$\begin{aligned}\mathcal{H}_1 &\sim \left(e^{-\mathrm{i}\omega_0 t} + e^{\mathrm{i}\omega_0 t}\right) e^{-\mathrm{i}\omega_X t} \left|\mathrm{X}\right\rangle\!\left\langle\mathrm{G}\right| + \text{ H.c.} \\ &= \left(e^{-\mathrm{i}(\omega_0+\omega_X)t} + e^{-\mathrm{i}(\omega_X-\omega_0)}\right) \left|\mathrm{X}\right\rangle\!\left\langle\mathrm{G}\right| + \text{ H.c. .}\end{aligned} \tag{2.23}$$

This transformation yields two frequency components, namely the sum of frequencies $\omega_X + \omega_0$, and the difference of frequencies $\omega_X - \omega_0$. The difference of frequencies is easily resolvable and will naturally be of high amplitude. In contrast, the sum of frequencies is difficult to resolve due to the small time step required and is typically of low amplitude. Moreover, the sum frequency component tends to average out over time when larger frequencies are considered, which is depicted in Fig. 2.2, where the dynamics of the interaction picture transformation are also shown. Consequently, this component is omitted from the Hamiltonian, which is then transformed back into the Schrödinger frame.

The resulting Hamiltonian for the example given then reads

$$\mathcal{H}_1 \approx \Omega_0 e^{\mathrm{i}\omega_0 t} \left|\mathrm{X}\right\rangle\!\left\langle\mathrm{G}\right| + \text{ H.c. .} \tag{2.24}$$

A similar transformation can be applied when investigating the cavity coupling operator by transforming the product $|i\rangle\!\langle j|\,\hat{\mathrm{b}}$ for all combinations of the electronic state indices i and j. Within this transformation, the corresponding to sum frequencies are removed. In general, this method is referred to as the *Rotating Wave Approximation* (RWA) [202]. The omitted terms can be interpreted as representing non-physical processes, such as the simultaneous creation of photons and excitation of the quantum state, or the simultaneous annihilation of photons and relaxation of the state. These processes do not conserve energy and are generally not allowed, but they can occur over very short timescales due to the Heisenberg uncertainty principle.

Avoiding the RWA can reveal important physical effects that may be otherwise overlooked. These effects become particularly significant in systems that are either strongly driven or strongly coupled, where the coupling or driving strength Ω_0 approaches or exceeds the transition frequency ω_X. In such cases, a more comprehensive treatment that does not depend on the RWA is required to accurately describe the temporal dynamics of the system [203, 204]. Nevertheless, within the scope of this work, the coupling strengths are generally low enough to validate the use of the RWA.

In the context of the complete system Hamiltonian in Eq. (2.2), this approach means

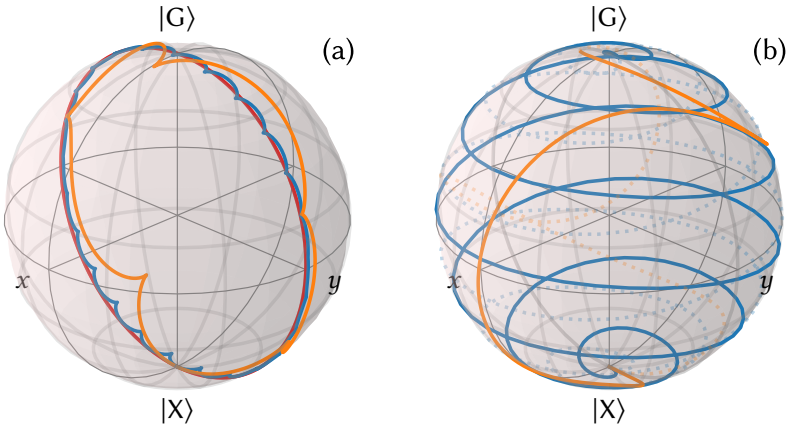

Figure 2.2: State dynamics using the rotating wave approximation and interaction picture transformation for a simple two-level system, illustrated on the Bloch sphere. Rabi oscillations between two states $|\mathrm{G}\rangle$ and $|\mathrm{X}\rangle$ are shown for frequencies $\omega_{\mathrm{X}} = 5\mathrm{Hz}$ (orange line), $\omega_{\mathrm{X}} = 50\mathrm{Hz}$ (blue line), and $\omega_{\mathrm{X}} \gg 50\mathrm{Hz}$ (red line). Simulations utilizing the interaction picture without the rotating wave approximation are depicted in panel (a), while the same simulations without the interaction picture transformation are shown in panel (b). In the latter, only a single transition from the ground to the excited state is shown.

imposing restrictions on the order of the components, specifically setting $E_i > E_j$ for the electronic operators. Because the results presented in this work use weak driving of the electronic states and weak coupling to photonic cavities, the RWA is always applied.

2.4 External Oscillator - Laser Driving

In this section, the methods for optically driving the system using external lasers are briefly introduced. All systems are driven with a central frequency ω and rely on the rotating wave approximation with

$$\Omega(t) = \Omega_0(t) e^{-\mathrm{i}\omega_0(t-t_0)}\,, \tag{2.25}$$

where $\Omega_0(t)$ is the temporal envelope. Once more, the toy Hamiltonian from Eq. (2.24) is used. The methods for driving the system utilized in this work vary only in their envelopes,

specifically

$$\Omega_0(t) = A_0 \qquad \text{(CW / Constant Envelope),} \tag{2.26}$$

$$\Omega_0(t) = A_0 \exp\left[-0.5\left(\frac{t-t_0}{\tau}\right)^{2\cdot p}\right] \qquad \text{(Gaussian Envelope) and} \tag{2.27}$$

$$\Omega_0(t) = A_0 \operatorname{sech}\left[\left(\frac{t-t_0}{\tau}\right)^{p}\right] \qquad \text{(Sechant Envelope) .} \tag{2.28}$$

Here, $A_0 = \hbar\omega_0$ denotes the pulse amplitude. For continuous wave (CW) driving, $\Omega_0(t)$ is constant at all times. For pulsed driving, $\Omega_0(t)$ can take various forms, including Gaussian or hyperbolic secant (sech) shaped envelopes. For finite envelopes, the pulse width τ determines the temporal broadness of the pulse. For the reference materials used in this work. the width is typically limited to a few pico seconds [205].

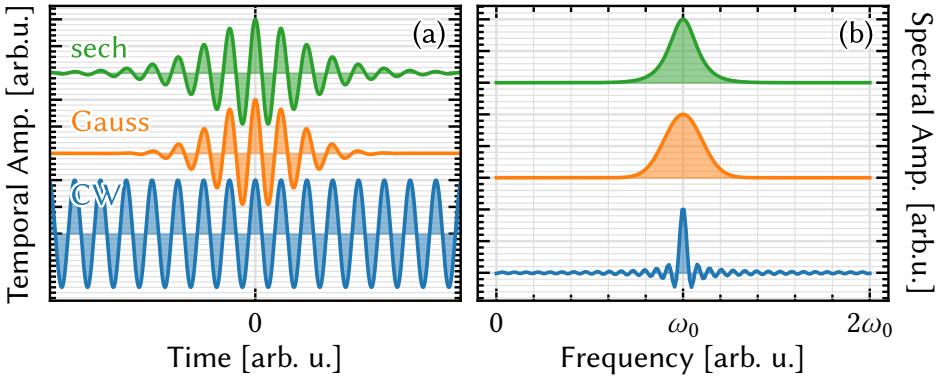

Figure 2.3: Pulse envelopes and their respective Fourier transformations. (a) Temporal profiles for continuous wave (CW), Gaussian, and sech (hyperbolic secant) envelopes. The sech is treatable analytically. **(b)** Fourier Transforms of the respective envelope functions, illustrating their spectral characteristics.

The steepness of the envelope can be controlled using the exponential scaling p. Increasing p results in a *flat top* envelope. Notably, with $p > 1$, the spectral width of the envelopes remains the same while the spectrum starts to adopt the tails of the CW envelope. This is because the overall width of the envelope does not change with increasing p, and thus sets a limit on the spectral width. The envelopes and their respective spectra are visualized in Fig. 2.3 for $p = 1$, which is used throughout this work.

Furthermore, the term *bandwidth* is introduced to characterize the envelope of a pulse,

defined as the reciprocal of the pulse length $\sigma = 1/\tau$. In the case of a CW pulse, the bandwidth is zero, ideally targeting only a single frequency.

The sech pulses have the advantage of being analytically treatable. While Gaussian pulses are predominantly used in this work, sech pulses are explicitly employed in Chapter 7. Depending on the method to generate pulsed lasers in an optical setup, experimental results for the pulse envelopes may also deviate significantly from an idealized Gaussian envelope [206].

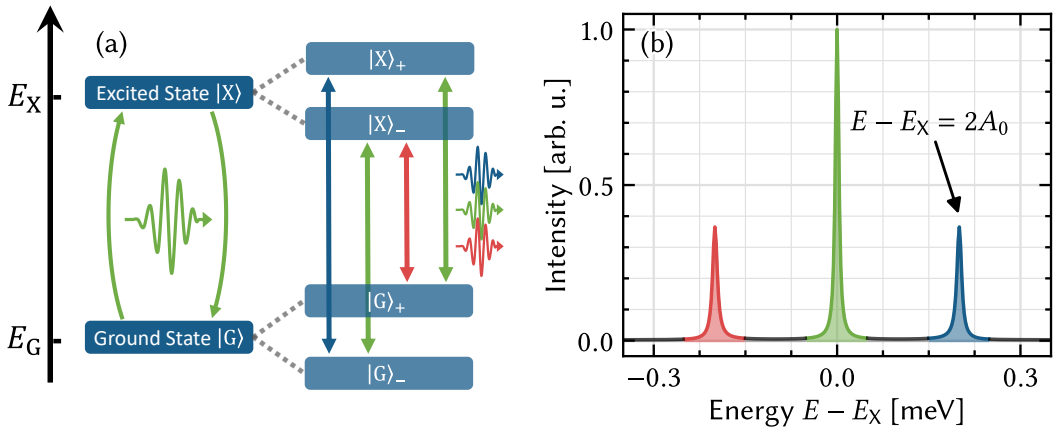

Figure 2.4: Laser dressed state model and spectral intensity for the toy Hamiltonian with $A_0 = 0.1\,\text{meV}$, illustrated in panel (a), with the corresponding spectral intensity shown in panel (b). A Fourier transform is applied to analyze the emission spectrum, revealing side peaks at $|E - E_0| = 2A_0$. During the presence of the laser pulse, the electronic states shift in linear proportion to the laser amplitude, leading to the formation of the Mollow triplet. The emission at $E_0 \pm 2A_0$ is highlighted in blue and red, respectively. To achieve a smooth spectrum, $\gamma_{\text{rad}} = 5\,\mu\text{eV}$ is used. The shaded areas in panel (b) correspond to the colored transitions depicted in panel (a).

The amplitude of the pulse A_0 is typically measured in units of energy. Because this measure is not very descriptive, the pulse is often characterized further by introducing the *pulse area*, defined as

$$\mathcal{A} = \int_{-\infty}^{\infty} \Omega(t)\mathrm{d}t. \tag{2.29}$$

By setting the pulse area to $\mathcal{A} = 2n\pi$, the parameters required to achieve n rotations through the Bloch sphere of the system can be derived. In the context of the toy model used in this chapter, a rotation within the Bloch sphere induced by the pulse area translates into

the evolution of the state vector $\Psi = \cos(\theta)\,|\mathrm{G}\rangle + \sin(\theta)\,|\mathrm{X}\rangle$ with $\theta \in [0, 2n\pi]$, effectively changing the population and optionally the phase of the quantum state. In this work, either the pulse amplitude A_0 or both the pulse area $\mathcal{A}$ and the pulse length τ are provided, indicating that A_0 will be calculated according to the desired pulse area.

All driving methods result in a *Stark shift* of the energies [168, 207], a general displacement of the energy levels linearly proportional to the amplitude of the laser driving. Additionally, the energy levels split symmetrically, forming a *dressed state* picture. Here, new optical transitions arise, as visualized in Fig. 2.4, panel (a). From the emission from these dressed states, the *Mollow triplet* emerges [208], characterized by two side peaks in the resonance spectrum. For a resonant continuous wave driving with amplitude A_0, these side peaks are symmetrical around the center frequency at $|E - E_0| = 2A_0$, as shown in Fig. 2.4, panel (b). For pulsed driving, the Mollow triplet is usually not visible due to the short timescales of the excitation.

Electron Phonon Coupling 3

In the semiconductor environment of a quantum dot, lattice vibrations manifest as bosonic quasi-particles known as *phonons*. These quantized lattice vibrations are visualized schematically in Fig. 3.1 and can lead to complex system dynamics, often resulting in dissipative effects such as the dephasing of the electronic coherences. However, phonons can also facilitate constructive processes, including phonon-assisted excitation of the quantum dot population through emission or phonon-assisted Purcell enhancement via absorption of phonons.

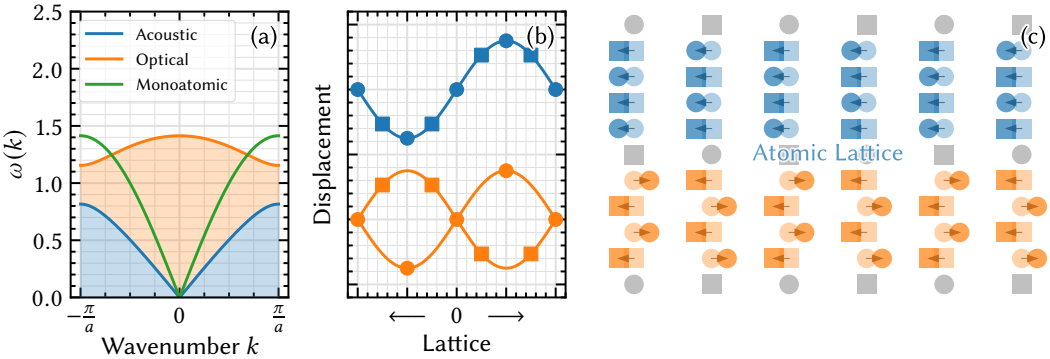

Figure 3.1: Schematic representation of both acoustic and optical phonons in a mono- (green) and bi-atomic (blue, orange) lattice. **(a)** Phonon dispersion relation for a one-dimensional bi-atomic chain of atoms with $M_2 = 2M_1$ and M_i as the atomic mass. **(b)** Displacement of the atoms for acoustic (blue) and optical (orange) phonons. The circles and squares mark different types of atoms. While acoustic phonons also exist in mono-atomic lattices, optical phonons only exist in structures with more than a single type of atom. **(c)** Schematic displacement in an atomic lattice. While the acoustic phonons result in a displacement of all atoms in the same direction, the optical phonons result in opposing displacements, forming a dipole able to engage in direct optical manipulation.

Phonon interactions are inherently non-instantaneous, introducing *memory effects* due to their dependence on the past states of the system. As quanta of lattice vibrations, phonons propagate at finite speeds, leading to delays in system responses. This non-instantaneous interaction results in non-Markovian dynamics, where the temporal evolution of any of the system states is influenced by their history rather than solely their current state. Accurately

modeling these interactions requires the inclusion of memory effects, as they directly affect the behavior of the quantum dot.

In contrast, the von Neumann equation Eq. (2.8) assumes Markovian dynamics, where the system evolves based only on its present state. Non-Markovian dynamics, however, require consideration of past states. To simplify the modeling process, Markov approximations can be employed to selectively remove memory effects, resulting in more simplified rate equations. Though less precise, this approach provides a practical means to capture certain phonon effects in a fully Markovian framework.

In this work, the Polaron Master Equation (PME) is established to describe electron-phonon coupling [149, 209] using only a single retardation of time. While this method captures many of the experimentally visible phonon dynamics, it becomes insufficient for fast, sub-picosecond dynamics due to the nature of the Markov approximation. This method is compared with a more computationally expensive approach that operates without these approximations, known as the Path Integral (PI) method [210] to demonstrate the viability of the polaron master equation in the context of this work. Both methods share a common aspect that completely characterizes the phonons regardless of the method for numerical evaluation: their spectral density.

3.1 Phonon Spectral Density

The general spectral distribution of a given set of phonons is defined by

$$J(\omega) = \sum_{\vec{q}} \lambda_{\vec{q}} \delta\left(\omega - \omega_{\vec{q}}\right) , \tag{3.1}$$

with wave vector $\vec{q}$ and $\delta(\circ)$ as the delta function. For the longitudinal-acoustic (LA) phonons typically dominating the phonon contributions in semiconductor materials at low frequencies, the deformation interaction potential $\lambda_{\vec{q}} = \lambda_{\vec{q}}^{(e)} - \lambda_{\vec{q}}^{(h)}$ describes the coupling of the quantum dot and the phonons [192]. Here, $e(h)$ denoted the electron (hole) contributions, respectively. As the number of phonons increases, the summation over discrete phonon modes is replaced by an integral of the density of states over a continuous frequency spectrum. This involves using the phonon density of states (DOS) and the phonon frequency distribution, the latter typically guided by empirical data. Under these assumptions, the spectral distribution can be written as $J(\omega) = \mathrm{DOS}(\omega) f(\omega)$. This work assumes only longitudinal acoustic phonons to be present, as optical phonons require

significantly more energy to be excited, as displayed in the phonon dispersion relation in Fig. 3.1, panel (a). At low frequencies, the density of states follows $\mathrm{DOS}(\omega) \propto \omega$, with $f(\omega)$ incorporating an exponential cutoff. This results in the spectral distribution

$$J(\omega) = \frac{\omega^N}{4\pi^2 \rho_\mathrm{M} \hbar c_s^5} \left(D_e e^{-\omega^2 a_e^2/(4c_s^2)} - D_h e^{-\omega^2 a_h^2/(4c_s^2)} \right)^2 \tag{3.2}$$

where ρ_M is the mass density of the semiconductor material, c_s is the speed of sound within that material, $a_{e(h)}$ is the electron (hole) radius, and $D_{e(h)}$ represents the electron (hole) energy [211–213]. Assuming $a_e \approx a_h$, the sum of the two exponential functions can be approximated using a single exponential function, simplifying Eq. (3.2) to:

$$J(\omega) \approx \frac{\omega^N (D_e - D_h)^2}{4\pi^2 \rho_\mathrm{M} \hbar c_s^5} e^{-\frac{\omega^2 a_h^2}{2c_s^2}} \,. \tag{3.3}$$

By grouping all the factors into unified parameters, the final spectral density is obtained with

$$J(\omega) = \alpha_p \omega^N e^{-\frac{\omega^2}{2\omega_b^2}} \,. \tag{3.4}$$

This work uses Eq. (3.4) exclusively, as it provides a compact and practical representation of the phonon spectral density. It is characterized completely by the phonon coupling strength α_p, ohmicity N and phonon cutoff energy ω_b. If not stated otherwise, for the results presented in this work, $\alpha_p = 0.03\,\mathrm{ps}^2$, $N = 1$ and $\omega_b = 1\,\mathrm{meV}$. The electron-phonon coupling constant α_p is strongly dependent on the respective quantum dot and can vary significantly [214].

The ohmicity N classifies the spectral density based on its behaviour at low frequencies. Different ohmicities are visualized in Fig. 3.2,panel (b). An ohmic spectral density, obtained for $N = 1$, is characterized by $J(\omega) \propto \omega$. This type of spectral density grows linearly at low frequencies, is typically associated with resistive environments, akin to classical friction, and is commonly used for systems interacting with phonon baths. For $N < 1$, the spectral density is sub-ohmic, meaning it grows more slowly with frequency. This behavior is often linked to long-time correlations and noise, forming a frequency enhancement similar to a low-pass filter. Conversely, a super-ohmic spectral density, achieved for $N > 1$, grows rapidly at low frequencies. This form is typically used in models involving high-frequency phonon components, such as the quantum dot cavity systems investigated in this work. The super-ohmic spectral density $J(\omega)$ with $N = 3$ is displayed in Fig. 3.2, panel (a) and

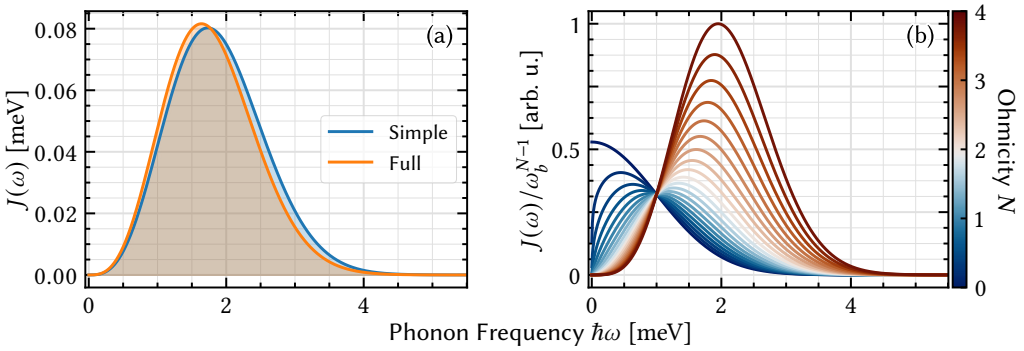

Figure 3.2: Phonon spectral density function $J(\omega)$ depicted as a function of phonon frequency ω. **(a)** Comparison between a simple model from Eq. (3.4) for $\alpha = 0.03\,\mathrm{ps}^2$ and the full model Eq. (3.2) with $D_e = 7\,\mathrm{eV}$, $D_j = -3.5\,\mathrm{eV}$, $\rho = 5.37\,\mathrm{g/cm}^3$, $c_s = 5110\,\mathrm{m/s}$, $e_h/e_r = 1.15$ and $a_e = 3.4\,\mathrm{nm}$. Both feature $N = 3$. The simple model closely approximates the general formula when $a_h \approx a_e$, and is generally adequate for the results discussed in this work. **(b)** Examination of the phonon density as it varies with both the frequency ω and the ohmicity N, demonstrating resemblance to low-pass filter envelopes for $N < 1$ and the high-pass filter envelopes for $N > 1$.

compares both Eqs. (3.2) and (3.4). While both methods do not perfectly coincide, the simple model is usually sufficient to accurately characterize the phonon bath. Increasing the phonon coupling α leads to linear increases in the spectral density. The spectral density can also be tailored beyond Eq. (3.2) to match different physical systems, featuring different spectral densities [210].

3.2 Polaron Master Equation

With the phonon spectral density now established, the subsequent step involves determining the numerical incorporation of phonons. A large ensemble of phonons constitutes a *phonon bath*, represented by a collection of bosonic oscillators. These oscillators then couple to the electronic states $|i\rangle\langle i|$. The resulting Hamiltonian is expressed as

$$\mathcal{H}_2 = \underbrace{\sum_{\vec{q}} \hbar\omega_{\vec{q}} \hat{b}^\dagger_{\vec{q}} \hat{b}_{\vec{q}}}_{H_{\text{Bath}}\text{ - Bath Oscillator}} + \underbrace{\sum_{i\in S} |i\rangle\langle i| \sum_{\vec{q}} \hbar\omega_{\vec{q}} \left(\lambda_{\vec{q},i} b^\dagger_{\vec{q}} + \lambda^*_{\vec{q},i} b_{\vec{q}}\right)}_{H_{\text{QD-Bath}}\text{ - QD-Bath Interaction}} \tag{3.5}$$

$$= H_{\text{Bath}} + H_{\text{QD-Bath}}\,. \tag{3.6}$$

In numerical treatments, resolving the exact dynamics of the phonon bath can be computationally prohibitive. Therefore, the phonon bath is often assumed to remain constant, implying no changes in the phonon density over time. This assumption is justified because, on the time scales relevant to many quantum simulations, the slow evolution of the bath properties relative to the fast dynamics of the electronic and photonic states allows for an effective approximation in which the impact of the phonons is captured through an averaged or static model. Essentially, the bath is modeled as a constant cloud of phonons that follows the electrons of the quantum dot. This interaction is effectively described using a quasi-particle known as the *polaron* [149, 208], which significantly simplifies the treatment of the phonon Hamiltonian.

To model the interaction of the constant phonon cloud and the quantum dot states, a transformation into the *polaron frame* is employed using a *polaron transformation*. This transformation is defined by the unitary operator $\hat{\mathcal{U}} = e^{S}$, which modifies the original Hamiltonian to encapsulate phonon effects within altered system parameters. In this frame, the oscillator components of the Hamiltonian are traced out of the total density matrix, effectively neglecting the time evolution of the bath and reducing the complexity of the dynamics to a more manageable form. The derivation and implications of the polaron transformation, as outlined in detail in [149, 208], are reproduced and discussed in the following section.

By employing the polaron transformation, the essential effects of phonon interactions on the quantum dot states are retained, while the computational complexity is significantly reduced. This approach facilitates an efficient and accurate numerical treatment of the phonon bath, enabling the exploration of various quantum phenomena influenced by phonon interactions. It is particularly valuable in understanding the impact of phonons on quantum coherence and dephasing processes in quantum dot systems, thereby aiding in the design of more robust quantum information processing devices.

3.2.1 Polaron Transformation

The polaron transformation is applied using a unitary transformation $\hat{\mathcal{U}} = e^{\hat{S}}$ such that the transformed Hamiltonian in the polaron frame reads

$$\tilde{\mathcal{H}} = e^{\hat{S}} \mathcal{H} e^{-\hat{S}} \,. \tag{3.7}$$

The transformation operator $\hat{S}$ is defined by [215]

$$\hat{S} = \sum_i |i\rangle\langle i| \sum_{\vec{q}} \frac{\lambda_{\vec{q},i}}{\omega_{\vec{q}}} \left(b_{\vec{q}}^\dagger - b_{\vec{q}} \right) . \tag{3.8}$$

This operator is similar to the interaction component of the polaron Hamiltonian, except for a reversed sign for the phonon annihilator in Eq. (3.8). The transformation operator is designed to remove the quantum-dot-bath interaction component, allowing the usual von Neumann equation to resolve the temporal dynamics of the quantum dot system.

The transformation is evaluated using the Baker-Campbell-Hausdorff formula [216]

$$e^{\hat{S}} H e^{-\hat{S}} = H + [\hat{S}, H] + \frac{1}{2!} \left[\hat{S}, [\hat{S}, H] \right] + \dots , \tag{3.9}$$

with $[A, B] = AB - BA$ as the commutator.

Each part of the complete Hamiltonian in Eq. (2.3) is transformed into the polaron frame individually. The time independent part of the Hamiltonian describing the energy configuration of the system

$$\tilde{\mathcal{H}}_0 = \mathcal{H}_0 , \tag{3.10}$$

is unaffected by the polaron transformation. As such, the interaction picture transformation also remains unaffected. Furthermore, the transformation of the interaction component

$$\tilde{\mathcal{H}}_1 = \langle \mathcal{B} \rangle \, \mathcal{H}_1 , \tag{3.11}$$

results in linear scaling with the expectation value of thermal displacement operator $\langle B \rangle = \langle B \rangle_{i,j} \propto \lambda_{i,i}$, effectively re-normalizing the quantum-dot-cavity as well as the quantum-dot-pulse coupling. Due to different couplings of the states to the phonon bath, the average thermal displacement depends on the respective electronic state indices i, j. For example, the biexciton coupling scales with twice the exciton coupling, where $\lambda_\mathrm{B} = 2\lambda_\mathrm{X}$. The expectation value of the thermal displacement operator is given by

$$\langle \mathcal{B} \rangle = \langle \mathcal{B}_\pm \rangle = \exp \left[-\frac{1}{2} \int_0^\infty \frac{J(\omega)}{\omega^2} \coth \left(\frac{\hbar\omega}{2k_\mathrm{B}T} \right) \right] . \tag{3.12}$$

Finally, the transformed polaron Hamiltonian reads

$$\tilde{\mathcal{H}}_2 = H_\mathrm{Bath} + \hat{\mathcal{X}}_g \hat{\zeta}_g + \hat{\mathcal{X}}_u \hat{\zeta}_u - E_P , \tag{3.13}$$

The interaction with the phonon bath results in a static shift of the electronic state energies

$$E_P = \sum_{\vec{q}} \sum_i \frac{\lambda_{\vec{q}}^2}{\omega_{\vec{q}}} |i\rangle\langle i| \ , \tag{3.14}$$

which is absorbed into the definition of the respective state energies E_i. As such, it is not explicitly included in the numerical evaluation of the system. The interaction component in Eq. (3.13) is constructed by [208]

$$\hat{\zeta}_g = \frac{1}{2} \left(\mathcal{B}_+ + \mathcal{B}_- - 2 \langle \mathcal{B} \rangle \right) \tag{3.15}$$

and

$$\hat{\zeta}_u = \frac{1}{2\mathrm{i}} \left(\mathcal{B}_+ - \mathcal{B}_- \right) \ . \tag{3.16}$$

The polaron operators guiding the dynamics of the system read

$$\hat{X}_g = \chi + \text{ H.c.} \tag{3.17}$$

and

$$\hat{X}_u = \mathrm{i} \left(\chi - \text{ H.c.} \right) \ . \tag{3.18}$$

Here, χ is defined using the non-conjugated elements of $\mathcal{H}_1$ from Eq. (2.2), such that $\mathcal{H}_1 = \chi + \text{ H.c.}$. At this point, the density matrix required to resolve this system is still governed by the bath oscillators H_{Bath} in Eq. (3.13). To reduce the Hilbert space to the density matrix of the quantum-dot-cavity system of interest, the phonon modes, described by their respective wave vector $\vec{q}$, are partially traced over, effectively numerically ignoring the bath oscillator. As mentioned prior, the phonon bath is assumed to be constant and as such, does not change in time, justifying this approach.

A Born-Markov approximation is applied, assuming $\rho(t)$ to be constant within the context of the interaction period. The resulting polaron rate contribution reads [208]

Equation 3.19

$$\mathcal{L}^{\text{Polaron}} \left[\rho(t) \right] = - \int_0^{\tau_{\text{max}}} \mathrm{d}\tau \sum_{i \in \{g,u\}} \left(G_i(\tau) \left[\hat{X}_i(t), \hat{X}_i(t, t-\tau) \rho(t) \right] \right) + \text{ H.c.} \ .$$

In this context, Eq. (3.19) represents a Lindblad-type rate that can be seamlessly integrated into the pre-existing von Neumann equation Eq. (2.8). The phonon cutoff time depends on the specific system under investigation and is determined such that beyond this point, the phonon correlations $\Phi(\tau)$ become zero, as illustrated in Fig. 3.3. In this work, it is set to $\tau_{\text{max}} = 4\,\text{ps}$.

The polaron Green functions required for the evaluation of Eq. (3.19) are defined as

$$G_g = \langle \mathcal{B} \rangle^2 \left(\cosh(\phi(\tau)) - 1 \right) \,, \tag{3.20}$$

and

$$G_u = \langle \mathcal{B} \rangle^2 \sinh(\phi(\tau)) \,. \tag{3.21}$$

The phonon correlation function required by the polaron Green functions reads

$$\phi(\tau) = \int_0^\infty \frac{J(\omega)}{\omega^2} \left[\coth\left(\frac{\hbar\omega}{2k_\text{B}T} \right) \cos(\omega\tau) - \text{i} \sin(\omega\tau) \right] \text{d}\omega \,, \tag{3.22}$$

which is characterized primarily by the spectral density of the phonons $J(\omega)$ as well as the temperature of the environment T. Notably, the imaginary part of the correlation function, visualized in Fig. 3.3, is not influenced by the temperature of the system.

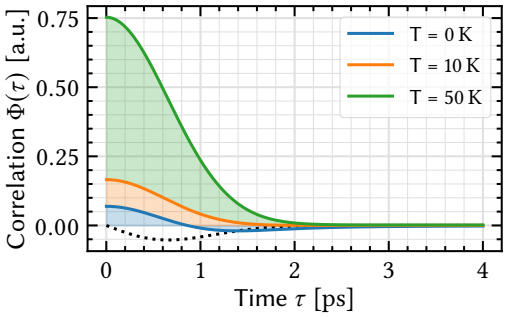

Figure 3.3: Polaron frame correlation function $\Phi(\tau)$, as described by Eq. (3.22), displayed for various temperatures. The solid lines represent the real components of the correlation function. The dotted black line illustrates the imaginary component, which remains constant across all temperatures.

The polaron transformed operator $\hat{X}_i(t, t-\tau)$ is given by

$$\hat{X}_i(t, t-\tau) = \tilde{\hat{\mathcal{U}}}(t,\tau)\hat{X}_i(t)\tilde{\hat{\mathcal{U}}}^{\dagger}(t,\tau)\,, \tag{3.23}$$

with the commonly used approximation

$$\tilde{\hat{\mathcal{U}}}(t,\tau) \approx e^{-\mathrm{i}/\hbar\tilde{\mathcal{H}}_1\tau}\,. \tag{3.24}$$

This procedure mirrors the regular interaction picture transformation using $\mathcal{H}_0$. However, unlike the exact interaction picture transformation, where $\mathcal{H}_0$ commutes with itself, $\mathcal{H}_1$ does not commute at different times, making the transformation in Eq. (3.24) an approximation.

For these approximations to be exact, it would require that $[\mathcal{H}(t_1), \mathcal{H}(t_2)] = 0$. While the polaron frame approximation is not entirely precise due to the time-dependence of $\mathcal{H}_1(t)$ in the exponential function, it adequately captures the phonon contribution for the scope of this work. The polaron frame introduces an inherent error that surpasses that of the time evolution operator approximation. However, since the time scales are restricted to the phonon cut-off time $\tau_{\max}$, the resulting error is minimal, making this approach widely accepted in the literature [149, 157, 159, 208].

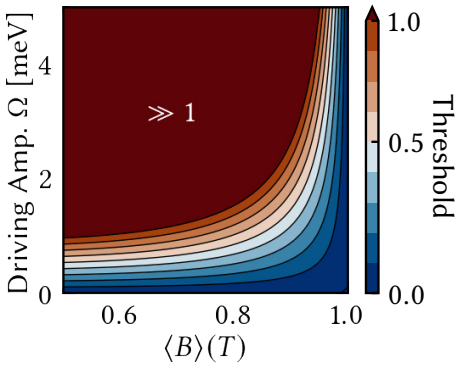

Figure 3.4: Bounds of validity for the polaron master equation derived from Eq. (3.25), analyzed for varying values of the expected $\langle B \rangle$ factor and the amplitude of the driving pulse. The analysis highlights that the applicability of the polaron master equation is limited, particularly as the amplitude of the driving pulse increases, leading to rapid breaches of these bounds.

An advanced approach to applying the polaron transformation involves accurately integrating the Hamiltonian or using the von Neumann equation to calculate the transformation [80]. While this increases the numerical complexity, the overall results remain largely unaffected for the parameters considered in this work. This is corroborated by comparisons with the path integral method outlined in Section 3.3, which does not rely on the approximations inherent in the polaron frame. Despite these approximations, the polaron master equation yields results that align well with experimental data, particularly for low temperatures and weak interaction

strengths in the quantum dot-cavity system and its environment.

Moreover, the polaron master equation has been shown to accurately describe phonon interactions under the condition [208, 215]

$$\left(\frac{\Omega_i}{\omega_\mathrm{p}}\right)\left(1-\langle B\rangle^4\right) \ll 1\,, \tag{3.25}$$

These bounds are further visualized in Fig. 3.4. For low temperatures, resulting in near unity $\langle B\rangle$ values, and small pulse amplitudes Ω_i, such as those used in simple excitation processes or transition pulses, the polaron master equation provides an accurate description of electron-phonon interactions. Similar thresholds exist for cavity interactions. However, the coupling rates in these cases are typically much smaller where $g \ll \Omega_i$, making the polaron master equation even more applicable. This ensures that the model remains robust and accurate across a range of scenarios, providing valuable insights into the behavior of quantum dot systems coupled with phonons and cavities. The polaron master equation simplifies the complex dynamics between the quantum dot and phonon bath, making it a powerful tool for studying these interactions.

Analytical Phonon Rates

An additional Markov approximation is employed, such that $\chi(t,\tau) = \chi(t)$, effectively neglecting all memory and time retardation effects. This approximation reduces the polaron contribution to a simple Lindblad rate, allowing for a clearer distinction between pulse or laser-induced phonon transition rates and cavity transition rates. Additionally, the resulting analytical rates can be investigated directly to determine the fundamental behaviour of the electron-phonon interactions.

The resulting Lindbladian rate contribution reads [147]

$$\mathcal{L}^{\text{Phonons}}\left[\rho(t)\right] = \sum_{i,j\in S}\Gamma_{i,j}^{L,\pm}\mathcal{L}_{|i\rangle\langle j|}\left[\rho(t)\right] + \sum_{c\in M}\Gamma_{i,j}^{\mathrm{C},\pm}\mathcal{L}_{|i\rangle\langle j|\hat{\mathrm{b}}_\mathrm{c}^\dagger}\left[\rho(t)\right]\ . \tag{3.26}$$

Expression Eq. (3.26) can be directly incorporated into the von Neumann equation. The

phonon-assisted laser-induced transition rates are given by [149]

$$\Gamma_{i,j}^{L,\pm} = \frac{2\left|\langle B\rangle\, \Omega_{i,j}(t)\right|^2}{\hbar} \int_0^\infty \mathrm{Re}\{(\cosh(\phi(\tau)) - 1)\, f(t,\tau) + \sinh(\phi(\tau)) \cos(\eta(t)\tau)\} \mp \mathrm{Im}\left\{\left(e^{\phi(\tau)} - 1\right) \frac{\Delta_{i,j}^L \sin(\eta(t)\tau)}{\eta(t)}\right\} \mathrm{d}\tau, \tag{3.27}$$

where

$$\eta(t) = \sqrt{|\langle \mathcal{B}\rangle\, \Omega_i(t)|^2 + \left(\Delta_{i,j}^L\right)^2} \tag{3.28}$$

and

$$f(t,\tau) = \frac{\left(\Delta_{i,j}^L\right)^2 \cos(\eta(t)\tau) + \left|\langle B\rangle\, \Omega_{i,j}(t)\right|^2}{\eta^2(t)}. \tag{3.29}$$

The quantum-dot-pulse detuning is defined as $\Delta_{i,j}^L = (E_j - E_i)/\hbar - \omega_{i,j}$, where $\omega_{i,j}$ is the pulse frequency driving the electronic transition between the electronic states $|i\rangle$ and $|j\rangle$. The cavity-assisted induced transitions, as defined in [147], are expressed as

$$\Gamma_{i,j}^{C,\pm} = \frac{\langle \mathcal{B}\rangle^2\, g^2}{\hbar^2} \mathrm{Re}\left\{\int_0^\infty e^{\pm \mathrm{i}\Delta_{i,j}^C \tau} \left(e^{\phi(\tau)} - 1\right) \mathrm{d}\tau\right\}. \tag{3.30}$$

The quantum-dot-cavity detuning is given by $\Delta_{i,j}^C = (E_j - E_i)/\hbar - \omega_\mathrm{c}$, with $\omega_\mathrm{c} = E_\mathrm{c}/\hbar$ as the central cavity frequency.

Both rates are visualized in Fig. 3.5. Although this simplified phonon rate is not extensively employed in this work, it proves useful for quick numerical investigations due to its low computational complexity as well as providing insights into the phonon resonances. Here, the most obvious limitation of the polaron master equation derived is evident: without a pulse or laser and without a cavity, there are no phonon interactions. This is despite the fact that phonons could also influence the free radiative decay described by Eq. (2.11). At low temperatures, the emission and absorption of phonons are clearly separated, with a maximum at $\hbar\omega_b$. Although not evident from comparing Eqs. (3.27) and (3.30), both the pulse and cavity rates are shaped very similarly when both are analyzed using their respective detunings and only significantly differ in their amplitude.

The rates for commonly used pulse amplitudes are significantly larger than those for commonly used cavity couplings, as indicated by the much larger values for the rates in

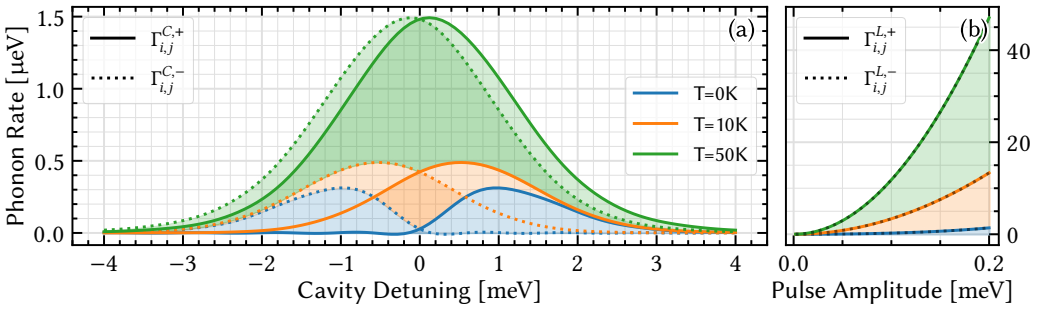

Figure 3.5: Phonon rates of the polaron rate equations for varying temperatures. Real parts of the phonon emission (solid lines) and absorption (dotted lines) are depicted. **(a)** Cavity-induced phonon transition rates based on Eq. (3.30) for varying dot-cavity detunings $\Delta E^{\mathrm{c}} = E_{\mathrm{X}} - E_{\mathrm{c}}$. The coupling is set to $\hbar g = 50\,\mu\mathrm{eV}$ with a phonon coupling of $\alpha = 0.03\,\mathrm{ps}^2$. **(b)** Pulse-induced phonon transition rates based on Eq. (3.27) for resonant pulses and for varying pulse amplitudes.

panel (b) compared to panel (a) in Fig. 3.5. This suggests that pulse-induced electron-phonon interactions are significantly more relevant than cavity-mediated phonon interactions in typical experimental setups, even when strong light-matter coupling with g on the order of several hundred μeV is present.

3.3 Path Integral Method: Augmented Density Matrix Formalism

To provide a comprehensive comparison and validation of the polaron master equation, the path integral approach is briefly explored. The elements of the density matrix are expressed using the sum of all possible paths that the system can take, provided the system dynamics are Hamiltonian, meaning the propagation Hamiltonian is self-adjoint. This principle also holds for the reduced density matrix obtained by tracing over the phonon bath oscillators, as done previously using the polaron frame.

The sum-over-paths representation of the density matrix elements is given by [210, 217]

$$\rho_{m_i,n_i} = \sum_{\substack{m_0,\ldots,m_{k-1}\\ n_0,\ldots,n_{k-1}}} R^{m_k,\ldots,m_0}_{n_k,\ldots,n_0} \text{ with } R^{m_k,\ldots,m_0}_{n_k,\ldots,n_0} = \rho_{m_0,n_0} \prod_{l=1}^{k} \mathcal{M}^{m_{l-1},n_{l-1}}_{m_l,n_l} \exp\left[\sum_{l=1}^{k}\sum_{l'=1}^{l} S^{m_{l'},n_{l'}}_{m_l,n_l}\right] . \tag{3.31}$$

Here, $R^{m_k,\ldots,m_0}_{n_k,\ldots,n_0}$ is a tensor of rank $2k$, where each index n_i and m_i represents a matrix index in the Hilbert space of the reduced density matrix. Consequently, these indices can range from 0 to the number of rows or columns of the reduced density matrix. The number of rows and columns are equal, with rows = cols = $\dim(\rho)$.

In this context, a path is defined as any possible sequence of states $m_0, \ldots, m_{k-1}$ that the system traverses in the total Hilbert space over the time interval from t_0 to t_{k-1}. This sum will include $\dim(\rho)^{2k}$ terms. The elements ρ_{m_0,n_0} represent the initial density matrix $\rho(t=0)$. From Eq. (3.31), the recurrence

$$R^{n_k,\ldots,n_0}_{m_k,\ldots,m_0} = \mathcal{M}^{m_{k-1},n_{k-1}}_{m_k,n_k} \exp\left[\sum_{l=1}^{k} S^{m_l,n_l}_{m_k,n_k}\right] R^{n_{k-1},\ldots,n_0}_{m_{k-1},\ldots,m_0} \tag{3.32}$$

arises, which defines the next path integral tensor using the previously calculated result, with initial condition $\mathcal{R}^{n_0}_{m_0} = \rho_{m_0,n_0}$.

The memory function or *influence functional* is defined as

$$S^{m_{l'},n_{l'}}_{m_l,n_l} = -\mathcal{K}_{m_{l'},m_l} - \mathcal{K}^*_{n_l,n_{l'}} + K^*_{m_l,n_{l'}} + \mathcal{K}_{m_{l'},n_l}\,, \tag{3.33}$$

with the phonon memory kernel

$$\begin{aligned}
\mathcal{K}_{n_l m_l}(0) &= \int_0^\infty \mathrm{d}\omega \frac{J(\omega)}{\omega^2}\left[\coth\left(\frac{\hbar\omega}{2k_BT}\right)(1-\cos(\omega\Delta t)) + \mathrm{i}\sin(\omega\Delta t) - \mathrm{i}\omega\Delta t\right]\,,\\
\mathcal{K}_{n_l m_l}(\tau>0) &= \int_0^\infty \mathrm{d}\omega \frac{J(\omega)}{\omega^2}(1-\cos(\omega\Delta t))\left[\coth\left(\frac{\hbar\omega}{2k_BT}\right)\cos(\omega\tau) - \mathrm{i}\sin(\omega\tau)\right]\,.
\end{aligned} \tag{3.34}$$

In this case, the polaron shift induced by the phonons is described by $\Delta E = -\int_0^\infty \mathrm{i}\frac{J(\omega)}{\omega}\Delta t \mathrm{d}\omega$. As with the polaron master equation approach, this shift will be absorbed into the definitions of the state energies and as such numerically neglected.

The propagator, which defines the evolution of the system from time t_1 to time t_2 is given by

$$\mathcal{M}_{t_1,t_2}[\hat{\mathrm{O}}] = \mathcal{T}\exp\left[\int_{t_1}^{t_2} \mathcal{L}[t]\mathrm{d}t\right]\,. \tag{3.35}$$

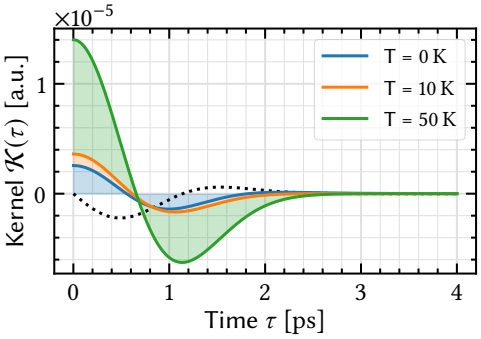

Figure 3.6: Path integral kernel functions derived from Eq. (3.34), across various temperatures. Consistent with the behavior observed in the Polaron Equation Kernel function, the imaginary part of the path integral kernel (dotted line) remains constant for all temperatures.

Here, $\mathcal{L}[t]$ is the total Liouvillian of the system as defined in Eq. (2.8). Recalling the derivation of the von Neumann equation in Eq. (2.8), this operator is also used to calculate the time evolution using the regular von Neumann equation for a phonon free simulation, or the polaron master equation for the polaron solution with electron-phonon interactions. The time ordering operator $\mathcal{T}$ ensures that the treatment of the exponential function results in matrix products that obey ascending orders of t, independent of the method used for the evaluation.

For a time independent Hamiltonian in $\mathcal{L}[t]$, a simple matrix exponential can be used to calculate Eq. (3.35). However, in this work, with a time dependent Hamiltonian, the von Neumann equation is used to calculate the evolution of $\hat{\mathrm{O}}(t_1) = |m_{-1}\rangle\langle n_{l-1}|$ towards $\hat{\mathrm{O}}(t_2) = |m_l\rangle\langle n_l|$. The individual factors $\mathcal{M}_{m_l,n_l}^{m_{l-1},n_{l-1}}$ are obtained by calculating

$$\mathcal{M}_{m_l,n_l}^{m_{l-1},n_{l-1}} = \langle m_l|\, \mathcal{M}_{t_1,t_2}\left[|m_{l-1}\rangle\langle n_{l-1}|\right] |n_l\rangle \ . \tag{3.36}$$

This comprehensive framework captures the influence of the phonon bath oscillators on the temporal evolution of the system across different paths within the total Hilbert space, without the use of any additional approximation. While this statement is generally true, the total number of elements inside the path integral tensor array in Eq. (3.31) with rank $2k$ is N^{2k}. Here, $k = t_{\max}/\Delta t$ represents the maximum number of time steps used for the path integral. Evidently, this number will grow to huge proportions, even for small systems and a small number of time steps. As an example, assuming a simple two level system with $N = 2$ and 100 time steps, the path integral requires $2^{2\cdot 100}$ elements to be saved and propagated for the next time step, which is uniterable even on the strongest computing hardware. By exploiting the finite length of the memory kernel functions $\mathcal{K}(\tau)$, which is visualized in Fig. 3.6, the maximum depth of the memory, and with it, the rank of the path integral tensor is truncated. Assuming the kernel functions are zero at $\tau_{\max}$, by choosing a fixed time step Δt, the required rank of the tensor is calculated using $N_c = \tau_{\max}/\Delta t$. From

here, the *augmented density matrix* (ADM) is introduced as the recursion

$$\rho^{n_k,\ldots,n_{k-N_c+1}}_{m_k,\ldots,m_{k-N_c+1}} = \mathcal{M}^{m_{k-1},n_{k-1}}_{m_k,n_k} \exp\left[\sum_{l=1}^{k} S^{m_l,n_l}_{m_k,n_k}\right] \rho^{n_{k-1},\ldots,n_{k-N_c+1}}_{m_{k-1},\ldots,m_{k-N_c+1}} . \tag{3.37}$$

From the ADM, the reduced density matrix in the original Hilbert space can be reconstructed by tracing over all possible paths, resulting in

$$\rho_{n_k,m_k}(t_k) = \sum_{\substack{m_{k-1},\ldots,m_{k-N_c+1} \\ n_{k-1},\ldots,n_{k-N_c+1}}} \rho^{n_{k-1},\ldots,n_{k-N_c+1}}_{m_{k-1},\ldots,m_{k-N_c+1}} . \tag{3.38}$$

The first N_c iterations of the path integral tensor are performed using Eq. (3.32). Then, Eq. (3.37) is utilized for the remaining iterations. Because of this truncation, the rank of the ADM does not increase beyond $2N_c$, and thus, the total number of elements inside the tensor remain at N^{2N_c}. With a carefully configured N_c, the ADM is iterable even for larger systems on regular consumer hardware, albeit with numerical effort significantly larger than for the polaron master equation when the system size scales beyond a two level system.

3.3.1 Partially Summed Augmented Density Matrix

While the augmented density matrix significantly reduces numerical effort compared to full tensor propagation, it still scales exponentially for larger systems when compared to the polaron master equation. For systems with more than two electronic states where phonon coupling is identical for different states, states can be grouped based on their phonon coupling. This approach tracks the phonon bath influence depending on the phonon coupling value λ. The path integral memory function $S^{m_{l'},n_{l'}}_{m_l,n_l}$ depends solely on the states according to their phonon coupling value λ within the phonon spectral density Eq. (3.1). If two or more states share the same phonon coupling, they can be grouped using the same memory function. Using the notation $\lambda^g := \lambda^{(s,g)}$, where λ is the phonon coupling in Eq. (3.2), states are renamed such that $|m\rangle \to |g,s\rangle$ and $|n\rangle \to |\bar{g},\bar{s}\rangle$ where g is the group with unique coupling and s is the state index within that group. The influence function then results in

$$\sum_{l=k-N_c}^{k} S^{m_l,n_l}_{m_k,n_k} = \sum_{l=k-N_c}^{k} S^{(g_l,s_l),(\bar{g}_l,\bar{s}_l)}_{(g_k,s_k),(\bar{g}_k,\bar{s}_k)} = \sum_{l=k-N_c}^{k} S^{g_l,\bar{g}_l}_{g_k,\bar{g}_k} , \tag{3.39}$$

indicating that the influence function no longer depends on the state index withing the groups. Inserting this into Eq. (3.37) results in the new definition of the augmented density matrix with

$$\rho^{(\bar{g}_k,\bar{s}_k),\bar{g}_{k-1},\ldots,\bar{g}_{k-N_c+1}}_{(g_k,s_k),g_{k-1},\ldots,g_{k-N_c+1}} = \sum_{\substack{s_{k-1}\\ \bar{s}_{k-1}}} \mathcal{M}^{(g_{k-1},s_{k-1}),(\bar{g}_{k-1},\bar{s}_{k-1})}_{(g_k,s_k),(\bar{g}_k,\bar{s}_k)} \sum_{\substack{g_{k-N_c}\\ \bar{g}_{k-N_c}}} \exp\left[\sum_{l=1}^{k} S^{g_l,\bar{g}_l}_{g_k,\bar{g}_k}\right] \rho^{(\bar{g}_{k-1},\bar{s}_{k-1}),\bar{g}_{k-2},\ldots,\bar{g}_{k-N_c}}_{(g_{k-1},s_{k-1}),g_{k-2},\ldots,g_{k-N_c}} \,. \tag{3.40}$$

The reduced density matrix is then constructed via

$$\rho_{n_k,m_k}(t_k) = \sum_{\substack{s_{k-1},\ldots,s_{k-N_c+1}\\ \bar{s}_{k-1},\ldots,\bar{s}_{k-N_c+1}}} \rho^{(\bar{g}_k,\bar{s}_k),(\bar{g}_{k-1},\bar{s}_{k-1}),\ldots,(\bar{g}_{k-N_c+1},\bar{s}_{k-N_c+1})}_{(g_k,s_k),(g_{k-1},s_{k-1}),\ldots,(g_{k-N_c+1},s_{k-N_c+1})} \,. \tag{3.41}$$

The number of terms to iterate over is reduced from N^{2N_c} to $N^2 N_g^{2(N_c-1)}$, with N_g being the number of unique group indices. This reduction is achieved without any approximation, maintaining numerical exactness by cleverly grouping the non-unique parts of the path integral density tensor. Naturally, this method addresses all of the limitations of the polaron master equation, such as neglected time retardation effects and the absence of phonon interactions without a light field or pulse.

The path integral implementation used in this work[1] provides substantial improvements in modeling quantum phenomena when compared to the polaron master equation [162, 213, 218]. Due to the high computational complexity of the biexciton and trion systems studied in Chapters 5 to 7, this approach becomes impractical for routine use, as the numerical effort escalates quickly with system dimensionality. Nevertheless, for simplified systems, the path integral remains a valuable validation tool for the polaron master equation within the specific parameter ranges explored. The comparison between these two methods and their consistency is further discussed in Section 3.4.

While more advanced approaches, such as the process tensor method for iterating the path integral [217], exist, the current implementation is effectively limited the validation of the polaron master equation for the purposes of this study. This validation is critical to ensuring the accuracy and reliability of the quantum models employed, with the path integral method providing a benchmark for confirming the robustness of the polaron master equation within the context of these investigations.

[1] Although the implementation of the path integral method was specifically carried out for this work, the underlying theory was not developed by the author of this study.

3.4 Phonon Assisted Processes

To understand the phonon-induced effects, it is instructive to consider their qualitative visibility across different methods, which in this work are limited to the polaron master equation Eq. (3.19), and the path integral approach Eq. (3.40). While these methods may yield different quantitative results, they can all reveal key phonon-induced phenomena. Consider a simple two-level system inside a single mode cavity, where the system is excited using a laser pulse with a Gaussian envelope. This system is equivalent to using the JCM Hamiltonian from Eq. (2.16) with the laser driving from Eq. (2.25). The interaction Hamiltonian for this setup is then given by

$$\mathcal{H}_1 = |\mathrm{X}\rangle\langle\mathrm{G}| \left[\Omega_L(t) + \hbar g \hat{\mathrm{b}}\right] + \text{ H.c. }. \tag{3.42}$$

Here, $E_\mathrm{X} = 1\,\mathrm{eV}$ describes the energy of a single exciton-to-ground state transition, referencing a single exciton. The cavity interaction is characterized by the cavity coupling $\hbar g = 50\,\mu\mathrm{eV}$. The reference case involves scanning the pulse detuning $\Delta_L = E_\mathrm{X} - E_L$ or cavity detuning $\Delta_C = E_\mathrm{X} - E_\mathrm{c}$, as shown in Fig. 3.7 in panel (a). Here, no electron-phonon coupling is included by using the regular von Neuman equation.

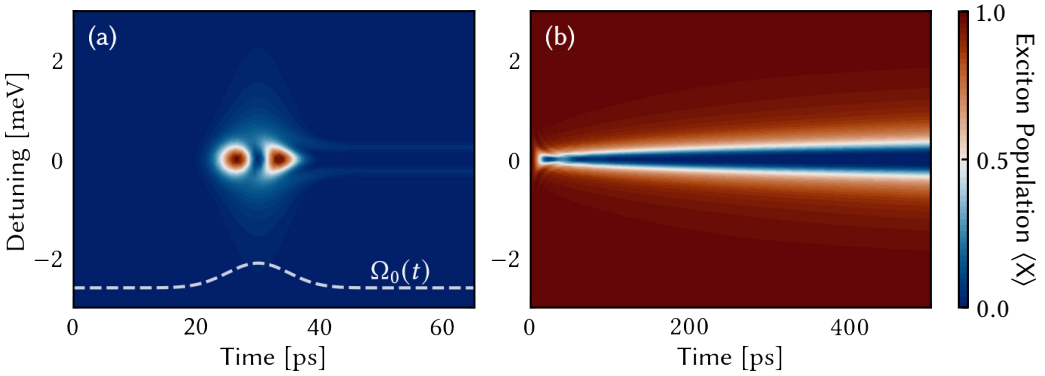

Figure 3.7: Phonon free excitation and decay for $E_\mathrm{X} = 1\,\mathrm{eV}$. **(a)** Excitation dynamics of the exciton using a $\mathcal{A}_0 = 4\pi$ pulse of length $\tau = 5\,\mathrm{ps}$, centered at $t_0 = 30\,\mathrm{ps}$. The pulse envelope $\Omega_L(t)$ is indicated by the white dashed line and is not to scale. **(b)** Decay dynamics of the exciton into a cavity characterized by $\hbar g = \hbar\kappa = 50\,\mu\mathrm{eV}$.

Moderately strong pulses and cavity parameters, comparable to those used for later results, are employed. In this scenario, the excitation is symmetric around a detuning of zero in both the cavity and the pulse investigations. The excitation using a pulse is most efficient at direct resonance where $\hbar\omega_L = E_\mathrm{X}$, and the cavity enhancement is most efficient at $E_\mathrm{c} = E_\mathrm{X}$.

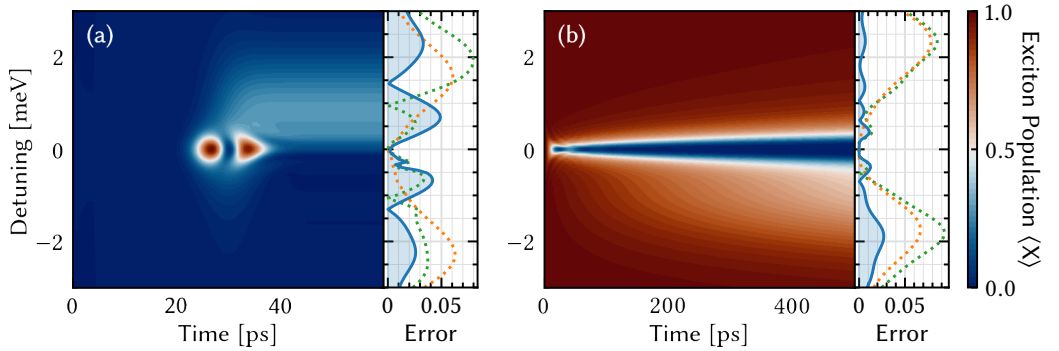

Figure 3.8: Phonon assisted excitation and decay for $E_X = 1\,\text{eV}$. The temperature is set to $T = 0\,\text{K}$, highlighting the isolated effects on red- or blue-detuned systems for a system with minimal phonon interaction. The phonon coupling constant is fixed at $\alpha = 0.03\,\text{ps}^2$. For the path integral approach, a configuration with $N_C = 7$ with a step size of $\Delta t = 0.57\,\text{ps}$ is used. The plots include errors on the right side, indicating mismatches between the polaron master equation and path integral solutions at the end of the simulations (blue lines). Here, the error is estimated using the absolute differences of the final states with error $= \text{abs}(\langle X\rangle_{\text{PME}}(t_{\max}) - \langle X\rangle_{\text{PI}}(t_{\max}))$. **(a)** Excitation dynamics of the exciton using a $\mathcal{A}_0 = 4\pi$ pulse of length $\tau = 5\,\text{ps}$, centered at $t_0 = 30\,\text{ps}$. **(b)** Decay dynamics of the exciton into a cavity characterized by $\hbar g = \hbar\kappa = 50\,\mu\text{eV}$. The orange dotted line and green dotted line represent errors for lower-resolution path integral ($N_C = 4, \Delta t = 1\,\text{ps}$) and polaron master equation solutions, respectively, compared to the higher-resolution path integral solution.

Next, the electron-phonon interactions are included using the polaron master equation, as displayed in Fig. 3.8. Investigating the pulse detuning in panel (a), a side band of nonzero excitation emerges at $E_X + 1\,\text{meV}$, coinciding with the phonon cutoff energy in Eq. (3.4) [82]. Here, the pulse generates non-zero populations of the excited state. The blue-detuned laser can still excite the two-level system because a phonon is emitted to bridge the excess energy of the pulse. This effect is also visible in analytical rates from Eq. (3.26), but with much greater amplitude, suggesting a strong overestimation of phonon interactions. A comparison with path integral results, shown at the side of the panel, indicates low errors in this parameter regime, suggesting that the polaron master equation is applicable here. Investigating the cavity enhanced decay of an initially fully excited two level system in Fig. 3.7 in panel (b), a different side band emerges at $E_X - 1\,\text{meV}$, again coinciding with the phonon cutoff energy. Similar to the pulsed case, the analytical rates also show this side band, albeit with exaggerated phonon influences. The comparison with the path integral method shows that the overall precision of the polaron master equation solution is sufficient for the investigated parameters. The red-detuned cavity Purcell enhances the decay of the

electronic state beyond the regular enhancement because a phonon can be absorbed to bridge the energy gap between the two-level system and the cavity resonance.

Descending into the range of viability for the polaron master equation, less accurate regimes are explored, particularly with stronger pulses. Pulses can be strong in two senses: they can be long, allowing for prolonged electron-phonon interactions, or they can be large in amplitude, permitting short but intense interactions. The worst case involves both conditions.

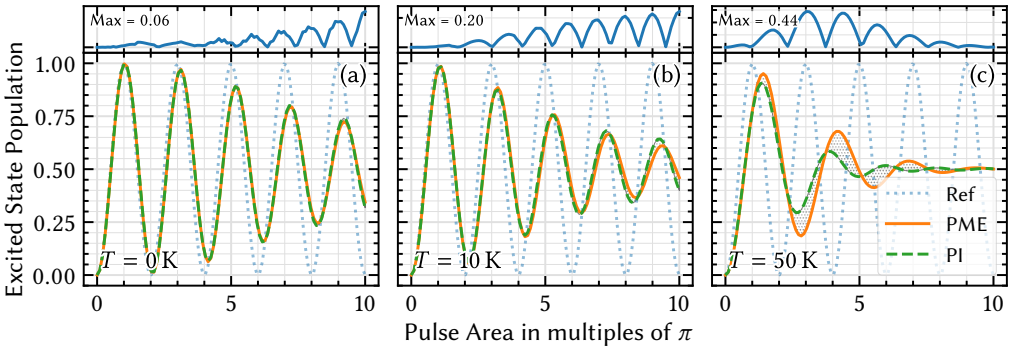

Figure 3.9: Comparison of Rabi rotations obtained using the polaron master equation and the Path Integral Method at temperatures $T = 0\,\mathrm{K}$, $T = 10\,\mathrm{K}$, and $T = 50\,\mathrm{K}$ **((a-c))**. Each plot displays the relative differences between the polaron master equation and path integral results at the top. The error is estimated using the absolute differences of the final states with error $= |(\langle \mathrm{X} \rangle_{\mathrm{PME}} (t_{\max}) - \langle \mathrm{X} \rangle_{\mathrm{PI}} (t_{\max}))|$. A smaller error indicates more precise alignment between the polaron master equation and path integral results throughout all pulse areas. Reference solutions with no phonon interaction (dotted) show the dephasing induced by both methods.

Here, the scanning the amplitude of a $\tau_p = 5\,\mathrm{ps}$ excitation pulse at different temperatures is investigated for the two-level system without a cavity. The resulting dynamics show *Rabi rotations* of the two-level population [37, 194, 219]. Here, the final occupation of the target electronic state oscillates with rising pulse amplitudes, indicating that maximum excitation efficiency is achieved for $\mathcal{A} = (2n+1)\pi$, with n being a positive integer. The results are visualized in Fig. 3.9. Relative deviations of the polaron master equation solutions from the path integral results are shown in the upper plots. It is evident that for small temperatures, the polaron master equation yields excellent results even for larger pulse amplitudes. However, for temperatures $T > 10\,\mathrm{K}$, the results quickly deviate from the path integral method [213]. Here, the polaron master equation can still be used to obtain qualitative insights into the electron phonon interactions, but similarly to the analytical rates, a quantitative description of the interaction is not guaranteed. For example, the *revival*

of Rabi rotations, investigated in Section 3.4.1, is not observed using the polaron master equation. Nevertheless, this analysis highlights the importance of considering phonon-induced effects in quantum systems and demonstrates the strengths and limitations of various modeling approaches. Providentially, the pulse and cavity parameters shown in the following work all remain in the regime of viability of the polaron master equation.

3.4.1 Strong Driving - Revival of Rabi Rotations

To further explore the limits of the polaron master equation used in this work, the same two-level system without a cavity is considered, now scanning for larger pulse areas as displayed in Fig. 3.11. The results are depicted for three different temperatures. At $T = 0\,\mathrm{K}$, the electron phonon interaction becomes minimal. The polaron master equation and path integral methods agree well for pulse areas of a few multiples of π.

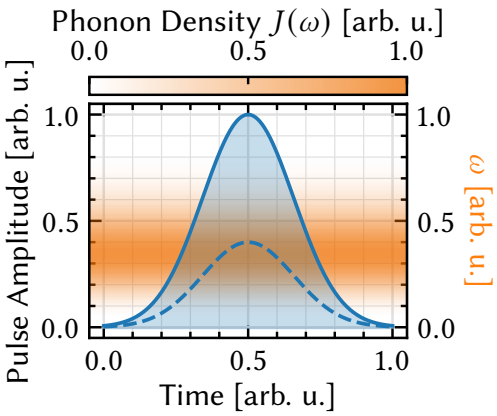

Figure 3.10: Illustration of the revival mechanism depicting an arbitrary spectral density for the phonons and an arbitrary Gaussian pulse. When the pulse amplitude exceeds the operational range of the phonon spectral density (dashed to solid line), the system undergoes effectively phonon-free dynamics. *Reproduced and enhanced from Hanschke et al. [206].*

Beyond this range, the polaron master equation shows no further dephasing induced by the phonons. The path integral solution initially aligns with this result but starts to show stronger dephasing for larger pulse areas. This unexpected and physically unmotivated behavior arises from the limited resolution of the path integral implementation. To resolve higher pulse areas accurately, smaller time steps Δt are required in the path integral method, which quickly becomes computationally infeasible. Without increased precision, numerical errors emerge, leading to the observed dephasing.

At low temperatures, in this case $T = 10\,\mathrm{K}$, the polaron master equation and path integral methods agree well for smaller pulse areas, as previously demonstrated in Fig. 3.9. For larger pulse amplitudes, the polaron master equation results in stronger dephasing until a maximally mixed state is reached, with

a 50% occupation of both the ground and excited states. Conversely, the path integral solution exhibits a *revival of the Rabi rotations*, where the dephasing weakens for larger pulse areas. In Fig. 3.11, the state occupation shows an initial dephasing followed by a revival and then a later increase in dephasing. This behavior, again, is not physically motivated and results from the limited precision of the path integral implementation, indicating that both the polaron master equation and the path integral implementation used in this work reach their respective limits to accurately describe the time evolution of the system.

At higher temperatures, here $T = 50\,\mathrm{K}$, the path integral and polaron master equation solutions diverge quickly. The path integral method still shows a slight revival of oscillations, while the polaron master equation solution consistently leads to a maximally mixed state. This divergence highlights the limitations of the polaron master equation at higher temperatures and the need for more precise numerical methods to capture the intricate dynamics accurately. The viable range of the path integral implementation is limited to pulse energies of a few meV, beyond which significantly increased numerical precision is required. Furthermore, although not shown here, the path integral and polaron master equation methods agree for longer when pulses are longer. For pulse amplitudes greater than $25 - 30\pi$ the process tensor approach is necessary due to time resolution constraints. However, this approach was not implemented or utilized in this work. Additionally, the computational effort for the process tensor approach remains substantially higher than for the polaron master equation, with simulations that take minutes using the polaron master equation potentially requiring hours with the more sophisticated path integral implementations.

The amplitude of Rabi rotations undergoes a *revival* process due to the pulse amplitude exceeding the amplitude of the phonon spectral density, as illustrated in Fig. 3.10. At smaller amplitudes, the pulse does not significantly overlap with the phonon spectral density, resulting in weak electron-phonon interactions. Consequently, dephasing is minimal.

As the pulse amplitude increases and begins to overlap more significantly with the spectral density, stronger electron-phonon interactions occur. This leads to pronounced dephasing, driving the system towards a maximally mixed state. In the context of a simple two-level system, this corresponds to a 50:50 superposition of the ground and excited states.

However, at even larger pulse amplitudes, the energy of the pulse surpasses the phonon spectral density. This results in weaker phonon interactions during most of the pulse duration, leading to a revival of the amplitude of the Rabi rotations. It is important to note that the second dephasing observed in the simulations is a numerical artifact due to the limited precision of the path integral method. This conclusion is supported by the process

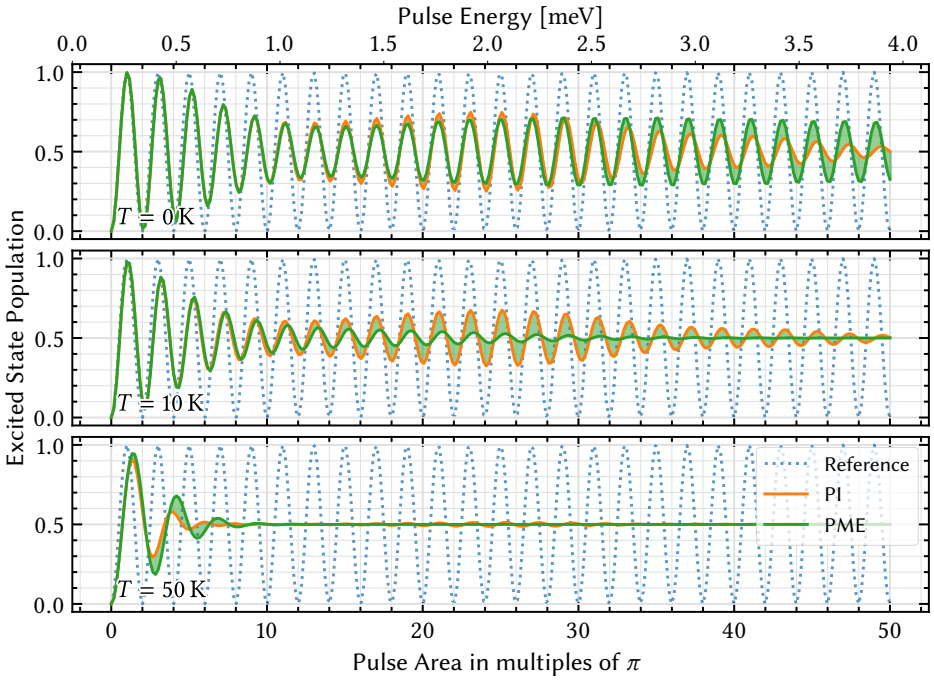

Figure 3.11: Scan of the excitation amplitudes for resonant pulses illustrating the Rabi rotations of the system with configurations from Fig. 3.8. Different temperatures reveal the strong dephasing effects induced by the phonons and the revival of the Rabi rotations achieved through the path integral method. This revival is not visible in the polaron master equation solution, highlighting more pronounced limitations of the polaron master equation under these conditions.

tensor approach, which provides exact numerical simulations and shows no evidence of a second dephasing, as corroborated by experimental data [206].

Results for a scanned pulse area are shown in Fig. 3.12, where the pulse width is varied using a slit-blocking approach. This method allows for tunable pulse lengths, albeit with reduced control over pulse shapes, leading to slight deviations between experimental and theoretical Gaussian pulses. Despite these discrepancies, the revival mechanism is strongly supported by the experimental measurements.

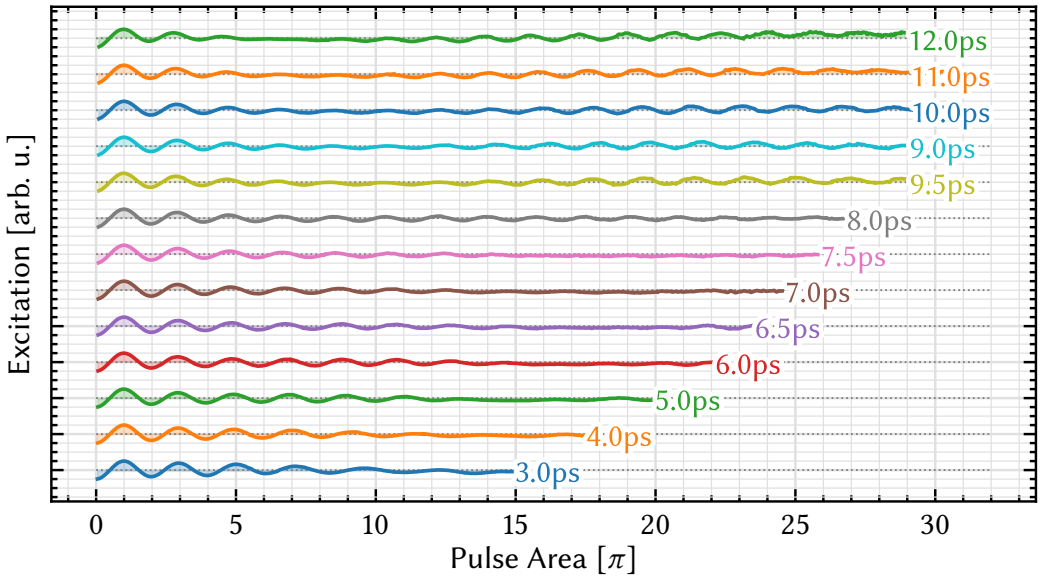

Figure 3.12: Experimental data for the revival of Rabi rotations at $T \approx 5.4\,\mathrm{K}$ with varying pulse lengths. The pulse lengths are obtained by using a slit to block portions of the incoming light, resulting in Gauss-like pulse shapes that resemble sinc envelopes. For display purposes, different pulse lengths are shifted accordingly along the y-axis. *Reproduced and enhanced from Hanschke et al. [206].*

Interim Summary

The polaron master equation provides an accurate description of the system within a specific parameter range, particularly at low temperatures and low pulse amplitudes, as investigated in this work. However, as the system parameters move beyond this range, discrepancies arise between the results obtained from the polaron master equation and those from the numerically exact path integral method. These discrepancies indicate that the polaron master equation is no longer sufficient to accurately capture the temporal dynamics of the system. The path integral method, being capable of fully resolving these dynamics, serves as a reliable benchmark for validating the polaron master equation. Nonetheless, as the pulse amplitudes continue to increase, even the path integral implementation used in this study encounters limitations in accurately describing the system. Despite these challenges, the polaron master equation remains robust and reliable within the low-temperature, low-pulse amplitude regimes explored in this work.

Photon Quantum Properties and Statistics

4

With the system definition, time evolution methods, incorporation of losses, and electron-phonon interactions now established, the next step includes the introduction of quantitative figures of merit. These metrics are essential for characterizing the resulting dynamics beyond simple state occupations.

The simplest quantity to consider is the emission probability. This property can be calculated from both the electronic states and the photonic cavity occupation, such that

$$\mathcal{P}(\hat{\mathrm{O}}, \gamma) = \gamma \int_0^{t_{\max}} \left\langle \hat{\mathrm{O}} \right\rangle \, \mathrm{d}t \; . \tag{4.1}$$

Here, $\hat{\mathrm{O}}$ is an electronic or photonic state operator within the system, and γ is the rate at which that state decays. For electronic states, $\hat{\mathrm{O}} = |i\rangle\langle i|$ with $i \in S$. For the photonic states, $\hat{\mathrm{O}} = \hat{\mathrm{n}}_{\mathrm{c}}$ with $\mathrm{c} \in M$. The photon emission probability can be used to determine the brightness of a source. For instance, if a single photon is desired to be emitted from the structure within the time frame $[0, t_{\max}]$, the emission probability should ideally converge to one, with $\mathcal{P} = 1$. Conversely, if no emission is desired from a state, the emission probability should ideally approach zero, such that $\mathcal{P} = 0$.

4.1 First Order Correlations

Beyond the emission probability, the evaluation of correlation functions becomes necessary to capture the self-correlating and cross-correlating behavior of the system operators [190]. These functions provide deeper insights into the temporal and spatial coherence properties of the emitted photons and can reveal intricate details about the interaction dynamics within the system [220]. The analysis of correlation functions allows for a more comprehensive characterization of the quantum states and their evolution, facilitating the development of advanced quantum technologies.

The first order correlation function is defined as [145, 174, 178, 190]

$$\mathcal{G}_{ij}^{(1)}(t,\tau) = \left\langle \hat{\mathrm{O}}_i^{\dagger}(t+\tau)\hat{\mathrm{O}}_j(t) \right\rangle , \tag{4.2}$$

which requires the evaluation of not only the regular temporal dynamics of the density matrix, but also the additional τ evolution of the operator $\hat{\mathrm{O}}_i$. The expectation value is determined analogously to Eq. (2.9) by calculating the trace of the density matrix and the corresponding operator products. The time evolution of the state operators is expressed using the unitary time transformation, which propagates the state from time t_1 to time t_2. For visualization purposes, the notation $\hat{\mathcal{U}}_{t_1\to t_2} \equiv \hat{\mathcal{U}}(t_1,t_2)$ is adopted. The expectation value results in

$$\begin{aligned}\mathcal{G}_{ij}^{(1)}(t,\tau) &= \mathrm{Tr}\left\{\hat{\mathrm{O}}_i(t)\rho(0)\hat{\mathrm{O}}_j^{\dagger}(t+\tau)\right\} \\ &= \mathrm{Tr}\left\{\rho(0)\hat{\mathcal{U}}_{0\to t}^{\dagger}\hat{\mathrm{O}}_i\hat{\mathcal{U}}_{0\to t}\hat{\mathcal{U}}_{0\to t+\tau}^{\dagger}\hat{\mathrm{O}}_j^{\dagger}\hat{\mathcal{U}}_{0\to t+\tau}\right\} ,\end{aligned} \tag{4.3}$$

with $\hat{\mathcal{U}}_{0\to t+\tau}^{\dagger} = \hat{\mathcal{U}}_{0\to t}^{\dagger}\hat{\mathcal{U}}_{t\to t+\tau}^{\dagger}$. Absorbing the initial time propagation $\hat{\mathcal{U}}_{0\to t}^{\dagger}$ into the density matrix with $\hat{\mathcal{U}}_{0\to t}^{\dagger}\rho(0)\hat{\mathcal{U}}_{0\to t} = \rho(t)$, the expectation value can be further expressed as

$$\begin{aligned}\mathcal{G}_{ij}^{(1)}(t,\tau) &= \mathrm{Tr}\left\{\rho(t)\hat{\mathrm{O}}_i\hat{\mathcal{U}}_{t\to t+\tau}^{\dagger}\hat{\mathrm{O}}_j^{\dagger}\hat{\mathcal{U}}_{t\to t+\tau}\right\} \\ &= \mathrm{Tr}\left\{\hat{\mathcal{U}}_{t\to t+\tau}\rho(t)\hat{\mathrm{O}}_i\hat{\mathcal{U}}_{t\to t+\tau}^{\dagger}\hat{\mathrm{O}}_j^{\dagger}\right\} \\ &= \mathrm{Tr}\left\{\tilde{\rho}_i(t+\tau)\hat{\mathrm{O}}_j^{\dagger}\right\} .\end{aligned} \tag{4.4}$$

Here, the modified density matrix is given by

$$\tilde{\rho}_i(t+\tau) = \hat{\mathcal{U}}_{t\to t+\tau}^{\dagger}\rho(t)\hat{\mathrm{O}}_i\hat{\mathcal{U}}_{t\to t+\tau} . \tag{4.5}$$

In the literature, this procedure is referenced to as the *quantum regression theorem* [209, 221]. The evaluation of the two-time correlation function necessitates the initial propagation in time of $\rho(t=0)$ up to $t = t_{\mathrm{max}}$, followed by an additional propagation of the matrix product $\rho(t)\hat{\mathrm{O}}_i$. To minimize the required computational resources for this second time evolution for any given $\rho(t)$, the overall t and τ range on which $\mathcal{G}_{ij}^{(1)}(t,\tau)$ is evaluated can be significantly reduced, provided numerical convergence is still assured. Furthermore, propagating the correlation function for $t+\tau$ beyond the maximum propagation time for $\rho(t)$, which is t_{max}, is generally unnecessary. This is because simulations are performed

for $t_{\max}$ values that are sufficiently large to ensure convergence for $\rho(t)$. Consequently, no further dynamics arise beyond $t_{\max}$. This is illustrated in Fig. 4.1, where panel (a) shows an example of $\mathcal{G}_{ii}^{(1)}(t,\tau)$. The hatched area indicates the t,τ regime that is not evaluated. Similarly, panel (b) in Fig. 4.1 demonstrates the cutoff of the dynamics if $t_{\max}$ is chosen inappropriately, indicating missing convergence of the results.

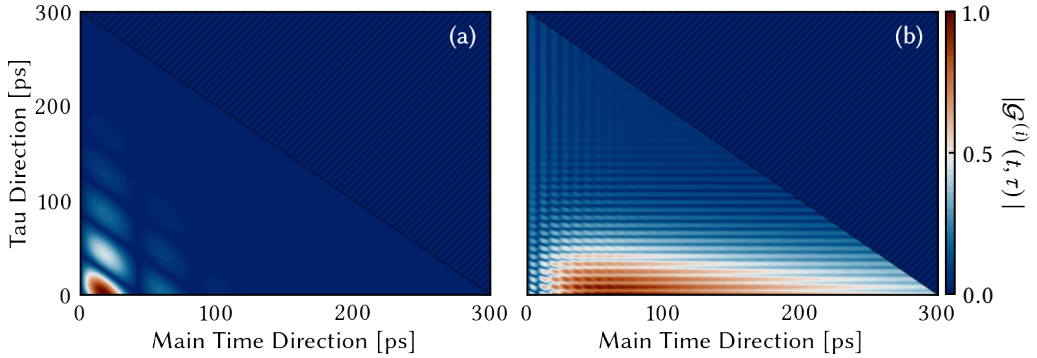

Figure 4.1: Correlation functions $\mathcal{G}^{(1)}(t,\tau)$ and $\mathcal{G}^{(2)}(t,\tau)$ for an initially fully excited quantum dot, with initial states **(a)** $\Psi_0 = |\mathrm{X}\rangle\langle\mathrm{X}|$ and **(b)** $\Psi_0 = |\mathrm{B}\rangle\langle\mathrm{B}|$, respectively. To maintain efficiency and reduce simulation times, only the lower triangular matrix defined by t and τ, indicated by the hatched area, is evaluated, which reduces the number of evaluations of the time derivative in Eq. (2.8) by half. The results presented use the regular von Neumann equation with no electron-phonon coupling.

4.1.1 Visibility

The interferometric visibility $\mathcal{V}$ is a figure of merit used to measure contrast and coherence in light sources. Using $\hat{\mathrm{O}}_i = \hat{\mathrm{O}}_j$, the visibility is given by

$$\mathcal{V} = \frac{2\int_0^{t_{\max}}\int_0^{t_{\max}-t} |\mathcal{G}_{ii}^{(1)}(t,\tau)|^2 \mathrm{d}\tau\mathrm{d}t}{\left(\int_0^{t_{\max}} \left\langle \hat{\mathrm{O}}_i^\dagger \hat{\mathrm{O}}_i \right\rangle \mathrm{d}t\right)^2}\,. \tag{4.6}$$

In experimental setups, the light field is split using beam splitters. After a time delay is introduced, the fields are recombined. This can be measured using devices such as a Mach–Zehnder interferometer [222–224], Michelson interferometer [225, 226], or Sagnac interferometer [227]. A light source emits strongly coherent photons if the resulting visibility is 1. For example, the emission from a two-level system or a single photon from a cavity, given ideal excitation and lossless emission, results in a visibility close to unity values.

However, a general numerical problem arises when the Hilbert space is not limited to

one photon and the emission of more than one photon becomes possible. Hence, using the Hong-Ou-Mandel indistinguishability, described in Section 4.2.1, is generally superior. Otherwise, the visibility may exceed unity, which is a result not physically motivated. The indistinguishability is more strongly bounded, ensuring more reliable and realistic calculations of coherence and contrast. Nevertheless, because the visibility requires only the first order correlation function to be evaluated, it is numerically much cheaper to evaluate and as such, finds application as a fast benchmarking tool.

4.1.2 Emission Spectrum

The strongest use case for the first order correlation function lies in its connection with the emission frequency of the corresponding photons generated by the decay of $\hat{\mathrm{n}}_i = \hat{\mathrm{O}}_i^\dagger \hat{\mathrm{O}}_i$, for any given electronic state or cavity mode operator $\hat{\mathrm{O}}_i$. Calculating the self-correlation of $\hat{\mathrm{O}}_i$ using the first order correlation function reveals oscillations corresponding to the emission frequency.

By applying a discrete Fourier transform to the τ-direction of $\mathcal{G}^{(1)}(t,\tau)$ and integrating over the different spectra, the total emission spectrum of the system over the time period $[0, t_{\max}]$ is obtained [112, 228]. This process results in what is known as the Eberly-Wodkiewicz spectrum [229, 230], often referenced as the *physical emission spectrum*, and is given by

Equation 4.7

$$\mathcal{S}(t_{\max}, \omega) = \mathrm{Re} \int_0^{t_{\max}} \int_0^{t_{\max}-t} D(t+\tau)\mathcal{G}_{ii}^{(1)}(t,\tau)\, D(t) e^{-\mathrm{i}\omega\tau} \mathrm{d}\tau \mathrm{d}t \ .$$

Here, $D(t)$ are detector functions [228]. While detector functions were used in some investigations, none of the results in this work include them, and as such, $D(t) = 1$.

Especially for the correlation functions, the polaron master equation is known to introduce slight errors, as demonstrated in Fig. 4.2. However, with the path integral implementation, the results align with the expected physical behavior. Since the exact phonon spectra are not the focus of this work, these slight mismatches between polaron master equation and path integral are not evident in any of the results shown. For strong coupling with $\hbar g > \hbar\kappa$, Rabi-splitting occurs for the exciton-to-ground emission [228, 231]. Both methods correctly resolve this behaviour.

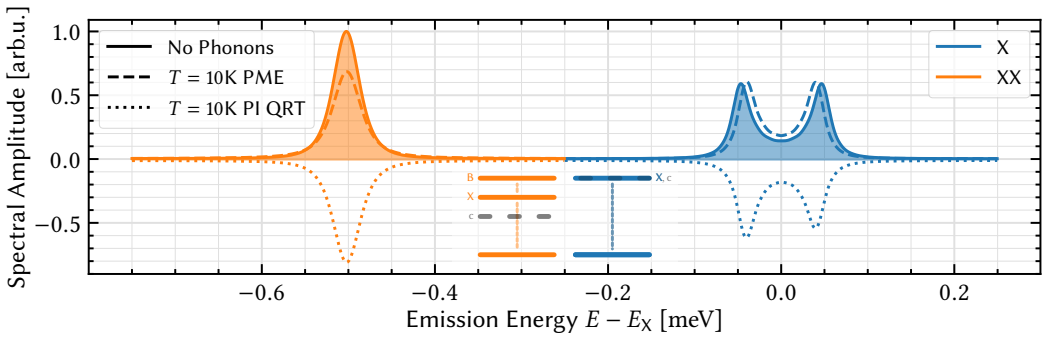

Figure 4.2: Cavity emission spectra for a quantum dot biexciton system initiated from fully excited exciton and biexciton states, $\Psi_0 = |\mathrm{X}\rangle\langle\mathrm{X}|$ and $|\mathrm{B}\rangle\langle\mathrm{B}|$, respectively. The first-order correlation function is evaluated, and the Eberly-Wodkievic (EW) spectrum Eq. (4.7) is computed. The results encompass scenarios both without phonon interactions and with phonon effects modeled using the polaron master equation and path integral (mirrored on the y-axis) method. For an equitable comparison, the quantum regression theorem is applied to the path integral method, although more precise methodologies are available [221].

Overall, the Eberly-Wodkiewicz spectrum provides a comprehensive view of the emission properties of the system and allows for the tailoring of the emitter structure towards desired wavelengths.

4.2 Second Order Correlations

Higher-order correlation functions are employed to assess the non-classical characteristics of the emission and to extract detailed information on multi-photon correlations. Specifically, the second-order correlation function is defined as

$$\mathcal{G}^{(2)}_{ijkl}(t,\tau) = \left\langle \hat{\mathrm{O}}^{\dagger}_i(t)\hat{\mathrm{O}}^{\dagger}_j(t+\tau)\hat{\mathrm{O}}_k(t+\tau)\hat{\mathrm{O}}_l(t)\right\rangle . \tag{4.8}$$

Using an approach equivalent to the calculation of the first order correlation functions Eq. (4.2),

$$\mathcal{G}^{(2)}_{ijkl}(t,\tau) = \mathrm{Tr}\left\{\tilde{\rho}_{il}(t+\tau)\hat{\mathrm{O}}^{\dagger}_j\hat{\mathrm{O}}_k\right\} \tag{4.9}$$

is obtained. The modified density matrix is defined by

$$\tilde{\rho}_{il}(t+\tau) = \hat{\mathcal{U}}^{\dagger}_{t\to t+\tau}\hat{\mathrm{O}}_l\rho(t)\hat{\mathrm{O}}_i^{\dagger}\hat{\mathcal{U}}_{t\to t+\tau} \,. \tag{4.10}$$

Similar to the first order correlation function, the second order correlation function also requires one additional time propagation for each $\rho(t)$ used in the t-τ grid. The two time correlation function Eq. (4.9) can be reduced in dimension by integrating over either t or τ, resulting in

$$\overline{\mathcal{G}}^{(2)}_{ijkl}(t) = \int_0^{t-t_{\max}} \overline{\mathcal{G}}^{(2)}_{ijkl}(t,\tau)\,\mathrm{d}\tau \tag{4.11}$$

and

$$\overline{\mathcal{G}}^{(2)}_{ijkl}(\tau) = \int_0^{\tau-t_{\max}} \overline{\mathcal{G}}^{(2)}_{ijkl}(t,\tau)\,\mathrm{d}t \,. \tag{4.12}$$

Integrating Eq. (4.9) over both temporal dimensions t and τ then yields the reduced correlation function

$$\overline{\overline{\mathcal{G}}}^{(2)}_{ijkl} = \int_0^{t_{\max}} \mathrm{d}t \int_0^{t-t_{\max}} \overline{\mathcal{G}}^{(2)}_{ijkl}(t,\tau)\,\mathrm{d}\tau \,. \tag{4.13}$$

Note, that similar reductions can also be performed for correlation functions of different orders.

The second-order correlation function provides insights into phenomena such as photon bunching and anti-bunching. Photon bunching occurs when photons tend to arrive together in clusters. This behavior is typically observed in thermal or chaotic light sources and is characterized by $\overline{\mathcal{G}}^{(2)}_{iiii}(t) > 1$. Photon anti-bunching, on the other hand, is a signature of single-photon sources where photons are emitted one at a time, leading to $\overline{\mathcal{G}}^{(2)}_{iiii}(t) = 0$. Anti-bunching is a clear indicator of the quantum nature of light, as it reveals the presence of non-classical light fields that cannot be explained by classical wave theory.

For an ideal single-photon source, the second-order correlation function, $\overline{\overline{\mathcal{G}}}^{(2)}_{iiii}$, is zero. Therefore, the probability of detecting two photons simultaneously is zero, highlighting the quantum property of the light source. Such behavior is critical for applications in quantum information processing and quantum communication, where the generation of single photons on demand is essential. From here, the *single photon purity* is defined using

$$\mathcal{P} = 1 - \overline{\overline{\mathcal{G}}}^{(2)}_{iiii} \,. \tag{4.14}$$

The second-order correlation function thus serves as a crucial figure of merit for evaluating the quantum characteristics of light fields. It allows for the distinction between classical and quantum light sources and provides insights into the underlying physics governing photon emission processes [130]. The analysis of $\mathcal{G}^{(2)}$ provides deep insights into the coherence properties, statistical distributions, and interaction dynamics of photons.

4.2.1 Indistinguishability

The indistinguishability of a photon is a measure of how deterministically a source emits photons. This property is typically assessed using the Hong-Ou-Mandel (HOM) interference setup [128, 190, 232]. In this setup, two photons are directed towards a beam splitter. If the photons are indistinguishable, they will interfere quantum mechanically, coalescing and exiting the beam splitter together into the same output path, resulting in only one of the detectors triggering. Conversely, if the photons are distinguishable, they behave independently, making it equally likely for them to exit through separate paths, thereby triggering both detectors. This setup, illustrated in Fig. 4.3, demonstrates the fundamental quantum principle where indistinguishability affects the path correlations of photons.

Figure 4.3: Hong-Ou-Mandel interference setup. The Hong-Ou-Mandel measurement is an interferometric technique used for simple correlation measurements to test the indistinguishability of two photons. In this setup, two photons are sent into a 50:50 beam splitter, and the coincidence detection at the output is recorded. When the photons are perfectly indistinguishable, they exhibit quantum interference, resulting in a reduction or complete suppression of coincidence counts, known as the HOM dip.

The single-photon HOM-indistinguishability [153] is quantified as

Equation 4.15

$$\mathcal{I} = 1 - p_{c,i} = 1 - \frac{\int_0^{t_{\max}} \mathrm{d}t \int_0^{t_{\max}-t} 2G^{(2)}_{\mathrm{HOM},i}(t,\tau)\mathrm{d}\tau}{\int_0^{t_{\max}} \mathrm{d}t \int_0^{t_{\max}-t} \left(2G^{(2)}_{\mathrm{pop},i}(t,\tau) - \left|\left\langle \hat{\mathrm{O}}_i(t+\tau)\right\rangle \left\langle \hat{\mathrm{O}}_i^{\dagger}(t)\right\rangle\right|^2\right)\mathrm{d}\tau} \,.$$

Here, the cross-correlation term is given by

$$G^{(2)}_{\mathrm{HOM},i}(t,\tau) = \frac{1}{2}\left(G^{(2)}_{\mathrm{pop},i}(t,\tau) + \mathcal{G}^{(2)}_{iiii}(t,\tau) - \left|\mathcal{G}^{(1)}_{ii}(t,\tau)\right|^2\right) \tag{4.16}$$

with

$$G^{(2)}_{\mathrm{pop},i}(t) = \left\langle \hat{\mathrm{O}}_i^{\dagger}\hat{\mathrm{O}}_i\right\rangle(t)\left\langle \hat{\mathrm{O}}_i^{\dagger}\hat{\mathrm{O}}_i\right\rangle(t+\tau)\,. \tag{4.17}$$

Here, $p_{c,i}$ is the probability of coincidence detection when photons are distinguishable. The numerator in the indistinguishability expression represents the integral of the HOM cross-correlation function $G^{(2)}_{\mathrm{HOM},i}(t,\tau)$, capturing the joint probability of detecting both photons in the same output path. The denominator includes the population correlation function $G^{(2)}_{\mathrm{pop},i}(t,\tau)$ and the square of the first-order coherence function $\mathcal{G}^{(1)}_{ii}(t,\tau)$, reflecting the probability distributions of individual photon detections.

In this work, the notation $\mathcal{I}_{i\to j}$ is frequently used to represent the indistinguishability of a photon arising from the electronic transition operator $\hat{\mathrm{O}} = |j\rangle\langle i|$. Additionally, $\mathcal{I}_{\mathrm{c}}$ is employed to denote the indistinguishability of photons emitted by a cavity mode with $\hat{O} = \hat{\mathrm{b}}_{\mathrm{c}}$. A similar approach is used for the visibility.

The HOM setup is a powerful tool for measuring the indistinguishability of photons, which is directly linked to their quantum mechanical properties. The degree of indistinguishability reflects the quantum nature of the light field; perfectly indistinguishable photons result in zero coincidence counts, indicating complete indistinguishability in the HOM experiment. This measure is crucial for applications in quantum information and quantum communication, where the reliability and coherence of single-photon sources are essential. Many quantum information applications require photons with high, close to unity indistinguishability to ensure reliable execution of various quantum protocols.

The indistinguishability is a robust figure of merit and provides a clear, bounded measure of

the quantum characteristics of the light. This makes it an indispensable metric for evaluating the performance of single-photon emitters and other quantum light sources.

4.2.2 Entanglement Measure - Concurrence

Entanglement is a fundamental resource in quantum information processing, playing a crucial role in a variety of quantum protocols. While the both the visibility as well as indistinguishability are figures of merit to assess the quality of single photons [233], entanglement occurs when two or more quantum particles, such as photons, become interconnected in such a way that the state of one particle cannot be described independently of the state of the other, regardless of the distance separating them. This non-classical correlation is a cornerstone of quantum mechanics and provides the basis for many of the advanced capabilities in quantum technologies.

Characterizing entanglement numerically is challenging [233, 234]. Entanglement can be analyzed through the photon correlation of the two allegedly connected photons. The corresponding two-photon matrix is then defined as

$$\rho_{\mathrm{TPM}} = \begin{bmatrix} \overline{\overline{\mathcal{G}}}^{(2)}_{1111} & \overline{\overline{\mathcal{G}}}^{(2)}_{1112} & \overline{\overline{\mathcal{G}}}^{(2)}_{1121} & \overline{\overline{\mathcal{G}}}^{(2)}_{1122} \\ \overline{\overline{\mathcal{G}}}^{(2)}_{1211} & \overline{\overline{\mathcal{G}}}^{(2)}_{1212} & \overline{\overline{\mathcal{G}}}^{(2)}_{1221} & \overline{\overline{\mathcal{G}}}^{(2)}_{1222} \\ \overline{\overline{\mathcal{G}}}^{(2)}_{2111} & \overline{\overline{\mathcal{G}}}^{(2)}_{2112} & \overline{\overline{\mathcal{G}}}^{(2)}_{2121} & \overline{\overline{\mathcal{G}}}^{(2)}_{2122} \\ \overline{\overline{\mathcal{G}}}^{(2)}_{2211} & \overline{\overline{\mathcal{G}}}^{(2)}_{2212} & \overline{\overline{\mathcal{G}}}^{(2)}_{2221} & \overline{\overline{\mathcal{G}}}^{(2)}_{2222} \end{bmatrix} \tag{4.18}$$

where second order correlation functions are used to trace the photon characteristics out of the density matrix ρ. This two photon matrix already displays a simple figure of merit for the entanglement. The off-diagonal element $\overline{\overline{\mathcal{G}}}^{(2)}_{1122}$ (blue in Eq. (4.18)) represents the correlation of two photons of mode 1 or two photons of mode 2. If this element is non-zero, both photon modes are entangled, where a photon in mode 1 heralds the emission of a photon in mode 2. On the other hand, if the matrix element $\overline{\overline{\mathcal{G}}}^{(2)}_{1221}$ (orange in Eq. (4.18)) is non-zero, the emission of a photon in mode 1 entails the emission of a photon in mode 2, and vice versa.

While the two-photon matrix elements can be used to characterize entanglement, they are usually not equal to the entanglement. Hence, in this work, a figure of merit which verifies entanglement is employed: the concurrence [155]. The concurrence rises linearly with the

degree of entanglement [235] and is defined using the spin-flipped two-photon matrix

$$\tilde{\rho}_{\mathrm{TPM}} = (\sigma_y \otimes \sigma_y) \cdot \rho_{\mathrm{TPM}} \cdot (\sigma_y \otimes \sigma_y) \,, \tag{4.19}$$

which is calculated according to Eq. (A.5). Using Eq. (4.19), using $\rho := \rho_{\mathrm{TPM}}$, the fidelity matrix of the the two-photon matrix is given by

$$\mathcal{R}(\rho) = \sqrt{\sqrt{\rho}\tilde{\rho}\sqrt{\rho}} \,. \tag{4.20}$$

Finally, the concurrence is constructed using

$$C = \max\left\{0, \lambda_4 - \sum_{i<4} \lambda_i\right\} \,, \tag{4.21}$$

where λ_i are the eigenvalues of $\mathcal{R}(\rho_{\mathrm{TPM}})$, sorted in ascending order. The concurrence serves as a figure of merit to quantify how far the two-photon matrix is from being highly symmetrical when a spin flip is applied. Further elaboration is available in Appendix A.2.2. The eigenvalues reflect this property when only 11 or 12 entanglement is present. Ideally in this case, only a single eigenvalue will be non-zero, while the remaining eigenvalues are zero. If the remaining eigenvalues are larger, they quantify losses in the concurrence and thus, in the entanglement. In Fig. 4.4, the reconstruction of the concurrence using both the eigenvalues as well as eigenvectors is visualized. Since the direction of the normalized eigenvectors is not of interest, the eigenvalues suffice for the calculation of the concurrence C.

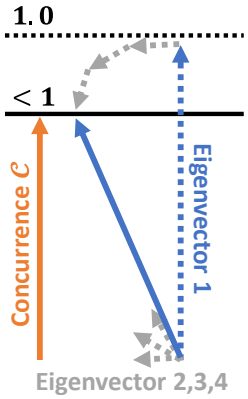

Figure 4.4: Visual representation of the reduction in concurrence through non-zero eigenvalues. The sum of all Eigenvectors multiplied with their respective eigenvalues yields the final concurrence vector.

As an example, assume two polarization modes H and V. A perfectly entangled state is then defined by either of the four Bell states [155, 236]

$$\Phi_{\pm} = \frac{1}{\sqrt{2}} \left(|\mathrm{HH,VV}\rangle \pm e^{\mathrm{i}\phi} |\mathrm{VV,HH}\rangle \right) \tag{4.22}$$

and

$$\Psi_{\pm} = \frac{1}{\sqrt{2}} \left(|\mathrm{HV,VH}\rangle \pm e^{\mathrm{i}\phi} |\mathrm{VH,HV}\rangle \right) \tag{4.23}$$

with phase mismatch ϕ. The former two states denote HH or VV entanglement, while the latter two states denote HV or VH entanglement. The corresponding ideal (blue + orange) and lossy (blue only) two-photon matrices regarding these states are displayed in Fig. 4.5. In this work, HH/VV entanglement is addressed exclusively, as the linear emission channel arises naturally from the decay of a biexciton, which is investigated in Chapters 5 and 6. The HV/VH entanglement can be generated from the same system, for example by using continuous wave (cw) driving of the system [155], but is not considered in this work. Furthermore, the fine structure splitting of the biexciton is known to limit the achievable concurrence. Specifically, a non-zero fine structure splitting will result in $\phi = -E_{\mathrm{fsp}}/\hbar t$. Consequently, both states suffer from a *precession* of the state correlations directly proportional to the fine structure splitting energy, reducing the entanglement [138]. Additionally, literature indicates that the method of exciting electronic states significantly influences the maximally achievable entanglement, especially when using resonant excitation [154].

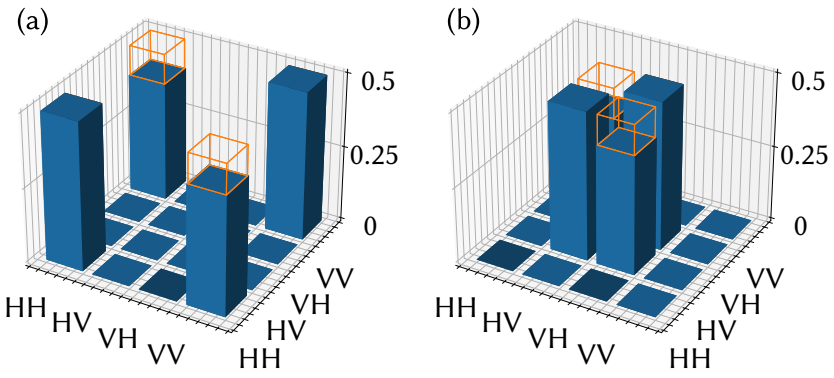

Figure 4.5: Two photon matrices for **(a)** HH/VV and **(b)** HV/VH entanglement, respectively, both in a lossy environment. The matrix elements are normalized by their trace. The orange boxes highlight the ideal matrix values that would be expected in the absence of losses.

4.3 Time Bin Photon Statistics

Until now, operators have been unique within the total Hilbert space of the system. Consequently, different operators cannot obey the same matrix representation and must differ in at least one of its elements. In this section, operators that are equal in their matrix representation but reside at different times are investigated.

4.3.1 Time Shifted Operators

Primarily, an operator can be shifted by a constant temporal offset, further referred to as the time bin length T. This creates two operators that, although relying within the same Hilbert space and being equal in their matrix representations, are different through their temporal restrictions. The operator then emits in distinct time bins [178, 237] and follows the notion

$$\hat{\mathrm{O}}_T(t) = \hat{\mathrm{O}}(t + T_{\mathrm{bin}}) = \hat{\mathcal{U}}_{t\to t+T_{\mathrm{bin}}}\hat{\mathrm{O}}(t)\hat{\mathcal{U}}^{\dagger}_{t\to t+T_{\mathrm{bin}}} \,. \tag{4.24}$$

Previously, the first and second order correlation functions were defined using a $t-\tau$ representation. For simplicity, the time bin correlations adopt a different notation, specifically defining the start and end times. First order correlations are not required in this context. Instead, this work is confined to the investigation of second and third order correlations. Generally, higher order correlations may be needed depending on the application. However, these higher order correlations require significantly increased numerical effort to compute, which can make them challenging to calculate or even infeasible to iterate over in practical scenarios.

Instead, the correlation functions are defined as

$$\mathcal{G}^{(2)}_{ijkl}(t_1, t_2) = \langle \hat{\mathrm{O}}^{\dagger}(t_1 + T_i)\hat{\mathrm{O}}^{\dagger}(t_2 + T_j)\hat{\mathrm{O}}(t_2 + T_k)\hat{\mathrm{O}}(t_1 + T_l)\rangle \tag{4.25}$$

and

$$\mathcal{G}^{(3)}_{ijklmn}(t_1, t_2, t_3) = \langle \hat{\mathrm{O}}^{\dagger}(t_1 + T_i)\hat{\mathrm{O}}^{\dagger}(t_2 + T_j)\hat{\mathrm{O}}^{\dagger}(t_3 + T_k)\hat{\mathrm{O}}(t_3 + T_l)\hat{\mathrm{O}}(t_2 + T_m)\hat{\mathrm{O}}(t_1 + T_n)\rangle \,, \tag{4.26}$$

with t_i being an integration window of size T_{bin}. Each of the operators $\hat{\mathrm{O}}^{(\dagger)}(t_i)$ can be shifted by the time bin length, which is annotated using the early ($i = E$) or late ($i = L$)

notation, where for the late time bin, t_i is shifted by T_{bin} such that $T_i = 0$ when $i = E$ and $T_i = T_{\text{bin}}$ when $i = L$. The two-time integrated correlation functions then result in

$$\bar{\bar{\mathcal{G}}}^{(2)}_{ijkl} = \int dt_1 \int dt_2 \, \bar{\bar{\mathcal{G}}}^{(2)}_{ijkl}(t_1, t_2) \tag{4.27}$$

and

$$\bar{\bar{\mathcal{G}}}^{(3)}_{ijklmn} = \int dt_1 \int dt_2 \int dt_3 \, \bar{\bar{\mathcal{G}}}^{(3)}_{ijklmn}(t_1, t_2, t_3)\,, \tag{4.28}$$

which is equivalent to using Eq. (4.13), adjusted for the time integration windows t_i.

4.3.2 Stabilizer Generator Expectation Values of a Linear Cluster State

The target of investigation in Chapter 7 is to classify the entanglement in trains of photons emitted at different times. Two consecutive photon emissions form a photonic qubit, where the emission of the photons is separated by the bin length T_{bin}. The first photon is denoted as the *early* photon, while the second photon is denoted as the *late* photon. A naive approach to characterizing the multi photon emission of this system is to use the N-dimensional N photon matrix. Then, correlations between photons can be directly extracted from the off-diagonal elements of these matrices. However, the numerical effort required to calculate even third order correlation functions greatly increases compared to first or second order correlations, due to the additional time integral required. Hence, a different approach is used. The *stabilizer formalism* is introduced to characterize this special emission of photons, by using local estimates of the entanglement [185, 186].

Initially, a stabilizer generator for the desired state is defined. In this case, a one dimensional linear cluster state is investigated. This state can be characterized by repeated executions of $\hat{X}$, $\hat{Y}$ and $\hat{Z}$ Pauli-rotations, where

$$\hat{X} = \begin{pmatrix} 0 & 1 \\ 1 & 0 \end{pmatrix},\ \hat{Y} = \begin{pmatrix} 0 & -\mathrm{i} \\ \mathrm{i} & 0 \end{pmatrix},\ \hat{Z} = \begin{pmatrix} 1 & 0 \\ 0 & -1 \end{pmatrix} \tag{4.29}$$

are the Pauli matrices for a two photon state. From here, the Φ operator is defined as

$$\Phi = \cos(\varphi)\,\hat{X} + \mathrm{i}\sin(\varphi)\,\hat{Y}\,. \tag{4.30}$$

This operator projects a rotation through the $\hat{X}$ and $\hat{Y}$ Pauli matrices, allowing for a degree of freedom using the rotation angle φ. Then, the expectation value of the required stabilizer

expressions are using. Namely,

$$\langle \hat{\Phi} \otimes \hat{Z} \rangle = 2 \frac{\overline{\overline{\mathcal{G}}}^{(2)}_{EEEL} - \overline{\overline{\mathcal{G}}}^{(2)}_{ELLL}}{\overline{\overline{\mathcal{G}}}^{(2)}_{\text{tot}}} \tag{4.31}$$

and

$$\langle \hat{Z} \otimes \hat{\Phi} \otimes \hat{Z} \rangle = 2 \frac{\overline{\overline{\mathcal{G}}}^{(3)}_{EEEELE} + \overline{\overline{\mathcal{G}}}^{(3)}_{LELLLL} - \overline{\overline{\mathcal{G}}}^{(3)}_{EELLLE} - \overline{\overline{\mathcal{G}}}^{(3)}_{LEEELL}}{\overline{\overline{\mathcal{G}}}^{(3)}_{\text{tot}}} \,. \tag{4.32}$$

Here, $\otimes$ marks the tensor product of two matrices. When adhering to the emission protocol of the one dimensional linear cluster state, the final state is a superposition of these stabilizer expressions. Hence, by calculating how well the emitted photons meet these criteria locally, conclusions for the total entanglement of the emitted train of photons can be drawn. Specifically, high values for both expectation values Eqs. (4.31) and (4.32) signify strong local entanglement.

In the case of Eqs. (4.31) and (4.32), the initial integration window t_0 is given by $t_0 \in [0, T_{\text{bin}}]$. However, later stabilizer expectation values can be calculated by advancing the initial integration window. Generally, $t_n \in [nT_{\text{bin}}, (n+1)T_{\text{bin}}]$. The integration window is denoted by adding the superscript to the stabilizer expectation values. In the special case where $n = 0$, these indices may also be omitted.

Both stabilizer expressions are normalized through their respective photon populations, with

$$\overline{\overline{\mathcal{G}}}^{(2)}_{\text{tot}} = \sum_{i,j \in \{E,L\}} \overline{\overline{\mathcal{G}}}^{(2)}_{ijji} \text{ and } \overline{\overline{\mathcal{G}}}^{(3)}_{\text{tot}} = \sum_{i,j,k \in \{E,L\}} \overline{\overline{\mathcal{G}}}^{(3)}_{ijkkji} \,. \tag{4.33}$$

Finally, the N partite entanglement Witness is defined using

$$\mathcal{W} = (N-1) - \langle \hat{X}^{(1)} \hat{Z}^{(2)} \rangle - \sum_{i>1} \langle \hat{Z}^{(i-1)} \hat{X}^{(i)} \hat{Z}^{(i+1)} \rangle \,. \tag{4.34}$$

To derive the lower bound on the number of entangled photonic qubits, Eq. (4.34) is set to zero and solved for N, where N represents the number of entangled particles. The resulting bounding equation is expressed as

$$N < \frac{\langle \hat{X}\hat{Z} \rangle}{1 - \langle \hat{Z}\hat{X}\hat{Z} \rangle} + 1 \,. \tag{4.35}$$

In this context, the term $\langle \hat{X}\hat{Z} \rangle$ corresponds to the expectation value $\langle \hat{X}^{(1)}\hat{Z}^{(2)} \rangle$, and $\hat{Z}\hat{X}\hat{Z}$ is defined as $\langle \hat{Z}^{(i-1)}\hat{X}^{(i)}\hat{Z}^{(i+1)} \rangle$ for all indices i. The bounding condition from Eq. (4.35) assumes that the stabilizers are uniform across the system, except for the differentiation between the first two stabilizers. This assumption simplifies the calculation by treating the later stabilizers as equal and independent of i.

Interim Summary

The first and second-order correlation functions are crucial for analyzing the correlations of emitted photons. In this study, these functions are evaluated using the quantum regression theorem, which provides a robust framework for the calculation of correlation functions of any order. This approach enables the determination of key properties such as the single-photon purity, the emission spectrum, visibility as well as the indistinguishability of single photons. Additionally, the twin-photon concurrence, which is essential for characterizing entanglement, is also derived from these correlation functions. Expanding this framework to include third-order correlation functions allows for a systematic characterization of time-bin entanglement in linear photonic cluster states.

Part II

Quantum Dot - Photon Physics

Enhancing Quantum Dot Excitation Using the Quantum Confined Stark Effect

5

Quantum dots have the potential to be ideal photon emitters for quantum information processing. A quantum dot is a microscopic structure composed of semiconductor material that can be triggered to emit photons using lasers. For many applications, low photon numbers are desired, which can be achieved by deterministically exciting the quantum dot exactly once. However, to excite the dot states, the laser energy must be similar to the ground and excited state transition of the quantum dot exciton. This requirement introduces several challenges, such as separating the laser and the emission, mixing of excitation and emission processes, and phonon interactions for resonant pulses. These effects are particularly problematic for the delicate excitation of a biexciton and other higher order states [20, 205] and provide the key motivation for this chapter.

In this chapter, a quantum-dot-cavity system is utilized. The respective configuration of the electronic state and photonic mode energies is visualized in Fig. 5.1. This system includes the horizontally (H) and vertically (V) polarized exciton states as well as the biexciton state, which are represented by the blue energy levels. This system is mediated by a degenerate two-mode cavity, shown in green and orange, which separately Purcell enhances the horizontally and vertically polarized selection rules of the exciton-to-ground transitions or the two-photon transition of the electronic system, respectively.

The energy of the exciton is set to $E_X = 1.366\,\text{eV}$, a value commonly achieved in InGaAs quantum dots. The exciton states are separated by the fine structure splitting energy E_{fsp}, previously introduced in Section 1.2. For the main results of this chapter, E_{fsp} is fixed at $1\,\mu\text{eV}$, which remains within realistic parameters for highly symmetrical quantum dots [238]. The fine structure splitting negatively impacts the concurrence and, consequently, the entanglement of twin photons emitted from the biexciton [138, 142, 239]. This effect arises due to the phase mismatch between the excitons caused by the splitting. The resulting phase ϕ, included in Eq. (4.22), induces a precession of the exciton state coherences when

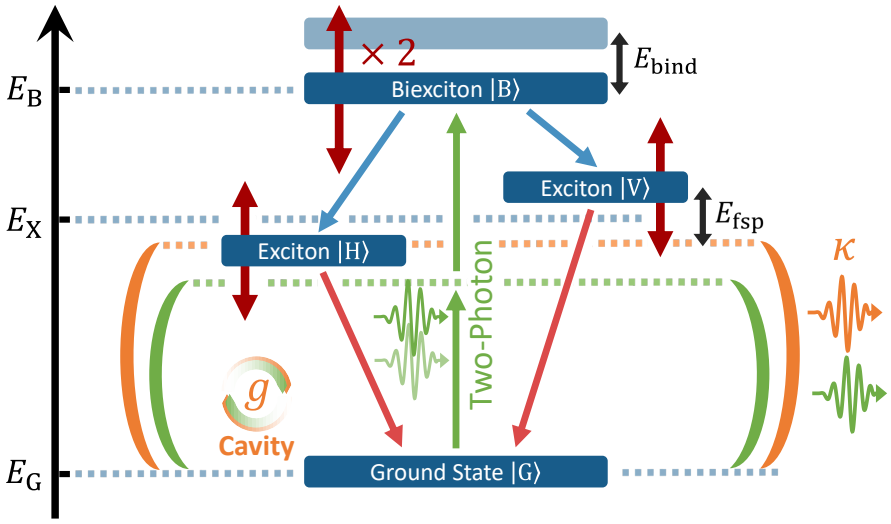

Figure 5.1: Electronic structure of the biexciton and the QCSS for a quantum dot inside a cavity. The shift induced by the quantum confined Stark shift is indicated in using the red arrows. Because of the biexciton-exciton energy relation $E_B = 2E_X - E_{bind}$, the energy of the biexciton state is shifted twice as fast as the exciton energy. Two main cavity configurations are visualized, one for a cavity resonant with the two photon transition at $E_c = E_{TP}$ (green) and one for the cavity resonant with the exciton-to-ground transition $E_c = E_X$ (orange). *Reproduced and enhanced from Bauch et al. [145].*

projected onto a Bloch sphere. The energy of the biexciton is reduced by the binding energy, set to 1 meV in this study unless otherwise noted [109]. Larger binding energies increase the effort required to form a biexciton from two excitons, which in turn enhances the biexciton's stability and lifetime. Consequently, lower binding energies lead to shorter biexciton lifetimes. The resulting Hamiltonian

Equation 5.1

$$\mathcal{H}_0 = \sum_{s\in\{H,V,B\}} E_s |s\rangle\langle s| + \sum_{c\in\{H,V\}} E_c \hat{n}_c$$
$$\mathcal{H}_1 = \sum_{i\in\{H,V\}} \left([|G\rangle\langle i| + |i\rangle\langle B|] \left[\Omega_i(t) + \hbar g \hat{b}_i \right] + \text{H.c.} \right) + \mathcal{H}_\Delta$$

includes four electronic states, specifically the ground state |G⟩, two exciton states |H⟩ and |V⟩ as well as the biexciton state |B⟩. The electronic states couple to two cavity modes, defined by their respective occupation number operator $\hat{n}_{H/V}$.

The time dependent sub-Hamiltonian $\mathcal{H}_\Delta$ describes the *quantum confined Stark shift* (QCSS) of the states, as detailed in Section 5.3 [138, 167]. This operator induces a time-dependent shift in the individual energies of the states, which can be controlled by applying external electric fields to the semiconductor structure [60, 107, 134]. Implementing a precise and rapid electric shift in a realistic system presents significant challenges, making it a complex area of research. The Stark shift, indicated by the red arrows in Fig. 5.1, is the central mechanism utilized in this chapter to achieve high-fidelity excitation of various electronic states.

This chapter begins by examining the fundamental dynamics of a biexciton coupled to a cavity, as explored in Section 5.1, using an idealized, fully excited biexciton state. This section establishes reference values for key quantum properties, including single-photon and twin-photon emissions, which serve as a basis for comparison in subsequent analyses.

Two main approaches for the excitation of the biexciton are considered, either through sequential excitation of an exciton state or via direct two-photon excitation [44, 154, 240], where the pulse energy is tuned to exactly half of the biexciton energy. This results in a nonlinear absorption of two photons [219, 241] and, consequently, the generation of biexciton population. In the literature, the former is hardly used due to the exciton, which temporarily becomes the ground state of the biexciton, undergoing distinct decay dynamics during the excitation, thus creating an unstable ground state for the biexciton.

The chapter progresses to explore different methods for the excitation process in Section 5.2. These methods include resonant excitation, phonon-assisted excitation, the recently developed SUPER (swing-up of quantum emitter population) excitation [163, 164, 166], and the QCSS excitation [145]. The QCSS method, which is the primary focus of the underlying work of this chapter [145], is thoroughly investigated. Data supporting the findings are available at the corresponding Zenodo archive [242]. The chapter also evaluates and compares quantum properties such as single-photon indistinguishability and concurrence with their respective reference values.

5.1 Biexciton Baseline

To provide a foundation for comparison with the later results, first the exciton and biexciton properties are investigated. Simulations for an initially fully excited biexciton with $\rho_0 = |B\rangle\langle B|$ are investigated in Fig. 5.2. The ideal, lossless system is compared to a system that includes electron-phonon coupling using the polaron master equation and other losses incorporated through Lindblad contributions. In the ideal system, phonons, radiative decay, and pure dephasing are absent, with only cavity losses being non-zero. The cavity losses provide the mechanism for the emission of photons from the cavity, while electronic losses contribute destructively to the cavity photons. This scenario establishes a reference for the achievable properties of the cavity photons. Results including electron-phonon coupling are obtained using the polaron master equation with coupling $\alpha = 0.03\,\mathrm{ps}^2$.

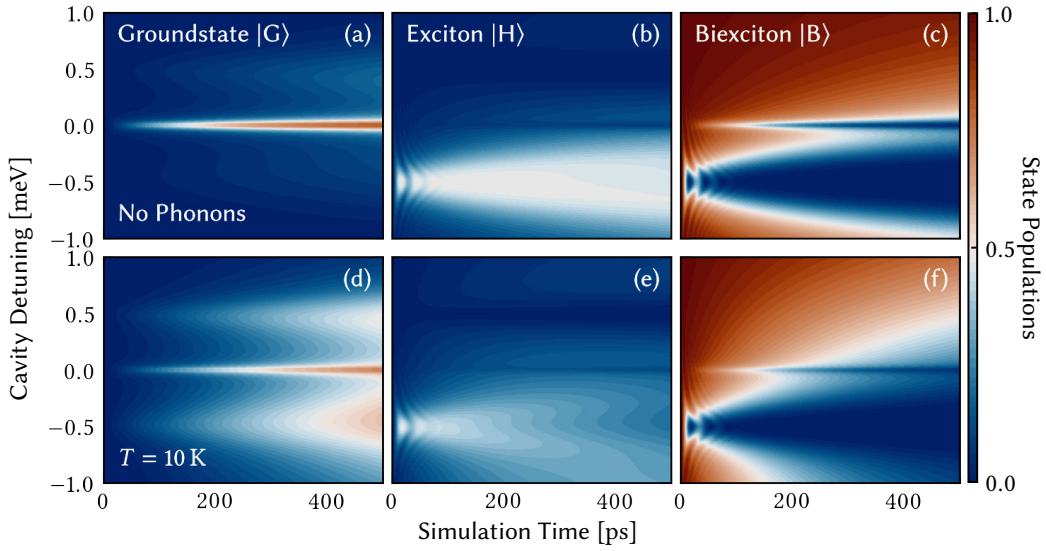

Figure 5.2: Decay of a fully initialized biexciton into a two-mode cavity with no phonon interaction **(a-c)** and with phonon interaction at 10 K **(d-f)**. The phonon solution is calculated using the polaron master equation. Here, $E_{\mathrm{bind}} = 1\,\mathrm{meV}$.

The cavity detuning $\Delta_c = E_c - E_B/2$ is varied along the y-axis by modulating the cavity energy E_c. The biexciton energy E_B remains constant. The y-axis is centered around the two-photon resonance at $E_{TP} = E_B/2$. The time evolution of the states is displayed on the x-axis. The z-axis, mediated using colors, shows the populations of the ground state in panels a,d, the horizontally polarized exciton in panels b,e as well as the biexciton in panels c,f.

When the cavity energy is set to the exciton-to-ground resonance, therefore $E_c = E_X$ (compare Fig. 5.1 orange cavity), resulting in a detuning of $\Delta_c = 0.5\,\text{meV}$ no significant enhancement of the biexciton decay is observed. This outcome is anticipated, as the cavity and the biexciton energies differ by twice the binding energy, with $|E_c - E_B| = 2E_{\text{bind}}$, significantly reducing the Purcell enhancement for this transition, as dictated by Eq. (2.15). Regarding the Purcell enhancement, with electron-phonon coupling enabled, the transition is slightly enhanced again due to the phonon side band, resulting in a faster decay of the biexciton into the two exciton states. Evidently, if the simulation starts in the exciton state instead with $\rho_0 = |X\rangle\langle X|$, a simple, resonant decay of the exciton is observed.

When the cavity energy is set to the two-photon resonance at $E_c = E_B/2$ and therefore $\Delta_c = 0$, the biexciton decays directly into the ground state without populating any of the two exciton states. As demonstrated further in this section, this process yields two photons with high concurrence and therefore high entanglement. With electron-phonon interactions, this transition is not significantly enhanced because the cavity is energetically exceeding the two photon transition energy.

When the cavity energy is set to the biexciton-to-exciton resonance such that $E_c = E_B - E_X$ with $\Delta_c = -0.5\,\text{meV}$, the biexciton quickly decays into both exciton states simultaneously. Since the separation of the exciton and the biexciton energies is symmetrical, as in one of the excitons is shifted energetically upwards while the other one is shifted downwards, they are almost equally populated. Therefore, the resulting exciton population in Fig. 5.2, panel (b) is maximized at 50%. When including electron-phonon coupling, the biexciton-to-exciton transition is slightly enhanced, while the exciton-to-ground transition is strongly enhanced. This is directly attributable to the cavity being energetically below the currently excited state, with $E_c = E_B - E_X < E_B/2 < E_X$. Hence, the exciton-to-ground transition is cavity enhanced through the phonon side band. This leads to a significantly accelerated decay of the exciton, as shown in Fig. 5.2, panels (d,e).

For the subsequent investigations of Section 5.3, these findings provide eminent guidelines for the biexciton emission, as the energetic placement of the cavity is crucial to minimize unwanted electron-phonon interactions.

5.1.1 Baseline Quantum Properties

The first and elementary quantum property of the emitted photons is the emission spectrum of the cavity, evaluated using Eq. (4.7) and visualized in Fig. 5.3. Again, the cavity detuning

is varied on the y-axis. The x-axis displays the emission energy relative to the two-photon emission energy, varied between $E_B/2 \pm 1.5\,\text{meV}$. The emission spectrum exhibits *Rabi splitting* for the cavity at the exciton-ground resonance with $E_c = E_X$ and $\Delta_c = -0.5\,\text{meV}$, which is in well accordance with Fig. 4.2 in Section 4.1.2. Rabi splitting also occurs for the cavity at the biexciton-exciton resonance where $E_c = E_B - E_X$ with $\Delta_c = 0.5\,\text{meV}$. Here, both the resonant biexciton-to-exciton as well as the off-resonant exciton-to-ground transition experience Rabi splitting. However, for the cavity at the two-photon resonance, only single peaks in the spectrum are observed, with no Rabi-splitting for any of the transitions. The central peak coincides well with the literature [243] as well as previous results outlined in Fig. 4.2. With electron-phonon coupling enabled, significant background emission arises, indicated by the spectral emission not approaching zero in Fig. 5.3, panel (b), for cavity energies not at any of the resonances.

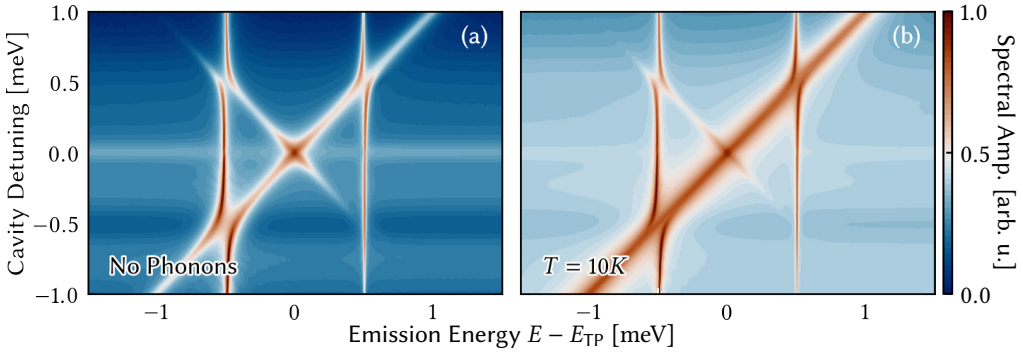

Figure 5.3: Cavity emission spectra for the decay of a fully excited biexciton, as shown in Fig. 5.2. The plot features cavity detuning on the y-axis against emission frequency on the x-axis, effectively mapping how the spectral characteristics vary with changes in cavity detuning.

Progressing along the path of the photon quantum properties, the single-photon indistinguishability is calculated and analyzed through Section 4.2.1. The numerical results are visualized in Fig. 5.4 in panel (a). Explicitly, two scenarios with different initial states are compared. Starting in a fully initialized exciton state with $\rho_0 = |X\rangle\langle X|$ (blue lines), the indistinguishability is maximized to practically unity values for $E_c = E_X$, well adhering to the literature [156] and various experiments [55, 75, 92]. Because the electronic system does not experience any losses, the indistinguishability also remains high throughout the range of investigated cavity detunings, albeit while experiencing greatly reduced Purcell enhancement. For large cavity detunings, the exciton does not fully decay during the simulation time, resulting in a partial emission of a photon with emission probabilities $\mathcal{P} < 1$. Comparable results are achieved when including electron-phonon coupling, which

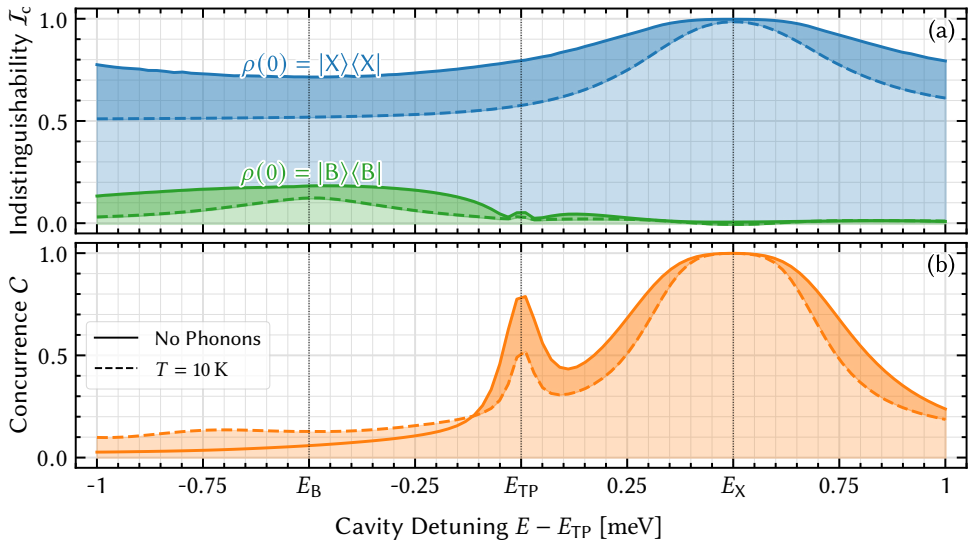

Figure 5.4: Quantum properties of photons emitted from a cavity during the decay of a fully excited exciton or biexciton. **(a)** Achievable indistinguishability when initializing the system in either a fully excited exciton (blue line) or a fully excited biexciton (orange line) state. **(b)** Achievable concurrence for an initially fully excited biexciton state. Both panels show results for scenarios without phonon interactions (solid lines) and with phonon interactions modeled by the polaron master equation at a temperature of $T = 10\,\mathrm{K}$.

reduces the indistinguishability due to the phonon-induced dephasing. At the exciton resonance, the exciton decays rapidly, allowing minimal time for the occurrence of dephasing. Starting in a fully excited biexciton state with $\rho_0 = |B\rangle\langle B|$ (green lines), no significant indistinguishability is achieved for any of the investigated cavity detunings. This directly results from the strong interaction between the emission processes. For the biexciton at the biexciton-to-exciton resonance where $E_c = E_B/2$, the indistinguishability rises slightly. Here, the biexciton emits a photon through the rapid decay into the individual exciton states. Assuming the simulation ends prematurely after the biexciton decayed into the excitons, this indistinguishability would approach unity. However, as the simulation continues and photon emission from the exciton follows the photon emission from the biexciton at a different energy E_X, the indistinguishability diminishes. Theoretically, the indistinguishability can be revived by applying a spectral filter to the simulation - or the experiment - effectively dismissing the emission from the exciton. Since no spectral filter is applied in this work, the indistinguishability originating from the biexciton-to-exciton transition remains low

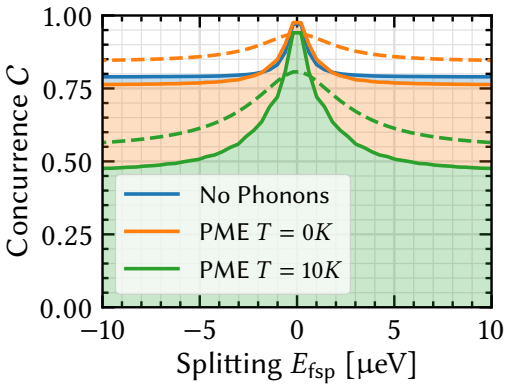

Figure 5.5: Concurrence for varying exciton fine structure splittings for simulations with no phonons and with polaron master equation phonons at different temperatures. The dashed lines is with radiative decay $\gamma_{\mathrm{rad}} = 1\,\mu\mathrm{eV}$ and pure dephasing with rate $\gamma_{\mathrm{dep}} = 1\,\mu\mathrm{eV}$. The width of peak changes with the exciton energy, the cavity coupling and decay as well as the overall phonon coupling rates.

Expanding the investigation towards the entanglement entails calculating the concurrence of the emitted cavity photons. Following the concurrence introduced in Section 4.2.2, identical parameter ranges are investigated in Fig. 5.4 in panel (b). For a cavity energy tuned to exactly the two-photon resonance with $E_{\mathrm{c}} = E_{\mathrm{B}}/2$, an increase in concurrence is observed. This behaviour is consistent with the literature [142]. For the cavity energy approximating the exciton-to-ground transition resonance, the concurrence approaches unity values. Here, the biexciton quickly decays, leaving an almost perfect 50:50 superposition of both excitons. Measuring one of these photons will perfectly herald the corresponding exciton, which is still maximally excited at 50%, hence greatly increasing the concurrence. Due to the large detuning of the exciton-to-ground resonance and the cavity, the Purcell enhancement for this transition is negligible. Consequently, the exciton lifetime remains high with decay times surpassing the nanosecond scale. This is valid only in the absence of radiative decay of the states into non-cavity modes and dephasing of state coherences. Such conditions yield very little emission probability for the second cavity photon, rendering this scenario unsuitable for practical applications.

Extending the analysis of the concurrence, the fine structure splitting energy is varied. Numerical results for $E_{\mathrm{fsp}} \in [-10\,\mu\mathrm{eV}, 10\,\mu\mathrm{eV}]$ are visualized in Fig. 5.5, showing the achievable concurrence for various sets of parameters. Note, that the regular von Neumann equation Eq. (2.8) is used for the phonon-free case, while the polaron master equation Eq. (3.19) equation is used in all other cases. For all simulations, a strong peak in concurrence is observed for vanishing fine structure splitting energies. The concurrence plateaus for finite, non-zero fine structure splittings, which is in well agreement with the literature [84, 140, 234]. Specifically, increasing the temperature lowers the overall achievable concurrence.

This is most prominently observed for larger fine structure splittings. Adding electronic losses using a radiative decay rate as well as a pure dephasing rate of 1 µeV (dashed lines) reveals an overall increase of the concurrence, as well as a broadening of the central peak. The radiative decay increases the rate of decay of the biexciton, while simultaneously lowering the number cavity photons emitted through the two photon transition. This results in less time for the states to suffer from dephasing through any source, thus increasing the concurrence.

Ultimately, an isolated biexciton is investigated. Here, no cavity is present, i.e. $\hbar g = 0$. In Fig. 5.6, the indistinguishability and the concurrence of the photons emitted through the radiative decay of the sates are examined. For the numerical evaluation, the electronic transition operator $|i\rangle\langle j|$, with $i \neq j$, is used instead of the cavity operator $\hat{b}_c$. The rate of radiative decay is varied on the x-axis. These investigations reveal the lower bounds of achievable quantum properties without Purcell enhancement. For simulations incorporating Purcell enhancement, these results indicate the efficiency and practicality of the cavity. When the quantum properties degrade below the values achievable without Purcell enhancement, the selected cavity parameters are not advantageous. The indistinguishability of a photon emitted by either the biexciton-to-exciton or by the exciton-to-ground transition is not influenced by the rate of decay and remains at a constant $\mathcal{I}^{\text{ref}}_{\text{X}\to\text{G}} \approx 0.83$. In Chapter 7, this value is shown to be dependent on the ratio of the decay rates of the exciton and biexciton, where $\gamma_{\text{rad,B}}/\gamma_{\text{rad,X}}$ sets a fundamental limit on the achievable indistinguishability from the free decay. In contrast, the concurrence shows a strong dependence on the rate of decay. Moreover, the concurrence is strongly dependent on the rate of radiative decay. For the values employed in this work, $C^{\text{ref}} \approx 0.8$ is assumed.

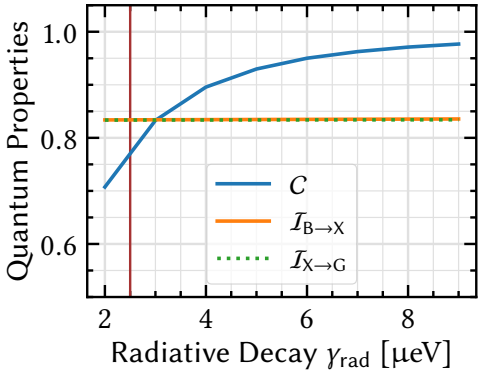

Figure 5.6: Baseline indistinguishabilities and concurrence for photons emitted from an isolated biexciton with no cavity. The indistinguishabilities for the photons emitted through the exciton-ground and biexciton-exciton transition overlap. The red line indicates 2.5 µeV, which is used in Chapter 6. Here, the spearation of the excitons is $E_{\text{fsp}} = 2$ µeV with $E_{\text{H/V}} = E_{\text{X}} \pm E_{\text{fsp}}/2$.

Interim Summary

The biexciton offers multiple excitation and decay pathways, including dynamics involving single excitons, two-photon processes, and cascaded transitions. The natural decay of the biexciton results in an inherent limitation on the indistinguishability of the emitted photons, with a maximum value of approximately $\mathcal{I}^{\mathrm{ref}}_{\mathrm{X}\to\mathrm{G}} \approx 0.83$. However, this limitation can be significantly mitigated by employing Purcell enhancement, where a cavity accelerates the decay rate of the states. Through this method, it is possible to achieve indistinguishability values approaching unity, even in the presence of losses. The concurrence, and thus the entanglement, of the two-photon emission from the biexciton can be optimized by minimizing the fine structure splitting. Concurrence values exceeding $\mathcal{C}^{\mathrm{ref}} \approx 0.8$ are achievable by inducing a rapid decay of the biexciton, which can be further enhanced by the use of a cavity. This rapid decay ensures minimal dephasing, thereby preserving the coherence of the emitted photon pairs and enhancing their entanglement.

5.2 Exciting the Quantum Dot States

The baseline simulations are performed for an initially fully excited state. In a realistic system, this state has to be populated by a viable *excitation method*. The following section introduces various pulsed laser excitation approaches, leading to the central method investigated in this chapter. The following methods are also visualized in Fig. 5.7.

The investigation begins with using simple π pulses for the excitation. The π pulse is defined by evaluating the pulse area Eq. (2.29) for a fixed integral magnitude of $\mathcal{A} = \pi$, adapting the variable pulse parameters, such as its amplitude and temporal length, accordingly. This configuration excites an isolated exciton or biexciton with very high fidelity, reaching unity values for optimized pulse parameters. Otherwise, when a cavity is enhancing the same transition used for the excitation, more complex dynamics arise. Here, the differentiation between a *cavity off-resonant excitation* and a *cavity resonant excitation* is convenient. For a cavity resonant excitation pulse with a pulse bandwidth similar to the magnitude of the loss rates of the system, the excitation process and the decay dynamics will occur on similar time scales. Consequently, these processes coalesce, resulting in significant reductions in excitation fidelity. This is a substantial problem, especially for longer pulse durations. Reducing the pulse lengths solves the problem of temporally intermingling processes, but leads to new problems when the complexity of the configuration surpasses

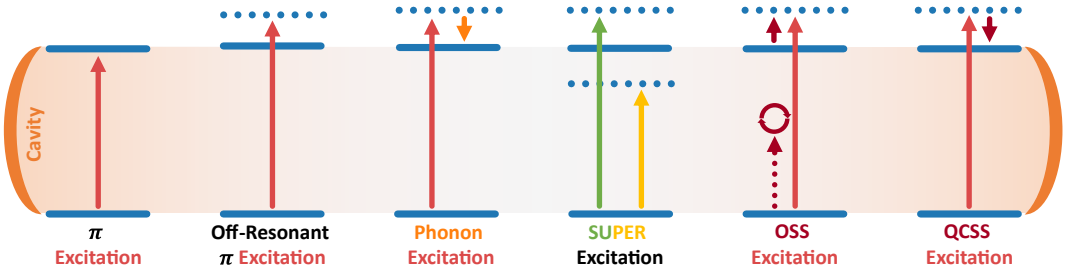

Figure 5.7: Different excitation schemes to either fully or partially excite the quantum dot states, illustrated using a simple two level system. The cavity on left and right indicate the final resonance and Purcell enhanced emission. The lower solid line represents the initial or ground state of the system, while the upper solid line shows the final state after excitation. Shifts in the energy level of the excited state are indicated by dotted lines, representing either the actual intermediate energy levels of the excited state or virtual states, highlighting the dynamic changes in energy during the excitation process.

that of a simple two level system. When the pulse is shorter in the temporal domain, its spectral bandwidth increases. Electronic or photonic transitions that fit inside the range of the pulse bandwidth are driven simultaneously, which is undesired in most cases. Here, systems like the biexciton or trion cannot be efficiently excited because of the strong spectral overlap of all of the available transitions. Reducing the Purcell enhancement, and with it, the cavity mediated decay rate, achieves similar results, albeit with diminishing the versatility of the cavity. This necessitates either accepting the reduced excitation fidelity or switching to alternative excitation methods. In simple experimental setups, the former is commonly endorsed, and is considered in Section 5.3. Regardless of the use of a cavity, a resonant pulse must be separated from the quantum dot emission in the experiment. An immediately apparent solution to the aforementioned set of problems is to introduce detuning for the electronic states and the cavity. For a sufficiently off-resonant cavity, the Purcell enhancement becomes weak enough to separate the timescales of the excitation and the cavity mediated decay processes, albeit dealing with the same problems as for a resonant cavity when the pulse lengths become too short. Separation in the experiment becomes trivial, as simple spectral filtering is sufficient to isolate the desired emission [244]. Furthermore, Section 5.3 demonstrates the long lifetimes of this approach, which consequently allows for losses to dominate the emission and significantly reduce the quality and usability of the emitted photons.

Further exploring the detuned excitation, phonon-assisted side band excitation is considered. Here, the pulse is detuned from the electronic transitions. The pulse energy is tuned to

centralize around the phonon side band at $E_X + \hbar\omega_b$. The off-resonant nature of this excitation method necessitates using strong pulses with large amplitudes. Emerging as the main advantage of this method, the pulse is inherently off-resonant with the electronic system, eliminating the need for further spectral separation. However, a significant problem persists, as the cavity enhancement and thus the Purcell enhancement remains strong, leading to similar timescales for the excitation and emission process and thus, mixing of these dynamics during the excitation. Hence, this approach is not pursued in this work, retaining any electron-phonon coupling as loss.

Expanding the analysis of detuned excitation, the optical Stark shift (OSS) is exploited to induce a temporary detuning to the electronic states. When a pulse is interacting with the electronic states, the energy levels are split and shifted symmetrically around their original positions, which are commonly referred to as *dressed states*. This shift is used to move the resonances away from the cavity, creating a temporary detuning. A second pulse then off-resonantly excites the system. This method is briefly investigated in Section 5.4 using continuous wave (CW) driving to induce the Stark shift. A second Gaussian pulse then excites the respective ground state into the corresponding excited state. A specification of this scheme is the SUPER scheme. Here, the continuous wave driving is replaced with a second Gaussian pulse. In this case, both pulses are strongly detuned from the resonances, as elaborated and briefly described in Section 5.4.1.

Finalizing the investigations of detuned excitation, the quantum confined Stark shift (QCSS) is explored. Here, temporary detuning is achieved electronically [118, 145, 245, 246] instead of optically [164, 168, 247] or via strain [60, 146], introducing the main topic of this chapter based on [145]. By applying an electric field, the energy of the states is shifted similarly to the optical Stark shift [245]. The desired electronic state is excited using a resonant Gaussian pulse. The cavity is designed to be inherently off-resonant with the electronic transitions. After exciting the desired electronic state, its energy is shifted into resonance with the cavity using the QCSS. This method combines the advantages of cavity-off-resonant excitation and the fast resonant decay of a cavity-resonant electronic system.

5.3 Quantum Confined Stark Shift of the Resonances

The application of an electric field to the quantum dot interferes with the wave function of the electronic states. The induced potential difference distorts the potential well containing the charged particles. This mechanism is depicted in Fig. 5.8. This distortion results in new

energy states, effectively increasing or decreasing the energy at which the electronic state resides. The change in energy is described by the time-dependent shift $\Delta E(t)$, which can be included into the usual Hamilton formalism. For the biexciton system in this chapter, the additional Hamiltonian component is given by

$$\mathcal{H}_\Delta = \sum_{i\in\{\mathrm{H,V,B}\}} \Delta E_i(t)\,|i\rangle\langle i|\ . \tag{5.2}$$

Reconstructing the exciton energies $E_{\mathrm{H/V}}$ as well as the biexciton energy E_{B} leads to

$$\Delta E_{\mathrm{H,V}}(t) = f(t)\ ,\ \Delta E_{\mathrm{B}}(t) = 2f(t)\ , \tag{5.3}$$

which is done numerically every at every time step. Here, $f(t)$ is the temporal envelope of the shift. Notably, the biexciton energy intrinsically shifts with twice the speed of the exciton energies. The strategy for using the quantum confined Stark effect (QCSS) for excitation involves a cavity off-resonant configuration of the electronic states. The dot is then excited utilizing any of the available methods, populating the exciton (X) or biexciton (B) state. Because of the off-resonant cavity, the excitation process is desired to offer high excitation fidelity. The QCSS is then exploited, shifting the electronic state energies into resonance with the cavity to achieve rapid decay of the states, resulting in successive emission of photons. Ideally, these photons exhibit high degrees of indistinguishability or concurrence, which is the central study in [145]. In the following, the QCSS approach is compared with the OSS method.

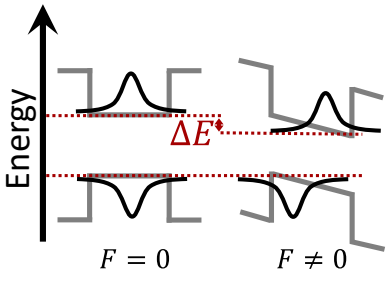

Figure 5.8: Quantum confined Stark shift (QCSS) for a wavefunction inside a potential well with external electric field F. *Reproduced and enhanced from Bauch et al. [145].*

Intuitively, the QCSS can be used either to shift the system out of resonance during the excitation process or to shift the system into resonance after the excitation to enable the Purcell enhanced emission. The former approach requires only a short shift but necessitates precise timing and amplitudes for the shift. The latter approach offers a perfect resonance condition for the excitation pulse and subsequently creates resonance with the cavity. Given the relatively broad cavity mode, even with small losses, using the QCSS to shift the electronic states into resonance with the cavity appears favorable. Additionally, this

also simplifies the experimental setup, as resonance with the cavity is not required to be perfect, whereas perfect resonance with the excitation pulse is mandatory to achieve high excitation fidelity. The temporal setup used in this work is illustrated in Fig. 5.9. In this scheme, the excitation pulse $\Omega(t)$, illustrated in blue, excites the electronic system, which at this point in time is off-resonant with the cavity, with maximized excitation fidelity. As previously noted, this process could involve more advanced excitation methods, although this work is limited to a single, resonant Gaussian excitation pulse. The QCSS $\Delta E(t) \propto f(t)$, illustrated in orange, then shifts the desired electronic transition into resonance with the cavity. The respective electronic state subsequently decays, emitting a photon $\langle \hat{n} \rangle$, which is highlighted in green.

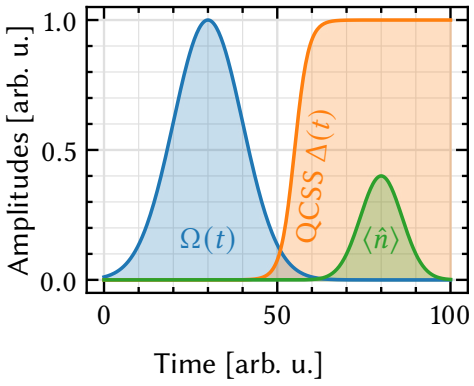

Figure 5.9: Schematic of the quantum confined Stark shifted (QCSS) Excitation Scheme with excitation pulse $\Omega(t)$, electronic shift of the energy induced by the QCSS $\Delta(t)$ through the application of an electric field to the quantum dot, as well as the emission of a cavity photon, indicated by $\langle \hat{n} \rangle$. *Reproduced and enhanced from Bauch et al. [145].*

The initial cavity detuning is set to $E_c - E_X = 1\,\text{meV}$ or $E_c - E_B = 3\,\text{meV}$ when investigating the excitation of the exciton or biexciton, respectively. The energy of the cavity is configured above the electronic resonances to minimize mediation through the phonon side band. The cavity coupling is fixed to $\hbar g = 66\,\mu\text{eV}$ and cavity losses set to $\hbar\kappa = 66\,\mu\text{eV}$, mirroring the settings used in [145]. The state populations are analyzed after a total simulation time of $t_{\text{max}} = 300\,\text{ps}$. The pulse area excitation parameters are $\mathcal{A}_0 = 1\,\pi$ for the exciton and $\mathcal{A}_0 = 3.3\,\pi$ for the biexciton, with the respective excitation fidelity close to unity. In both scenarios, the excitation occurs through the horizontally polarized channel H. Notably, the required pulse amplitude for the biexciton depends on the binding energy used, as higher binding energies require larger pulse energies to successfully bind two excitons into the biexciton. The total amplitude of the shift $\max(f(t))$ is scanned in Fig. 5.10, with the maximum rate of the electronic shift set to $\left.\frac{\mathrm{d}f(t)}{\mathrm{d}t}\right|_{\text{max}} = 100\,\mu\text{eVps}^{-1}$. While achieving such ultrafast electric control of the energies is challenging experimentally, it remains within the realm of realistic possibilities.

Investigating the exciton, analyzed in panel (a), a single point of resonance is found when

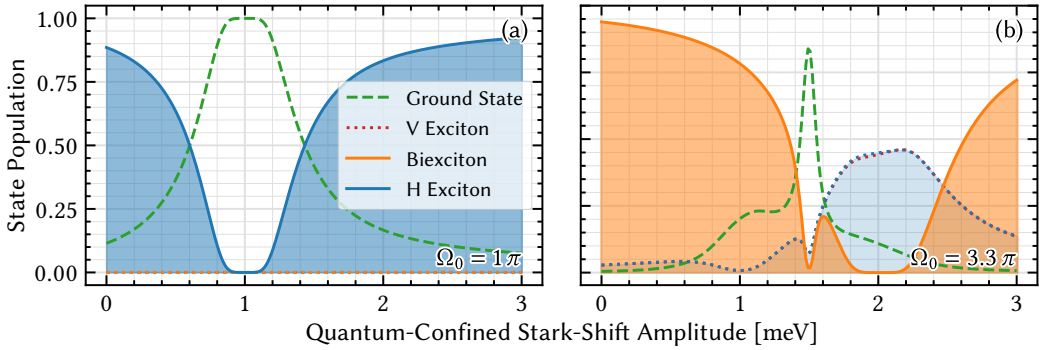

Figure 5.10: Amplitude scan of the electronic shift induced by the quantum confined Stark shift. Both plots show the final occupation of the electronic states after a total simulation time of $t_{\max} = 300\,\text{ps}$ with no phonon interaction. The exciton in panel **(a)** is excited using a pulse area of $\mathcal{A}_0 = \pi$ with $\hbar\omega_0 = E_X$. The biexciton in panel **(b)** is excited using a $\mathcal{A}_0 = 3.3\,\pi$ with $\hbar\omega_0 = E_B/2$.

the shift compensates the initial detuning exactly. Here, $\max(f(t)) = 1\,\text{meV}$. The exciton is allowed to fully decay within the investigated time period. The width of this resonance condition is shallow, with a buffer of approximately 0.1 meV around the main peak. This buffer arises from the spectral width of the cavity mode and is the reason for selecting this setup for this study. No other electronic levels are excited, leaving both the biexciton and the vertically polarized exciton unoccupied. Thus, setting the shift to match the initial detuning achieves high-fidelity excitation and emission using the QCSS method. Proceeding to the excitation of the biexciton, analyzed in panel (b), multiple regions of resonance occur. At a shift amplitude of approximately $\max(f(t)) \approx 1\,\text{meV}$, the rate at which the ground state occupation rises is slightly enhanced because the cavity is in resonance with the exciton-ground transition. At $\max(f(t)) = 1.5\,\text{meV}$, exactly half of the initial detuning, the energy of the cavity equals the energy of the two photon transition of the biexciton. This leaves the biexciton to resonantly decay while emitting two photons. This resonance is very sharp, indicating the need for precise tuning of the Stark shift. The final ground state occupation is around 90%, with some population lost to the individual exciton states. At the biexciton-to-exciton transition, the final ground state occupation decreases as both individual excitons are excited. The cavity strongly enhances the biexciton-to-exciton transition, resulting in a rapid decay of the biexciton into these states. However, the now populated exciton states remain highly occupied due to the off-resonant cavity. The required maximum shift is set to $\max(f(t)) = 1\,\text{meV}$ and $\max(f(t)) = 1.5\,\text{meV}$ for the excitation of the exciton and biexciton, respectively. The temporal dynamics of the excitation and decay process is investigated in Fig. 5.11. Simulations for cavity-free excitation, simple

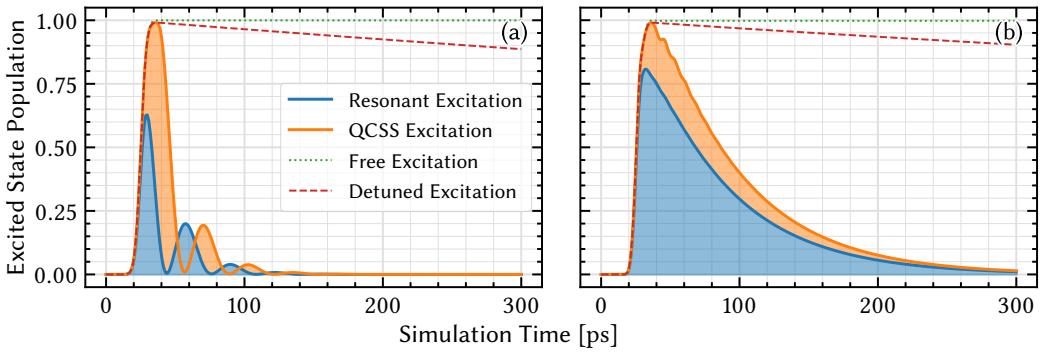

Figure 5.11: Quantum dot dynamics and cavity emission using the QCSS excitation method. The exciton in panel **(a)** is excited with $\max(\Delta(t)) = 1\,\text{meV}$, bridging exactly the dot-cavity detuning. The biexciton in panel **(b)** is excited with $\max(\Delta(t)) = 1.5\,\text{meV}$, bridging the dot-cavity detuning and the additional $E_{\text{bind}} = 1\,\text{meV}$ gap. Cases for resonant π-pulse (3.3π-pulse) excitation with (resonant excitation, solid blue line) and without (free excitation, dotted green line) cavity are compared with off-resonant excitation with (QCSS excitation, solid orange line) and without (detuned excitation, dashed red line) the electronic shift. *Reproduced and enhanced from Bauch et al. [145].*

cavity-resonant excitation, cavity-detuned excitation, and QCSS excitation are compared. In the absence of a cavity (green dotted lines), neither the exciton nor the biexciton decays due to the lack of additional loss mechanisms, resulting in high excitation fidelities but missing the emission. In the detuned excitation case (red dashed lines), the excitation fidelities are high, but any emission occurs slowly. In the resonant excitation case (blue solid lines), excitation fidelities are significantly lowered due the aforementioned mixing of the excitation and emission processes. The QCSS excitation (orange solid lines) mirrors the detuned or free excitation during the excitation phase and then proceeds to also mirror the resonant decay of the state following the shift. This demonstrates the effectiveness of QCSS in achieving high-fidelity excitation and emission and achieves the desired excitation and decay dynamics.

Interim Summary

The QCSS excitation achieves near-unity excitation fidelities similar to a simple, resonant excitation without a cavity while also leveraging the strong Purcell-enhanced decay and photon emission enabled by a cavity. This is accomplished by shifting the electronic stats through ultrafast electric control of their energies, creating resonance with the cavity from an initially off-resonant system. This approach effectively combines the advantages of both the off-resonant excitation and resonant emission.

5.4 Optical Stark Shift and SUPER excitation

Before further investigating the quantum properties of the QCSS excitation, a similar setup using the optical Stark shift, induced by another laser, is briefly discussed. As previously introduced, the approach is equivalent to the QCSS, but instead of an electric field, a second laser is used.

The cavity is initially resonant. The motivation behind this comparison is the practical difficulty of implementing the QCSS, which requires ultrafast electronics and complex applications for electronic contacts. Therefore, the use of a second optical pump Ω_2 to induce a static optical Stark shift is considered as an alternative, which is much easier to implement in the experiment.

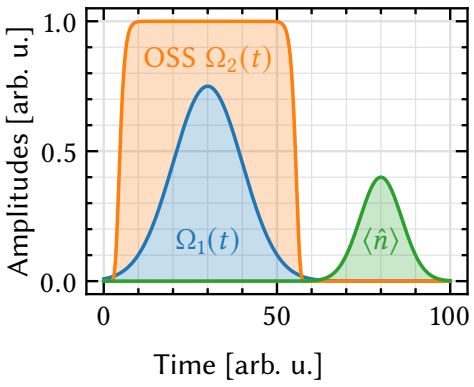

Figure 5.12: Schematic of the optical Stark shifted excitation scheme with excitation pulse $\Omega_1(t)$, Stark shifting pulse $\Omega_2(t)$ which results in the energy shift $\Delta(t)$, as well as the emission of a cavity photon, indicated by $\langle\hat{n}\rangle$.

Sustaining the OSS for the entire emission process is unfeasible, because it would result in off-resonant pumping of the system. Ultimately, setups with continuous wave driving of the system result in stationary states, which statistically emit photons [155, 213]. Instead, the OSS is only utilized during the excitation of the respective electronic state. To ensure comparability with previous results, the biexciton system is considered even when only exciting the exciton. The corresponding excitation scheme is illustrated in Fig. 5.12.

The OSS is induced by a temporary CW pulse, with a pulse energy off-resonant with all of the electronic states. To achieve a significant shift in energies, large amplitudes for the CW pulse are used. Large amplitudes result in strong dephasing due to phonons if electron-phonon interactions are included. Hence, the lossless case with no phonons is investigated exclusively. The area of the Gaussian excitation pulse is set to $\mathcal{A}_1 = 1\,\pi$ or $\mathcal{A}_1 = 3.3\,\pi$ for exciting the exciton or biexciton, respectively.

The initial step involves finding a suitable pulse for the Stark shift by scanning the amplitude of the second pulse. Numerical results for the excitation of the exciton is displayed in

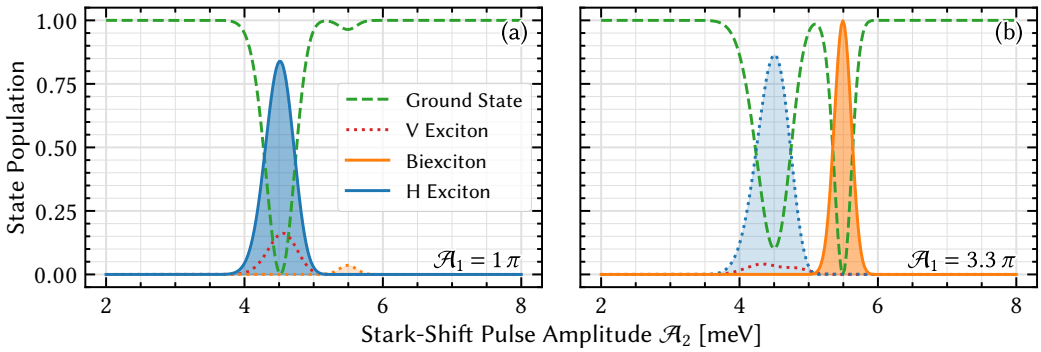

Figure 5.13: Scan the optical Stark shifting pulse amplitude. Both plots show the final occupation of the electronic states after a total simulation time of $t_{\max} = 100\,\text{ps}$ with no cavity and no phonon interaction. The exciton in panel **(a)** is resonantly excited using pulse with $\mathcal{A}_1 = \pi$ and $\hbar\omega_1 = E_X$. The biexciton in panel **(b)** is excited using a $\mathcal{A}_1 = 3.3\,\pi$ pulse with $\hbar\omega_1 = E_B/2$. Amplitudes are not to scale.

Fig. 5.13, panel (a). Similar to the QCSS excitation, only a single, clear resonance condition is observed. However, a full excitation of the horizontally polarized exciton is not achieved due to the significant population of the vertically polarized exciton. Following the same logic as with the QCSS excitation, the optimal amplitude of the CW pulse emerges to be approximately $A_2 = 4.5\,\text{meV}$. The excitation of the biexciton is depicted in Fig. 5.13, panel (b). Here, multiple resonances are visible. Notably, the exciton can also be significantly excited using the stronger excitation pulse. The biexciton is successfully excited with high fidelity at an amplitude of the CW pulse of approximately $A_2 = 5.5\,\text{meV}$.

Utilizing the previously discovered amplitudes for the CW pulse, the temporal dynamics of this excitation method is investigated in Fig. 5.14. Here, panel (a) shows the dynamics of the excitation of the exciton, and panel (b) shows the dynamics of the excitation of the biexciton. In this scenario, excitation of the vertically polarized exciton occurs in both cases, most prominently with the excitation of the biexciton due to the stronger pulses. Furthermore, the excitation efficiency is slightly beneath unity due to interactions with the cavity.

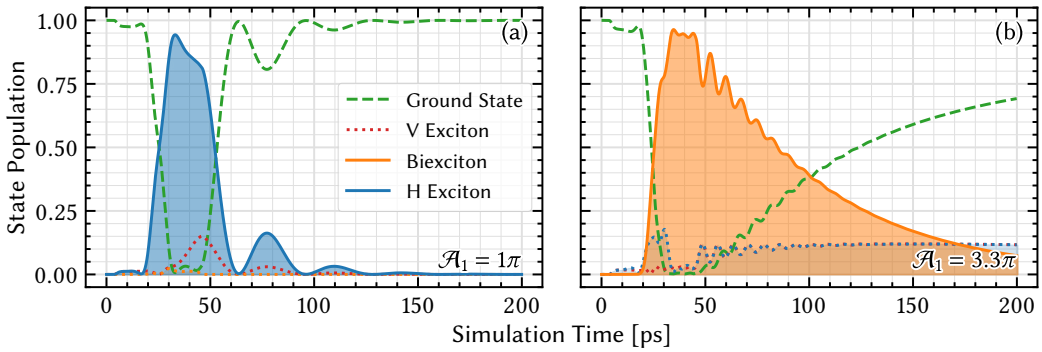

Figure 5.14: Quantum dot dynamics and cavity emission using the OSS excitation method. The exciton in panel **(a)** (blue line) is excited with a detuning of the Ω_Δ pulse of 4.5 meV. The biexciton in panel **(b)** (orange line) is excited with a detuning of 5.5 meV. Both panels show the resonant decay of the state population into a cavity. The blue and red dotted lines representing the individual excitons overlap for later times.

5.4.1 SUPER Excitation

Recent advances in excitation methods have surfaced the *swing-up of quantum emitter population* (SUPER) technique [164–166]. The methodology is similar to the OSS excitation, but instead of using a continuous wave laser to induce the shift, the SUPER method employs two Gaussian pulses. Both of these pulses are strongly detuned from the electronic resonances and require large pulse amplitudes.

Recent experimental [165] and theoretical [163, 164, 166] efforts have demonstrated the efficacy of this excitation method, showing that it performs well in practical applications. Numerical analyses have also indicated that the SUPER method exhibits strong resistance to phonon interactions [162]. This resistance can be attributed to the use of continuous wave lasers, which typically result in continuous pulse application and thereby promote strong phonon interactions due to electron-phonon coupling. In contrast, the SUPER method employs two concurrent, detuned pulses that significantly reduce these interactions. The large amplitudes of these pulses quickly exceed the phonon spectral density, leading to an almost phonon-free interaction [162].

The performance of the continuous wave and the SUPER excitation methods is displayed in Fig. 5.15. In these studies, a simple two-level system without a cavity is used for simplicity. In panel (a), a constant CW pulse is employed, while in panel (b), a strongly detuned Gaussian pulse with a large amplitude is used. In both panels, the amplitude of a second Gaussian pulse is investigated. Its amplitude is varied along the y-axis, and its detuning is

varied along the x-axis. The results show that, in both cases, regions of strong excitation fidelity close to unity values emerge.

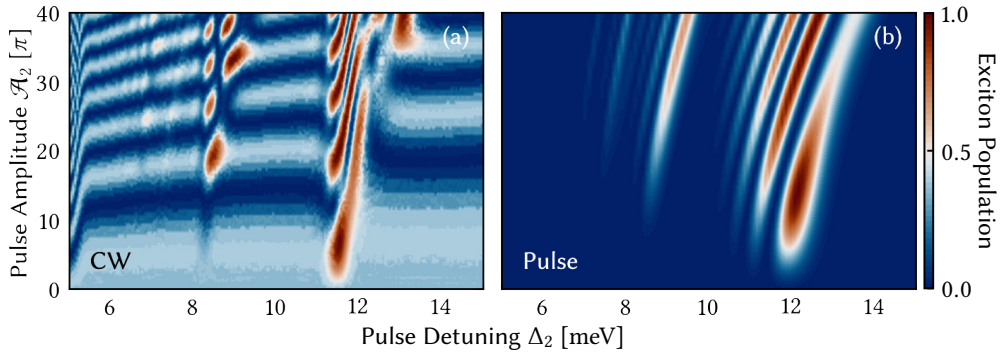

Figure 5.15: SUPER excitation of a single exciton. **(a)** Excitation using a single Gaussian pulse combined with a continuous wave (CW) pulse, with the x-axis detailing the detuning of the Gaussian pulse and its amplitude on the y-axis. **(b)** Excitation using two Gaussian pulses, where the x-axis details the detuning and the y-axis the amplitude of one of the pulses. Each configuration demonstrates how variations in pulse detuning and amplitude influence the excitation of the exciton.

Interim Summary

Using an optical pulse to induce an OSS instead of an electrical QCSS proves to be suitable for the excitation of the electronic states. Electron-phonon interactions will significantly diminish the excitation fidelities when using a CW pulse, rendering this approach unfavorable. On the other hand, SUPER is able to efficiently excite the system even through strong electron-phonon interactions. Unlike the QCSS excitation, both methods still suffer from the premature decay of the electronic state population when combined with a cavity, making the former more advantageous when managing strong Purcell enhancements.

5.5 Quantum Correlations

Having established the time dynamics of the Quantum Confined Stark Shift (QCSS) excitation, it is essential to investigate the corresponding quantum properties. As detailed in Part I, a deterministic photon source necessitates reliable, on-demand emission of photons with high indistinguishability. Ideally, twin photons should exhibit high concurrence, and consequently, high entanglement. This section explores the quantum properties of the

photons emitted from the quantum-dot cavity system using the QCSS excitation method. Comparisons with conventional excitation methods illustrates the performance of this method.

5.5.1 Spectral Characteristics

The emission spectrum, being the most straightforward property, is investigated first. As demonstrated in Section 5.1 and Fig. 5.3, the emission spectrum for an ideal exciton decay consists of two individual peaks separated by the cavity coupling constant $\pm\hbar g$, a phenomenon known as Rabi splitting. For the biexciton decay, a single narrow emission peak around the central cavity frequency is anticipated. The width of the spectral peaks is mediated by the loss rate of the cavity κ.

In Fig. 5.16, the spectra for the simulations displayed in Fig. 5.14 are presented. The emission energy is displayed on the x-axis, while the cavity loss rate increases on the y-axis. Due to the initial detuning, the resonance condition is created from $E = E_0 - E_\Delta$. Here, E_0 is either E_X for the exciton, or $E_B/2$ for the biexciton. In the context of Fig. 5.16, the resonance condition is restored from the left when using the x-axis as the reference.

For the photon emission through the decay of the exciton, shown in panel (a), an initial Rabi splitting of the energies is observed. The emission dominates at $E_X - \hbar g$ because this resonance condition is spectrally reached first, leaving only a fraction of the population to emit at $E_X + \hbar g$. Furthermore, the emission broadens significantly for larger loss rates, where both of the Rabi-split peaks merge into one. Except for the asymmetry of the spectrum, this behaviour mirrors the spectral properties of a resonant decay of an exciton.

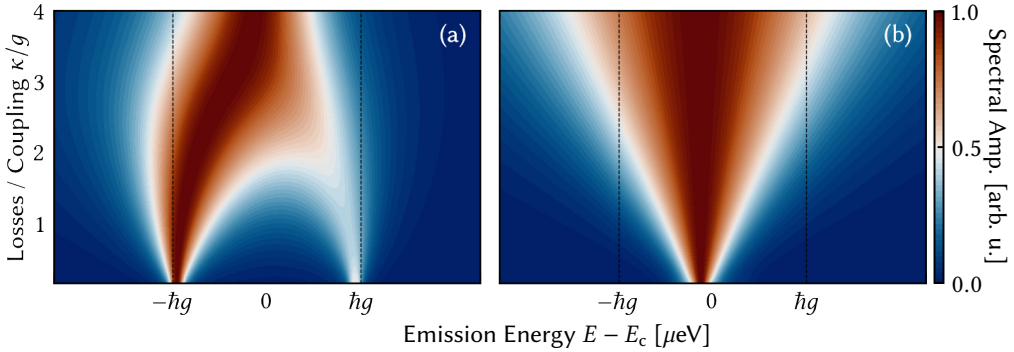

Figure 5.16: Emission spectra for different cavity Q-factors for the exciton emission in panel **(a)** as well as the biexciton emission in panel **(b)**. All spectra are calculated using the Eberly-Wodkiewicz spectrum. *Reproduced and enhanced from Bauch et al. [145].*

For the photon emission resulting from the decay of the biexciton, shown in panel (b), a single central peak emerges. This peak displays minimal asymmetry. As cavity losses increase, the emission broadens. This behavior reflects the resonant decay of the biexciton via the two-photon transition.

These results correspond to a maximum electronic shift speed of 100 μeVps^{-1}. Importantly, in both scenarios, the emission closely resembles that of a resonant decay. Faster shifts yield results more closely aligned with resonant decay, whereas slower shifts lead to increased asymmetry.

By examining the spectral characteristics, the QCSS excitation method demonstrates its potential to achieve high-fidelity photon emission with properties comparable to resonant excitation methods.

5.5.2 Photon Properties

The quantum properties of the photons are investigated similarly to the emission spectra in Section 5.5.1. For the photon emission from the exciton, the focus is on assessing the single photon indistinguishability. In contrast, for the photon emission from the biexciton, the evaluation centers on the concurrence and, consequently, the entanglement. These properties are depicted in Fig. 5.17 at temperatures of $T = 0\,\text{K}$, representing an idealized scenario with active electron-phonon coupling, and $T = 4.2\,\text{K}$, corresponding to the temperature achievable through cooling using liquid helium [248]. All results are derived using the polaron master equation. Additionally, in this study, the pure dephasing of the states is set to $\gamma_{\text{dep}} = 1 \cdot \mu\text{eVK}^{-1}$ using $\hat{\text{O}} = \sqrt{\gamma_{\text{dep}}}\,(|i\rangle\langle i| - |j\rangle\langle j|)$ for $i, j \in \{\text{G}, \text{X}_\text{H}, \text{X}_\text{V}, \text{B}\}$ and $E_i > E_j$. Changing the rate of cavity losses κ is investigated, visualized on the x-axis of the respective plots.

The indistinguishability for a system excited with a single resonant pulse and a resonant cavity (dotted lines) is displayed in Fig. 5.17, panel (a). The indistinguishability plateaus at $\mathcal{I}_\text{c}^\text{resonant} \leq 0.85$, which is close to the reference value $\mathcal{I}_{\text{X}\to\text{G}}^\text{ref} \approx 0.83$ for a cavity-free emission, as displayed in Fig. 5.6. Using the QCSS for the excitation with an initially detuned cavity, the indistinguishability rises to $\mathcal{I}_\text{c}^\text{QCSS} \approx 0.98$ for $T = 0\,\text{K}$ and $\mathcal{I}_\text{c}^\text{QCSS} \approx 0.95$ for $T = 4.2\,\text{K}$. These values significantly surpass those of the resonant excitation method and are close to the achievable maximum values, obtained by starting the simulations in a fully excited exciton state (dashed lines).

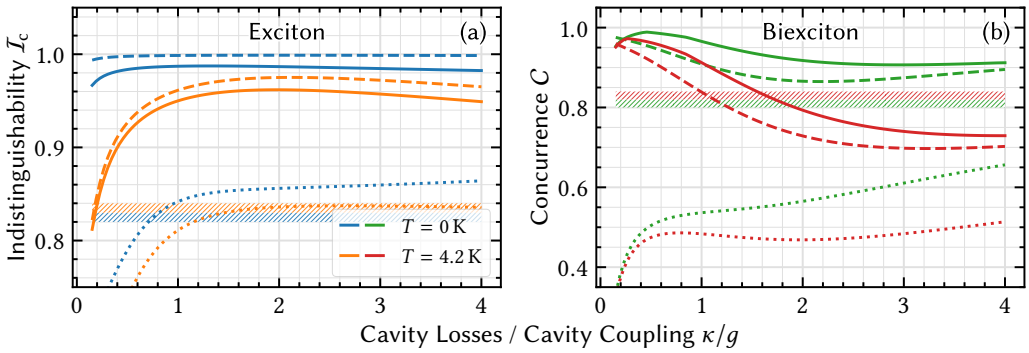

Figure 5.17: Quantum property benchmark for the QCSS excitation (solid lines) compared to the resonant excitation (dotted lines) of the exciton in panel **(a)** and the biexciton in panel **(b)**. The upper limit of reachable indistinguishability or concurrence is depicted by starting the simulation in the respective excited state (dashed lines). Results are presented for both $T = 0\,\mathrm{K}$ and $T = 4.2\,\mathrm{K}$, demonstrating performance across these temperatures. In both cases, the respective reference values according to the lossless biexciton baseline from Fig. 5.6 are indicated using the hatched areas. *Reproduced and enhanced from Bauch et al. [145].*

The corresponding emission probabilities are displayed in Fig. 5.18, panel (a). When using a resonant pulse, the emission probability exceeds unity, adversely affecting the deterministic behavior of the emitter. In contrast, the emission probabilities for the QCSS excitation remain slightly below their ideal reference values. When the simulation starts in a fully excited state, the emission probability of the cavity photons is only reduced by the electronic losses. However, for the QCSS excitation case, further reductions occur because the emission process is prolonged by the time required to shift the energies.

Examining the twin photons from the biexciton in Fig. 5.18, panel (b), it is observed that the concurrence using the QCSS excitation even exceeds its reference value when initially starting the simulation in the biexciton state. This occurs because the emission probabilities, depicted in Fig. 5.18, panel (b), are significantly lower for the QCSS case when compared to the reference case. As a result, the reduced photon population is less susceptible to phonon-induced dephasing, which slightly increases the concurrence of the emitted photons.

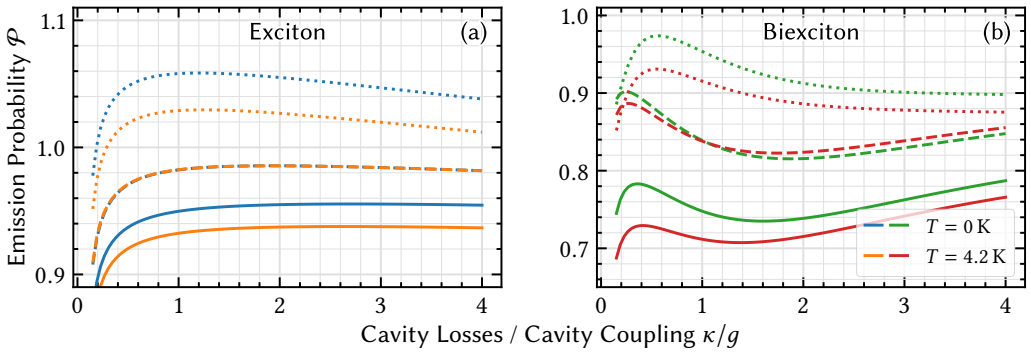

Figure 5.18: Emission probabilities for the QCSS excitation (solid lines) compared to the resonant excitation (dotted lines) of the exciton in panel **(a)** and the biexciton in panel **(b)**. Data shown correspond to Fig. 5.17. Results are presented for both $T = 0\,\mathrm{K}$ and $T = 4.2\,\mathrm{K}$.

5.6 Concluding the Stark Shifted Excitation

The biexciton system is introduced alongside various excitation methods, including the newly emerging SUPER scheme and the Quantum Confined Stark Shifted (QCSS) excitation. The QCSS excitation method is theoretically proven to be effective. This method produces highly indistinguishable photons emitted from the exciton and allows for strong entanglement of twin photons emitted from the biexciton. One significant advantage of QCSS is the feasibility of using long pulses due to the cavity-off-resonant excitation and thus, initially low Purcell enhancement. However, a disadvantage of the QCSS method is its complicated experimental setup. While SUPER requires synchronization of two lasers, QCSS necessitates ultrafast electric control of the state energies. This control can be implemented through piezoelectric components or by applying voltage changes directly via electronic contacts, enabling rapid modulation of the potential difference within the material [24, 25, 107, 249].

The QCSS excitation outperforms SUPER excitation in terms of indistinguishability. This is because the QCSS method not only avoids stimulated emission by separating the laser and emitter but also prevents premature cavity decay of the population. Fortunately, QCSS and SUPER are not mutually exclusive, as the excitation pulse in the QCSS method can be exchanged for a SUPER excitation. Starting with an electronic system and an off-resonant cavity, SUPER can be used to excite the system. Afterwards, the electronic shift used in the QCSS method is applied to achieve resonance between the desired electronic transition and the cavity. This approach combines the phonon-free, high-fidelity excitation of SUPER with

the benefits of QCSS, including off-resonant excitation and resonant decay. Consequently, this combination ensures perfect separation of the excitation and emission in both time and frequency domains, maximizing the quality of the emitted photons. This method for high fidelity excitation of the quantum dot states mark the central result from this chapter and the underlying work [145].

Interim Summary

Using the QCSS method for excitation, high indistinguishability for single photons and strong concurrence for twin photons are achievable, highlighting its potential for quantum information applications. Despite the complexity of this setup, the QCSS provides the ability to produce high-quality quantum states, which makes this method a promising technique for future quantum dot experiments and applications. The QCSS method is further capable of outperforming simple resonant excitation methods and competes well with the recently emerged SUPER scheme.

Generating Indistinguishable and Simultaneously Entangled Photons

6

In the previous chapter, various methods for exciting the electronic system are investigated. Regardless of the excitation method used, the emitted photons exhibit either high indistinguishability or strong entanglement. However, achieving high values for both properties simultaneously presents a significant challenge [92, 170]. This limitation arises from an intrinsic constraint imposed by the decay rate of the biexciton [74].

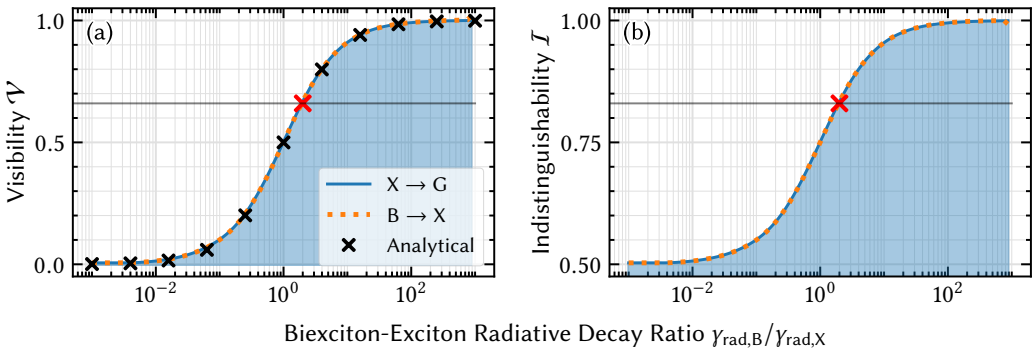

Figure 6.1: Comparison of the visibility and indistinguishability of a simple two-level system with artificially modified radiative decay rates for the biexciton. **(a)** Analytical results, evaluated through Eq. (6.1), and results obtained using the von Neumann equation Eq. (2.8) for the visibility. **(b)** Indistinguishability for the same simulation depicted in panel (a). The red crosses indicate the natural decay ratio of the biexciton system, $\gamma_{\mathrm{rad,B}}/\gamma_{\mathrm{rad,X}} = 2$, resulting in a visibility of $\mathcal{V}^{\mathrm{nat}}_{\mathrm{X}\to\mathrm{G}} = 0.66$, correlating with an indistinguishability of $\mathcal{I}^{\mathrm{nat}}_{\mathrm{X}\to\mathrm{G}} = 0.83$. Notably, values for the natural visibility and indistinguishability of both possible photon emissions coincide, with $\mathcal{V}^{\mathrm{nat}}_{\mathrm{X}\to\mathrm{G}} \approx \mathcal{V}^{\mathrm{nat}}_{\mathrm{B}\to\mathrm{X}}$ and thus $\mathcal{I}^{\mathrm{nat}}_{\mathrm{X}\to\mathrm{G}} \approx \mathcal{I}^{\mathrm{nat}}_{\mathrm{B}\to\mathrm{X}}$. *Reproduced and enhanced from Bauch et al. [174].*

In Section 4.1.1, the visibility was introduced as a figure of merit for single-photon indistinguishability, focusing on first-order correlations. By considering a simple three-level system, approximating an isolated biexciton system with no cavity and only one available intermediate exciton state, an analytical expression for the visibility of the emitted photon

can be derived [74]. The resulting analytical expression reads

$$\tilde{\mathcal{V}}_{\mathrm{X}\to\mathrm{G}}^{\mathrm{analytical}} = \left[1 + \gamma_{\mathrm{rad,X}}/\gamma_{\mathrm{rad,B}}\right]^{-1} . \tag{6.1}$$

The evaluation of Eq. (6.1) while varying the decay rate ratio of the biexciton and exciton is illustrated in Fig. 6.1, panel **(a)** (black crosses). The visibility reaches a minimum when $\gamma_{\mathrm{rad,B}} \ll \gamma_{\mathrm{rad,X}}$, quickly approaching zero. When the radiative decay rate of the biexciton is twice that of the exciton, the visibility reaches $\mathcal{V}_{\mathrm{X}\to\mathrm{G}}^{\mathrm{nat}} = 2/3 \approx 0.66$, as marked by a red cross in Fig. 6.1, panel **(a)**. The corresponding value for the single-photon indistinguishability in panel **(b)** is $\mathcal{I}_{\mathrm{X}\to\mathrm{G}}^{\mathrm{nat}} = 0.5(1 + 2/3) \approx 0.83$. These values serve as a lower bound, where setups yielding lower indistinguishability values are considered ineffective for the intended purposes. However, when $\gamma_{\mathrm{rad,B}} \gg \gamma_{\mathrm{rad,X}}$, both the visibility and the indistinguishability exceed the reference values, approaching unity.

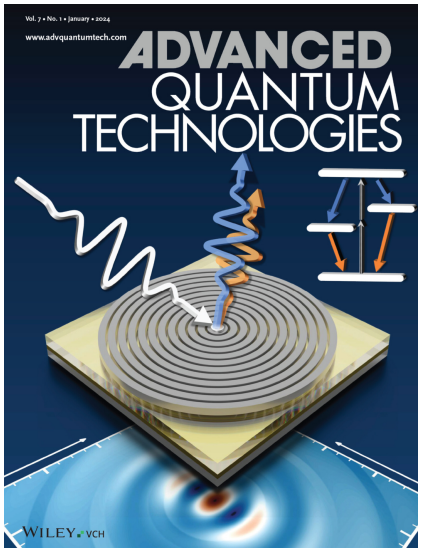

Figure 6.2: Cover page of the Advanced Quantum Technologies journal issue from January, 2024.

The analytical visibility in Fig. 6.1, panel **(a)**, agrees well with numerical results for a four-level biexciton system. As discussed in Section 4.2.1, the visibility neglects multi-photon influences, which is why the indistinguishability is preferred in simulations that include these processes. Since, in this case, the indistinguishability behaves equivalently to the visibility, it will be used exclusively in this chapter.

In summary, for an isolated biexciton system, increasing the decay rate of the biexciton significantly enhances indistinguishability [74]. Numerical results show that photon indistinguishabilities from both the biexciton-to-exciton transition $\mathcal{I}_{\mathrm{B}\to\mathrm{X}}$ and the exciton-to-ground transition $\mathcal{I}_{\mathrm{X}\to\mathrm{G}}$ scale equally with the decay rate. Introducing a system that facilitates the rapid emission from the biexciton consequently results in the emission of two photons that are both highly indistinguishable and, ideally, strongly entangled.

The central focus of this chapter is to achieve the rapid decay of the biexciton using a cavity resonator, similar to the one described in Chapter 5. This cavity is tuned to

primarily enhance the biexciton-to-exciton transition, allowing modulation of the biexciton-exciton decay rate ratio. By leveraging the cavity resonator, the inherent limitations of the biexciton system can be mitigated. The resulting system theoretically emits photons that are both indistinguishable and entangled. Additionally, the quantum-dot-cavity system is tuned for emission in the telecom-C band at $\lambda = 1550\,\mathrm{nm}$, enabling broad applications of the structure [92, 94, 195]. This dual achievement marks a significant advancement for quantum dot technologies, promising enhanced performance in quantum information processing applications.

This work highlights the publication Bauch et al., *On-demand indistinguishable and entangled photons using tailored cavity designs*, [174], which is prominently featured on the cover page of the Advanced Quantum Technologies Journal from January 2024. The data for this work is available on the corresponding Zenodo archive [250]. The cover image is presented in Fig. 6.2.

6.1 Quantum Dot - Reflector Structure

The system examined in this chapter closely parallels the one discussed in Chapter 5, consisting of a biexciton with two individual excitons and a two-mode cavity that enhances both horizontally and vertically polarized selection rules. The Hamiltonian that governs the time evolution of this system remains consistent with the one in Eq. (5.1), excluding the temporal shift of the energies. A visual representation of this system is provided in Fig. 6.3.

This chapter aims to identify a suitable reflector structure—a cavity—that effectively enhances the Purcell effect of the electronic transitions. This enhancement is crucial to ensure that the emitted photons exhibit high degrees of indistinguishability and entanglement. As previously discussed, photons generated by the biexciton system naturally have limited indistinguishability, and their entanglement is highly susceptible to loss. Employing a cavity that strongly enhances only the biexciton-to-exciton transition does not result in high indistinguishability for both photons. Therefore, a cavity that facilitates rapid emission for both the biexciton-to-exciton and exciton-to-ground transitions is necessary. These transitions are separated by the biexciton binding energy E_{bind}, which requires a broad cavity mode to enhance both.

A structure that meets these criteria is the *circular Bragg reflector*, also known as a *bullseye cavity* due to its geometric shape [89, 172, 196, 251, 252]. This configuration consists of

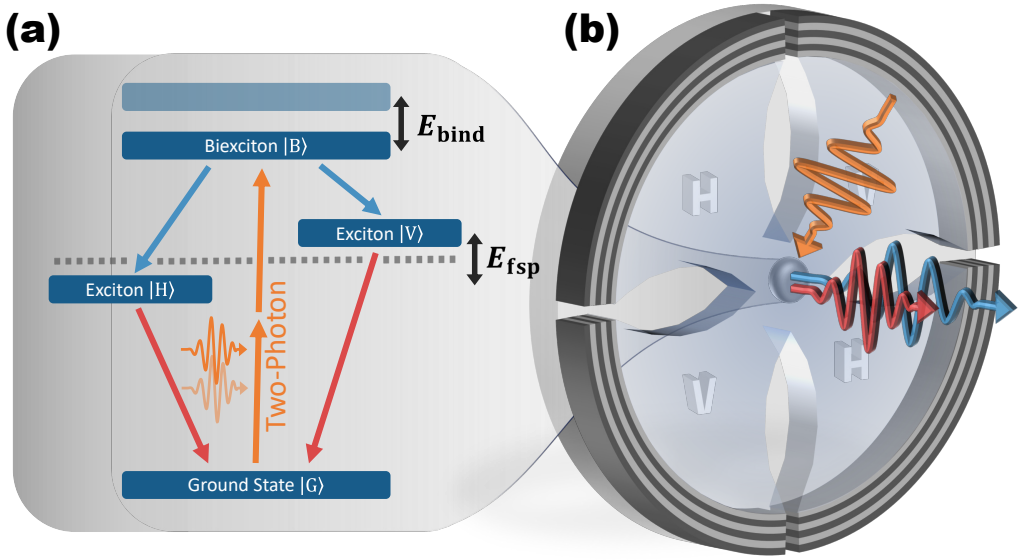

Figure 6.3: Quantum dot biexciton and circular Bragg reflector structure. The biexciton system in panel **(a)** features a finite binding energy E_{bind}, indicated by the transparent blue level, as well as the exciton fine structure splitting energy E_{fsp}. The simulations feature either an initially fully excited biexciton or two-photon excitation, indicated by the orange arrow. The biexciton may then decay through the exciton cascade, indicated by the blue and red arrows, which is accelerated by the circular Bragg reflector (cavity) in panel **(b)**. This cavity Purcell enhances the quantum dot transitions and mediates the emission of photons. *Reproduced and enhanced from Bauch et al. [174].*

concentric circles with the quantum dot positioned at the center, where the field intensity is maximized. The cavity is fabricated on a glass substrate using semiconductor material, specifically InGaAs in this study. The circular Bragg grating is highly configurable with respect to its target wavelength, as the thickness and height of the gratings can be adjusted accordingly.

Circular Bragg reflectors are prominent for emission around the telecom-C band. In this work, the electronic system is configured with the exciton energy set to $E_{\text{X}} = 0.8\,\text{eV}$, with $E_{\text{fsp}} = 1\,\mu\text{eV}$. Thus, the energies of the horizontally and vertically polarized excitons are $E_{\text{H/V}} = E_{\text{X}} \pm E_{\text{fsp}}$. Using a binding energy of $E_{\text{bind}} = 5\,\text{meV}$, the biexciton energy is $E_{\text{B}} = 2E_{\text{X}} - E_{\text{bind}} = 1.595\,\text{eV}$.

The optical resonators in this study are subjected to numerical investigations with a high degree of tunability, unconstrained by the practical limitations of the implementation. To

ensure feasibility for experimental applications, Maxwell simulations are employed to model the behavior of light within the cavity. These simulations confirm that the investigated structures can be practically realized. The primary objective is to optimize the transition enhancements to achieve maximum photon quality, guided by microscopic simulations of the quantum states. This approach is a collaborative effort with the electrical engineering group of Prof. Dr. Jens Förstner from Paderborn University [174]. This section covers only a limited aspect of the numerical optimization of semiconductor microcavities, a topic that remains an active area of research [253].

In this work, the Maxwell optimizer can modify the inner cavity radius, grating period, grating height, and the spacing between individual gratings. Each of these parameters represents a degree of freedom, increasing the computational complexity. A notable aspect of the work presented in [174] is the independent adjustment of the first trench width in relation to the other gratings. This approach enables finer optimization but comes with the trade-off of higher computational costs, which is why it is seldom used in the literature. The cavity design and its parameter blueprint are shown in Fig. 6.4.

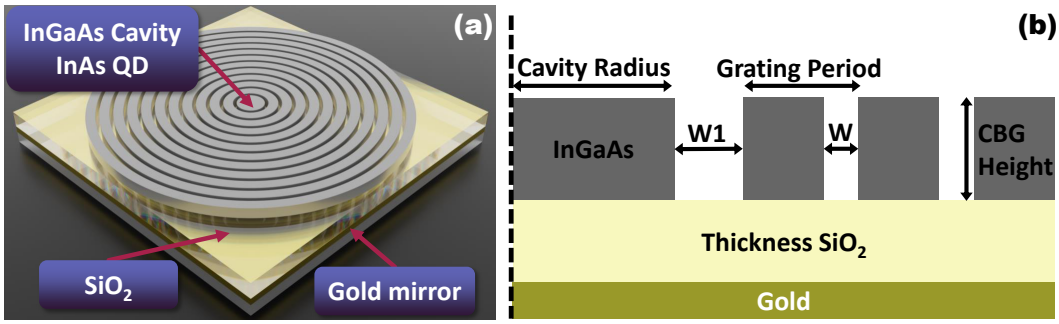

Figure 6.4: Circular Bragg reflector optimization via Maxwell equations solved on a finite grid. Panel **(a)** shows a rendered image of the cavity structure. Panel **(b)** provides a detailed two-dimensional slice of the structure, highlighting the parameters available for numerical optimization. Each parameter represents a degree of freedom for the optimizer [174].

A comparison between the spectrum of the Maxwell-optimized cavity and quantum simulation results is provided in Fig. 6.5. Panel **(a)** displays the cavity spectrum designed to maximize the indistinguishability and concurrence simultaneously, with the vertical dashed line indicating the exciton energy and the solid line marking the biexciton resonance. The optimization specifically targets Purcell enhancement at the biexciton-to-exciton transition energy $E_B - E_X$, with less emphasis on enhancing the exciton-to-ground transition energy E_X. The results from the quantum simulations (orange) are mirrored along the x-axis to

allow for better comparison with the Maxwell-optimized cavity (blue). Panel **(b)** shows the first normalized field mode of the cavity, demonstrating the alignment of the maximum field intensity precisely at the center of the cavity, which maximizes the light-matter interaction.

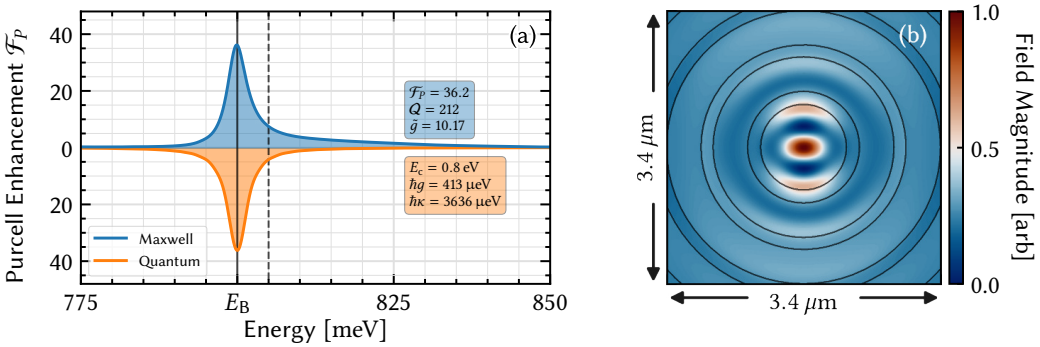

Figure 6.5: Comparison between Maxwell-optimized cavity spectrum and quantum simulation (a) Cavity spectrum designed for maximum indistinguishability and concurrence. The vertical dashed line marks the exciton energy, and the solid line indicates the biexciton resonance. The optimization targets Purcell enhancement at the biexciton-to-exciton transition energy $E_B - E_X$. The quantum simulation results (orange) are mirrored along the x-axis for better comparison with the Maxwell-optimized cavity (blue). The parameters resulting from the Maxwell simulations are provided in 6.6. **(b)** Normalized field mode of the cavity, showing maximum field intensity at the cavity's center, enhancing light-matter interaction [174].

The Maxwell optimizer employs a gradient descent method to identify the optimal set of parameters by minimizing a loss function, which is qualitatively defined as

$$f(x) \equiv f_{\text{Purcell Enhancement out of Target Range}} + f_{\text{Mismatching Target Wavelength}} + f_{\text{Quantum Slope Equation}} + f_{\text{Mismatch Target } Q \text{ Range}} \,. \tag{6.2}$$

Further details on the loss function are available in Appendix A.3. Essentially, the loss function penalizes Purcell enhancements that fall outside the desired range, as well as mismatches in the target wavelength and the target Q-factor range. Additionally, if the resulting cavity parameters lead to low quantum properties of the photons, such as reduced indistinguishability or low concurrence, the loss function value increases through the quantum slope equation. The structural cavity parameters are illustrated in Fig. 6.4, panel **(b)**. The target wavelength is set to 1550 nm. The subsequent chapter aims to assess the quantum slope equation of the loss function. Maxwell simulations of the cavity ensure that the cavity parameters are achievable in a realistic system, emphasizing the practical

implementability of the design. An example of the resulting cavity spectrum obtained by the Maxwell optimizer and a comparison with the results obtained from microscopic simulations conducted in this work are shown in Fig. 6.5, panel **(a)**. The corresponding Maxwell parameters are listed in Fig. 6.6. These parameters provide a direct link between the theoretical results and their experimental implementation, serving as a blueprint for practical application [174].

Dimension [nm]	**Optimal Cavity Fig. 6.5, panel (a)**
Grating Period	563.3
1. Trench Width	154.3
Trench Width	161
Cavity Radius	584.1
CBG Height	450.6
Thickness SiO_2	359.6

Figure 6.6: Optimized resonator properties for various optimization objectives are provided. The resonator described in Fig. 6.5, panel (b) is designed to achieve high cavity coupling values $\hbar g$, low Q-values, moderate double-digit Purcell enhancement, and includes optimization for a temperature of $T = 4.2\,\mathrm{K}$. The latter is strongly guided by microscopic simulations using the polaron master equation. Further details are available in the respective publication [174].

6.2 Quantum Properties

Circular Bragg reflectors provide high coupling values with $g > 200\,\mu\mathrm{eV}$. To begin, the cavity losses must be evaluated to determine whether strong effective coupling, characterized by low cavity loss rates κ, or weak effective coupling, where κ is large, is preferable. The optimal Purcell enhancement is achieved by adjusting the ratio κ/g and identifying the appropriate cavity resonance.

The emission from the exciton-to-ground transition originates from the radiative decay of the exciton. In contrast, the photon from the biexciton-to-exciton transition arises from a combination of cavity emission and radiative emission, which are integrated into a single operator. This integration implies that while the cavity directly contributes to the photon population from the biexciton, it also functions as a loss channel for the exciton decay. This distinction is crucial because, in typical scenarios, radiative decay is treated as a loss, whereas here, the cavity plays that role. For the distinct photons originating from the

biexciton-to-exciton transition as well as the exciton-to-ground transition, the operators

$$\hat{O}_{B,i} = \underbrace{|X_i\rangle\langle B| + \hat{b}_i}_{B\to X} \quad \text{and} \quad \hat{O}_{X,i} = \underbrace{|G\rangle\langle X_i|}_{X\to G} \tag{6.3}$$

are used. The former operator accounts for the emission from both the radiative decay of the biexciton-to-exciton transition and the cavity mode coupled to this transition, while the latter operator includes only the radiative decay of the exciton. In simulations that incorporate the cavity, the corresponding indistinguishabilities are linked to these operators.

Numerical simulations starting in the biexciton state with $\rho_0 = |B\rangle\langle B|$ are presented in Fig. 6.7. Here, the indistinguishabilities of the photon from the radiative emission of the biexciton-to-exciton transition, enhanced by the cavity, are displayed in panel (a). The indistinguishability of the photon from the radiative emission of the exciton-to-ground transition is shown in panel (b). The concurrence of both photons is depicted in panel (c). The rate of cavity losses is varied on the y-axis, while the cavity energy is varied on the x-axis.

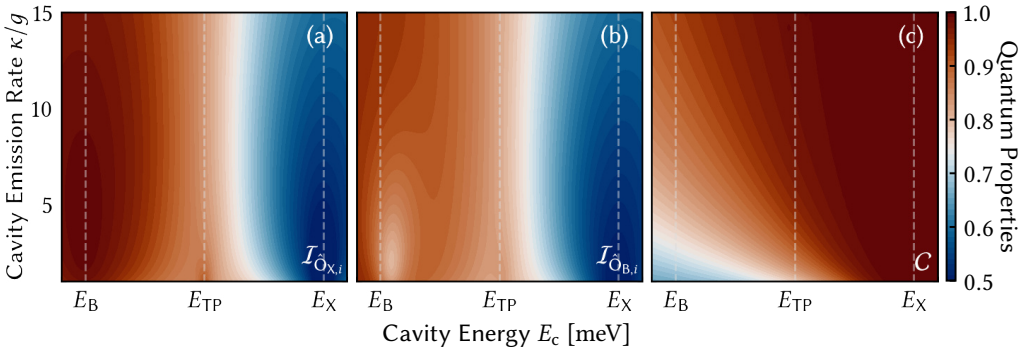

Figure 6.7: Quantum properties of the non-optimized emitter system. Panel **(a)** illustrates the indistinguishability of the exciton photon, panel **(b)** displays the indistinguishability of the biexcitons super operator photon from Eq. (6.3) and panel **(c)** explores their concurrence. The visualization spans over the complete energy range encapsulating both the exciton as well as the biexciton resonances. The cavity emission rate κ is specified relative to the cavity coupling g. In all panels, the initial state is $\rho_0 = |B\rangle\langle B|$. *Reproduced and enhanced from Bauch et al. [174].*

For a cavity configuration to be desirable, all three properties should ideally be maximized. It is directly visible that the indistinguishabilities of both photons are high when the cavity is energetically placed around the biexciton-to-exciton transition, significantly reducing the biexciton's lifetime. This is consistent with the previously introduced conditions. However,

the concurrence is maximized when the cavity is around the exciton-to-ground transition, where it perfectly heralds the respective photons, thus increasing the concurrence. In this configuration, the indistinguishabilities are minimized. Consequently, the former configuration, where the cavity is placed around the biexciton-to-exciton transition, is the only viable one for applications in quantum information technologies. Furthermore, a cavity with low effective coupling, where $\kappa/g \gg 1$, appears to be desirable.

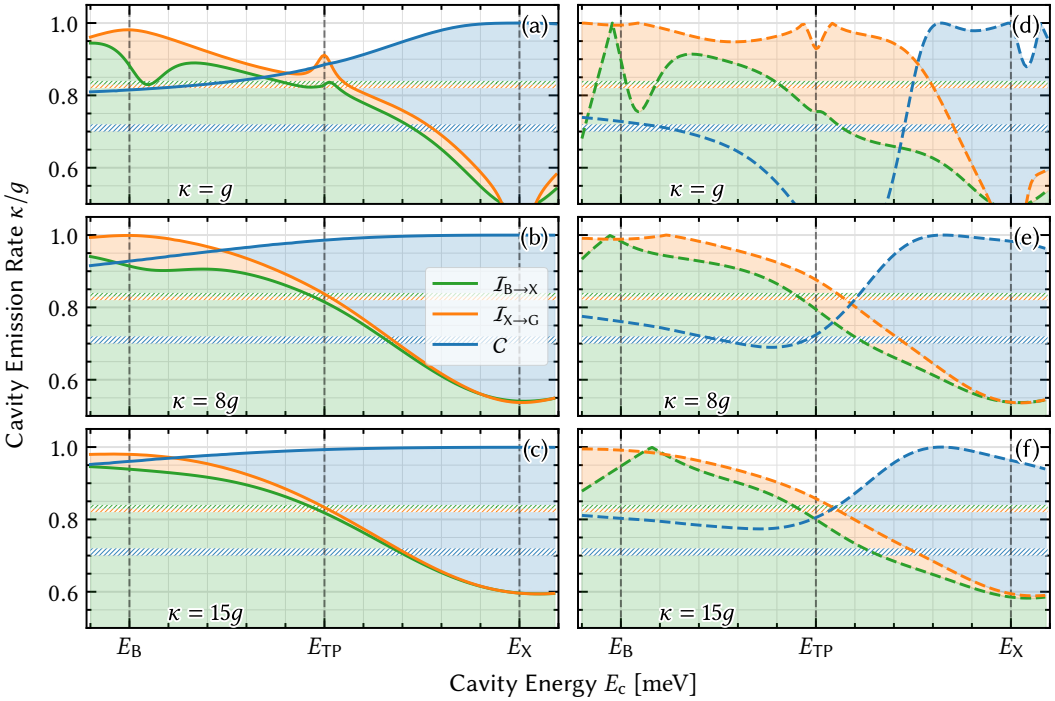

Figure 6.8: Slices of the quantum properties of the non-optimized emitter system for a high-Q cavity with $\kappa = g$ in panels **(a,d)**, for a low-Q cavity with $\kappa = 8g$ in panels **(b,e)** as well as a very low-Q cavity with $\kappa = 15g$ in panels **(c,f)**. Each set of panels contrasts simulations conducted without electron-phonon interaction (left panels) against those with phonons, utilizing the polaron master equation at $T = 4.2\,\mathrm{K}$ (right panels). The hatched area represents the indistinguishability (blue) or concurrence (green) achievable using a biexciton system without Purcell enhancement.

Moreover, Fig. 6.8 displays three distinct slices of Fig. 6.7, specifically at $\kappa \in \{g, 8g, 15g\}$ in panels (a-c), respectively. Simulations including electron-phonon coupling at $T = 4.2\,\mathrm{K}$ using the polaron master equation with otherwise the same parameters are shown in panels panels (d-f). It is important to note that no pure dephasing through the Lindblad rates is included in these results; all dephasing is the direct result from electron-phonon interactions through the polaron master equation.

In these simulations, it becomes even more evident that a cavity with high loss rates, and thus a very broad cavity mode, is favored for maximizing the quantum properties of the photons. The reference values, highlighted by the hatched areas in Fig. 6.8, reflect the values for an isolated biexciton with $\gamma_{\mathrm{rad}} = 2.5\ \mu\mathrm{eV}$, as previously introduced in Fig. 5.6.

The qualitative behavior of the indistinguishabilities, when including electron-phonon coupling, is similar to the lossless case. Here, phonons can contribute constructively, further increasing the achievable indistinguishability from the biexciton-to-exciton photon. The sharp creases in the figure result from insufficient resolution on the x-axis. Despite this, the indistinguishability when using the circular Bragg reflector still greatly surpasses the reference value.

However, the concurrence is significantly reduced when electron-phonon coupling is enabled. This reduction occurs because dephasing, while not as detrimental to the single photon indistinguishability, is very destructive for the two photon entanglement. Nevertheless, the concurrence still surpasses its reference value, especially for low-Q cavities and thus low effective couplings.

Interim Summary

The circular Bragg reflector structure introduced in this chapter offers high raw light-matter coupling with $\hbar g$ on the order of several hundred μeV, which is ideal for decreasing the lifetime of the biexciton. Low-Q values are preferred, where cavity losses are high. The emitted photons from this structure exhibit high indistinguishability, significantly surpassing the reference value of $\mathcal{I}^{\mathrm{nat}}_{\mathrm{X}\to\mathrm{G}} \approx 0.83$ for free-space emission with no Purcell enhancement. Additionally, the two-photon concurrence C, and consequently the entanglement, is markedly increased for a Purcell enhanced emission using the circular Bragg reflector.

6.2.1 Finding Optimal Purcell Enhancements through Temperature Optimization

This preliminary analysis reveals a strong dependency on phonons. In this section, electron-phonon coupling is actively used as an optimization parameter. For a low-Q cavity, setting the target cavity energy to exactly the biexciton-to-exciton transition simplifies the investigation, while keeping in mind that slight further increases in indistinguishability are still possible.

A first approach involves a gradual activation of the cavity by incrementally increasing either the Purcell enhancement or the raw cavity coupling g. In the scenario focusing on the Purcell enhancement, the cavity coupling is set to a high value with $\hbar g = 200\,\mu\text{eV}$. Conversely, in the scenario emphasizing raw cavity coupling, the rate of cavity losses is fixed at $\hbar\kappa = 3\,\text{meV}$. These results are illustrated in Fig. 6.9. Low Purcell enhancements, with $\mathcal{F}_P \approx 20$, appear to be optimal, effectively balancing the quantum properties of the system. This is indicated by the gray line, which combines all three quantum properties using multiplication and appears to maximize around low Purcell enhancements. These results are congruent when including electron-phonon coupling at $T = 4.2\,\text{K}$. The sharp transitions in the phonon results arise from the fact that at lower Purcell enhancements, electron-phonon interactions contribute constructively, but as the Purcell enhancement increases, the interaction becomes increasingly destructive through the increased dephasing.

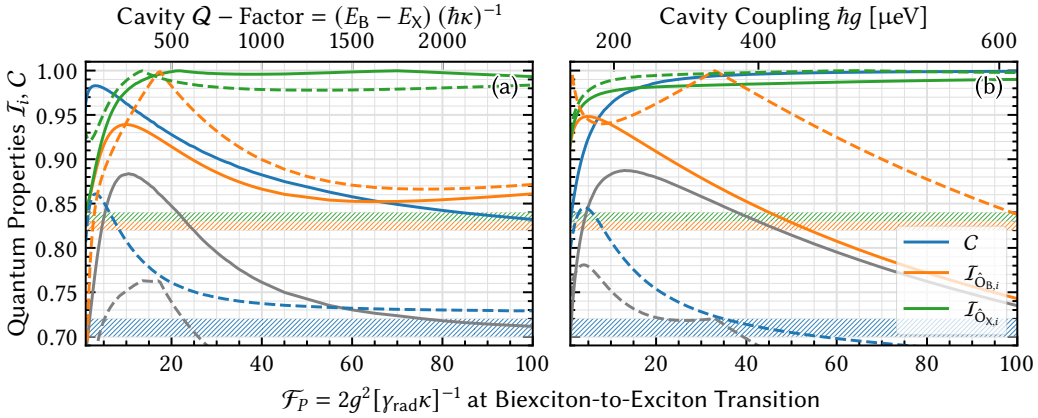

Figure 6.9: Quantum properties for a gradually enabled cavity contrasting tuning the cavity via the Purcell enhancement in panel (a) and via the raw cavity coupling in panel (b). For all simulations, $\gamma_{rad} = 2.5\,\mu\text{eV}$. Simulations with electron-phonon coupling (dashed lines) are conducted at a temperature of $T = 4.2\,\text{K}$. The hatched areas represent the reference values for an isolated biexciton with no cavity, in a lossless scenario. *Reproduced and enhanced from Bauch et al. [174].*

In Fig. 6.10, the cavity coupling is varied on the y-axis and the Purcell enhancement on the x-axis. Because the rate of radiative decay is fixed to $\gamma_{rad} = 2.5\,\mu\text{eV}$, this effectively varies the cavity losses in conjunction with the coupling value on the x-axis. Initially, in the phonon-free case, high values are observed throughout all investigated ranges, supporting that a low-Q cavity around the biexciton-to-exciton transition is sufficient to significantly enhance the photon properties.

Notably, the indistinguishability of the biexciton-to-exciton photon is maximized for smaller

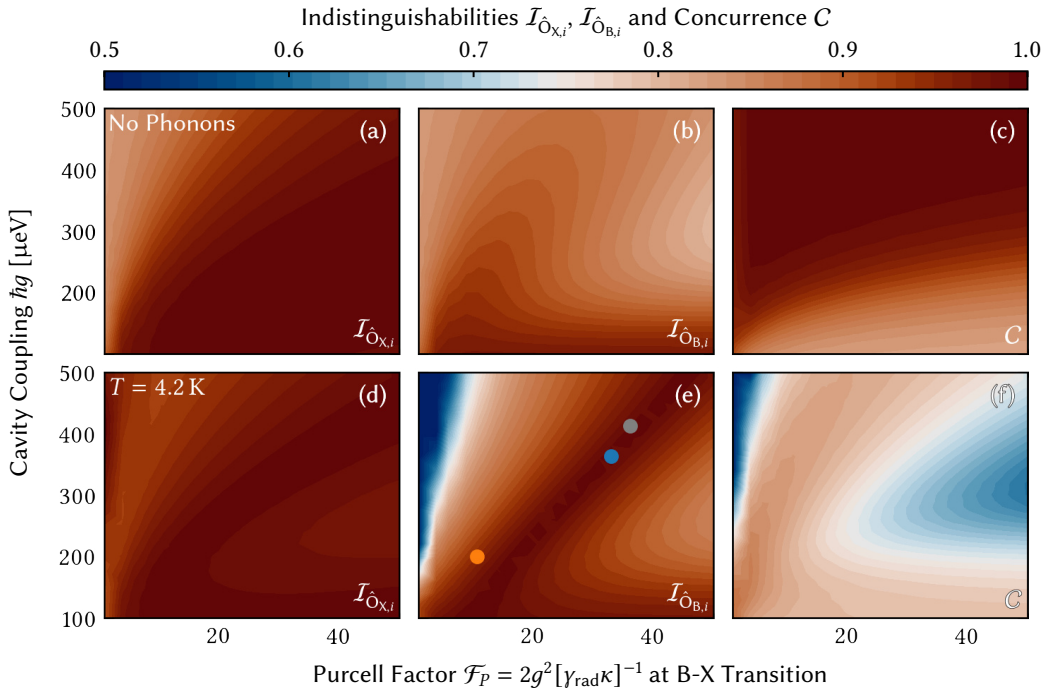

Figure 6.10: Quantum properties with active electron-phonon coupling contrasting approaches using the regular von-Neumann equation with no electron-phonon interactions in panels **(a-c)** and the polaron master equation in panels **(d-f)**. The latter simulations are conducted at a temperature of $T = 4.2\,\mathrm{K}$. Across these analyses, the achievable cavity parameters identified by the Maxwell optimizer are indicated by colored dots, highlighting that such high raw coupling values can be implemented in a real system. The orange and blue dots correspond to simulations depicted in Fig. 6.16, while the gray dot corresponds to Maxwell simulations guided to maximize the Purcell enhancement while remaining within the boundaries indicated by the simulations of the quantum dot system, corresponding the the spectrum in Fig. 6.5, panel (a). *Reproduced and enhanced from Bauch et al. [174].*

raw coupling values, while the concurrence is maximized for larger couplings. This is because larger coupling values induce Rabi oscillations, diminishing the indistinguishability due to the re-excitation of the system. For the concurrence, however, this has the opposite effect. When including electron-phonon coupling at $T = 4.2\,\mathrm{K}$, a sharp resonance in the biexciton-to-exciton indistinguishability is observed. The concurrence also shows a similar resonance, unfortunately at different parameters. This further supports the limitation that not all properties can be efficiently maximized simultaneously. Since increasing the indistinguishability is most important for applications in quantum information processing, choosing a parameter set at which the indistinguishabilities are maximized is key.

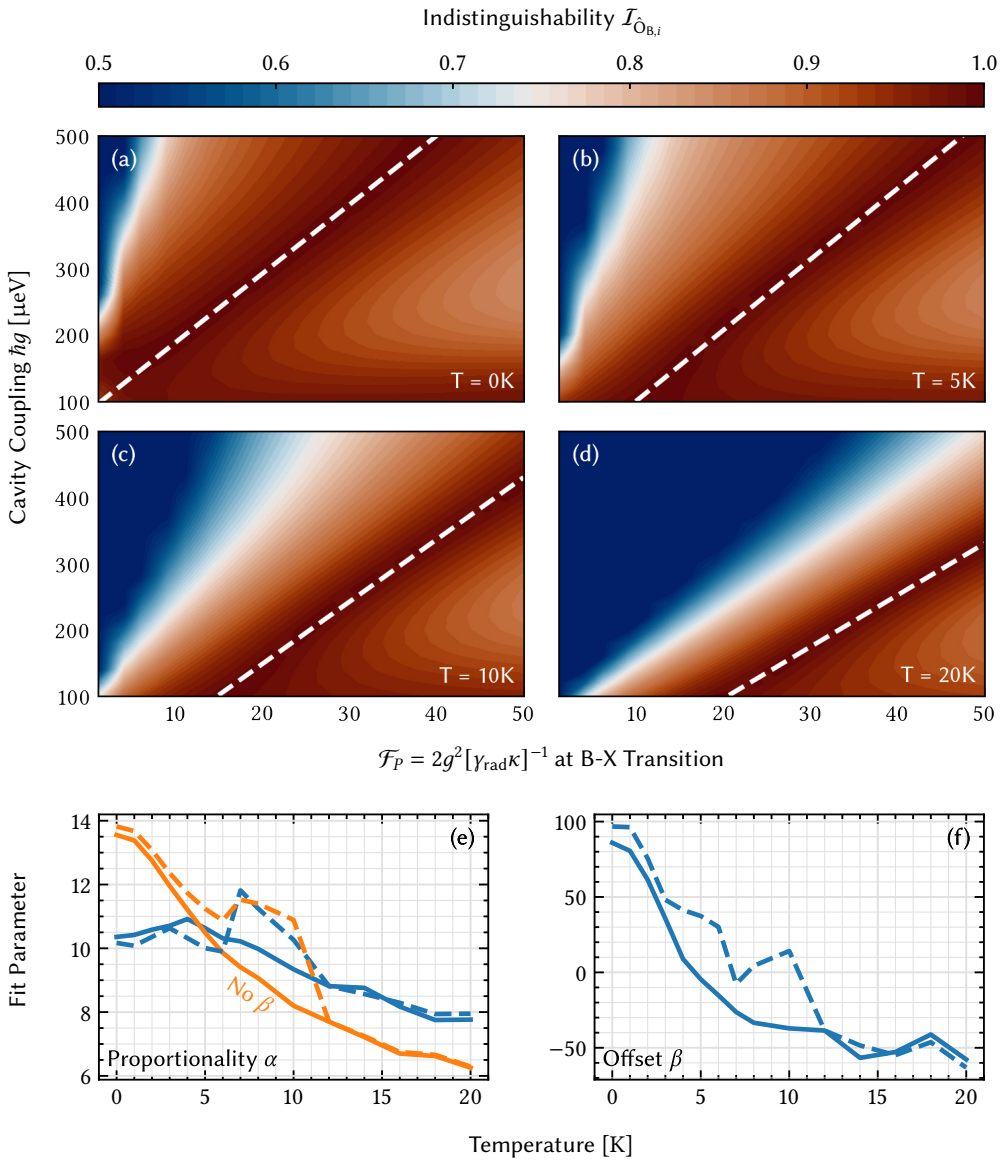

Figure 6.11: Quantum properties at different temperatures. (a-d) Indistinguishability of the biexciton photon at four temperatures, with all calculations performed using the polaron master equation. The maximum indistinguishability at each temperature is fitted using $\mathcal{I}_{\hat{O}_{B,i}}(\mathcal{F}_P) = \alpha\mathcal{F}_P + \beta$. **(e,f)** Dependencies of $\alpha(T)$ and $\beta(T)$ derived from these fits (solid lines). Additionally, panel (e) includes the fitting parameter $\alpha'(T)$ for an alternative linear function f', where $\beta' = 0$ for all temperatures. Additionally, fits using all three properties are compared (dashed lines). The values for α and β can then be used by the Maxwell optimizer to ensure the resulting cavity lies on the optimal line for a given temperature. *Reproduced and enhanced from Bauch et al. [174].*

It remains crucial to examine how changes in temperature affect the dynamics of this behavior. Furthermore, Fig. 6.11 shows the same simulations as Fig. 6.10 for different temperatures in panels (a-d). These panels show the indistinguishability of the biexciton-to-exciton photon only, as the indistinguishability of the exciton-to-ground photon is inherently high, and the concurrence is taken as is, accepting that it may be slightly lower than optimal.

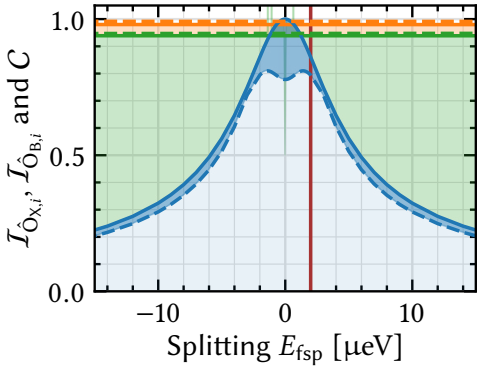

Figure 6.12: Quantum properties for different fine structure splittings for the phonon free case (solid lines) and for a solution using the polaron master equation at $T = 4.2$ K (dotted lines). The indistinguishabilities of the exciton photon using the operator $\hat{O}_{X,i}$ (orange) as well as the biexciton photon using $\hat{O}_{B,i}$ (green) remain constant, while the concurrence (blue) tends to drop and plateau, similar to Fig. 5.5. The red line indicates the fine structure splitting used for the main results. *Reproduced from Bauch et al. [174].*

A shift of the resonance is observed with rising temperatures; the optimal cavity parameters drift to slightly lower raw couplings, but higher Purcell enhancement, indicating higher Q cavities. The white dashed lines indicate a linear fit through the maximum of the indistinguishability. The fit uses $\mathcal{I}_{\hat{O}_{B,i}}(\mathcal{F}_P) = \alpha\mathcal{F}_P + \beta$, where α is the slope and β is the offset. Notably, only the single photon indistinguishability originating from the Purcell enhanced biexciton-to-exciton transition is used for the optimization, since the indistinguishability from the exciton-to-ground transition remains high throughout the entire parameter range investigated.

Panels (e,f) display the temperature dependent parameters $\alpha(T)$ and $\beta(T)$ (blue lines). Notably, panel (e) also shows a fit when using $\beta(T) = 0$. Furthermore, when using all three properties instead of the single indistinguishability, similar behavior arises (dashed lines), although slightly different predictive capabilities of these curves emerge. This is because including the concurrence in the fit results in different optimal parameters for temperatures between 5 K and 10 K.

The concurrence of the biexciton photons is highly susceptible to the fine structure splitting energy, as previously introduced in Section 4.2.2. Moreover, Fig. 6.12 presents a scan of

the fine structure splitting energy for a set of cavity parameters that yield high values for all properties. Here, $\hbar g = 200\,\mu\text{eV}$ and $\hbar\kappa = 3\,\text{meV}$. The Purcell enhancement for this configuration is $\mathcal{F}_P \approx 10.5$. By comparison with Fig. 6.10, this results in high values for all properties in scenarios with and without electron-phonon coupling at low temperatures.

In Fig. 6.12, photons exhibit high indistinguishability of both photons as well as high values for their concurrence simultaneously, whereas for the previously introduced reference values in Fig. 5.5, the photons are either indistinguishable *or* entangled, but never both. The red line indicates the fine structure splitting used in the results of this chapter. Notably, further increasing the concurrence is possible by reducing the fine structure splitting, similar to the isolated biexciton case introduced earlier. However, in this scenario, active electron-phonon coupling does not reduce the concurrence as significantly for $|E_{\text{fsp}}| \gg 0$, while substantial reductions are observed for $E_{\text{fsp}} \approx 0$.

These findings also support that the previous results are close to the absolute maximum achievable with this configuration.

6.2.2 Optimal Case with Excitation of the States

This section synthesizes the insights from Chapter 5 and applies the excitation schemes to the cavity configuration that yields the best possible photon properties. Specifically, resonant excitation, QCSS excitation, and SUPER excitation are applied to the optimal parameter set from Fig. 6.10 at $T = 4.2\,\text{K}$.

For the resonant excitation, a $\mathcal{A}_0 = 6.75\pi$ pulse is used to excite the biexciton state. This configuration offers near unity excitation fidelity for the isolated biexciton without a cavity. For the QCSS excitation, the electronic system and the cavity are detuned such that no significant overlap between the cavity mode and the electronic states occurs initially. Due to the broad cavity mode, the initial detuning is set to a large $10 \cdot E_{\text{bind}}$. The duration of the QCSS is set to 200 ps, resulting in shift speed of 50 μeV/ps. The excitation pulse is then the same as for the resonant excitation.

For the SUPER excitation, a pulse that optimally excites the biexciton is determined using a simple gradient descent optimizer. As Fig. 5.15 demonstrates for the exciton case, there are numerous areas of resonance, which are also strongly dependent on the energy configuration of the system as well as the pulse lengths. The configurations in Fig. 6.13 result in a swing-up of the biexciton population, achieving an excitation fidelity close to unity for a system without a cavity. Notably, these parameters are established for a phonon-free

and isolated system with no cavity present. Hence, excitation fidelities including these features are slightly lowered. When exciting an exciton using SUPER, a virtual phonon-free excitation is possible due to the strong pulse amplitudes. In the case of the biexciton however, this is not true anymore, since the overlap of the electronic resonances results in population of the individual excitons. This significantly reduces the excitation fidelity. Nevertheless, SUPER is still used for comparison purposes.

τ [ps]	A_1 [meV]	A_2 [meV]	E_1 [meV]	E_2 [meV]
1	16.235	13.025	793.592	797.190
2	8.124	4.125	797.400	780.822
3	4.392	2.866	790.185	796.040
4	3.701	2.743	790.044	795.710
5	3.063	2.709	790.208	795.628
6	2.409	2.538	797.400	769.963
7	2.207	1.679	797.400	795.650
8	2.334	2.552	795.524	790.537
9	1.995	1.901	797.400	795.348
10	1.835	1.395	797.289	796.894

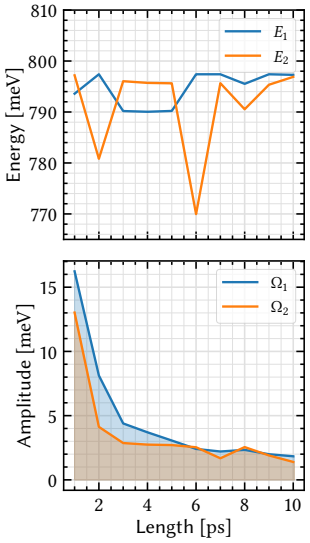

Figure 6.13: SUPER parameters to excite an isolated biexciton in a lossless case with no electron-phonon coupling. The configuration for each fixed pulse width has four degrees of freedom. A global optimizer is employed to find suitable pulse amplitudes and frequencies in a predefined range below the biexcitons two photon resonance. The pulse amplitude is unbound, while the pulse energy is bound by $[0.77, 0.7974]$meV to ensure both pulses are energetically far below the electronic transitions. The parameters are visualized in the graphs on the right.

Different pulse lengths for the respective excitation schemes are displayed in Fig. 6.16. Two scenarios from Fig. 6.10 are investigated, marked with colored dots. Specifically, a scenario with lower raw coupling where $\hbar g = 200\,\mu$eV and $\hbar\kappa = 3\,$meV, resulting in a Purcell enhancement of the biexciton-to-exciton transition of $\mathcal{F}_P \approx 10.5$, is compared to a scenario with very strong raw coupling where $\hbar g = 363\,\mu$eV and $\hbar\kappa = 3189\,\mu$eV, resulting in a Purcell enhancement of $\mathcal{F}_P \approx 33$. The latter configuration remains achievable in realistic implementations, as supported by the Maxwell simulations of the cavity.

For a pulse directly exciting the biexciton from the ground state, as investigated in [174],

Width τ [ps]	A_1 [meV]	Pulse Area $\mathcal{A}_1[\pi]$
1	1.367	3.314
2	0.907	4.400
3	0.732	5.325
4	0.627	6.078
5	0.557	6.750
6	0.506	7.356
7	0.467	7.919
8	0.435	8.444
9	0.409	8.938
10	0.388	9.405

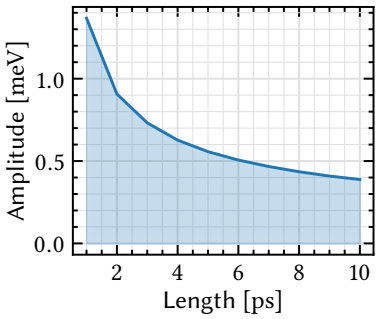

Figure 6.14: QCSS and resonant excitation parameters to excite an isolated biexciton in a lossless case with no electron-phonon coupling. The pulse areas are relative to the exciton, which is why the biexciton requires multiple πs of excitation area. The pulse amplitude is visualized in the graph on the right.

the pulse

$$|\mathrm{B}\rangle\langle\mathrm{G}|\,\Omega(t) + \mathrm{H.c.} \tag{6.4}$$

generates biexciton population without intermediate population of the excitons, resulting in a direct $|\mathrm{G}\rangle \rightarrow |\mathrm{B}\rangle$ transition. This approach is also used in the respective literature [74] and results in ideal excitation of the biexciton by analytically evaluating the excitation through the exciton cascade. Here, calculating the pulse areas directly translates into the respective excitation. With this excitation method, both cavity configurations investigated yield high values for the calculated properties, most notably for short pulses.

When using the excitation through the exciton cascade, where the pulse

$$|\mathrm{X}\rangle\langle\mathrm{G}|\,\Omega(t) + |\mathrm{B}\rangle\langle\mathrm{X}|\,\Omega(t) + \mathrm{H.c.} \tag{6.5}$$

is employed, resulting in a $|\mathrm{G}\rangle \rightarrow |\mathrm{X}\rangle \rightarrow |\mathrm{B}\rangle$ transition. Here, the pulse area does not directly translate into the corresponding excitation, as the pulse respective pulse amplitude has to be calculated for the cascade instead of a single transition. The resulting pulse amplitudes and the translation into the pulse area are provided in 6.14. A more drastic reduction of the quantum properties occurs because the broad cavity mode leads to intermediate exciton population decay, reducing all properties. The latter configuration is optimized to maximize the indistinguishabilities at $T = 4.2\,\mathrm{K}$, and values with electron-phonon coupling

significantly exceed their reference values without electron-phonon coupling, reflecting the results of the previous sections. In contrast, lower values are observed for the second scenario due to the stronger raw coupling, which significantly hinders the emission process, resulting in lower quantum properties. Here, the values fall below the reference values for emission from an isolated biexciton, visualized in Fig. 6.16 by the hatched areas.

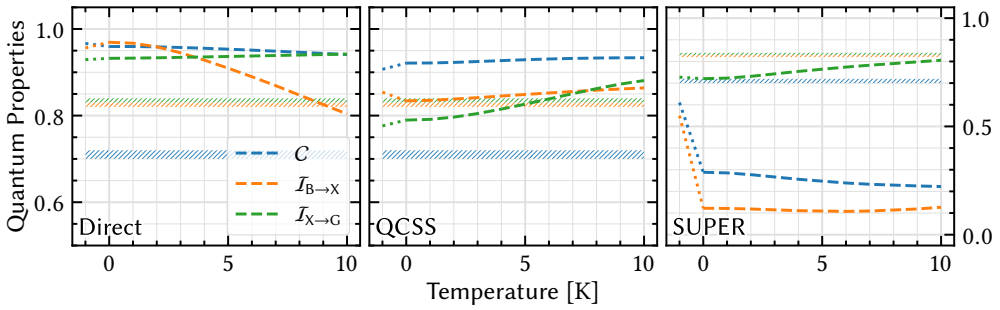

Figure 6.15: Quantum properties for different temperatures at a finite excitation pulse length of $\sigma = 4$ ps using the polaron master equation. Panel **(a)** demonstrates the QCSS Excitation and constrasts the resonant two photon excitation in panel **(b)** as well as the SUPER excitation in panel **(c)**. The dotted lines represent the transition from a system with no electron-phonon coupling to electron-phonon coupling at various temperatures. Both cases use the respective excitation method. Note, that SUPER is visualized at a different scale compared to the direct resonant and QCSS excitation. *Reproduced and enhanced from Bauch et al. [174].*

The interesting part comes with using different excitation methods. As previously described in Section 5.4.1, the SUPER scheme results in a near phonon-free excitation for a two-level system, due to the strong pulses surpassing the spectral density of the phonons. However, for the biexciton, this drastically changes. Even in the phonon-free case, the broad cavity mode induces strong mixing of the excitation and decay processes, because the detuning induced by the already strong pulses is insufficient. Furthermore, the strong pulses cause off-resonant excitation, which translates directly into undesired cavity population. These processes combined significantly degrade all properties in both scenarios, leading to highly unpredictable behavior. For SUPER pulses longer than 2 ps, the quantum properties diminish below their reference values due to the aforementioned processes. In this specific case, SUPER is not suitable for excitation. Notably, the pulses use excitation paths through the exciton cascade and not the direct ground-to-biexciton transition, meaning the benchmark for comparison is the cascaded excitation.

Using the QCSS excitation performs significantly better than SUPER in this case. Here, a very

fast shift is employed, which shifts all electronic states by 10 meV over a duration of only 20 ps. However, the simple resonant and direct excitation still surpasses the QCSS excitation. This occurs because the emission and decay of the electronic states happen on timescales similar to the shift of the electronic states, even though the shift is already very fast and possibly in an unrealistic regime. Nevertheless, the QCSS uses the cascaded excitation, and the comparison values (panels (c,d)) are greatly surpassed, especially for longer pulses. Moreover, the quantum properties plateau for longer pulse lengths instead of diminishing further as in the resonant cascaded excitation. These investigations demonstrate that QCSS excitation is suitable for the scenarios investigated, strongly outperforming SUPER.

Concluding, the SUPER excitation scheme cannot be utilized to a viable degree in the investigated scenarios. However, the QCSS excitation method demonstrates potential for application. Nevertheless, the gain is negligible in most cases due to the necessity for an extremely fast electronic shift to effectively separate the timescales of the emission and the shift. Without achieving this separation, no significant improvement is observed. If the lifetime of the states were longer, QCSS excitation would be highly beneficial, as the issues with SUPER would persist, though it would perform slightly better under these conditions.

The excitation using a 4 ps pulse with variable temperatures is illustrated in Fig. 6.15. Panels (a-c) compare direct resonant excitation, QCSS excitation, and SUPER excitation, respectively. Notably, increasing the temperature is less detrimental to the concurrence when using QCSS excitation compared to direct resonant excitation, although the values are generally lowered. For SUPER excitation, the concurrence exhibits a similar trend, while the indistinguishabilities are significantly reduced.

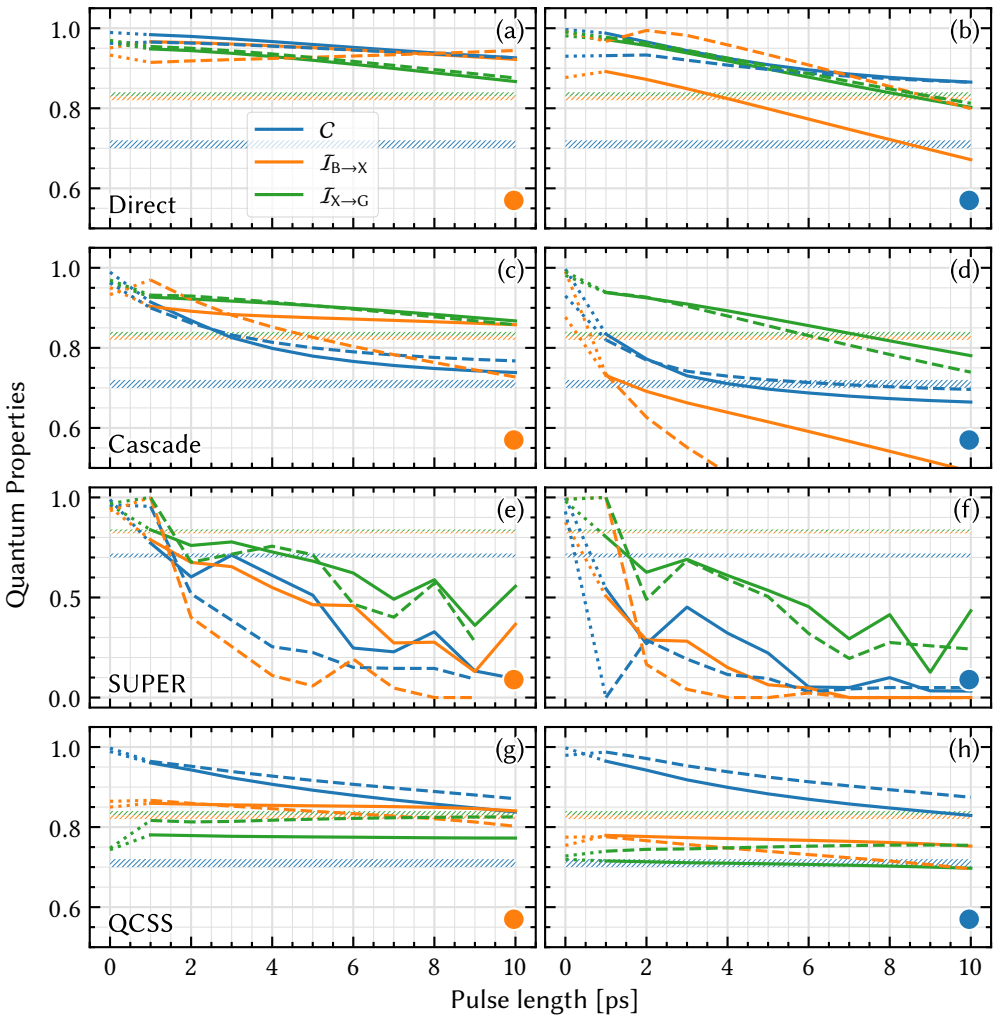

Figure 6.16: Quantum properties for different excitation pulse lengths for the phonon free case (solid lines) and for a solution using the polaron master equation at $T = 4.2\,\mathrm{K}$ (dashed lines). Panels **(a,b)** demonstrate the resonant two photon excitation using a direct $|\mathrm{G}\rangle \longrightarrow |\mathrm{B}\rangle$ transition and contrast the cascaded excitation with $|\mathrm{G}\rangle \longrightarrow |\mathrm{X}\rangle \longrightarrow |\mathrm{B}\rangle$ in panel **(c,d)**. SUPER excitation is displayed in panels **(e,f)** and QCSS excitation in panels **(g,h)**. A pulse width of $\tau = 0$ represents the reference case, starting the simulation in the biexciton state. The leftmost panels show results for $\hbar g = 200\,\mu\mathrm{eV}, \hbar\kappa = 3\,\mathrm{meV}$, marked with an orange dot in Fig. 6.10. The rightmost panels show results for $\hbar g \approx 363\,\mu\mathrm{eV}, \hbar\kappa \approx 3189\,\mu\mathrm{eV}$, marked with a blue dot in Fig. 6.10. The hatched areas represent the respective reference values for the indistinguishability (orange/green) and concurrence (blue). The dotted lines mark the transition from staring in the biexciton state to the respective pulsed excitation. *Reproduced and enhanced from Bauch et al. [174].*

6.3 Concluding the Purcell enhanced two photon emission

The previously established biexciton system extended further. The quantum dot is configured to emit at the telecom-C band at 1550 nm. A cavity is employed to enhance the biexciton-to-exciton transition, aiming to decrease the lifetime of the biexciton. As a result, the indistinguishabilities of the emitted photons is greatly increased. Investigations reveal, that also enhancing the exciton decay further increases both the indistinguishability of the exciton-to-ground photon and the repetition rate of the process. Therefore, a cavity with broad spectral Purcell enhancement is required.

A physical implementation that fulfills these criteria is the circular Bragg reflector, composed of circular arrangements of semiconductor mirrors. Maxwell simulations of these structures ensure their physical implementability, confirming that the cavities used in microscopic simulations are feasible in experimental implementations. The biexciton state is either fully populated at the start of the simulations or initialized using various excitation methods, including the aforementioned QCSS and SUPER methods. When starting in the ideal, fully excited biexciton state, a low-Q cavity with strong raw coupling significantly increases the indistinguishabilities of both the biexciton-to-exciton and exciton-to-ground photons, while maintaining high two-photon concurrence. This setup generates photons that are individually highly indistinguishable and entangled, overcoming an intrinsic limitation of the biexciton system.

Electron-phonon coupling is employed to further optimize the system, leveraging constructive phonon enhancement. These scenarios improve and support the results obtained from a lossless system. When the excitation process is included, the quantum properties remain high, especially for short pulse lengths. The maintenance of the indistinguishability from the Purcell enhanced biexciton-to-exciton transition marks the central result of this chapter and the underlying work [174]. Advanced excitation schemes such as the SUPER excitation do not provide a substantial advantage over a simple, resonant excitation. Moreover, employing the QCSS excitation introduced in the previous chapter provides a slight benefit for specific configurations, most notably when using long pulses and a cascaded excitation. Because of the spectrally broad cavity mode, excitation using short, yet spectrally narrow pulses is optimal.

Resonator setups employing higher raw cavity couplings may produce photons with increased concurrence, albeit with a slight reduction in indistinguishabilities. Future numerical research aims to optimize the ideal structure that achieves unity values for the desired properties, including the emission probabilities. Given the numerous degrees of freedom involved, this is a substantial undertaking, likely to span multiple research papers and close collaborations with Maxwell simulations.

Interim Summary

A circular Bragg reflector and a quantum dot are used to theoretically investigate the emission of photons at telecom wavelengths, aiming to circumvent the intrinsic limitations on single photon indistinguishability of the biexciton system. The optimal resonator configuration for generating highly indistinguishable photons that are also strongly entangled is achieved using a cavity with low Q values, broad emission resonance, and strong raw light-matter coupling. This setup allows the optimization of both indistinguishabilities and the concurrence towards unity values. In realistic implementations with electron-phonon coupling, finite excitation pulses and non-zero fine structure splittings, the concurrence is slightly reduced and the indistinguishabilities of both photons remain high, with values of $\mathcal{I} > 95\%$. With rising temperatures, the indistinguishability remains high, whereas the concurrence, due to its significant dependency on dephasing, diminishes rapidly.

Time-Bin Quantum Correlations in Deterministic Photonic Cluster States

7

Up to this point, the electronic system within the quantum dot was specifically focused on excitons and biexcitons. The introduction of an optical resonator to Purcell enhance one or more of the electronic transitions has facilitated the rapid emission of high quality photons. These photons exhibit various characteristics, such as high indistinguishability and strong entanglement, precisely benchmarking their quantum properties.

This chapter explores an alternative approach utilizing stacked quantum dots, which induces the mixing of two distinct sets of electronic states [177, 254]. This results in the formation of spin-hole trions [177, 255, 256] which are interconnected through intrinsically arising transitions, forming a Λ-type energy configuration [257]. The Λ-system, named for its resemblance to the Greek letter, can emit photons that are entangled in time rather than polarization. This system is optically addressable, allowing for the manipulation of states through optical means. While other methods, such as using magnetic fields, exist for state manipulation [33, 258], this work focuses on optical manipulation. The underlying quantum dot composition ensures the deterministic addressability of this structure [259, 260]. The resulting emission patterns form complex structures of time-entangled photons [181, 182, 259, 261]. These photons are best described by a set of interconnected nodes, forming a graph.

7.1 Graph States

A graph is a structure comprising nodes, each of which can have various connections to other nodes. For instance, a parent node may connect to two child nodes, with each child node potentially having none, one, or two child nodes. This configuration results in a binary tree graph, a common data structure in computer science. Another example

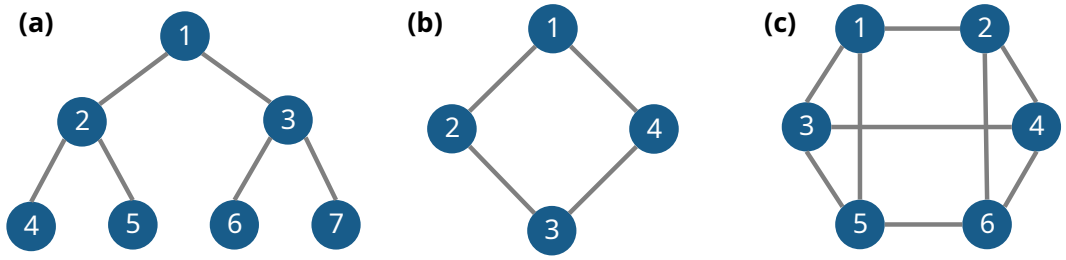

Figure 7.1: Different graphs constructed with nodes and connections featuring a binary tree graph in panel **(a)**, a circular graph in panel **(b)**, and an interconnected hexagonal graph in panel **(c)**.

involves multiple nodes connected to form loops or having multiple connections. These examples are illustrated in Fig. 7.1.

Graphs can be characterized by numerous figures of merit, one of which is colorability. A graph that can be colored with N different colors, such that no adjacent nodes share the same color, is termed an N-colorable graph.

This work focuses on the generation of photonic cluster states, describable using an N-colorable graph. In these graphs, each node represents a photonic particle, and each connection signifies its entanglement with neighboring elements. Different connections can contribute to various aspects of entanglement, resulting in what is known as a *graph state* [184, 233, 260]. The experimental implementation of entangled graph states is a significant area of interest in the literature [235, 262–266]. The photonic particles in this study are photonic qubits. Each qubit can represent a maximum of two photons, where the presence of the first photon denotes a logical zero, and the presence of the second photon denotes a logical one [17]. Although other conventions exist, even with higher number of photons forming complex qudits [267], this work adopts this specific representation.

Among the various graph states explored in the literature, Greenberger-Horne-Zeilinger (GHZ) states have received significant attention. In this state, all particles are entangled with a central particle, as illustrated in Fig. 7.2, panel (a) [268, 269]. Another state of interest is the one-dimensional linear cluster state, where all nodes are connected to at most two neighboring nodes. This forms a two-colorable, linear graph of entangled photonic qubits, as depicted in Fig. 7.2, panel (b). These one-dimensional linear cluster states serve as the foundation for the investigations presented in the following chapter and are comprehensively analyzed in Bauch et al., *Time-bin entanglement in the deterministic generation*

of linear photonic cluster states, [187], with related data accessible via the corresponding Zenodo archive [270].

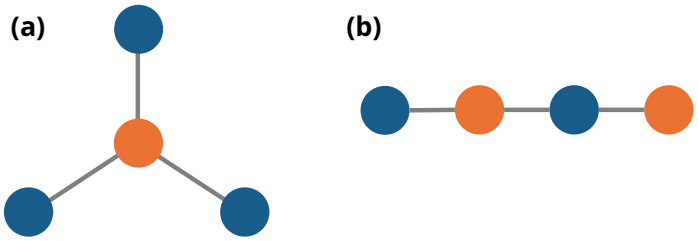

Figure 7.2: Different primitive cluster states including a Greenberger–Horne–Zeilinger (GHZ) state in panel **(a)** and a simple linear cluster state in panel **(b)**. Both states belong to a subset of two-colorable graph states and can be further processed to generate higher-order graph or cluster states [271].

Graph states have numerous applications in quantum information processing [272]. Depending on the specific protocol, high-dimensional photonic graph states may be required to achieve the desired functionality [273]. For example, in quantum computing, graph states are used as a resource for one-way quantum computation, where the computation proceeds through a series of measurements on an entangled resource state. In quantum communication, graph states enable the creation of complex entangled networks that facilitate secure information transfer and distributed quantum protocols. The versatility and robustness of graph states make them indispensable for advancing various quantum technologies, illustrating the necessity for generating high-dimensional photonic graph states in practical quantum information systems [256, 273].

7.2 Time Bin Entanglement

A graph state, or cluster state, necessitates at least two entangled particles [184, 272, 274, 275], with polarization entanglement being most commonly utilized [76]. This has been previously demonstrated in the earlier chapters, although the resulting emission was not explicitly referred to as a graph state, despite fitting the technical definition. However, as the number of particles increases, maintaining high polarization entanglement becomes increasingly challenging, particularly when photons are transmitted through optical fibers. Losses quickly degrade polarization entanglement, significantly limiting the size of the graph state that can be achieved. This limitation is addressed by using time entanglement [178, 275, 276]. With photons are entangled in time, the degradation of

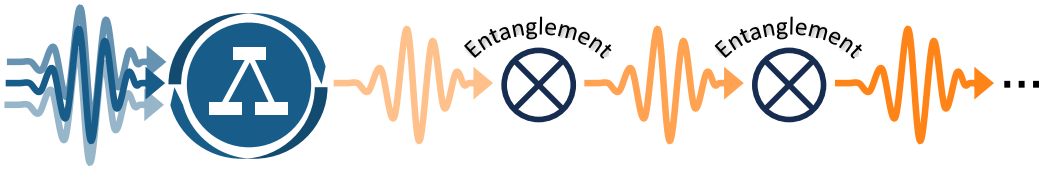

Figure 7.3: Schematic emission of perfectly distinguishable and time bin entangled single photons from a repeatedly triggered single photon emitter. The excitation pulses, depicted in blue, activate the source. These pulses initiate photon emissions, depicted in orange, or induce changes in state coherences. The result is the emission of photons with high degrees of temporal entanglement. *Reproduced from Bauch et al. [187].*

polarization coherence is avoided, resulting in longer entanglement lifetimes. Consequently, temporal entanglement is more suitable for creating graph states with a larger number of particles.

To generate photonic graph states, a deterministic photon emitter is essential. In this work, a stacked quantum dot structure is used as the reference physical system for the numerical investigations. The configuration merges the electronic properties of two individual quantum dots, forming a spin-hole trion. The ground states of this trion can be excited, similar to an exciton, and emit a photon through radiative decay. Due to slight intentional positioning mismatches between the quantum dots, the wave functions of the ground states mix, resulting in a combined emitter with a Λ-shaped energy structure, allowing either ground state to be excited for photon emission, while the ground state populations can be rotated through an intrinsically emerging transition state. Other potential systems for this emitter include biexcitons with dark exciton photon storage, color centers [257], and vacancies. Few-photon graph states have been experimentally demonstrated [272].

The emitter, schematically illustrated in Fig. 7.3, is repeatedly triggered using sech-shaped pulses, chosen for their analytical tractability based on prior research. While Gaussian pulses could be used without significantly altering the results, sech pulses are employed here to maintain consistency with earlier investigations.

The emitter generates photons, and by carefully controlling the phase at which the photons are emitted, strong entanglement between the individual timed emissions is achieved. The time slots at which the distinct temporal separation between the photons occurs are referred to as *time bins* [179, 183, 237]. In this work, two photon emission cycles constitute a photonic qubit. Correlations between these qubits are then evaluated numerically. The

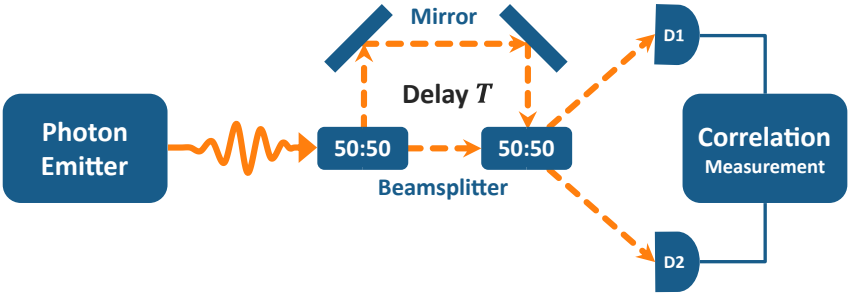

Figure 7.4: Simplified illustration of a possible measurement process for time bin entangled photons. Photons produced by an emitter are directed to a beam splitter, which divides the incoming photon stream into multiple side branches. Each branch introduces a time delay matching integer multiples of the bin length T_{bin}. Subsequently, photons are recombined at a final beam splitter and channeled towards photodetectors. The correlation measurements performed at this stage provide insights into the photon correlations.

time bins are exemplary given as

$$t_0 < t_1 < t_1 + T_{\text{bin}} < 2T_{\text{bin}} < t_2 < t_2 + T_{\text{bin}} < 4T_{\text{bin}} < t_3 < t_3 + T_{\text{bin}} < 6T_{\text{bin}} < \dots , \tag{7.1}$$

with t_i denoting the beginning of the ith time bin and T_{bin} defining the length of the individual time bins.

Since the emission of individual photons originates from a simplified exciton-like two-level system, as visualized in Fig. 7.5, the indistinguishabilities and purities of the emitted photons are intrinsically high. This has also been confirmed by other studies [176, 277]. Similarly, the emission probabilities are close to their maximum values. The emission of an individual photon takes approximately 4 ns, as no cavity is used to enhance the emission, with the radiative decay $\gamma_{\text{rad}} = 1.3\ \mu\text{eV}$ being the sole cause of the emission.

In an experimental setup, time bin correlations can be measured using a standard beam splitter configuration, similar to that employed in a Hong-Ou-Mandel (HOM) interference measurement. Instead of directly measuring photon correlations, multiple branches are implemented to induce a time delay that exactly matches the length of a time bin. This concept is illustrated in a simplified manner in Fig. 7.4. For the case of a linear graph state, two detectors can then measure coincidence counts for the photons, providing information on the time bin correlations [179]. For more complex graph states, additional detectors and more sophisticated delay setups may be required to accurately measure the correlations.

Projecting this setup onto photonic qubits rather than single photons allows for the measure-

ment of qubit correlations. This approach is explored numerically in Section 7.6, where the stabilizers of the graph states are evaluated. By assessing the temporal entanglement of the photonic qubits, the effectiveness of the entanglement generation process is determined.

In practical terms, the experimental setup involves splitting the photonic stream into different paths, where each path introduces a controlled time delay. These delays are engineered to match the intervals between the time bins. Therefore, the temporal separation of the photons is maintained, and the entanglement properties can be measured accurately. Coincidence counting between the detectors provides a direct measure of the temporal correlations, thereby verifying the entanglement of the photonic qubits.

For more intricate graph states, where the complexity of the state increases with the number of nodes and connections, a more elaborate arrangement of beam splitters and detectors is necessary. Each detector in such a setup would correspond to different nodes of the graph, and the timing of the detections would reflect the entanglement properties of the entire state.

By using this method, one can effectively measure the entanglement properties of photonic qubits, thus enabling the practical implementation of photonic graph states for quantum information processing applications. This detailed approach ensures that the experimental setup can accurately capture the temporal entanglement, providing a robust foundation for further experimental and theoretical investigations into complex photonic states.

7.3 Extended Λ System

In the previous section, the emitter was introduced, showcasing a Λ-shaped energy structure through the mixing of two individual spin-hole trions. The system is illustrated in Fig. 7.5. The quantum dots, figuratively represented by $|\mathrm{QD}_1\rangle$ and $|\mathrm{QD}_2\rangle$, have individual ground states $|\mathrm{G}_1\rangle$ and $|\mathrm{G}_2\rangle$. These states can be excited through their respective *cycling transitions* using Gaussian or sech-shaped pulses. In this study, only one of the excited states is utilized for emission, hence only one cycling transition is highlighted. Nevertheless, both excited states, $|\mathrm{X}_1\rangle$ and $|X_2\rangle$, undergo radiative decay with a rate γ_{Cyc}. This decay mechanism, introduced via a Lindblad rate, is consistent with the methodology used in the previous chapter.

The ground states are separated by a splitting energy Δ_{GS} and are coupled to a common set of transition states. Within this framework, there are two transition states: a target

transition and a loss transition. Population caught in the loss transition state is lost in subsequent cycles when no relaxation path of the transition into the ground states is included through e.g. radiative loss. The occupation of the ground states can be represented on a Bloch sphere. Applying a sech-shaped pulse to the ground-to-transition-state transition results in rotations within this Bloch sphere, allowing for both the population of the ground states and their phase to be manipulated. This mechanism ultimately enables the system to emit time-entangled photons.

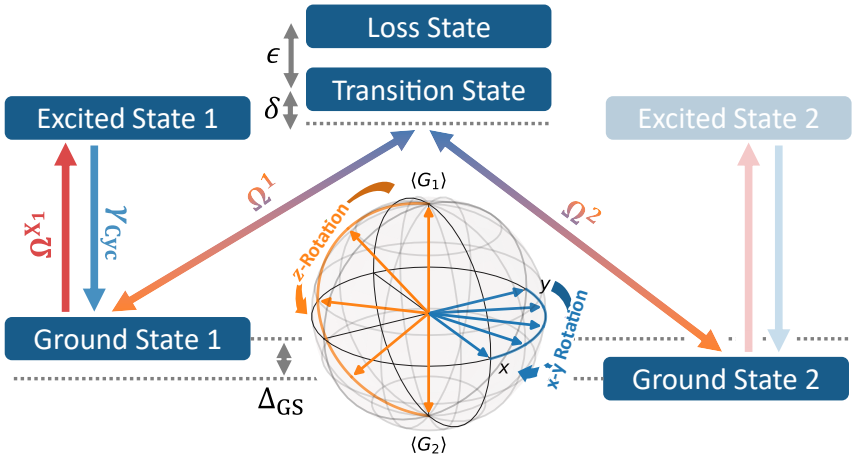

Figure 7.5: Λ system energy structure with two distinct ground states $|G_1\rangle$ and $|G_2\rangle$. The ground states are coupled through a target transition and loss transition state and separated by the splitting energy Δ_{GS}. The transitions are accessible through the optical pulses Ω^i with $i \in \{1, 2\}$. Each ground state can be individually excited into their corresponding excited states $|X_i\rangle$ through the pulse-driven cycling transition Ω^i. The excited state may then radiatively decay with rate γ_{Cyc}. Inset is a Bloch representation of the systems rotations. *Reproduced from Bauch et al. [187].*

The two individual ground states of the underlying electronic system of the quantum dot form a coherent superposition state due to their intrinsic coupling, effectively creating a two-level system for each transition. The use of sech-shaped pulses is particularly advantageous due to their analytical tractability and prior application in related studies. Although Gaussian pulses can be employed, sech-shaped pulses are chosen here to maintain consistency with previous research and to exploit their analytical benefits.

The radiative decay from the excited states to the ground states occurs at the rate γ_{Cyc} using $\hat{O} = \sqrt{\gamma_{Cyc}}\,|G\rangle\langle X_i|$ and the Lindblad contribution defined in Eq. (2.11). This decay process is critical for the emission of photons and is incorporated into the model using Lindblad operators. The separation between the ground states, Δ_{GS}, provides the necessary energy

difference to facilitate the transitions.

The Hamiltonian governing the dynamics of this system is given by

Equation 7.2

$$\mathcal{H}_0 = \sum_{i\in\{1,2\}} E_i \left|\mathrm{X}_i\right\rangle\!\left\langle\mathrm{X}_i\right| + \sum_{s\in\{\mathrm{T},\mathrm{U}\}} E_s \left|s\right\rangle\!\left\langle s\right|$$
$$\mathcal{H}_1 = \sum_{i\in\{1,2\}} \left[\left|\mathrm{G}_i\right\rangle\!\left\langle\mathrm{X}_i\right| \Omega^{\mathrm{X}_i}(t) + \left(\left|\mathrm{G}_i\right\rangle\!\left\langle\mathrm{T}\right| + \left|\mathrm{G}_i\right\rangle\!\left\langle\mathrm{U}\right|\right) \Omega^{i}(t) + \mathrm{H.c.}\right] ,$$

where $|\mathrm{G}_i\rangle$ represents the ground states, and $|\mathrm{X}_i\rangle$ denotes the respective excited states, with $\Omega^{\mathrm{X}_i}(t)$ as the sech-shaped pulse driving the excitation of these transitions. The state $|\mathrm{X}_1\rangle$ is specifically utilized for photon emission, thus only $\Omega^{\mathrm{X}_1}(t)$ is considered for this purpose. Additionally, the Hamiltonian includes transitions from the ground states to a target state $|\mathrm{T}\rangle$ and an unwanted state $|\mathrm{U}\rangle$, both driven by the pulse $\Omega^{i}(t)$. The transition pulse facilitates population and coherence transitions between the respective ground states.

During the emission process, the system undergoes a series of coherent rotations of the ground state populations, indicated using the Bloch sphere representation in Fig. 7.5. By precisely controlling the phase and population of the ground states through tailored pulse sequences, time-entangled photons are generated. The entanglement arises from the coherent superposition of the ground states, with each transition state contributing to the entanglement properties.

This Λ-shaped emitter, with its ability to emit time-entangled photons, serves as a robust platform for generating complex photonic states. The flexibility in pulse shaping and the intrinsic properties of the quantum dots ensure high-quality photon emission, making it suitable for advanced quantum information processing applications. The detailed control over the emission process, facilitated by the sech-shaped pulses, allows for precise manipulation of the quantum states, thereby enabling the generation of highly entangled photonic states with desirable properties.

7.4 Linear Cluster State Emission Protocol

The graph state investigated in this chapter is a one-dimensional linear cluster state. This state can be generated using the following protocol [254]:

- Start or prepare the system in $|\Psi\rangle = \frac{1}{\sqrt{2}}(|G_1\rangle + |G_2\rangle)$
- Step 1: Drive Ω^{X_1} using a π-pulse, followed by emission of first photon
- Step 2: Perform $R_\vartheta(\pi)$ through the Λ-System
- Step 3: Drive Ω^{X_1} using a π-pulse, followed by emission of second photon
- Step 4: Perform $R_\vartheta(\pi/2)$ through the Λ-System
- Repeat steps 1-4 N times
- Perform a final $\hat{Z}$ projection to decouple the emitter.

In this work, only steps 1-4 are investigated. Note, that even though a stacked quantum dot is used as the emitter in this chapter, the protocol to generate the specific cluster state is not limited to this system, so long as the spin rotations can be performed. An arbitrary rotation within the Bloch sphere of the two ground states is denoted by $\mathcal{R}_\vartheta(\Theta)$, where ϑ represents the angle in the x-y plane and Θ denotes the angle in the z direction. Compare Fig. 7.5 for a visual representation within the Bloch sphere. In this work, the x-y angle is part of the degrees of freedom and can be tuned by adjusting the phases of the pulses. Specifically, by adjusting the individual pulse phases ϕ_1 and ϕ_2 of the individual pulses Ω^1 and Ω^2, respectively, the angle of rotation in the x-y plane can be adjusted. This is explored in detail in Section 7.6.1. Furthermore, by adjusting the detuning Δ_i of the individual pulses Ω^i, the angle in the z-direction is tuned. Facilitating the z rotations is crucial for the implementation of the protocol. This aspect is investigated in Section 7.5.

All simulations depicted in this chapter begin with the initial state $|\Psi\rangle = \frac{1}{\sqrt{2}}(|G_1\rangle + |G_2\rangle)$, which is commonly achievable using a $\pi/2$ rotation through the Λ-system [254]. Following this initialization, steps 1 to 4 of the emission protocol are iteratively executed as many times as necessary. An example with three repetitions of the protocol is illustrated in Fig. 7.6. The transition pulses do not alter the state population, hence they are referred to as being *transitionless*. Notably, the electronic coherences, represented by the green and orange lines, approach zero after the application of the first cycling transition pulse. Although this may appear unconventional initially, the coherences are transferred to the emitted photons where

they reappear in the photon correlations. These correlations are subsequently analyzed using the time shifted correlation functions described in Section 7.6. The transfer of the coherences is essential for evaluating the temporal entanglement properties of the photonic emissions.

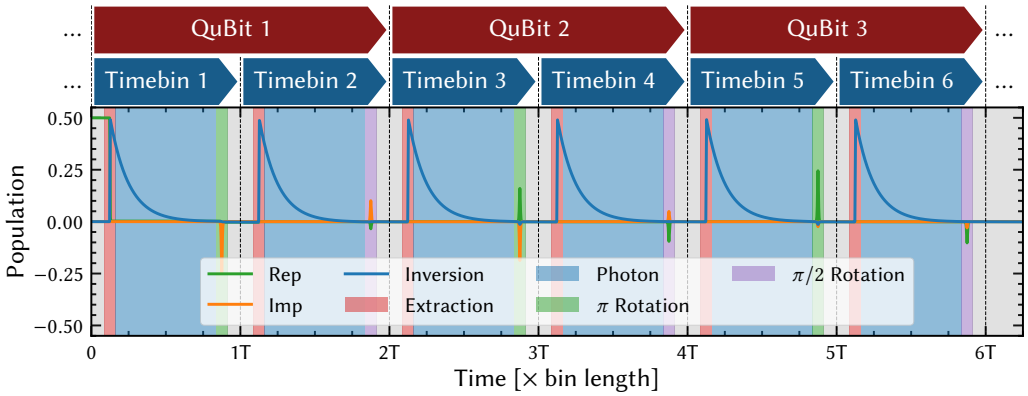

Figure 7.6: Time dynamics of the linear cluster state emission protocol calculated in a phonon free environment for hyperbolic-sec shaped transition and excitation pulses. The emission protocol is simulated until $t = 6T$. The individual photonic qubits are composed of up to two individual time bin photons. *Reproduced from Bauch et al. [187].*

7.5 Finding Optimal Rotations

Before achieving the results shown in Fig. 7.6, it is necessary to determine suitable pulse parameters such that the sech pulse accomplishes the desired rotations through the specified axis within the Bloch sphere representation. The total pulse area applied to both transitions is set to $\mathcal{A}_0 = \sqrt{\mathcal{A}_1^2 + \mathcal{A}_2^2} = 1\,\pi$, implying that the amplitudes of the individual pulses are $\mathcal{A}_{1,2} = 1/\sqrt{2}\pi$ due to the square-root scaling of the superposition state. The sign of all pulses is set to +1, indicating that the sign of the pulse envelopes $\mathrm{sign}[\Omega_0^i(t=0)]$ is equal for all i. This approach differs from some of the literature, where one of the pulses may be scaled by −1, resulting in an intrinsic phase shift of π for the respective pulse. For the latter scenario, the acquired state phase of the ground state superpositions $|1\rangle = \frac{1}{\sqrt{2}}(|G_1\rangle + |G_2\rangle)$ and $|2\rangle = \frac{1}{\sqrt{2}}(|G_1\rangle - |G_2\rangle)$ after the application of a sech-pulse are given by [177]

$$\Theta_1 = 2\mathrm{arctan}\left(\frac{\sigma}{\delta}\right) \quad \text{and} \quad \Theta_2 = 2\mathrm{arctan}\left(\frac{\sigma}{\delta - \epsilon}\right) . \tag{7.3}$$

Here, $\sigma = 1/\tau$ is the bandwidth of the pulse, where τ is the pulse width. In the following investigation, for the rotation pulses, $\tau = 16\,\text{ps}$, resulting in a pulse band width of $\sigma \approx 41\,\mu\text{eV}$. The separation of the target and unwanted transition states is given by $\epsilon = 0.5\,\text{meV}$.

The total angle of rotation is then given by

$$\Theta = \Theta_1 - \Theta_2 = 2\text{arctan}\left(\frac{-\sigma\epsilon}{(\delta-\epsilon)\delta+\sigma^2}\right), \tag{7.4}$$

from which the analytical expression for the detuning required to achieve a given rotation Θ is derived as [177, 254]

$$\delta = \frac{1}{2}\left(\epsilon \pm \sqrt{\epsilon^2 + 4\epsilon\sigma\cot\left(\Theta/2\right) - 4\sigma^2}\right). \tag{7.5}$$

Here, the detuning δ of the pulses, as indicated in Fig. 7.5, adjusts the resulting angle in the z-direction of the Bloch sphere, leading to a rotation by an angle Θ. Both pulses are adjusted equally by the detuning

According to Eq. (7.5), achieving a rotation of $R_\vartheta(\pi)$ necessitates a detuning of $\delta = 3.5\,\mu\text{eV}$. Similarly, for a rotation of $R_\vartheta(\pi/2)$, a detuning of $\delta = -35\,\mu\text{eV}$ is required. However, when comparing these analytical predictions with the numerical results, which assume equal couplings of the pulses to the transitions with consistent signs for all pulses [257], three resonances are observed, as shown in Fig. 7.7. Numerically, the $R_\vartheta(\pi)$ rotation is achieved at $\delta = 1\,\mu\text{eV}$, and the $R_\vartheta(\pi/2)$ rotation at $\delta = -36.4\,\mu\text{eV}$. These slight discrepancies between the analytical and numerical results arise because the analytical formula is derived from a more simplified system that does not account for factors such as the Stark shifts of the pulses, the mixing of the excitation processes, and the equal couplings with the same signs used in the numerical approach. Additionally, a third resonance at $\delta = 45.7\,\mu\text{eV}$ results in a $R_\vartheta(\pi/2)$ rotation.

When losses of the transition states are included as additional radiative decay, significant reductions in rotation fidelities are observed, as indicated by comparing the solid orange lines with the dotted lines. Notably, the fidelity of the $R_\vartheta(\pi)$ rotation is reduced more significantly than that of the $R_\vartheta(\pi/2)$ rotation. Spin dephasing of the ground states is included via an additional Lindblad rate with $\hat{\text{O}} = \sqrt{\gamma_{\text{dep}}}\left(|s\rangle\langle s| - |\text{G}_i\rangle\langle\text{G}_i|\right)$ for $i \in \{1,2\}, s \in \{U,T\}$. The spin dephasing results in slight reductions in rotation fidelity and a general decay of ground state coherences. Spin dephasing is predicted to be more detrimental to the resulting quantum properties, as it primarily causes the decay of state coherences rather than affecting state occupations.

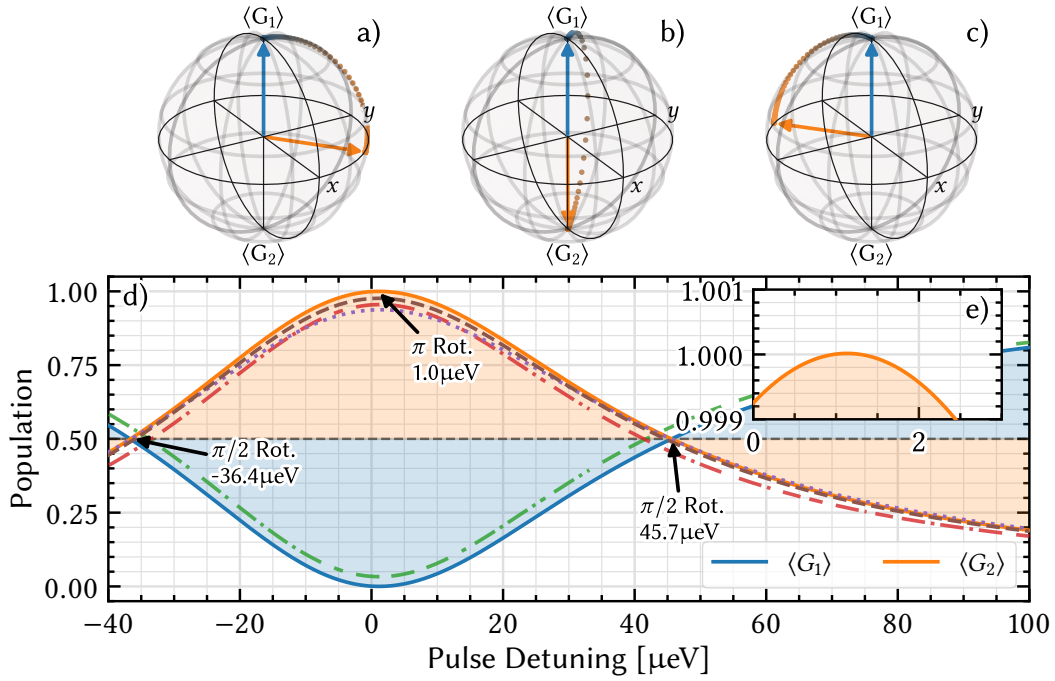

Figure 7.7: Optimal Bloch rotations required for the emission protocol of a 1D linear cluster state. The protocol requires $\Theta = \pi$ and $\Theta = \pi/2$ rotations, mediated by varying the transition pulse detunings. For the former, only one viable configuration exists in the investigated range of pulse detunings, while for the latter, two possible settings are available (compare panels **(a-c)**). In panel **(d)**, a completely lossless system (solid lines) is compared to a system with greatly exaggerated radiative decay of the transition states (dotted lines), spin dephasing of the ground states (dashed lines) and with active electron phonon coupling at a temperature of $T = 4.2\,\mathrm{K}$ using the polaron master equation (dash-dotted lines). In the case with phonons, the settings required to achieve the desired rotations change significantly. The inset in panel **(e)** depicts the slight shift in resonance for a π rotation due to the optical Stark shift of the system. *Reproduced and enhanced from Bauch et al. [187].*

Finally, incorporating electron-phonon coupling using the polaron master equation at a temperature of $T = 4.2\,\mathrm{K}$ reveals that rotation fidelities for $R_\vartheta(\pi)$ rotations are slightly reduced, and the detunings for $R_\vartheta(\pi/2)$ rotations exhibit a redshift of $\approx 5\,\mu\mathrm{eV}$. Illustrative examples of these rotations for a lossless system are presented in Fig. 7.7 in panels (a-c). From this analysis, it can be concluded that using $\delta = 1\,\mu\mathrm{eV}$ for a $R_\vartheta(\pi)$ rotation is optimal. Using $\delta = 45.7\,\mu\mathrm{eV}$ is favorable for the $R_\vartheta(\pi/2)$ rotation, as the pulses are further away from the unwanted transition, resulting in less population loss during the transition phases. When incorporating electron-phonon coupling, this value must be adjusted depending on the temperature.

Simulations for lossless transition states and no electron-phonon coupling are depicted in Fig. 7.6 using the pulse detunings derived in this section. With these parameters, the rotation fidelities are close to unity, surpassing 99.99%. Following the emission protocol in Section 7.4, the system is initialized in a superposition of both ground states at the beginning of the simulation. Then, a π pulse is applied to the cycling transition (red area), followed by the emission of a photon (blue area). An $R_\vartheta(\pi)$ rotation is then applied to the system (green area), resulting in a transitionless rotation that is transferred onto the photon coherences. This emission process repeats until a final $R_\vartheta(\pi/2)$ rotation is applied to the system. From this point, the next emission process begins. This double cycling of the system results in the emission of two time bins, forming the photonic qubit. The correlations of these qubits will be evaluated in the following section.

Interim Summary

The one-dimensional linear cluster state, a specific type of linear graph state, can be generated using a stacked quantum dot setup. This configuration inherently offers an extended Λ-system in its energy structure due to the intrinsic mixing of two spin-hole trions. The ground states are excited with simple pulses, leading to the sequential emission of photons. The Λ-system can be further manipulated using hyperbolic sech-shaped pulses, which facilitate rotations within the electronic coherences. These coherences are then transferred to the emitted photons, resulting in photon trains separated by a distinct time bin length, T_{bin}. Two of these photons form a photonic qubit, and multiple photonic qubits enable the formation of the linear cluster state.

7.6 QuBit Correlations

Now that the emitter has been introduced and the protocol for generating a one-dimensional linear cluster/graph state has been defined, viable parameters for achieving the required rotations have been found and the scheme has been implemented and evaluated over time, the quantum properties of the emitted photons can be assessed. As previously mentioned, the rate of radiative decay is set to $\gamma_{\text{Cyc}} = 1.2\,\mu\text{eV}$, resulting in a complete decay of the respective excited state in about 3.5 ns. This duration is extended to 4 ns to include a buffer for executing the required rotations.

In essence, the objective is to calculate N-photon correlations, resulting in the respective N-photon matrices. However, this task becomes numerically intensive for $N > 2$, undesirable

for $N > 3$, and numerically almost uniterable for $N > 4$ on standard computing hardware. Therefore, this work employs the *stabilizer formalism*, introduced in Section 4.3.2. The expectation values of the stabilizers provide insights into how well the current emission cycles follow the initial emission protocol. This is because the cluster state can be represented by a superposition of multiple stabilizer expressions. Thus, the stabilizers form a basis for the representation of the cluster state. Evaluating the proximity of the actual state at any point during the numerical evaluation to the ideal state provides insights into the fidelity of the process.

For a one-dimensional linear cluster state, the stabilizers are particularly useful. Each node in the cluster state corresponds to a qubit, and each qubit is entangled with its neighboring qubits. The stabilizers for such a state typically include operators that act on adjacent qubits, ensuring that the entanglement structure is maintained throughout the emission process. By measuring the stabilizer operators, a measure for how closely the generated state adheres to the ideal entanglement pattern of a linear cluster state is determined.

In this work, second and third-order correlation functions Eqs. (4.25) and (4.26) are used to calculate elements of the respective 2- or 3-photon matrices. These matrices are then further utilized in the evaluation of the stabilizer expectation values from Eqs. (4.31) and (4.32). The use of these stabilizers allows for an efficient and accurate assessment of the quantum properties of the emitted photons, providing a clear indication of the fidelity and entanglement quality of the generated one-dimensional linear cluster state. With correlation functions up to the third order, the entanglement of much larger trains of photonic qubits can be reliably evaluated. When the expectation values of the stabilizers are high, the temporal entanglement will also be high. This approach ensures that the generated photonic states are suitable for use in quantum information processing applications, where high fidelity and entanglement are crucial.

7.6.1 Phase Dependencies

This section begins by evaluating the first two stabilizers. According to the protocol for generating the cluster state, the first stabilizer expectation value is $\langle \hat{X}\hat{Z} \rangle$. Calculating the expectation value for this stabilizer using the two-photon matrix ρ_{2PM} provides insights into the numerical accuracy of the first $\hat{X}$ rotation and the subsequent $\hat{Z}$ rotation. This expectation value is calculated exclusively for $t_0 = 0$ and requires four time bins — or two photonic qubits — for evaluation.

Next, the second stabilizer expectation value, $\langle \hat{Z}\hat{X}\hat{Z} \rangle$, is investigated. Calculating this expectation value necessitates the three-photon density matrix $\rho_{3\mathrm{PM}}$. Both of these density matrices are evaluated using second- and third-order time-shifted correlation functions, respectively, which were previously introduced in Section 4.3.2. The three-photon density matrix is calculated for $t_0 = 0$. Here, six time bins - or three photonic qubits - are required. Later third order stabilizer expectation values with $t_0 > 0$ are investigated in Section 7.6.3.

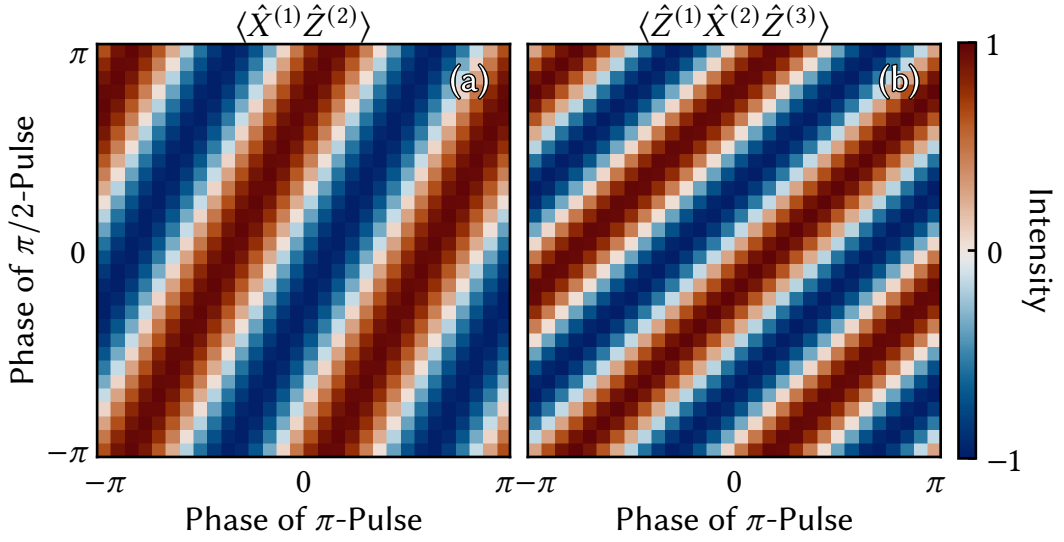

Figure 7.8: Phase dependency of the first stabilizer generator expectation values $\langle \hat{X}\hat{Z} \rangle$ in panel **(a)** and $\langle \hat{Z}\hat{X}\hat{Z} \rangle$ in panel **(b)** for hyperbolic-sec shaped pulses. The phases of both the π as well as the $\pi/2$ rotation pulses are varied along the x- and y-axis, respectively, exploring their impact on the expectation values. Despite the total magnitudes of the $\hat{\Phi} = \cos(\varphi)\hat{X} + i\sin(\varphi)\hat{Y}$ operator remaining close to unity, their real and imaginary components demonstrate notable phase dependencies. *Reproduced from Bauch et al. [187].*

While the Θ rotation is specified by the generation protocol, the ϑ rotation in $R_\vartheta(\Theta)$ can be adjusted. However, a stable ϑ is required for all pulses, meaning it must remain constant between pulses. Adjusting the phase φ of either Ω^i directly translates into the variation of ϑ, as visualized in Fig. 7.8. It becomes evident that as long as φ is consistent across all pulses, the total magnitude of the two stabilizers under investigation does not change significantly. This implies that tuning φ, and thereby ϑ, to maximize the real (or imaginary) parts of the stabilizer expectation values is feasible. Consequently, further research can focus on optimizing the magnitudes of the stabilizer expectation values, as maximizing the individual real or imaginary parts is achievable at all times.

7.6.2 Lossy Systems

In this section, the focus shifts to lossy transition states. Specifically, additional radiative decay mechanisms are introduced for both the target transition state $|T\rangle$ and the unwanted transition state $|U\rangle$. This inclusion reduces the rotation fidelities, as illustrated in Fig. 7.7. Additionally, the decay of spin coherences, referred to as spin-dephasing of the ground states, is investigated by incorporating further Lindblad rates for dephasing across different transitions. The dephasing time can range from a few hundred picoseconds to many nanoseconds [265, 278]. For small loss rates, and thus long lifetimes, the rotation fidelities remain high, achieving efficiencies greater than 99%. However, the stabilizer expectation values can drop significantly below these levels. These investigations provide valuable insights into the fidelity of the stabilizer expectation values and, consequently, the temporal entanglement.

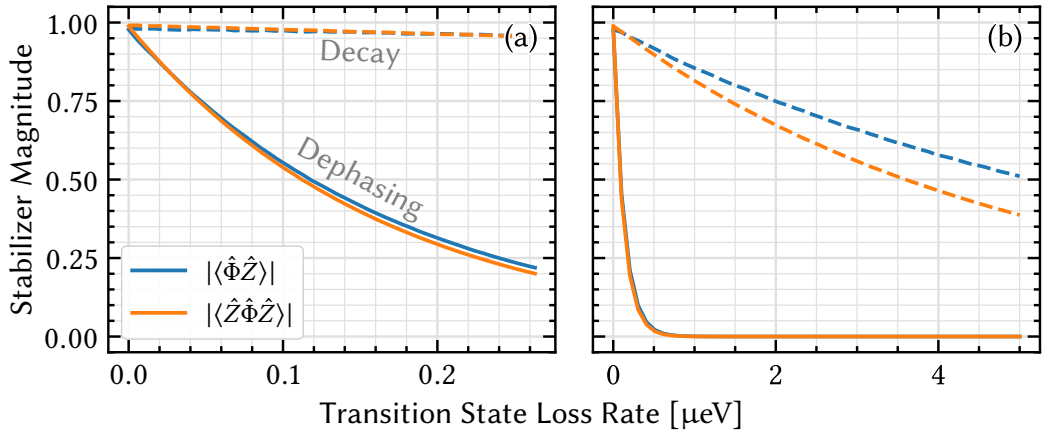

Figure 7.9: Stabilizer magnitudes at different rates of decay and dephasing for small loss rates in panel **(a)** and high loss rates in panel **(b)**. Cases with spin dephasing of the ground states (solid lines) and radiative decay of the transition states (dashed lines) are compared. In panel (b), the two solid curves overlap. *Reproduced from Bauch et al. [187].*

Simulations with either of the available loss mechanisms are shown in Fig. 7.9. Low radiative decay rates do not substantially reduce the magnitudes of the stabilizer expectation values. Even with strong radiative decay rates, reaching up to several μeV, the stabilizer magnitudes only diminish slowly. In contrast, spin dephasing rapidly decreases the magnitudes of the stabilizer expectation values. This effect is similar to the impact of dephasing on concurrence observed in previous chapters. These minimal reductions are due to the rotations occurring over very short time scales. Specifically, the pulse length is set to $\tau = 16\,\text{ps}$, providing insufficient time for radiative decay to significantly impact the system.

Because the correlations must persist through three photonic qubits rather than just two photons, spin dephasing has a more pronounced detrimental effect. Moreover, spin dephasing can be detrimental over extended periods because it occurs continuously, not just during pulse events. Even small spin dephasing values, corresponding to lifetimes on the order of many nanoseconds, significantly reduce the magnitudes of the stabilizer expectation values. This indicates that while the system can tolerate some level of radiative decay, maintaining high stabilizer expectation values requires minimizing spin dephasing to preserve the temporal entanglement essential for the functionality of the linear cluster state.

These findings highlight the importance of carefully managing both radiative decay and spin-dephasing in the design and operation of quantum-dot-based systems for generating photonic cluster states. The insights gained here will be crucial for optimizing the balance between the necessary rotational fidelities and the preservation of stabilizer expectation values, ensuring robust temporal entanglement in practical implementations.

7.6.3 Later Stabilizers

As previously introduced in the phase investigation of the first two stabilizers, it is prudent to evaluate the third-order stabilizer for later triplets of qubits. Specifically, setting $t_0 = 2nT$ allows for the calculation of the third-order stabilizer for subsequent qubits. Here, the notation $\left\langle \hat{Z}^{(i-1)}\hat{X}^{(i)}\hat{Z}^{(i+1)} \right\rangle$ is used, where $i > 0$. Notably, the previously used expectation value $\left\langle \hat{Z}\hat{X}\hat{Z} \right\rangle$ is defined as $\left\langle \hat{Z}^{(1)}\hat{X}^{(2)}\hat{Z}^{(3)} \right\rangle$. In Fig. 7.10, the third-order stabilizer expectation values are investigated for $i \in 1, 15$. The results for a lossless transition are compared with those for a small radiative decay rate of $\gamma_{\mathrm{rad}} = 0.66\,\mu\mathrm{eV}$, which results in a lifetime of the population trapped in the transition and unwanted states of $\tau_{\mathrm{rad}} \approx 1\,\mathrm{ns}$. Additionally, a system suffering from dephasing of the ground state spins with $\gamma_{\mathrm{dep}} = 0.066\,\mu\mathrm{eV}$, corresponding to a spin lifetime of $\tau_{\mathrm{rad}} \approx 13\,\mathrm{ns}$, is investigated.

Extraordinarily, the later stabilizers do not differ significantly from their respective neighbors for both loss mechanisms. This occurs because the stabilizer expectation values employ an initial projection using the $\hat{Z}$ Pauli matrix, resulting in an intrinsic normalization of the three-photon density matrix. Consequently, the entanglement from one qubit to the next is calculated locally in time. This implies that the loss in both mechanisms is similar for the first three qubits compared to the last three qubits investigated, leading to a constant magnitude of the stabilizer expectation values. Therefore, it is sufficient to calculate the

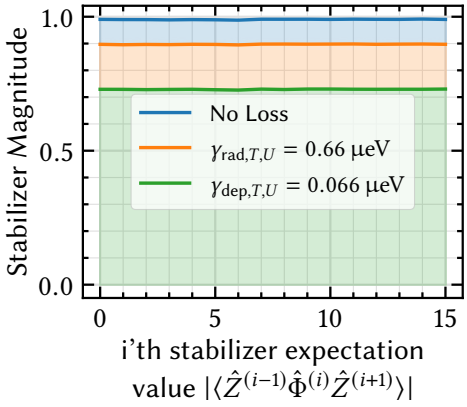

Figure 7.10: Higher order stabilizer generator expectation values for the $\langle \hat{Z}^{(i-1)}\hat{X}^{(i)}\hat{Z}^{(i+1)}\rangle$ stabilizer up to $i = 15$. Results for a lossless system (blue) as well as small radiative decay rates of the transition states (orange) and small rates for the sping dephasing of the ground states (green) are compared. Notable, through all loss mechanisms, the stabilizer magnitudes remain constant. *Reproduced from Bauch et al. [187].*

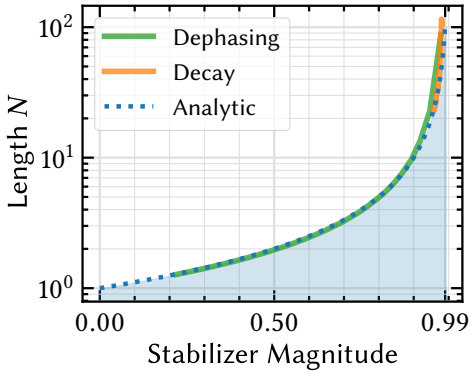

Figure 7.11: Achievable cluster state length for the analytic expression in Eq. (4.35) (blue dotted line). The results for small loss rates for both loss mechanisms (green, orange lines) from Fig. 7.9, panel (a) is overlayed, indicating the range of achievable cluster state length for the investigated scenario. *Reproduced and enhanced from Bauch et al. [187].*

first two stabilizer generator expectation values only, while still being able to assess the entanglement of much larger states.

By using $\langle \hat{X}\hat{Z}\rangle \neq \langle \hat{Z}\hat{X}\hat{Z}\rangle = \langle \hat{Z}^{(i-1)}\hat{X}^{(i)}\hat{Z}^{(i+1)}\rangle$ for all possible i, the lower bound for the achievable length of the one-dimensional linear cluster state can be calculated using Eq. (4.35). For the lossless transition states, the length is $N_{\text{no loss}} < 98$, limited only by the fidelity of the rotation pulses used. Notably, optimizing the pulse bandwidth and detuning can lead to even higher rotation fidelities, which in turn optimizes the length of the cluster state towards unity values. For the proposed rate of radiative decay for the transition and unwanted state, the length results in $N_{\text{Radiative}} < 9$. Here, even slight reductions in the magnitudes of the stabilizer expectation values greatly impact the lower bound of the length. Dephasing has the most detrimental effect, with $N_{\text{Dephasing}} < 3$, highlighting that maximizing the lifetime of the spins is crucial to achieving large cluster states.

In Fig. 7.11, the analytical expression for Eq. (4.35) is displayed on a logarithmic scale. The results from Fig. 7.9 panel (a) are inserted, showcasing the range of achievable lengths using the investigated ranges for loss. Most notably, a strong focus on optimizing the rotation

fidelities is required, where values far above 99.99% are necessary to maximize the cluster state length.

7.7 Concluding the Time Bin Entangled Photon Generation

A spin-hole trion is utilized to generate trains of entangled photons through pulsed transitions and excitations in an extended Λ-system. A viable physical system offering such an energy structure consists of stacked quantum dots. These quantum dots are intentionally slightly misaligned, resulting in the mixing of individual trion wavefunctions. This mixing ultimately leads to the coupling of both systems, forming a Λ-shaped energy structure where each ground state can be individually excited using simple Gaussian or hyperbolic sech-shaped pulses. The decay of the respective excited state leads to photon emission within a defined *time bin*.

The hyperbolic sech-shaped pulses are also employed to induce phase transitions within the ground state coherences, which are then transferred onto the emitted photons. In this specific setup, two emission cycles of photons are used to form a *photonic qubit*. These photonic qubits provide a robust foundation for various applications in quantum information processing.

The primary focus of this section is assessing the degree of entanglement among multiple photonic qubits. These qubits are generated by repeated cycling of the emission protocol designed for a one-dimensional linear cluster state. The protocol involves a specific sequence of rotations within the system, followed by excitation of the ground states and photon emission. The entanglement is assessed by calculating the *stabilizer generator expectation values*. These stabilizer generators form the basis for describing the cluster state, making the evaluation of their expectation values crucial for understanding the fidelity of the generation process.

For lossless rotations within the Λ-system, high degrees of temporal entanglement are reported. This strong entanglement enables the generation of cluster states with nearly triple-digit numbers of qubits. However, introducing losses such as radiative decay of the transition states or spin dephasing of the ground states significantly diminishes the entanglement, reducing the length of the cluster states to single-digit numbers.

The numerical evaluation of the stabilizer generator expectation values proves to be both viable and insightful, allowing for the assessment of entanglement in large numbers of

photons/qubits by only evaluating third-order correlation functions. This advancement brings the evaluation process within a feasible and iterative regime and marks the central result of this chapter and the underlying work [187].

Using a cavity around the extraction level to enhance and accelerate the emission process could be advantageous. This enhancement would likely mitigate the detrimental effects of dephasing by reducing the emission timescales, thereby enabling the creation of larger cluster states. This approach represents a promising direction for future research.

Interim Summary

A system with two stacked quantum dots is designed to create an extended Λ-system, which optically addressed to generate trains of temporally entangled photons, forming a one-dimensional linear cluster state. The cluster state is fundamentally composed of stabilizer generators, whose expectation values are calculated numerically to confirm the temporal entanglement within the cluster state. For lossless systems, the length of these entangled states is primarily limited by the fidelity of the rotation pulses. While minimizing losses is crucial to maintain the entanglement, in all scenarios investigated, even those including strong radiative decay and spin dephasing, achieving multi-partite entanglement is possible.

Conclusion and Outlook 8

Quantum information processing represents an emerging and transformative field with the potential to revolutionize many aspects of the digital world. The challenges of this field range from developing fundamental quantum information carriers and sources to creating complex quantum protocols requiring numerous interconnected carriers.

This thesis focuses on few-photon physics, specifically utilizing photons as information carriers generated from quantum dots and similar structures. Quantum dots, with their deterministic emission characteristics, are particularly well-suited for quantum information theory applications, offering precise control over photon emission.

Quantum dots can be triggered to emit photons using controlled laser pulses. Optical cavities around the quantum dot can be employed to further enhance or modify the emission characteristics, repetition rate and brightness of the photon source. This work introduces several frameworks for investigating quantum dot and cavity dynamics, with a focus on three central topics:

1. Enhancing the Quantum Dot Excitation Using Ultrafast Electric Control

Exciting electron-hole pairs within quantum dots, to form excitons or biexcitons, typically requires resonant laser pulses, followed by spectral or temporal filtering to isolate the desired photon emission from the quantum dot. This becomes particularly challenging when a cavity is used at the same energy level, especially under strong coupling conditions. To address this, the quantum confined Stark shift (QCSS) is employed, introducing a static detuning between the cavity and the quantum dot, enabling high-fidelity excitation of the desired state. The resonance between the dot and cavity is restored using ultrafast electric control through the quantum confined Stark effect, resulting in the emission of photons with high indistinguishability or entanglement. This method also maintains single-photon purity and brightness, even when using high-Q cavities, which typically impede the excitation. Future research involves experimental validation of these theoretical results, along with comparisons between QCSS and other advanced excitation schemes such as SUPER.

2. Achieving Simultaneous Indistinguishability and Entanglement in Two Photon Emission

Traditional quantum dots often emit photons that are either highly indistinguishable or highly entangled, but achieving both properties simultaneously is challenging. This limitation arises from the natural, free emission process, where the biexciton lifetime sets a fundamental bound on the visibility, therefore reducing the indistinguishability. To address this issue, a spectrally broad circular Bragg cavity with high raw light-matter coupling is introduced. This cavity enhances the electronic transitions, enabling the emission of photons that are both indistinguishable and entangled. Maxwell simulations confirm the feasibility of the cavity for experimental implementation while microscopic simulations ensure maximized photon quantum properties. The reference values established in this work lay the groundwork for practical and experimental implementations aimed at achieving simultaneous indistinguishability and entanglement in two-photon emission.

3. Generating One-Dimensional Linear Cluster States Through the Emission of Photon Trains

Moving beyond simple quantum dot cavity structures, a stacked quantum dot system is investigated using spin-hole trions, featuring a Λ-shaped energy configuration. By carefully controlling state coherences with hyperbolic sech-shaped pulses, trains of photons with specific phase relations and timings are generated. Each pair of photons forms a photonic qubit, which holds various applications in quantum information science. Qubit correlations are evaluated using stabilizer generator expectation values, providing insights into the fidelity of the generation of a one dimensional, linear cluster state. Even with significant losses, cluster states of significant length can be produced numerically. This method, which leverages the stabilizer formalism for assessing photonic qubits, opens the door for future exploration of more advanced graph states and their potential experimental implementation.

Methods

The theoretical foundation of this work is built upon the von Neumann equation, with the polaron master equation employed to incorporate electron-phonon coupling. The accuracy of the polaron master equation is validated through numerical comparisons with the more

advanced path integral method, ensuring the reliability of the findings across different modeling techniques. The dual validation of the polaron master equation with the path integral provides confidence in the results obtained for both idealized and realistic scenarios. This detailed analysis of loss mechanisms and electron-phonon interactions will be instrumental in optimizing quantum dot systems for quantum information processing applications.

Initial investigations of ideal systems, without losses or electron-phonon coupling, offer a baseline for understanding the fundamental behavior of quantum dots under optimal conditions. These idealized models provide a foundation for evaluating the more realistic systems explored later in the study. The comparison between ideal and realistic systems demonstrates that the key results remain robust even in the presence of losses and dephasing, highlighting their practical relevance for quantum dot implementations. The inclusion of electron-phonon interactions and realistic loss mechanisms ensures that the results are not only theoretically sound but also experimentally viable.

Outlook

The results of this study offer a foundation for future research in quantum information processing. Further applications of cavity resonators could enhance photon emission processes and facilitate the generation of high-fidelity quantum states. Investigations into alternative quantum dot designs or materials may lead to even greater control over photon properties. Additionally, exploring non-Markovian effects and refining numerical techniques for handling complex quantum systems could yield new insights into quantum dot cavity interactions, supporting and enhancing the findings presented in this work. Finally, experimental validation of the proposed techniques will be crucial in translating the theoretical findings into practical quantum information technologies. These accomplishments provide a valuable contribution to ongoing efforts in both theoretical research and experimental advancements in quantum optics and quantum information science.

Appendix A

This section presents selected extensions of the topics discussed in the main part of this work and serves as a supplementary addition.

A.1 Optical Activity of Excitons

An electron-hole pair bound through Coulomb interactions can be described by the electron-hole exchange Hamiltonian [279], which is given by

$$\mathcal{H}_{\text{exchange}} = -\sum_{i\in x,y,z}\left(a_i J_{h,i} S_{e,i} + b_i J_{h,i}^3 S_{e,i}\right) , \tag{A.1}$$

where $J_{h,i}$ is the hole angular momentum and $S_{e,i}$ is the electron spin, with a_i and b_i representing material-specific constants. For simplification, only the z-components of the angular momenta are considered. The valence band is split into light holes with $|J_{h,z}| = \frac{1}{2}$ and heavy holes with $|J_{h,z}| = \frac{3}{2}$. The electron spin is given by $|S_z| = \frac{1}{2}$.

The total angular momentum of the exciton is expressed as $M = J_{h,z} + S_{e,z}$, where M defines whether the exciton is optically active (bright) or inactive (dark). Dark excitons ($M = \pm 2$) cannot directly couple to photons, while bright excitons ($M = \pm 1$) interact with the electromagnetic field. However, dark excitons can be manipulated by mixing bright and dark states using external fields, such as magnetic fields [280, 281].

The exchange interaction Hamiltonian can be expressed in terms of the exciton basis states $|M\rangle$, specifically $|\pm 1\rangle$ and $|\pm 2\rangle$, under the assumption of no magnetic field and no light-heavy-hole mixing, as

$$\mathcal{H}_{\text{exchange}} = \begin{bmatrix} +\delta_0 & +\delta_- & 0 & 0 \\ +\delta_- & +\delta_0 & 0 & 0 \\ 0 & 0 & -\delta_0 & +\delta_+ \\ 0 & 0 & +\delta_+ & -\delta_0 \end{bmatrix} . \tag{A.2}$$

In this expression, $\delta_0 = \frac{3}{2}\left(a_z + \frac{9}{4}b_z\right)$, and $\delta_\pm = \frac{3}{4}\left(b_x \pm b_y\right)$ [139]. In symmetric quantum dot structures, where $b_x = b_y$, the exciton energies are degenerate. However, for asymmetric quantum dots with $b_x \neq b_y$, fine structure splitting occurs which results in new eigenstates, which are given by

$$|\mathrm{X}_1\rangle = \frac{1}{\sqrt{2}}\left(\mathrm{X}_+ + \mathrm{X}_-\right) \quad \text{and} \quad |\mathrm{X}_2\rangle = \frac{\mathrm{i}}{\sqrt{2}}\left(\mathrm{X}_+ - \mathrm{X}_-\right) . \tag{A.3}$$

These eigenstates correspond to the fine structure split excitons in an asymmetric quantum dot. The Coulomb interaction between electrons and holes in different excitons can result in an attractive force, leading to the formation of a biexciton. This biexciton is a bound state of two excitons, represented as $|\mathrm{X}_1\rangle \otimes |\mathrm{X}_2\rangle$, with the binding energy lowering the total energy of the biexciton.

A.2 Details on the Concurrence

This chapter provides an overview of the numerical calculation and simplification of concurrence, a key measure in evaluating quantum entanglement.

A.2.1 Spin-Flip Two-Photon Matrix

The spin-flip matrix used in the calculation of concurrence is first defined. Starting with the Pauli spin matrix σ_i, the matrix σ_y is given by

$$\sigma_y = \begin{pmatrix} 0 & -i \\ i & 0 \end{pmatrix} \tag{A.4}$$

Applying the tensor product of σ_y with itself leads to

$$\sigma_y \otimes \sigma_y = \begin{pmatrix} 0 & 0 & 0 & -1 \\ 0 & 0 & 1 & 0 \\ 0 & 1 & 0 & 0 \\ -1 & 0 & 0 & 0 \end{pmatrix} . \tag{A.5}$$

This matrix forms the basis for calculating the spin-flipped two-photon matrix, which is essential for determining concurrence through the two-photon density matrix.

A.2.2 Fidelity Matrix

The fidelity matrix is defined and investigated in the context of its application in the concurrence calculation. Assuming a general two-photon density matrix (TPM) in a Hilbert space limited to $N = 2$, the TPM is represented as

$$\rho_{\mathrm{TPM}} = \begin{bmatrix} \mathrm{HHHH} & 0 & 0 & \mathrm{HHVV} \\ 0 & \mathrm{HVHV} & \mathrm{VHHV} & 0 \\ 0 & \mathrm{HVVH} & \mathrm{VHVH} & 0 \\ \mathrm{VVHH} & 0 & 0 & \mathrm{VVVV} \end{bmatrix}. \tag{A.6}$$

Here, the off-diagonal elements are zero due to the constraint of $N = 2$, limiting the system to only second-order correlations.

The spin-flipped TPM is calculated by applying Eq. (4.19), resulting in

$$\tilde{\rho}_{\mathrm{TPM}} = \begin{bmatrix} \mathrm{VVVV} & 0 & 0 & \mathrm{VVHH} \\ 0 & \mathrm{VHVH} & \mathrm{HVVH} & 0 \\ 0 & \mathrm{VHHV} & \mathrm{HVHV} & 0 \\ \mathrm{HHVV} & 0 & 0 & \mathrm{HHHH} \end{bmatrix}. \tag{A.7}$$

This transformation corresponds to transposing the matrix along both diagonals, effectively swapping the populations and coherences of the states HH, VV, HV, and VH.

The fidelity matrix $\mathcal{R}$, calculated using Eq. (4.20), measures the similarity between the initial TPM and its spin-flipped counterpart. The concurrence is then defined as a figure of merit, quantifying how much the two matrices differ after the spin-flip operation.

A.2.3 Analytical Concurrence

For a specific two-photon density matrix of the form

$$\rho_{\mathrm{TPM}} = \begin{bmatrix} a & 0 & 0 & c - \mathrm{i}d \\ 0 & 0 & 0 & 0 \\ 0 & 0 & 0 & 0 \\ c + \mathrm{i}d & 0 & 0 & b \end{bmatrix}, \tag{A.8}$$

the eigenvalues of the fidelity matrix $\mathcal{R}$ can be calculated analytically. The magnitude of the coherence term is given by $|\varepsilon| = \sqrt{(c - \mathrm{i}d)(c + \mathrm{i}d)}$. Solving for the eigenvalues then

yields

$$\begin{aligned}\lambda_1 &= 0\\ \lambda_2 &= 0\\ \lambda_3 &= \sqrt{ab} - |\varepsilon|\\ \lambda_4 &= \sqrt{ab} + |\varepsilon| \,.\end{aligned} \tag{A.9}$$

From these eigenvalues, the concurrence is determined using Eq. (4.21), resulting in

$$C_{\text{simplified}} = 2|\varepsilon| \,. \tag{A.10}$$

The concurrence is highly dependent on the coherence between the states in the two-photon matrix and is independent of the overall photon intensity in either the horizontal or vertical polarizations. Instead, it is primarily influenced by the maximum degree of coherence between the states. Several methods for approximating concurrence exist [84, 234]. In this work, the analytical expression for concurrence is used mainly for comparison with numerical results, but it is generally not shown in the graphical representations.

A.3 Loss Function for the Maxwell Optimizer

This work employs Bayesian optimization in conjunction with electromagnetic simulations using Meep [282] to optimize optical cavities. The objective is to achieve specific spectral properties and quality factors (Q-factors) within these cavities. The optimization function $f(\mathbf{x})$ is defined as:

$$f(\mathbf{x}) = w_1 \left(\int_{\nu_{\text{min}}}^{\nu_{\text{lb}}} \mathcal{F}_P(\nu)\, \mathrm{d}\nu + \int_{\nu_{\text{ub}}}^{\nu_{\text{max}}} \mathcal{F}_P(\nu)\, \mathrm{d}\nu \right) + w_2 \left| \lambda_{\text{goal}} - \lambda_{\text{result}} \right| \tag{A.11}$$

$$+ w_3 \left| g_{\text{result}} - \alpha \mathcal{F}_P - \beta \right| + w_4 \left(1 - S\left(Q_{\text{result}}; Q_{\text{min}}\right) + S\left(Q_{\text{result}}; Q_{\text{max}}\right)\right) \tag{A.12}$$

where w_i are the weights and $S(x; x_0)$ is the sigmoid function defined as:

$$S(x; x_0) = \frac{1}{1 + e^{-(x - x_0)}}. \tag{A.13}$$

The frequency range of the simulation, ν_{min} and ν_{max}, corresponds to the desired available spectral range around the target mode. The bounds ν_{lb} and ν_{ub} are calculated for a chosen Q_{goal}. The bandwidth $B = \nu_{\text{goal}}/Q_{\text{goal}}$ is simply defined as $\nu_{\text{min}} = \nu_{\text{goal}} - B/2$ and $\nu_{\text{max}} = \nu_{\text{goal}} + B/2$.

The parameters g_{result} and $\mathcal{F}_P$ are evaluated at the optimal point, while α and β are obtained from quantum simulations. The quality factor Q_{result} is expected to lie within the desired low-Q region $[Q_{\text{min}}, Q_{\text{max}}]$. For $Q_{\text{result}} > Q_{\text{max}}$, an additional penalty term $w_5(Q_{\text{result}} - Q_{\text{max}})^2$ is included to further penalize high Q-factors.

Meep is an open-source software package for simulating electromagnetic systems using the finite-difference time-domain (FDTD) method [282, 283]. It is widely used for studying photonic crystals, waveguides, resonators, and other optical structures. Bayesian optimization is a strategy for optimizing objective functions that are expensive to evaluate [284–286]. It builds a probabilistic model of the objective function and uses this model to make decisions about where to sample next, thereby efficiently searching the parameter space.

The combination of Meep and Bayesian optimization allows for an efficient and systematic approach to optimizing optical cavities, ensuring that the resulting designs meet the specified criteria for spectral properties and Q-factors [287, 288].

A.4 Numerical Implementation

The numerical implementation of the time evolution for the von Neumann equation in this work is carried out using the RK45 Dormand-Prince method. This method, known for its reliability and accuracy, is particularly well-suited for solving ordinary differential equations (ODEs) numerically. The von Neumann equation, which governs the time evolution of the density matrix $\rho(t)$ in quantum mechanics, can be expressed as

$$\frac{\mathrm{d}\rho(t)}{\mathrm{d}t} = -\frac{i}{\hbar}[\mathcal{H}, \rho(t)] + \mathcal{L}[\rho(t)]\,, \tag{A.14}$$

which is equal to the definition from Eq. (2.8) used in the main text.

Here, $\mathcal{H}$ is the Hamiltonian of the system, $[\mathcal{H}, \rho(t)]$ denotes the commutator of $\mathcal{H}$ and $\rho(t)$, and $\mathcal{L}[\rho(t)]$ represents the Lindblad superoperator that accounts for dissipative processes.

To numerically solve the von Neumann equation, the continuous time evolution is discretized into small time steps. The RK45 Dormand-Prince method, an adaptive step-size integrator, is used to compute the evolution of the density matrix over time. This method provides both the solution and an estimate of the local error, allowing for automatic adjustment of the step size to maintain accuracy while optimizing computational efficiency.

The numerical implementation begins with the initialization phase, where the initial density matrix $\rho(0)$ is defined, and the Hamiltonian $\mathcal{H}$ along with the Lindblad superoperator $\mathcal{L}$ are specified. The RK45 Dormand-Prince method is then employed to integrate the ordinary differential equation (ODE) by combining two different order Runge-Kutta methods. This integration process provides an error estimate and adaptive step size control, ensuring precise calculations. At each time step, the RK45 method computes intermediate stages, which are subsequently combined to update the density matrix.

The time evolution process starts from the initial state $\rho(0)$, and the density matrix is iteratively evolved over each time step t_n to t_{n+1} using the RK45 method. The adaptive step size mechanism ensures that the error remains within a specified tolerance, achieving a balance between precision and computational efficiency. This approach allows for accurate and stable simulations of the time evolution of quantum systems.

A.4.1 Algorithm

The implementation of the RK45 Dormand-Prince method for the time evolution of the von Neumann equation involves several steps. Initially, the intermediate stages are computed as follows:

$$k_1 = f(t_n, \rho_n) \tag{A.15}$$

$$k_2 = f\left(t_n + \frac{1}{5}h, \rho_n + \frac{1}{5}hk_1\right) \tag{A.16}$$

$$k_3 = f\left(t_n + \frac{3}{10}h, \rho_n + \frac{3}{40}hk_1 + \frac{9}{40}hk_2\right) \tag{A.17}$$

$$k_4 = f\left(t_n + \frac{4}{5}h, \rho_n + \frac{44}{45}hk_1 - \frac{56}{15}hk_2 + \frac{32}{9}hk_3\right) \tag{A.18}$$

$$k_5 = f\left(t_n + \frac{8}{9}h, \rho_n + \frac{19372}{6561}hk_1 - \frac{25360}{2187}hk_2 + \frac{64448}{6561}hk_3 - \frac{212}{729}hk_4\right) \tag{A.19}$$

$$k_6 = f\left(t_n + h, \rho_n + \frac{9017}{3168}hk_1 - \frac{355}{33}hk_2 + \frac{46732}{5247}hk_3 + \frac{49}{176}hk_4 - \frac{5103}{18656}hk_5\right) \tag{A.20}$$

$$k_7 = f\left(t_n + h, \rho_n + \frac{35}{384}hk_1 + \frac{500}{1113}hk_3 + \frac{125}{192}hk_4 - \frac{2187}{6784}hk_5 + \frac{11}{84}hk_6\right) \tag{A.21}$$

Next, the density matrix is updated using the calculated intermediate stages:

$$\rho_{n+1} = \rho_n + h\left(\frac{35}{384}k_1 + \frac{500}{1113}k_3 + \frac{125}{192}k_4 - \frac{2187}{6784}k_5 + \frac{11}{84}k_6\right) \tag{A.22}$$

The local error is then estimated:

$$\text{error} = h\left(\frac{71}{57600}k_1 - \frac{71}{16695}k_3 + \frac{71}{1920}k_4 - \frac{17253}{339200}k_5 + \frac{22}{525}k_6 - \frac{1}{40}k_7\right) \tag{A.23}$$

where k_7 is an additional intermediate stage. Finally, the step size is adjusted based on the estimated error:

$$h_{\text{new}} = h \times \min\left(\max\left(dt_{\min}, \left(\frac{\text{tolerance}}{\text{error}}\right)^{1/5}\right), dt_{\max}\right) \tag{A.24}$$

This adaptive step size control ensures the integration maintains the desired accuracy while optimizing computational efficiency. Througout this work, an adaptive tolerance is

used. Because the points in time where high precision is required is available a priori. For sections where high numerical precision is required, for example in the presence of a pulse, or where short timescales apply, such as in the rapid decay of the biexciton in Chapter 6, tolerance $< 1 \cdot 10^{-10}$ is used. Otherwise, tolerance $< 1 \cdot 10^{-6}$ is sufficient for convergent results and faster numerical evaluation. The resulting time step dt is constrained within the bounds of $dt_{\text{min}} = 1\,\text{fs}$ and $dt_{\text{max}} = 5\,\text{ps}$. These constraints are not strictly necessary but are implemented to prevent the simulation from encountering abrupt divergence due to excessively large time steps or from stalling when time steps fall below the floating point precision threshold.

By employing the RK45 Dormand-Prince method, this work ensures precise and efficient numerical simulation of the time evolution of quantum systems, providing a robust framework for exploring quantum dynamics in various scenarios.

The software used for the simulations in this work and the respective publications [145, 174, 187] can be found on Bauch, *QDaCC-Software*, [289].

As a final note, results for chapter Chapter 7 are achieved using dense matrices, which results in significant decreases in the time required for each simulation, while all other results favour sparse matrices for fast evaluation.

Bibliography

B

[1] J. R. Powell, The quantum limit to moore's law, Proceedings of the IEEE **96**, 1247 (2008).

[2] Y. Taur, Cmos design near the limit of scaling, IBM Journal of Research and Development **46**, 213–222 (2002).

[3] H. Ilatikhameneh, T. Ameen, B. Novakovic, Y. Tan, G. Klimeck, and R. Rahman, Saving moore's law down to 1 nm channels with anisotropic effective mass, Scientific reports **6**, 31501 (2016).

[4] Y. Seon, J. Chang, C. Yoo, and J. Jeon, Device and circuit exploration of multi-nanosheet transistor for sub-3 nm technology node, Electronics **10**, 180 (2021).

[5] S. Dey, J. Jena, E. Mohapatra, T. Dash, S. Das, and C. Maiti, Design and simulation of vertically-stacked nanowire transistors at 3 nm technology nodes, Physica Scripta **95**, 014001 (2019).

[6] V. Kashcheyevs and P. Samuelsson, Classical-to-quantum crossover in electron on-demand emission, Physical Review B **95**, 245424 (2017).

[7] T. Beth and G. Leuchs, *Quantum information processing* (Wiley Online Library, 2005).

[8] F. Flamini, N. Spagnolo, and F. Sciarrino, Photonic quantum information processing: a review, Reports on Progress in Physics **82**, 016001 (2018).

[9] C. Monroe, Quantum information processing with atoms and photons, Nature **416**, 238–246 (2002).

[10] I. B. Djordjevic, *Quantum information processing, quantum computing, and quantum error correction: an engineering approach* (Academic Press, 2021).

[11] K. Chen, C.-M. Li, Q. Zhang, Y.-A. Chen, A. Goebel, S. Chen, A. Mair, and J.-W. Pan, Experimental realization of one-way quantum computing with two-photon four-qubit cluster states, Physical Review Letters **99**, 120503 (2007).

[12] Y.-X. Gong, X.-B. Zou, T. C. Ralph, S.-N. Zhu, and G.-C. Guo, Linear optical quantum computation with imperfect entangled photon-pair sources and inefficient non–photon-number-resolving detectors, Physical Review A **81**, 052303 (2010).

[13] Y.-M. He, Y. He, Y.-J. Wei, D. Wu, M. Atatüre, C. Schneider, S. Höfling, M. Kamp, C.-Y. Lu, and J.-W. Pan, On-demand semiconductor single-photon source with near-unity indistinguishability, Nature Nanotechnology **8**, 213 (2013).

[14] T. Jennewein, M. Barbieri, and A. G. White, Single-photon device requirements for operating linear optics quantum computing outside the post-selection basis, Journal of Modern Optics **58**, 276–287 (2011).

[15] R. Raussendorf and H. J. Briegel, A one-way quantum computer, Physical Review Letters **86**, 5188 (2001).

[16] P. Walther, K. J. Resch, T. Rudolph, E. Schenck, H. Weinfurter, V. Vedral, M. Aspelmeyer, and A. Zeilinger, Experimental one-way quantum computing, Nature **434**, 169–176 (2005).

[17] E. Knill, R. Laflamme, and G. J. Milburn, A scheme for efficient quantum computation with linear optics, Nature **409**, 46–52 (2001).

[18] T. Heindel, C. A. Kessler, M. Rau, C. Schneider, M. Fürst, F. Hargart, W.-M. Schulz, M. Eichfelder, R. Roßbach, S. Nauerth, M. Lermer, H. Weier, M. Jetter, M. Kamp, S. Reitzenstein, S. Höfling, P. Michler, H. Weinfurter, and A. Forchel, Quantum key distribution using quantum dot single-photon emitting diodes in the red and near infrared spectral range, New Journal of Physics **14**, 083001 (2012).

[19] Y. Shi, H. S. Poh, A. Ling, and C. Kurtsiefer, Fibre polarisation state compensation in entanglement-based quantum key distribution, Optics Express **29**, 37075–37080 (2021).

[20] M. Bozzio, M. Vyvlecka, M. Cosacchi, C. Nawrath, T. Seidelmann, J. C. Loredo, S. L. Portalupi, V. M. Axt, P. Michler, and P. Walther, Enhancing quantum cryptography with quantum dot single-photon sources, npj Quantum Information **8**, 104 (2022).

[21] N. Gisin, G. Ribordy, W. Tittel, and H. Zbinden, Quantum cryptography, Reviews of Modern Physics **74**, 145 (2002).

[22] T. Jennewein, C. Simon, G. Weihs, H. Weinfurter, and A. Zeilinger, Quantum cryptography with entangled photons, Physical Review Letters **84**, 4729 (2000).

[23] P. Michler, *Quantum dots for quantum information technologies*, Vol. 237 (Springer, 2017).

[24] R. J. Warburton, C. Schäflein, D. Haft, F. Bickel, A. Lorke, K. Karrai, J. M. Garcia, W. Schoenfeld, and P. M. Petroff, Optical emission from a charge-tunable quantum ring, Nature **405**, 926–929 (2000).

[25] F. T. Pedersen, Y. Wang, C. T. Olesen, S. Scholz, A. D. Wieck, A. Ludwig, M. C. Löbl, R. J. Warburton, L. Midolo, R. Uppu, and P. Lodahl, Near transform-limited quantum dot linewidths in a broadband photonic crystal waveguide, ACS Photonics **7**, 2343–2349 (2020).

[26] N. Tomm, S. Mahmoodian, N. O. Antoniadis, R. Schott, S. R. Valentin, A. D. Wieck, A. Ludwig, A. Javadi, and R. J. Warburton, Photon bound state dynamics from a single artificial atom, Nature Physics **19**, 857–862 (2023).

[27] H. Wunderlich, C. Wunderlich, K. Singer, and F. Schmidt-Kaler, Two-dimensional cluster-state preparation with linear ion traps, Physical Review A **79**, 052324 (2009).

[28] D. I. Schuster, A. A. Houck, J. A. Schreier, A. Wallraff, J. M. Gambetta, A. Blais, L. Frunzio, J. Majer, B. Johnson, M. H. Devoret, S. M. Girvin, and R. J. Schoelkopf, Resolving photon number states in a superconducting circuit, Nature **445**, 515–518 (2007).

[29] R. Sobolewski, A. Verevkin, G. Gol'tsman, A. Lipatov, and K. Wilsher, Ultrafast superconducting single-photon optical detectors and their applications, IEEE Transactions on Applied Superconductivity **13**, 1151–1157 (2003).

[30] C. M. Natarajan, M. G. Tanner, and R. H. Hadfield, Superconducting nanowire single-photon detectors: physics and applications, Superconductor Science and Technology **25**, 063001 (2012).

[31] Y. Li, F. Qian, J. Xiang, and C. M. Lieber, Nanowire electronic and optoelectronic devices, Materials Today **9**, 18 (2006).

[32] J. F. Neto, M. Bundgaard-Nielsen, N. Gregersen, and L. Vannucci, The 1d photonic wire as a single-photon source: implications of cqed to a phonon bath of reduced dimensionality, arXiv preprint arXiv:2407.14462 (2024).

[33] C. Santori, D. Fattal, S. M. Spillane, M. Fiorentino, R. G. Beausoleil, A. D. Greentree, P. Olivero, M. Draganski, J. R. Rabeau, P. Reichart, B. C. Gibson, S. Rubanov, D. N. Jamieson, and S. Prawer, Coherent population trapping in diamond nv centers at zero magnetic field, Optics Express **14**, 7986–7994 (2006).

[34] U. Banin, Y. Cao, D. Katz, and O. Millo, Identification of atomic-like electronic states in indium arsenide nanocrystal quantum dots, Nature **400**, 542 (1999).

[35] T. K. Bracht, T. Seidelmann, T. Kuhn, V. M. Axt, and D. E. Reiter, Phonon wave packet emission during state preparation of a semiconductor quantum dot using different schemes, Physica Status Solidi B **259**, 2100649 (2022).

[36] W. W. Chow and F. Jahnke, On the physics of semiconductor quantum dots for applications in lasers and quantum optics, Progress in Quantum Electronics **37**, 109–184 (2013).

[37] K. A. Fischer, L. Hanschke, M. Kremser, J. J. Finley, K. Müller, and J. Vučković, Pulsed Rabi oscillations in quantum two-level systems: beyond the area theorem, Quantum Science and Technology **3**, 014006 (2017).

[38] K. Hennessy, A. Badolato, M. Winger, D. Gerace, M. Atatüre, S. Gulde, S. Fält, E. L. Hu, and A. Imamoğlu, Quantum nature of a strongly coupled single quantum dot–cavity system, Nature **445**, 896 (2007).

[39] A. V. Kuhlmann, J. H. Prechtel, J. Houel, A. Ludwig, D. Reuter, A. D. Wieck, and R. J. Warburton, Transform-limited single photons from a single quantum dot, Nature Communications **6**, 8204 (2015).

[40] P. Michler, A. Kiraz, C. Becher, W. Schoenfeld, P. Petroff, L. Zhang, E. Hu, and A. Imamoglu, A quantum dot single-photon turnstile device, Science **290**, 2282–2285 (2000).

[41] P. Senellart, G. Solomon, and A. White, High-performance semiconductor quantum-dot single-photon sources, Nature Nanotechnology **12**, 1026 (2017).

[42] P. Lodahl, Quantum-dot based photonic quantum networks, Quantum Science and Technology **3**, 013001 (2017).

[43] M. Oxborrow and A. G. Sinclair, Single-photon sources, Contemporary Physics **46**, 173 (2005).

[44] L. Hanschke, K. A. Fischer, S. Appel, D. Lukin, J. Wierzbowski, S. Sun, R. Trivedi, J. Vučković, J. J. Finley, and K. Müller, Quantum dot single-photon sources with ultra-low multi-photon probability, npj Quantum Information **4**, 43 (2018).

[45] C. Santori, M. Pelton, G. Solomon, Y. Dale, and Y. Yamamoto, Triggered single photons from a quantum dot, Physical Review Letters **86**, 1502 (2001).

[46] N. Somaschi, V. Giesz, L. De Santis, J. C. Loredo, M. P. Almeida, G. Hornecker, S. L. Portalupi, T. Grange, C. Antón, J. Demory, C. Gómez, I. Sagnes, N. D. Lanzillotti-Kimura, A. Lemaítre, A. Auffeves, A. G. White, L. Lanco, and P. Senellart, Near-optimal single-photon sources in the solid state, Nature Photonics **10**, 340 (2016).

[47] Y. Lu, A. Bengtsson, J. J. Burnett, B. Suri, S. R. Sathyamoorthy, H. R. Nilsson, M. Scigliuzzo, J. Bylander, G. Johansson, and P. Delsing, Quantum efficiency, purity and stability of a tunable, narrowband microwave single-photon source, npj Quantum Information **7**, 140 (2021).

[48] C. Santori, D. Fattal, J. Vučković, G. S. Solomon, and Y. Yamamoto, Indistinguishable photons from a single-photon device, Nature **419**, 594–597 (2002).

[49] N. Tomm, A. Javadi, N. O. Antoniadis, D. Najer, M. C. Löbl, A. R. Korsch, R. Schott, S. R. Valentin, A. D. Wieck, A. Ludwig, and R. J. Warburton, A bright and fast source of coherent single photons, Nature Nanotechnology **16**, 399–403 (2021).

[50] H. Wang, Y.-M. He, T.-H. Chung, H. Hu, Y. Yu, S. Chen, X. Ding, M.-C. Chen, J. Qin, X. Yang, R.-Z. Liu, Z.-C. Duan, J.-P. Li, S. Gerhardt, K. Winkler, J. Jurkat, L.-J. Wang, N. Gregersen, Y.-H. Huo, Q. Dai, S. Yu, S. Höfling, C.-Y. Lu, and J.-W. Pan, Towards optimal single-photon sources from polarized microcavities, Nature Photonics **13**, 770–775 (2019).

[51] F. Sbresny, L. Hanschke, E. Schöll, W. Rauhaus, B. Scaparra, K. Boos, E. Zubizarreta Casalengua, H. Riedl, E. del Valle, J. J. Finley, K. D. Jöns, and K. Müller, Stimulated generation of indistinguishable single photons from a quantum ladder system, Physical Review Letters **128**, 093603 (2022).

[52] L. Mandel, Coherence and indistinguishability, Optical Letters **16**, 1882 (1991).

[53] P. K. Pathak and S. Hughes, Coherently triggered single photons from a quantum-dot cavity system, Physical Review B **82**, 045308 (2010).

[54] M. Reindl, J. H. Weber, D. Huber, C. Schimpf, S. F. Covre da Silva, S. L. Portalupi, R. Trotta, P. Michler, and A. Rastelli, Highly indistinguishable single photons from incoherently excited quantum dots, Physical Review B **100**, 155420 (2019).

[55] J. Liu, R. Su, Y. Wei, B. Yao, S. F. C. d. Silva, Y. Yu, J. Iles-Smith, K. Srinivasan, A. Rastelli, J. Li, and X. Wang, A solid-state source of strongly entangled photon pairs with high brightness and indistinguishability, Nature Nanotechnology **14**, 586–593 (2019).

[56] C. H. Bennett and G. Brassard, Quantum cryptography: public key distribution and coin tossing, Theoretical Computer Science **560**, 7–11 (2014).

[57] H. J. Kimble, The quantum internet, Nature **453**, 1023 (2008).

[58] A. Ruskuc, C.-J. Wu, J. Rochman, J. Choi, and A. Faraon, Nuclear spin-wave quantum register for a solid-state qubit, Nature **602**, 408–413 (2022).

[59] C. Hopfmann, W. Nie, N. L. Sharma, C. Weigelt, F. Ding, and O. G. Schmidt, Maximally entangled and gigahertz-clocked on-demand photon pair source, Physical Review B **103**, 075413 (2021).

[60] D. Huber, M. Reindl, S. F. Covre da Silva, C. Schimpf, J. Martin-Sánchez, H. Huang, G. Piredda, J. Edlinger, A. Rastelli, and R. Trotta, Strain-tunable GaAs quantum dot: a nearly dephasing-free source of entangled photon pairs on demand, Physical Review Letters **121**, 033902 (2018).

[61] A. Furusawa, J. L. Sørensen, S. L. Braunstein, C. A. Fuchs, H. J. Kimble, and E. S. Polzik, Unconditional quantum teleportation, Science **282**, 706 (1998).

[62] Q. Ruihong and M. Ying, "Research progress of quantum repeaters", in Journal of physics: conference series, Vol. 1237, 5 (IOP Publishing, 2019), p. 052032.

[63] K. Azuma, S. E. Economou, D. Elkouss, P. Hilaire, L. Jiang, H.-K. Lo, and I. Tzitrin, Quantum repeaters: from quantum networks to the quantum internet, Reviews of Modern Physics **95**, 045006 (2023).

[64] A. Broadbent and C. Schaffner, Quantum cryptography beyond quantum key distribution, Designs, Codes and Cryptography **78**, 351–382 (2016).

[65] R. Renner, Security of quantum key distribution, International Journal of Quantum Information **6**, 1–127 (2008).

[66] B. M. Terhal, Quantum error correction for quantum memories, Reviews of Modern Physics **87**, 307–346 (2015).

[67] D. A. Lidar and T. A. Brun, *Quantum error correction* (Cambridge university press, 2013).

[68] A. Harrow, P. Hayden, and D. Leung, Superdense coding of quantum states, Physical Review Letters **92**, 187901 (2004).

[69] C. H. Bennett, G. Brassard, and A. K. Ekert, Quantum cryptography, Scientific American **267**, 50–57 (1992).

[70] T. Monz, D. Nigg, E. A. Martinez, M. F. Brandl, P. Schindler, R. Rines, S. X. Wang, I. L. Chuang, and R. Blatt, Realization of a scalable shor algorithm, Science **351**, 1068–1070 (2016).

[71] E. Gerjuoy, Shor's factoring algorithm and modern cryptography. an illustration of the capabilities inherent in quantum computers, American Journal of Physics **73**, 521–540 (2005).

[72] Y. Wang and P. S. Krstic, Prospect of using grover's search in the noisy-intermediate-scale quantum-computer era, Physical Review A **102**, 042609 (2020).

[73] R. Hafenbrak, S. Ulrich, P. Michler, L. Wang, A. Rastelli, and O. Schmidt, Triggered polarization-entangled photon pairs from a single quantum dot up to 30 k, New Journal of Physics **9**, 315 (2007).

[74] E. Schöll, L. Schweickert, L. Hanschke, K. D. Zeuner, F. Sbresny, T. Lettner, R. Trivedi, M. Reindl, S. F. Covre da Silva, R. Trotta, J. J. Finley, J. Vu čkovi ć, K. Müller, A. Rastelli, V. Zwiller, and K. D. Jöns, Crux of using the cascaded emission of a three-level quantum ladder system to generate indistinguishable photons, Physical Review Letters **125**, 233605 (2020).

[75] D. Huber, M. Reindl, Y. Huo, H. Huang, J. S. Wildmann, O. G. Schmidt, A. Rastelli, and R. Trotta, Highly indistinguishable and strongly entangled photons from symmetric gaas quantum dots, Nature Communications **8**, 1–7 (2017).

[76] D. Huber, M. Reindl, J. Aberl, A. Rastelli, and R. Trotta, Semiconductor quantum dots as an ideal source of polarization-entangled photon pairs on-demand: a review, Journal of Optics **20**, 073002 (2018).

[77] G. Juska, V. Dimastrodonato, L. O. Mereni, A. Gocalinska, and E. Pelucchi, Towards quantum-dot arrays of entangled photon emitters, Nature Photonics **7**, 527–531 (2013).

[78] D. Koutnỳ, L. Ginés, M. Moczała-Dusanowska, S. Höfling, C. Schneider, A. Predojević, and M. Ježek, Deep learning of quantum entanglement from incomplete measurements, Science Advances **9**, eadd7131 (2023).

[79] J.-W. Pan, Z.-B. Chen, C.-Y. Lu, H. Weinfurter, A. Zeilinger, and M. Żukowski, Multiphoton entanglement and interferometry, Reviews of Modern Physics **84**, 777 (2012).

[80] T. Praschan, D. Heinze, D. Breddermann, A. Zrenner, A. Walther, and S. Schumacher, Pulse shaping for on-demand emission of single raman photons from a quantum-dot biexciton, Physical Review B **105**, 045302 (2022).

[81] M. Varnava, D. E. Browne, and T. Rudolph, How good must single photon sources and detectors be for efficient linear optical quantum computation?, Physical Review Letters **100**, 060502 (2008).

[82] S. Bounouar, M. Müller, A. M. Barth, M. Glässl, V. M. Axt, and P. Michler, Phonon-assisted robust and deterministic two-photon biexciton preparation in a quantum dot, Physical Review B **91**, 161302 (2015).

[83] D. A. Vajner, L. Rickert, T. Gao, K. Kaymazlar, and T. Heindel, Quantum communication using semiconductor quantum dots, Advanced Quantum Technologies **5**, 2100116 (2022).

[84] D. Heinze, D. Breddermann, A. Zrenner, and S. Schumacher, A quantum dot single-photon source with on-the-fly all-optical polarization control and timed emission, Nature Communications **6**, 8473 (2015).

[85] L. Schweickert, K. D. Jöns, K. D. Zeuner, S. F. Covre da Silva, H. Huang, T. Lettner, M. Reindl, J. Zichi, R. Trotta, A. Rastelli, and V. Zwiller, On-demand generation of background-free single photons from a solid-state source, Applied Physics Letters **112**, 093106 (2018).

[86] H. Wang, H. Hu, T.-H. Chung, J. Qin, X. Yang, J.-P. Li, R.-Z. Liu, H.-S. Zhong, Y.-M. He, X. Ding, Y.-H. Deng, Q. Dai, Y.-H. Huo, S. Höfling, C.-Y. Lu, and J.-W. Pan, On-demand semiconductor source of entangled photons which simultaneously has high fidelity, efficiency, and indistinguishability, Physical Review Letters **122**, 113602 (2019).

[87] D. Breddermann, T. Praschan, D. Heinze, R. Binder, and S. Schumacher, Microscopic theory of cavity-enhanced single-photon emission from optical two-photon raman processes, Physical Review B **97**, 125303 (2018).

[88] H. Jayakumar, A. Predojević, T. Huber, T. Kauten, G. S. Solomon, and G. Weihs, Deterministic photon pairs and coherent optical control of a single quantum dot, Physical Review Letters **110**, 135505 (2013).

[89] L. Rickert, F. Betz, M. Plock, S. Burger, and T. Heindel, High-performance designs for fiber-pigtailed quantum-light sources based on quantum dots in electrically-controlled circular bragg gratings, Optics Express **31**, 14750–14770 (2023).

[90] S. Strauf, N. G. Stoltz, M. T. Rakher, L. A. Coldren, P. M. Petroff, and D. Bouwmeester, High-frequency single-photon source with polarization control, Nature Photonics **1**, 704–708 (2007).

[91] A. Widhalm, A. Mukherjee, S. Krehs, N. Sharma, P. Kölling, A. Thiede, D. Reuter, J. Förstner, and A. Zrenner, Ultrafast electric phase control of a single exciton qubit, Applied Physics Letters **112**, 111105 (2018).

[92] R. Joos, S. Bauer, C. Rupp, S. Kolatschek, W. Fischer, C. Nawrath, P. Vijayan, R. Sittig, M. Jetter, S. L. Portalupi, and P. Michler, Triggered telecom C-band single-photon source with high brightness, high indistinguishability and sub-GHz spectral linewidth, arXiv preprint arXiv:2310.20647 (2023).

[93] S. Kolatschek, C. Nawrath, S. Bauer, J. Huang, J. Fischer, R. Sittig, M. Jetter, S. L. Portalupi, and P. Michler, Bright purcell enhanced single-photon source in the telecom o-band based on a quantum dot in a circular bragg grating, Nano Letters **21**, 7740–7745 (2021).

[94] C. Nawrath, F. Olbrich, M. Paul, S. L. Portalupi, M. Jetter, and P. Michler, Coherence and indistinguishability of highly pure single photons from non-resonantly and resonantly excited telecom c-band quantum dots, Applied Physics Letters **115**, 023103 (2019).

[95] R. Sittig, C. Nawrath, S. Kolatschek, S. Bauer, R. Schaber, J. Huang, P. Vijayan, P. Pruy, S. L. Portalupi, M. Jetter, and P. Michler, Thin-film ingaas metamorphic buffer for telecom c-band inas quantum dots and optical resonators on gaas platform, Nanophotonics **11**, 1109–1116 (2022).

[96] M. Ward, M. Dean, R. Stevenson, A. Bennett, D. Ellis, K. Cooper, I. Farrer, C. Nicoll, D. Ritchie, and A. Shields, Coherent dynamics of a telecom-wavelength entangled photon source, Nature Communications **5**, 3316 (2014).

[97] S. L. Portalupi, M. Jetter, and P. Michler, Inas quantum dots grown on metamorphic buffers as non-classical light sources at telecom c-band: a review, Semiconductor Science and Technology, 053001 (2019).

[98] W. Nolting, *Grundkurs Theoretische Physik 5/1 : Quantenmechanik - Grundlagen*, 7th ed., Springer-Lehrbuch (Berlin, Heidelberg : Springer-Verlag, 2009), pp. 85, 215.

[99] W. Nolting, *Grundkurs Theoretische Physik 6 : Statistische Physik*, 5. Auflage, Springer-Lehrbuch (Berlin, Heidelberg : Springer-Verlag Berlin Heidelberg, 2005).

[100] P. Chin, "Luminescent properties of semiconductor nanocrystals", Phd Thesis 1 (Research TU/e / Graduation TU/e) (Chemical Engineering and Chemistry, 2008).

[101] C. Kittel and P. McEuen, *Introduction to solid state physics* (John Wiley & Sons, 2018).

[102] K. Kang, A. Kepner, S. Gaponenko, S. W. Koch, Y. Hu, and N. Peyghambarian, Confinement-enhanced biexciton binding energy in semiconductor quantum dots, Physical Review B **48**, 15449 (1993).

[103] F. Jahnke, *Quantum optics with semiconductor nanostructures* (Elsevier, 2012).

[104] S. Stufler, P. Machnikowski, P. Ester, M. Bichler, V. M. Axt, T. Kuhn, and A. Zrenner, Two-photon rabi oscillations in a single $In_xGa_{1-x}As/GaAs$ quantum dot, Physical Review B **73**, 125304 (2006).

[105] L. Zhai, M. C. Löbl, G. N. Nguyen, J. Ritzmann, A. Javadi, C. Spinnler, A. D. Wieck, A. Ludwig, and R. J. Warburton, Low-noise GaAs quantum dots for quantum photonics, Nature Communications **11**, 4745 (2020).

[106] C. Bardot, M. Schwab, M. Bayer, S. Fafard, Z. Wasilewski, and P. Hawrylak, Exciton lifetime in inas/gaas quantum dot molecules, Physical Review B **72**, 035314 (2005).

[107] P. W. Fry, I. E. Itskevich, D. J. Mowbray, M. S. Skolnick, J. J. Finley, J. A. Barker, E. P. O'Reilly, L. R. Wilson, I. A. Larkin, P. A. Maksym, M. Hopkinson, M. Al-Khafaji, J. P. R. David, A. G. Cullis, G. Hill, and J. C. Clark, Inverted electron-hole alignment in InAs-GaAs self-assembled quantum dots, Physical Review Letters **84**, 733–736 (2000).

[108] S. Boyle, A. Ramsay, A. Fox, and M. Skolnick, Two-color two-photon rabi oscillation of biexciton in single InAs/GaAs quantum dot, Physica E: Low-Dimensional Systems and Nanostructures **42**, 2485 (2010).

[109] F. Ding, R. Singh, J. D. Plumhof, T. Zander, V. K řápek, Y. H. Chen, M. Benyoucef, V. Zwiller, K. Dörr, G. Bester, A. Rastelli, and O. G. Schmidt, Tuning the exciton binding energies in single self-assembled InGaAs/GaAs quantum dots by piezoelectric-induced biaxial stress, Physical Review Letters **104**, 067405 (2010).

[110] A. Laucht, N. Hauke, J. M. Villas-Bôas, F. Hofbauer, G. Böhm, M. Kaniber, and J. J. Finley, Dephasing of exciton polaritons in photoexcited InGaAs quantum dots in GaAs nanocavities, Physical Review Letters **103**, 087405 (2009).

[111] M. C. Löbl, S. Scholz, I. Söllner, J. Ritzmann, T. Denneulin, A. Kovács, B. E. Kardynał, A. D. Wieck, A. Ludwig, and R. J. Warburton, Excitons in InGaAs quantum dots without electron wetting layer states, Communications Physics **2**, 93 (2019).

[112] K. Roy-Choudhury and S. Hughes, Quantum theory of the emission spectrum from quantum dots coupled to structured photonic reservoirs and acoustic phonons, Physical Review B **92**, 205406 (2015).

[113] L. Tang, R. Ji, X. Cao, J. Lin, H. Jiang, X. Li, K. S. Teng, C. M. Luk, S. Zeng, J. Hao, and S. P. Lau, Deep ultraviolet photoluminescence of water-soluble self-passivated graphene quantum dots, ACS nano **6**, 5102–5110 (2012).

[114] L. Tang, R. Ji, X. Li, G. Bai, C. P. Liu, J. Hao, J. Lin, H. Jiang, K. S. Teng, Z. Yang, and S. P. Lau, Deep ultraviolet to near-infrared emission and photoresponse in layered n-doped graphene quantum dots, ACS nano **8**, 6312–6320 (2014).

[115] Y. Dong, H. Pang, S. Ren, C. Chen, Y. Chi, and T. Yu, Etching single-wall carbon nanotubes into green and yellow single-layer graphene quantum dots, Carbon **64**, 245–251 (2013).

[116] A. Graf, D. Sonnenberg, V. Paulava, A. Schliwa, C. Heyn, and W. Hansen, Excitonic states in gaas quantum dots fabricated by local droplet etching, Physical Review B **89**, 115314 (2014).

[117] K. Lim, H. S. Jang, and K. Woo, Synthesis of blue emitting inp/zns quantum dots through control of competition between etching and growth, Nanotechnology **23**, 485609 (2012).

[118] A. Alshaikh, R. H. Blick, and C. Heyn, Gaas cone-shell quantum dots in a lateral electric field: exciton stark-shift, lifetime, and fine-structure splitting, Nanomaterials **14**, 1174 (2024).

[119] Y. Pu, F. Cai, D. Wang, J.-X. Wang, and J.-F. Chen, Colloidal synthesis of semiconductor quantum dots toward large-scale production: a review, Industrial & Engineering Chemistry Research **57**, 1790–1802 (2018).

[120] S. B. Brichkin and V. F. Razumov, Colloidal quantum dots: synthesis, properties and applications, Russian Chemical Reviews **85**, 1297 (2016).

[121] C. R. Kagan, L. C. Bassett, C. B. Murray, and S. M. Thompson, Colloidal quantum dots as platforms for quantum information science, Chemical reviews **121**, 3186–3233 (2020).

[122] P. Holewa, S. Kadkhodazadeh, M. Gawełczyk, P. Baluta, A. Musiał, V. G. Dubrovskii, M. Syperek, and E. Semenova, Droplet epitaxy symmetric inas/inp quantum dots for quantum emission in the third telecom window: morphology, optical and electronic properties, Nanophotonics **11**, 1515–1526 (2022).

[123] T. Frey, P. Leek, M. Beck, A. Blais, T. Ihn, K. Ensslin, and A. Wallraff, Dipole coupling of a double quantum dot to a microwave resonator, Physical Review Letters **108**, 046807 (2012).

[124] E. T. Jaynes and F. W. Cummings, Comparison of quantum and semiclassical radiation theories with application to the beam maser, Proceedings of the IEEE **51**, 89–109 (1963).

[125] P. Meystre and M. Sargent, *Elements of quantum optics* (Springer Science & Business Media, 2007).

[126] L. Vannucci and N. Gregersen, Highly efficient and indistinguishable single-photon sources via phonon-decoupled two-color excitation, Physical Review B **107**, 195306 (2023).

[127] Y.-J. Wei, Y.-M. He, M.-C. Chen, Y.-N. Hu, Y. He, D. Wu, C. Schneider, M. Kamp, S. Höfling, C.-Y. Lu, and J.-W. Pan, Deterministic and robust generation of single photons from a single quantum dot with 99.5% indistinguishability using adiabatic rapid passage, Nano Letters **14**, 6515–6519 (2014).

[128] M. Gschrey, A. Thoma, P. Schnauber, M. Seifried, R. Schmidt, B. Wohlfeil, L. Krüger, J. .-. Schulze, T. Heindel, S. Burger, F. Schmidt, A. Strittmatter, S. Rodt, and S. Reitzenstein, Highly indistinguishable photons from deterministic quantum-dot microlenses utilizing three-dimensional in situ electron-beam lithography, Nature Communications **6**, 7662 (2015).

[129] X. Ding, Y. He, Z.-C. Duan, N. Gregersen, M.-C. Chen, S. Unsleber, S. Maier, C. Schneider, M. Kamp, S. Höfling, C.-Y. Lu, and J.-W. Pan, On-demand single photons with high extraction efficiency and near-unity indistinguishability from a resonantly driven quantum dot in a micropillar, Physical Review Letters **116**, 020401 (2016).

[130] B. Da Lio, C. Faurby, X. Zhou, M. L. Chan, R. Uppu, H. Thyrrestrup, S. Scholz, A. D. Wieck, A. Ludwig, P. Lodahl, and L. Midolo, A pure and indistinguishable single-photon source at telecommunication wavelength, Advanced Quantum Technologies **5**, 2200006 (2022).

[131] Y. Ota, S. Iwamoto, N. Kumagai, and Y. Arakawa, Spontaneous two-photon emission from a single quantum dot, Physical Review Letters **107**, 233602 (2011).

[132] E. del Valle, S. Zippilli, F. P. Laussy, A. Gonzalez-Tudela, G. Morigi, and C. Tejedor, Two-photon lasing by a single quantum dot in a high-q microcavity, Physical Review B **81**, 035302 (2010).

[133] Y. Chen, M. Zopf, R. Keil, F. Ding, and O. G. Schmidt, Highly-efficient extraction of entangled photons from quantum dots using a broadband optical antenna, Nature Communications **9**, 2994 (2018).

[134] M. Zeeshan, N. Sherlekar, A. Ahmadi, R. L. Williams, and M. E. Reimer, Proposed scheme to generate bright entangled photon pairs by application of a quadrupole field to a single quantum dot, Physical Review Letters **122**, 227401 (2019).

[135] S. E. Thomas, M. Billard, N. Coste, S. C. Wein, Priya, H. Ollivier, O. Krebs, L. Tazaïrt, A. Harouri, A. Lemaitre, I. Sagnes, C. Anton, L. Lanco, N. Somaschi, J. C. Loredo, and P. Senellart, Bright polarized single-photon source based on a linear dipole, Physical Review Letters **126**, 233601 (2021).

[136] N. Gisin and R. Thew, Quantum communication, Nature Photonics **1**, 165 (2007).

[137] A. Vaziri, G. Weihs, and A. Zeilinger, Experimental two-photon, three-dimensional entanglement for quantum communication, Physical Review Letters **89**, 240401 (2002).

[138] B. D. Gerardot, S. Seidl, P. A. Dalgarno, R. J. Warburton, D. Granados, J. M. Garcia, K. Kowalik, O. Krebs, K. Karrai, A. Badolato, and P. M. Petroff, Manipulating exciton fine structure in quantum dots with a lateral electric field, Applied Physics Letters **90**, 041101 (2007).

[139] M. Bayer, G. Ortner, O. Stern, A. Kuther, A. A. Gorbunov, A. Forchel, P. Hawrylak, S. Fafard, K. Hinzer, T. L. Reinecke, S. N. Walck, J. P. Reithmaier, F. Klopf, and F. Schäfer, Fine structure of neutral and charged excitons in self-assembled In(Ga)As/(Al)GaAs quantum dots, Physical Review B **65**, 195315 (2002).

[140] S. Schumacher, J. Förstner, A. Zrenner, M. Florian, C. Gies, P. Gartner, and F. Jahnke, Cavity-assisted emission of polarization-entangled photons from biexcitons in quantum dots with fine-structure splitting, Optics Express **20**, 5335–5342 (2012).

[141] S. Schumacher, J. Förstner, A. Zrenner, M. Florian, C. Gies, P. Gartner, and F. Jahnke, Cavity-assisted emission of polarization-entangled photons from biexcitons in quantum dots with fine-structure splitting, Optics Express **20**, 5335–5342 (2012).

[142] D. Heinze, A. Zrenner, and S. Schumacher, Polarization-entangled twin photons from two-photon quantum-dot emission, Physical Review B **95**, 245306 (2017).

[143] F. Hargart, M. Müller, K. Roy-Choudhury, S. L. Portalupi, C. Schneider, S. Höfling, M. Kamp, S. Hughes, and P. Michler, Cavity-enhanced simultaneous dressing of quantum dot exciton and biexciton states, Physical Review B **93**, 115308 (2016).

[144] J. P. Reithmaier, G. Sęk, A. Löffler, C. Hofmann, S. Kuhn, S. Reitzenstein, L. V. Keldysh, V. D. Kulakovskii, T. L. Reinecke, and A. Forchel, Strong coupling in a single quantum dot–semiconductor microcavity system, Nature **432**, 197 (2004).

[145] D. Bauch, D. Heinze, J. Förstner, K. D. Jöns, and S. Schumacher, Ultrafast electric control of cavity mediated single-photon and photon-pair generation with semiconductor quantum dots, Physical Review B **104**, 085308 (2021).

[146] M. Moczała-Dusanowska, Ł. Dusanowski, O. Iff, T. Huber, S. Kuhn, T. Czyszanowski, C. Schneider, and S. Höfling, Strain-tunable single-photon source based on a circular bragg grating cavity with embedded quantum dots, ACS Photonics **7**, 3474–3480 (2020).

[147] C. Roy and S. Hughes, Influence of electron–acoustic-phonon scattering on intensity power broadening in a coherently driven quantum-dot–cavity system, Physical Review X **1**, 021009 (2011).

[148] M. Glässl, A. M. Barth, and V. M. Axt, Proposed robust and high-fidelity preparation of excitons and biexcitons in semiconductor quantum dots making active use of phonons, Physical Review Letters **110**, 147401 (2013).

[149] R. Manson, K. Roy-Choudhury, and S. Hughes, Polaron master equation theory of pulse-driven phonon-assisted population inversion and single-photon emission from quantum-dot excitons, Physical Review B **93**, 155423 (2016).

[150] Z. X. Koong, E. Scerri, M. Rambach, M. Cygorek, M. Brotons-Gisbert, R. Picard, Y. Ma, S. I. Park, J. D. Song, E. M. Gauger, and B. D. Gerardot, Coherent dynamics in quantum emitters under dichromatic excitation, Physical Review Letters **126**, 047403 (2021).

[151] C. Gustin and S. Hughes, Efficient pulse-excitation techniques for single photon sources from quantum dots in optical cavities, Advanced Quantum Technologies **3**, 1900073 (2020).

[152] T. Kaldewey, S. Lüker, A. V. Kuhlmann, S. R. Valentin, A. Ludwig, A. D. Wieck, D. E. Reiter, T. Kuhn, and R. J. Warburton, Coherent and robust high-fidelity generation of a biexciton in a quantum dot by rapid adiabatic passage, Physical Review B **95**, 161302 (2017).

[153] C. Gustin and S. Hughes, Pulsed excitation dynamics in quantum-dot–cavity systems: limits to optimizing the fidelity of on-demand single-photon sources, Physical Review B **98**, 045309 (2018).

[154] T. Seidelmann, C. Schimpf, T. K. Bracht, M. Cosacchi, A. Vagov, A. Rastelli, D. E. Reiter, and V. M. Axt, Two-photon excitation sets limit to entangled photon pair generation from quantum emitters, Physical Review Letters **129**, 193604 (2022).

[155] T. Seidelmann, M. Cosacchi, M. Cygorek, D. E. Reiter, A. Vagov, and V. M. Axt, Different types of photon entanglement from a constantly driven quantum emitter inside a cavity, Advanced Quantum Technologies **4**, 2000108 (2020).

[156] J. Iles-Smith, D. P. McCutcheon, A. Nazir, and J. Mørk, Phonon scattering inhibits simultaneous near-unity efficiency and indistinguishability in semiconductor single-photon sources, Nature Photonics **11**, 521 (2017).

[157] J. H. Quilter, A. J. Brash, F. Liu, M. Glässl, A. M. Barth, V. M. Axt, A. J. Ramsay, M. S. Skolnick, and A. M. Fox, Phonon-assisted population inversion of a single InGaAs/GaAs quantum dot by pulsed laser excitation, Physical Review Letters **114**, 137401 (2015).

[158] Y.-M. He, H. Wang, C. Wang, M.-C. Chen, X. Ding, J. Qin, Z.-C. Duan, S. Chen, J.-P. Li, R.-Z. Liu, C. Schneider, M. Atatüre, S. Höfling, C.-Y. Lu, and J.-W. Pan, Coherently driving a single quantum two-level system with dichromatic laser pulses, Nature Physics **15**, 941–946 (2019).

[159] T. Kaldewey, S. Lüker, A. V. Kuhlmann, S. R. Valentin, J.-M. Chauveau, A. Ludwig, A. D. Wieck, D. E. Reiter, T. Kuhn, and R. J. Warburton, Demonstrating the decoupling regime of the electron-phonon interaction in a quantum dot using chirped optical excitation, Physical Review B **95**, 241306 (2017).

[160] C.-M. Simon, T. Belhadj, B. Chatel, T. Amand, P. Renucci, A. Lemaitre, O. Krebs, P. A. Dalgarno, R. J. Warburton, X. Marie, and B. Urbaszek, Robust quantum dot exciton generation via adiabatic passage with frequency-swept optical pulses, Physical Review Letters **106**, 166801 (2011).

[161] T. K. Bracht, M. Cosacchi, T. Seidelmann, M. Cygorek, A. Vagov, V. M. Axt, T. Heindel, and D. E. Reiter, Swing-up of quantum emitter population using detuned pulses, PRX Quantum **2**, 040354 (2021).

[162] T. K. Bracht, M. Cygorek, T. Seidelmann, V. M. Axt, and D. E. Reiter, Temperature-independent almost perfect photon entanglement from quantum dots via the super scheme, Optica Quantum **1**, 103–107 (2023).

[163] N. Heinisch, N. Köcher, D. Bauch, and S. Schumacher, Swing-up dynamics in quantum emitter cavity systems: near ideal single photons and entangled photon pairs, Physical Review Research **6**, L012017 (2024).

[164] T. K. Bracht, T. Seidelmann, Y. Karli, F. Kappe, V. Remesh, G. Weihs, V. M. Axt, and D. E. Reiter, Dressed-state analysis of two-color excitation schemes, Physical Review B **107**, 035425 (2023).

[165] K. Boos, F. Sbresny, S. K. Kim, M. Kremser, H. Riedl, F. W. Bopp, W. Rauhaus, B. Scaparra, K. D. Jöns, J. J. Finley, K. Müller, and L. Hanschke, Coherent dynamics of the swing-up excitation technique, arXiv preprint arXiv:2211.14289 (2022).

[166] Y. Karli, F. Kappe, V. Remesh, T. K. Bracht, J. Münzberg, S. Covre da Silva, T. Seidelmann, V. M. Axt, A. Rastelli, D. E. Reiter, and G. Weihs, Super scheme in action: experimental demonstration of red-detuned excitation of a quantum emitter, Nano Letters **22**, 6567–6572 (2022).

[167] D. M. Lukin, A. D. White, R. Trivedi, M. A. Guidry, N. Morioka, C. Babin, Ö. O. Soykal, J. Ul-Hassan, N. T. Son, T. Ohshima, P. K. Vasireddy, M. H. Nasr, S. Sun, J.-P. W. MacLean, C. Dory, E. A. Nanni, J. Wrachtrup, F. Kaiser, and J. Vučković, Spectrally reconfigurable quantum emitters enabled by optimized fast modulation, npj Quantum Information **6**, 80 (2020).

[168] B. Aln, F. Bickel, K. Karrai, R. J. Warburton, and P. M. Petroff, Stark-shift modulation absorption spectroscopy of single quantum dots, Applied Physics Letters **83**, 2235 (2003).

[169] A. F. Jarjour, R. A. Oliver, A. Tahraoui, M. J. Kappers, C. J. Humphreys, and R. A. Taylor, Control of the oscillator strength of the exciton in a single ingan-gan quantum dot, Physical Review Letters **99**, 197403 (2007).

[170] M. Müller, S. Bounouar, K. D. Jöns, M. Glässl, and P. Michler, On-demand generation of indistinguishable polarization-entangled photon pairs, Nature Photonics **8**, 224–228 (2014).

[171] K. D. Zeuner, K. D. Jöns, L. Schweickert, C. Reuterskiöld Hedlund, C. Nuñez Lobato, T. Lettner, K. Wang, S. Gyger, E. Schöll, S. Steinhauer, M. Hammar, and V. Zwiller, On-demand generation of entangled photon pairs in the telecom c-band with inas quantum dots, ACS Photonics **8**, 2337–2344 (2021).

[172] L. Rickert, T. Kupko, S. Rodt, S. Reitzenstein, and T. Heindel, Optimized designs for telecom-wavelength quantum light sources based on hybrid circular bragg gratings, Optics Express **27**, 36824–36837 (2019).

[173] C. Nawrath, H. Vural, J. Fischer, R. Schaber, S. L. Portalupi, M. Jetter, and P. Michler, Resonance fluorescence of single in(ga)as quantum dots emitting in the telecom c-band, Applied Physics Letters **118**, 244002 (2021).

[174] D. Bauch, D. Siebert, K. D. Jöns, J. Förstner, and S. Schumacher, On-demand indistinguishable and entangled photons using tailored cavity designs, Advanced Quantum Technologies **7**, 2300142 (2024).

[175] J. Claes, J. E. Bourassa, and S. Puri, Tailored cluster states with high threshold under biased noise, npj Quantum Information **9**, 9 (2023).

[176] D. Cogan, Z.-E. Su, O. Kenneth, and D. Gershoni, Deterministic generation of indistinguishable photons in a cluster state, Nature Photonics **17**, 324–329 (2023).

[177] A. Vezvaee, E. Takou, P. Hilaire, M. F. Doty, and S. E. Economou, Avoiding leakage and errors caused by unwanted transitions in lambda systems, PRX Quantum **4**, 030312 (2023).

[178] T. K. Bracht, F. Kappe, M. Cygorek, T. Seidelmann, Y. Karli, V. Remesh, G. Weihs, V. M. Axt, and D. E. Reiter, Theory of time-bin entangled photons from quantum emitters, arXiv preprint arXiv:2404.08348 (2024).

[179] T. Huber, A. Predojević, H. Zoubi, H. Jayakumar, G. S. Solomon, and G. Weihs, Measurement and modification of biexciton-exciton time correlations, Optics Express **21**, 9890–9898 (2013).

[180] H. Jayakumar, A. Predojević, T. Kauten, T. Huber, G. S. Solomon, and G. Weihs, Time-bin entangled photons from a quantum dot, Nature Communications **5**, 4251 (2014).

[181] J. Lee, B. Villa, A. Bennett, R. Stevenson, D. Ellis, I. Farrer, D. Ritchie, and A. Shields, A quantum dot as a source of time-bin entangled multi-photon states, Quantum Science and Technology **4**, 025011 (2019).

[182] C. Simon and J.-P. Poizat, Creating single time-bin-entangled photon pairs, Physical Review Letters **94**, 030502 (2005).

[183] K. Tiurev, P. L. Mirambell, M. B. Lauritzen, M. H. Appel, A. Tiranov, P. Lodahl, and A. S. Sørensen, Fidelity of time-bin-entangled multiphoton states from a quantum emitter, Physical Review A **104**, 052604 (2021).

[184] M. Hein, W. Dür, J. Eisert, R. Raussendorf, M. Nest, and H.-J. Briegel, Entanglement in graph states and its applications, arXiv preprint quant-ph/0602096 (2006).

[185] V. Gorini, A. Kossakowski, and E. C. G. Sudarshan, Completely positive dynamical semigroups of n-level systems, Journal of Mathematical Physics **17**, 821 (1976).

[186] G. Tóth and O. Gühne, Entanglement detection in the stabilizer formalism, Physical Review A **72**, 022340 (2005).

[187] D. Bauch, N. Köcher, N. Heinisch, and S. Schumacher, Time-bin entanglement in the deterministic generation of linear photonic cluster states, APL Quantum **1**, 036110 (2024).

[188] M. F. Frenzel, Atoms and photons - their interaction dynamics, arXiv preprint arXiv:1212.4339 (2012).

[189] W. Nolting, *Grundkurs Theoretische Physik 5/2: Quantenmechanik-Methoden und Anwendungen* (Springer, 2012).

[190] K. A. Fischer, K. Müller, K. G. Lagoudakis, and J. Vučković, Dynamical modeling of pulsed two-photon interference, New Journal of Physics **18**, 113053 (2016).

[191] G. Lindblad, On the generators of quantum dynamical semigroups, Communications in Mathematical Physics **48**, 119–130 (1976).

[192] B. Krummheuer, V. M. Axt, and T. Kuhn, Theory of pure dephasing and the resulting absorption line shape in semiconductor quantum dots, Physical Review B **65**, 195313 (2002).

[193] D. Cohen and Y. Imry, Dephasing at low temperatures, Physical Review B **59**, 11143–11146 (1999).

[194] A. J. Ramsay, A. V. Gopal, E. M. Gauger, A. Nazir, B. W. Lovett, A. M. Fox, and M. S. Skolnick, Damping of exciton Rabi rotations by acoustic phonons in optically excited InGaAs/GaAs quantum dots, Physical Review Letters **104**, 017402 (2010).

[195] M. D. Birowosuto, H. Sumikura, S. Matsuo, H. Taniyama, P. J. van Veldhoven, R. Nötzel, and M. Notomi, Fast purcell-enhanced single photon source in 1,550-nm telecom band from a resonant quantum dot-cavity coupling, Scientific Reports **2**, 1–5 (2012).

[196] R. Hekmati, J. P. Hadden, A. Mathew, S. G. Bishop, S. A. Lynch, and A. J. Bennett, Bullseye dielectric cavities for photon collection from a surface-mounted quantum-light-emitter, Scientific Reports **13**, 5316 (2023).

[197] B. W. Shore and P. L. Knight, The jaynes-cummings model, Journal of Modern Optics **40**, 1195–1238 (1993).

[198] C. Nietner, "Quantum phase transition of light in the jaynes-cummings lattice", PhD thesis (Diploma thesis, Freie Universität Berlin, 2010).

[199] E. T. Jaynes and F. W. Cummings, Comparison of quantum and semiclassical radiation theories with application to the beam maser, Proceedings of the IEEE **51**, 89–109 (1963).

[200] T. Stievater, X. Li, D. G. Steel, D. Gammon, D. Katzer, D. Park, C. Piermarocchi, and L. Sham, Rabi oscillations of excitons in single quantum dots, Physical Review Letters **87**, 133603 (2001).

[201] J. Piprek, *Semiconductor optoelectronic devices: introduction to physics and simulation* (Elsevier, 2013).

[202] E. K. Irish, Generalized rotating-wave approximation for arbitrarily large coupling, Physical Review Letters **99**, 173601 (2007).

[203] X. Wang, A. Miranowicz, H.-R. Li, and F. Nori, Observing pure effects of counter-rotating terms without ultrastrong coupling: a single photon can simultaneously excite two qubits, Physical Review A **96**, 063820 (2017).

[204] Y. Wu and X. Yang, Strong-coupling theory of periodically driven two-level systems, Physical Review Letters **98**, 013601 (2007).

[205] P.-L. Ardelt, L. Hanschke, K. A. Fischer, K. Müller, A. Kleinkauf, M. Koller, A. Bechtold, T. Simmet, J. Wierzbowski, H. Riedl, G. Abstreiter, and J. J. Finley, Dissipative preparation of the exciton and biexciton in self-assembled quantum dots on picosecond time scales, Physical Review B **90**, 241404 (2014).

[206] L. Hanschke, T. K. Bracht, E. Schöll, D. Bauch, E. Berger, P. Kallert, M. Peter, A. J. G. J. au2, S. F. C. da Silva, S. Manna, A. Rastelli, S. Schumacher, D. E. Reiter, and K. D. Jöns, Experimental measurement of the reappearance of rabi rotations in semiconductor quantum dots, arXiv preprint arXiv:2409.19167 (2024).

[207] M. Cosacchi, J. Wiercinski, T. Seidelmann, M. Cygorek, A. Vagov, D. Reiter, and V. Axt, On-demand generation of higher-order fock states in quantum-dot–cavity systems, Physical Review Research **2**, 033489 (2020).

[208] C. Roy and S. Hughes, Polaron master equation theory of the quantum-dot mollow triplet in a semiconductor cavity-qed system, Physical Review B **85**, 115309 (2012).

[209] H. Carmichael, *Statistical methods in quantum optics 1: Master equations and Fokker-Planck equations* (Springer-Verlag, Berlin, 1999).

[210] M. Cygorek, J. Keeling, B. W. Lovett, and E. M. Gauger, Sublinear scaling in non-markovian open quantum systems simulations, Physical Review X **14**, 011010 (2024).

[211] J. Wiercinski, E. M. Gauger, and M. Cygorek, Phonon coupling versus pure dephasing in the photon statistics of cooperative emitters, Physical Review Research **5**, 013176 (2023).

[212] T. Seidelmann, F. Ungar, A. M. Barth, A. Vagov, V. M. Axt, M. Cygorek, and T. Kuhn, Phonon-induced enhancement of photon entanglement in quantum dot-cavity systems, Physical Review Letters **123**, 137401 (2019).

[213] M. Cygorek, A. M. Barth, F. Ungar, A. Vagov, and V. M. Axt, Nonlinear cavity feeding and unconventional photon statistics in solid-state cavity qed revealed by many-level real-time path-integral calculations, Physical Review B **96**, 201201 (2017).

[214] C. Gustin and S. Hughes, Influence of electron-phonon scattering for an on-demand quantum dot single-photon source using cavity-assisted adiabatic passage, Physical Review B **96**, 085305 (2017).

[215] D. P. McCutcheon and A. Nazir, Quantum dot rabi rotations beyond the weak exciton-phonon coupling regime, New Journal of Physics **12**, 113042 (2010).

[216] J. Oteo, The baker–campbell–hausdorff formula and nested commutator identities, Journal of Mathematical Physics **32**, 419 (1991).

[217] M. Cygorek and E. M. Gauger, ACE: a general-purpose non-markovian open quantum systems simulation toolkit based on process tensors, arXiv preprint arXiv:2405.19319 (2024).

[218] M. Cosacchi, M. Cygorek, F. Ungar, A. M. Barth, A. Vagov, and V. M. Axt, Path-integral approach for nonequilibrium multitime correlation functions of open quantum systems coupled to markovian and non-markovian environments, Physical Review B **98**, 125302 (2018).

[219] K. A. Fischer, L. Hanschke, J. Wierzbowski, T. Simmet, C. Dory, J. J. Finley, J. Vučković, and K. Müller, Signatures of two-photon pulses from a quantum two-level system, Nature Physics **13**, 649–654 (2017).

[220] R. J. Glauber, The quantum theory of optical coherence, Physical Review **130**, 2529 (1963).

[221] M. Cosacchi, T. Seidelmann, M. Cygorek, A. Vagov, D. E. Reiter, and V. M. Axt, Accuracy of the quantum regression theorem for photon emission from a quantum dot, Physical Review Letters **127**, 100402 (2021).

[222] Y. Ji, Y. Chung, D. Sprinzak, M. Heiblum, D. Mahalu, and H. Shtrikman, An electronic mach–zehnder interferometer, Nature **422**, 415–418 (2003).

[223] J. Rarity, P. Tapster, E. Jakeman, T. Larchuk, R. Campos, M. Teich, and B. Saleh, Two-photon interference in a mach-zehnder interferometer, Physical Review Letters **65**, 1348 (1990).

[224] K. Zetie, S. Adams, and R. Tocknell, How does a mach-zehnder interferometer work?, Physics Education **35**, 46 (2000).

[225] J. Lawall and E. Kessler, Michelson interferometry with 10 pm accuracy, Review of Scientific Instruments **71**, 2669–2676 (2000).

[226] Ø. Langangen, A. Vaskinn, and B.-S. Skagerstam, Interference of light in a michelson-morley interferometer: a quantum optical approach, International Journal of Optics **2012**, 408067 (2012).

[227] E. Moan, R. Horne, T. Arpornthip, Z. Luo, A. Fallon, S. Berl, and C. Sackett, Quantum rotation sensing with dual sagnac interferometers in an atom-optical waveguide, Physical Review Letters **124**, 120403 (2020).

[228] A. Auffèves, B. Besga, J.-M. Gérard, and J.-P. Poizat, Spontaneous emission spectrum of a two-level atom in a very-high-q cavity, Physical Review A **77**, 063833 (2008).

[229] J. Eberly and K. Wodkiewicz, The time-dependent physical spectrum of light, Journal of the Optical Society of America **67**, 1252 (1977).

[230] I. M. Mirza and S. J. van Enk, Single-photon time-dependent spectra in quantum optomechanics, Physical Review A **90** (2014).

[231] G. Khitrova, H. Gibbs, M. Kira, S. W. Koch, and A. Scherer, Vacuum rabi splitting in semiconductors, Nature Physics **2**, 81 (2006).

[232] C.-K. Hong, Z.-Y. Ou, and L. Mandel, Measurement of subpicosecond time intervals between two photons by interference, Physical Review Letters **59**, 2044 (1987).

[233] N. Coste, D. Fioretto, N. Belabas, S. C. Wein, P. Hilaire, R. Frantzeskakis, M. Gundin, B. Goes, N. Somaschi, M. Morassi, A. Lemaître, I. Sagnes, A. Harouri, S. E. Economou, A. Auffeves, O. Krebs, L. Lanco, and P. Senellart, High-rate entanglement between a semiconductor spin and indistinguishable photons, Nature Photonics **17**, 582–587 (2023).

[234] M. Cygorek, F. Ungar, T. Seidelmann, A. M. Barth, A. Vagov, V. M. Axt, and T. Kuhn, Comparison of different concurrences characterizing photon pairs generated in the biexciton cascade in quantum dots coupled to microcavities, Physical Review B **98**, 045303 (2018).

[235] W. K. Wootters, Entanglement of formation of an arbitrary state of two qubits, Physical Review Letters **80**, 2245 (1998).

[236] T. Seidelmann, D. E. Reiter, M. Cosacchi, M. Cygorek, A. Vagov, and V. M. Axt, Time-dependent switching of the photon entanglement type using a driven quantum emitter–cavity system, Applied Physics Letters **118** (2021).

[237] P. Aumann, M. Prilmüller, F. Kappe, L. Ostermann, D. Dalacu, P. J. Poole, H. Ritsch, W. Lechner, and G. Weihs, Demonstration and modeling of time-bin entangled photons from a quantum dot in a nanowire, AIP Advances **12** (2022).

[238] Y. Huo, A. Rastelli, and O. Schmidt, Ultra-small excitonic fine structure splitting in highly symmetric quantum dots on GaAs (001) substrate, Applied Physics Letters **102** (2013).

[239] D. Heinze, "Quantenoptik mit halbleiterquantenpunkten", PhD thesis (Universität Paderborn, 2018).

[240] T. Seidelmann, T. K. Bracht, B. U. Lehner, C. Schimpf, M. Cosacchi, M. Cygorek, A. Vagov, A. Rastelli, D. E. Reiter, and V. M. Axt, Two-photon excitation with finite pulses unlocks pure dephasing-induced degradation of entangled photons emitted by quantum dots, Physical Review B **107**, 235304 (2023).

[241] T. Heindel, A. Thoma, M. von Helversen, M. Schmidt, A. Schlehahn, M. Gschrey, P. Schnauber, J. .-. Schulze, A. Strittmatter, J. Beyer, S. Rodt, A. Carmele, A. Knorr, and S. Reitzenstein, A bright triggered twin-photon source in the solid state, Nature Communications **8**, 14870 (2017).

[242] D. Bauch, D. Heinze, J. Förstner, K. D. Jöns, and S. Schumacher, *Ultrafast electric control of cavity mediated single-photon and photon-pair generation with semiconductor quantum dots* (Zenodo, 2021).

[243] A. Muller, W. Fang, J. Lawall, and G. S. Solomon, Emission spectrum of a dressed exciton-biexciton complex in a semiconductor quantum dot, Physical Review Letters **101**, 027401 (2008).

[244] E. Meyer-Scott, N. Montaut, J. Tiedau, L. Sansoni, H. Herrmann, T. J. Bartley, and C. Silberhorn, Limits on the heralding efficiencies and spectral purities of spectrally filtered single photons from photon-pair sources, Physical Review A **95**, 061803 (2017).

[245] S. Marcet, K. Ohtani, and H. Ohno, Vertical electric field tuning of the exciton fine structure splitting and photon correlation measurements of GaAs quantum dot, Applied Physics Letters **96**, 101117 (2010).

[246] T. Nakaoka, S. Tarucha, and Y. Arakawa, Electrical tuning of the g factor of single self-assembled quantum dots, Physical Review B **76**, 041301 (2007).

[247] A. Ramsay, A review of the coherent optical control of the exciton and spin states of semiconductor quantum dots, Semiconductor Science and Technology **25**, 103001 (2010).

[248] S. Collins, A helium cryostat, Review of Scientific Instruments **18**, 157–167 (1947).

[249] A. Mukherjee, A. Widhalm, D. Siebert, S. Krehs, N. Sharma, A. Thiede, D. Reuter, J. Förstner, and A. Zrenner, Electrically controlled rapid adiabatic passage in a single quantum dot, Applied Physics Letters **116** (2020).

[250] D. Bauch, D. Siebert, K. D. Jöns, J. Förstner, and S. Schumacher, *On-demand indistinguishable and entangled photons at telecom frequencies using tailored cavity designs*, version 1.0 (Zenodo, 2023).

[251] S. Ji, T. Tajiri, H. Kiyama, A. Oiwa, and S. Iwamoto, Design of bull's-eye optical cavity toward efficient quantum media conversion using gate-defined quantum dot, Japanese Journal of Applied Physics **60**, 102003 (2021).

[252] J. Scheuer and A. Yariv, Annular bragg defect mode resonators, Journal of the Optical Society of America B **20**, 2285–2291 (2003).

[253] L. Bremer, C. Jimenez, S. Thiele, K. Weber, T. Huber, S. Rodt, A. Herkommer, S. Burger, S. Höfling, H. Giessen, and S. Reitzenstein, Numerical optimization of single-mode fiber-coupled single-photon sources based on semiconductor quantum dots, Optics Express **30**, 15913–15928 (2022).

[254] A. Vezvaee, P. Hilaire, M. F. Doty, and S. E. Economou, Deterministic generation of entangled photonic cluster states from quantum dot molecules, Physical Review Applied **18**, L061003 (2022).

[255] C. Adelsberger, M. Benito, S. Bosco, J. Klinovaja, and D. Loss, Hole-spin qubits in ge nanowire quantum dots: interplay of orbital magnetic field, strain, and growth direction, Physical Review B **105**, 075308 (2022).

[256] S. E. Economou, J. I. Climente, A. Badolato, A. S. Bracker, D. Gammon, and M. F. Doty, Scalable qubit architecture based on holes in quantum dot molecules, Physical Review B **86**, 085319 (2012).

[257] C. Adambukulam, J. Scott, S. Lim, I. Aharonovich, A. Morello, and A. Laucht, Coherent all-optical control of a solid-state spin via a double Λ-system, arXiv preprint arXiv:2402.00244 (2024).

[258] M. Gimeno-Segovia, T. Rudolph, and S. E. Economou, Deterministic generation of large-scale entangled photonic cluster state from interacting solid state emitters, Physical Review Letters **123**, 070501 (2019).

[259] G. Pieplow, Y. Strocka, M. Isaza-Monsalve, J. H. Munns, and T. Schröder, Deterministic creation of large photonic multipartite entangled states with group-iv color centers in diamond, arXiv preprint arXiv:2312.03952 (2023).

[260] I. Schwartz, D. Cogan, E. R. Schmidgall, Y. Don, L. Gantz, O. Kenneth, N. H. Lindner, and D. Gershoni, Deterministic generation of a cluster state of entangled photons, Science **354**, 434–437 (2016).

[261] D. Istrati, Y. Pilnyak, J. C. Loredo, C. Antón, N. Somaschi, P. Hilaire, H. Ollivier, M. Esmann, L. Cohen, L. Vidro, C. Millet, A. Lemaître, I. Sagnes, A. Harouri, L. Lanco, P. Senellart, and H. S. Eisenberg, Sequential generation of linear cluster states from a single photon emitter, Nature Communications **11**, 5501 (2020).

[262] C.-Y. Lu, X.-Q. Zhou, O. Gühne, W.-B. Gao, J. Zhang, Z.-S. Yuan, A. Goebel, T. Yang, and J.-W. Pan, Experimental entanglement of six photons in graph states, Nature Physics **3**, 91–95 (2007).

[263] Y. Meng, M. L. Chan, R. B. Nielsen, M. H. Appel, Z. Liu, Y. Wang, N. Bart, A. D. Wieck, A. Ludwig, L. Midolo, A. Tiranov, A. S. Sørensen, and P. Lodahl, Deterministic photon source of genuine three-qubit entanglement, arXiv preprint arXiv:2310.12038 (2023).

[264] T. Nutz, A. Milne, P. Shadbolt, and T. Rudolph, Proposal for demonstration of long-range cluster state entanglement in the presence of photon loss, APL Photonics **2**, 066103 (2017).

[265] M. Veldhorst, J. C. C. Hwang, C. H. Yang, A. W. Leenstra, B. de Ronde, J. P. Dehollain, J. T. Muhonen, F. E. Hudson, K. M. Itoh, A. Morello, and A. S. Dzurak, An addressable quantum dot qubit with fault-tolerant control-fidelity, Nature Nanotechnology **9**, 981 (2014).

[266] A.-N. Zhang, C.-Y. Lu, X.-Q. Zhou, Y.-A. Chen, Z. Zhao, T. Yang, and J.-W. Pan, Experimental construction of optical multiqubit cluster states from bell states, Physical Review A **73**, 022330 (2006).

[267] Z. Raissi, E. Barnes, and S. E. Economou, Deterministic generation of qudit photonic graph states from quantum emitters, PRX Quantum **5**, 020346 (2024).

[268] E. Jung, M.-R. Hwang, Y. H. Ju, M.-S. Kim, S.-K. Yoo, H. Kim, D. Park, J.-W. Son, S. Tamaryan, and S.-K. Cha, Greenberger-horne-zeilinger versus w states: quantum teleportation through noisy channels, Physical Review A **78**, 012312 (2008).

[269] S.-B. Zheng, One-step synthesis of multiatom greenberger-horne-zeilinger states, Physical Review Letters **87**, 230404 (2001).

[270] D. Bauch, N. Köcher, N. Heinisch, and S. Schumacher, *Time-bin entanglement in the deterministic generation of linear photonic cluster states* (Zenodo, 2024).

[271] Y. Meng, C. F. D. Faurby, M. L. Chan, P. I. Sund, Z. Liu, Y. Wang, N. Bart, A. D. Wieck, A. Ludwig, L. Midolo, A. S. Sørensen, S. Paesani, and P. Lodahl, Photonic fusion of entangled resource states from a quantum emitter, arXiv preprint arXiv:2312.09070 (2023).

[272] J. C. Adcock, C. Vigliar, R. Santagati, J. W. Silverstone, and M. G. Thompson, Programmable four-photon graph states on a silicon chip, Nature Communications **10**, 3528 (2019).

[273] S. E. Economou, N. Lindner, and T. Rudolph, Optically generated 2-dimensional photonic cluster state from coupled quantum dots, Physical Review Letters **105**, 093601 (2010).

[274] K. Tiurev, M. H. Appel, P. L. Mirambell, M. B. Lauritzen, A. Tiranov, P. Lodahl, and A. S. Sørensen, High-fidelity multiphoton-entangled cluster state with solid-state quantum emitters in photonic nanostructures, Physical Review A **105**, L030601 (2022).

[275] G. Vallone, G. Donati, R. Ceccarelli, and P. Mataloni, Six-qubit two-photon hyperentangled cluster states: characterization and application to quantum computation, Physical Review A **81**, 052301 (2010).

[276] H. J. Briegel and R. Raussendorf, Persistent entanglement in arrays of interacting particles, Physical Review Letters **86**, 910 (2001).

[277] Z.-E. Su, B. Taitler, I. Schwartz, D. Cogan, I. Nassar, O. Kenneth, N. H. Lindner, and D. Gershoni, Continuous and deterministic all-photonic cluster state of indistinguishable photons, arXiv preprint arXiv:2403.03820 (2024).

[278] P. Borri, W. Langbein, S. Schneider, U. Woggon, R. L. Sellin, D. Ouyang, and D. Bimberg, Ultralong dephasing time in InGaAs quantum dots, Physical Review Letters **87**, 157401 (2001).

[279] H. Van Kesteren, E. Cosman, W. Van der Poel, and C. Foxon, Fine structure of excitons in type-ii gaas/alas quantum wells, Physical Review B **41**, 5283 (1990).

[280] M. Reischle, G. Beirne, R. Roßbach, M. Jetter, and P. Michler, Influence of the dark exciton state on the optical and quantum optical properties of single quantum dots, Physical Review Letters **101**, 146402 (2008).

[281] Z. Lu, D. Rhodes, Z. Li, D. V. Tuan, Y. Jiang, J. Ludwig, Z. Jiang, Z. Lian, S.-F. Shi, J. Hone, H. Dery, and D. Smirnov, Magnetic field mixing and splitting of bright and dark excitons in monolayer MoSe2, 2D Materials **7**, 015017 (2019).

[282] A. F. Oskooi, D. Roundy, M. Ibanescu, P. Bermel, J. Joannopoulos, and S. Johnson, Meep: a flexible free-software package for electromagnetic simulations by the fdtd method, Computer Physics Communications **181**, 687–702 (2010).

[283] Dassault Systémes, *CST Microwave Studio*, 2023.

[284] P. I. Frazier, A tutorial on Bayesian optimization, arXiv preprint arXiv:1807.02811 (2018).

[285] J. González, Z. Dai, P. Hennig, and N. D. Lawrence, Batch bayesian optimization via local penalization, Optimisation*.Proceedings of the 19th International Conference on Artificial Intelligence and Statistics, 648–657 (2016).

[286] T. G. authors, *GPyOpt: a bayesian optimization framework in python*, 2016.

[287] P.-I. Schneider, X. Garcia Santiago, V. Soltwisch, M. Hammerschmidt, S. Burger, and C. Rockstuhl, Benchmarking five global optimization approaches for nano-optical shape optimization and parameter reconstruction, ACS Photonics **6**, 2726–2733 (2019).

[288] A. Taflove, A. Oskooi, and S. G. Johnson, *Advances in FDTD computational electrodynamics: photonics and nanotechnology* (Artech house, 2013).

[289] D. Bauch, QDaCC-Software, version qdacc-0.1.7, 10.5281/zenodo.10809242 (2024).

Danksagung

An dieser Stelle möchte ich all jenen meinen tiefsten Dank aussprechen, die mich während meiner Forschungszeit an der Universität Paderborn unterstützt haben.

Mein besonderer Dank gilt Herrn Prof. Dr. Stefan Schumacher, der mir durch seine Unterstützung und Betreuung die Möglichkeit zur Promotion eröffnet hat. Ebenso danke ich den weiteren Gutachtern dieser Arbeit, Herrn Prof. Dr. Klaus D. Jöns, Prof. Dr. Jens Förstner und Dr. Hendrik Rose, für ihre Zeit, ihr wertvolles Feedback und ihre konstruktive Begleitung meines Projekts.

Für die zahlreichen fachlichen Diskussionen und Anregungen, die für den Fortschritt meiner Arbeit von großer Bedeutung waren, möchte ich mich besonders bei Dr. Moritz Cygorek bedanken.

Ein herzlicher Dank gilt auch meinen Kolleginnen und Kollegen, die mich während der Forschungsphase tatkräftig unterstützt und stets motiviert haben. Ebenso möchte ich meinen Freunden und meiner Familie von Herzen danken – insbesondere meiner wundervollen Partnerin Luisa Niggemeier, deren Unterstützung und Geduld während des Schreibens dieser Dissertation von unschätzbarem Wert waren.

Erklärung

Ich versichere, dass ich diese Arbeit selbstständig verfasst und keine anderen Quellen und Hilfsmittel als die angegebenen benutzt habe. Zu diesen Hilfsmitteln zählen auch text- oder bilderstellende KI-Werkzeuge (wie ChatGPT), die ebenfalls in der Arbeit kenntlich gemacht wurden. Die Stellen der Arbeit, die anderen Werken, auch text- oder bilderstellenden KI-Werkzeugen dem Wortlaut oder dem Sinn nach entnommen sind, habe ich in jedem einzelnen Fall unter Angabe der Quelle als Entlehnung kenntlich gemacht. Das Gleiche gilt auch für Zeichnungen, Kartenskizzen und Darstellungen.

Ort, Datum

Unterschrift